Time-critical design methods for suction caisson foundations

Stephen Karl Suryasentana

A dissertation submitted to the
University of Oxford in partial fulfillment
of the requirements for the degree of

Doctor of Philosophy
Engineering Science

Balliol College
Trinity 2018

Time-critical design methods for suction caisson foundations

Stephen Karl Suryasentana

DPhil Engineering Science
Balliol College, University of Oxford
Trinity 2018

Advisors: Prof. Byron W. Byrne, Prof. Harvey J. Burd, Avi Shonberg

Abstract

This thesis is centred around the development of a family of computationally efficient design methods called 'oxCaisson', that can predict the behaviour of suction caisson foundations under six degrees-of-freedom loading. These design methods were developed for applications where timeliness or speed is a crucial factor; hence the term 'time-critical design methods'.

oxCaisson is based on the Winkler framework, in which the soil response is represented by Winkler-type soil reactions that are either distributed along the caisson skirt length or concentrated at the caisson base. These soil reactions were calibrated against the results of rigorous, three-dimensional finite element (3DFE) analyses, making oxCaisson effectively a surrogate model for the 3DFE method.

The design methods developed are hierarchical in nature, where each subsequent design method builds upon previous ones. First, a design method called 'oxCaisson-LE' was developed for a 'toy problem', in which the soil was idealised as a homogeneous, linear elastic material. Then, the assumption of soil stiffness homogeneity is relaxed as an energy-based design method was developed for non-homogeneous stiffness profiles. Following that, the assumption of a fully rigid caisson is relaxed as the caisson skirt is modelled using deformable frame elements, which allows the prediction of flexible caisson behaviour (i.e. caissons with deformable skirts).

Next, a design method called 'oxCaisson-NLE' was developed to predict the caisson behaviour in small-strain, non-linear elastic soil. Then, a new elasto-plastic design method called 'oxCaisson-LEPP' was developed to predict the caisson behaviour in linear elastic, perfectly plastic soil. oxCaisson-LEPP combines the previously developed linear elastic soil reactions with plastic yield surfaces. To model cohesive soil, the plastic yield surfaces were calibrated against 3DFE analyses using linear elastic, perfectly plastic soil with a von Mises yield criterion.

Altogether, these design methods allow a rapid turnover of '3DFE-approximate' design evaluations, which is crucial for time-critical applications such as large scale foundation design optimisation.

Acknowledgements

It is my pleasure to thank the many people and organisations who made this thesis possible. Special thanks go to Ørsted (formerly DONG Energy) for providing me with the generous scholarship that made my DPhil study possible. In particular, I would like to thank everyone in the Geotechnical Engineering and R&D departments at Ørsted for welcoming me in the warmest way possible when I first started.

It is difficult to overstate my gratitude to my advisors, Prof. Byron Byrne, Prof. Harvey Burd and Avi Shonberg for their wonderful supervision throughout the DPhil experience. Thank you Avi for providing crucial, practical advice on my DPhil work and for the many stimulating conversations over geotechnical design. Thank you Harvey for your patience in explaining complicated concepts in the simplest, clearest way possible, for I would have been lost without your guidance. And of course, thank you Byron, for making the DPhil study and scholarship possible. Many thanks for your encouragement and sound advice. I am grateful for your trust in me and for giving me complete academic freedom. My sincere thanks must also go to Dr. Helen Dunne for computing the FELA results presented in Chapter 7 and to Prof. Chris Martin for his valuable feedback on the contents of the same chapter. It had been a wonderful collaboration experience. Many thanks also to my examiners, Prof. Guy Houlsby and Prof. George Mylonakis, for their kind feedback and valuable comments, which has certainly improved the final version of this thesis.

I would also like to thank my undergraduate professors at UWA, Prof. Barry Lehane, Prof. Martin Fahey and Prof. Marco Ghisalberti, for their great teaching, kind assistance with writing recommendation letters, giving wise advice, offering numerous teaching and research opportunities, and so on. My overwhelmingly positive experience in these opportunities had provided me with the confidence to pursue the DPhil study.

I am thankful to my research group peers for providing a fun environment in which to study and work. Many thanks also to the many friends that I have met in Oxford, both in Balliol and St Ebbe's. You have made my Oxford experience more fulfilling than I could ever imagine and I feel blessed to be part of this community.

I am indebted to my family who provided me a fun and supportive environment to grow and learn. Many thanks to my parents who loved me and supported my every decision in my life.

Lastly, and most importantly, I would like to thank my beloved wife Luna for her understanding, encouragement, entertainment and patience, especially during the writing period. Life has been an immense joy after having you in my life. May we grow old together, for the best is yet to be. To you, I dedicate this thesis.

Contents

Chapter 1

Introduction

Wind power, which makes use of wind turbines to convert wind currents into electricity, is one of the most promising sources of renewable energy. It is normally generated in wind farms, which are groups of wind turbines in the same location. These wind farms may be built either onshore or offshore, where the former offers the advantages of lower construction and maintenance costs, while the latter offers the advantages of less aesthetic impact and steadier and stronger wind.

The cost of offshore wind power has dropped substantially over the past few years. In 2012, the UK government had set a target to bring the cost of offshore wind power down by a third to £100/MWh by 2020. However, by 2016 (4 years ahead of schedule), the average cost of offshore wind power had already dropped to £97/MWh (ORE Catapult 2017). The drop in cost of offshore wind power is primarily driven by economies of scale resulting from bigger turbines and larger projects. With fewer turbines generating more power, the costs of installing and maintaining the wind farms are lower.

These offshore wind turbines are usually built on a variety of foundation types, of which the monopile is most commonly used (WindEurope 2017). Monopiles are large-diameter steel tubes that are driven or drilled into the soil to transfer loads to the soil. However, monopile foundations get uneconomically large as the wind turbines get larger and as the water depth increases. Thus, there is increasing interest in an alternative foundation type that might be more economical for larger wind turbines installed in deep waters ($>$ 40 m in water depth). This foundation type is a multi-footing structure founded on suction caissons, such as that shown in Fig. 1.1. A recent deployment of this foundation type is the 'suction bucket jacket' shown in Fig. 1.2, which was installed by Ørsted (formerly

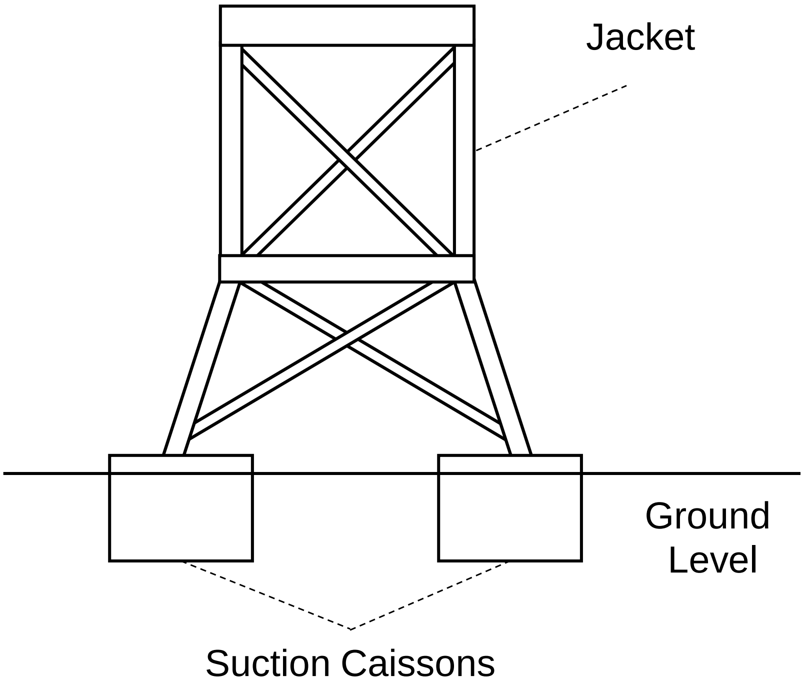

Figure 1.1: A schematic diagram of a multi-footing jacket structure, founded on suction caissons.

DONG Energy) in 2014 at the Borkum Riffgrund 1 wind farm. The suction bucket jacket consists of a three-legged jacket structure founded on suction caissons. While this foundation type has been in use for many years in the oil and gas industry, this was a first for the offshore wind industry. Other foundation types for offshore wind turbines include gravity based foundations, piled jackets, floating foundations etc., and the choice of foundation depends on many factors such as water depth, soil conditions and turbine size.

1.1 Background

A suction caisson (also known as a suction bucket, bucket foundation or skirted foundation) is a circular 'inverted bucket'-like foundation. Its key advantage over monopile foundations is its suction-aided installation process. After an initial penetration into the seabed under its own weight, water trapped inside the caisson is pumped out, which creates a differential of fluid pressure between the inside and outside of the caisson. This pressure differential forces the remainder of the caisson into the ground, as shown in Fig. 1.3. An added advantage is that this process can be reversed to uninstall the caission, making decommissioning easy. For installation in sand, the pressure differential also induces seepage

Figure 1.2: The suction bucket jacket structure deployed by Ørsted (formerly DONG Energy) at the Borkum Riffgrund 1 wind farm. (Source: Ørsted)

flow that reduces the penetration resistance at the tip and along the inner skirt, aiding the installation process (Houlsby & Byrne 2005*b*).

Suction caissons are primarily used as anchors for offshore oil and gas structures (Bye et al. 1995, Byrne & Houlsby 2003, Houlsby, Ibsen & Byrne 2005). However, they are highly suited for the offshore wind industry for many reasons. First, there is a growing trend of wind turbines getting larger. This may result in traditional monopile foundations becoming uneconomically large. Second, as more offshore wind farms move into deeper waters, the installation costs for monopile foundations may exceed that of caisson-based foundations. This is because the installation process for suction caissons is much faster

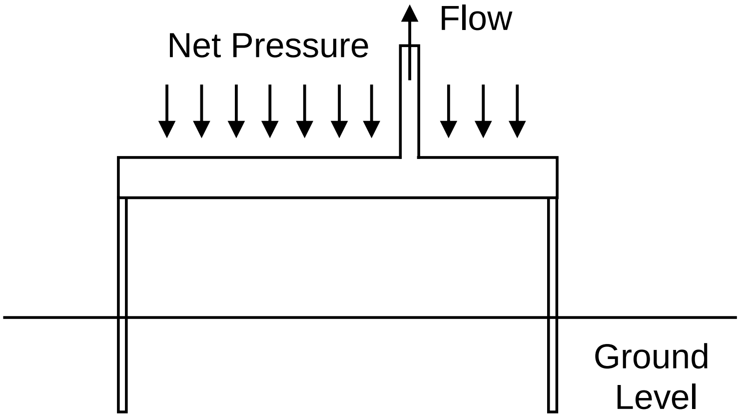

Figure 1.3: A schematic diagram of the suction-aided installation process of a suction caisson.

and requires less expensive equipment than that for monopile foundations. A caisson-based foundation can be deployed and installed within a few hours in a single operation, while a monopile foundation involves multiple operations that could take several days to complete, which might be exacerbated by weather-related delays (Byrne et al. 2000). Finally, environmental regulations in some countries (e.g. Germany) restrict the amount of noise allowable during installation. This is not an issue with suction caissons as the noise generated during installation is below the maximum allowable noise limits. In contrast, expensive, specialised equipment is usually needed to reduce the noise generated by the driving installation process for monopile foundations. This additional equipment cost may render monopile foundations less economical than caisson-based foundations.

1.1.1 Motivation

Given the favourable outlook for caisson-based foundations in the offshore wind industry, it is important that suitable design methods are in place to support their deployment in the years to come. However, the existing design methods for suction caissons are either accurate but slow, or fast but limited in accuracy (in the sense that they are only accurate for limited ground profiles and loading conditions). This is not an issue for the oil and gas industry as suction caissons are typically used for a few one-off structures, where accurate but slow design methods suffice. Note that accuracy here refers to the correctness of the solution to the assumed, and usually simplified, model representation of the real world problem, rather than how well the solution matches reality.

However, computational efficiency is a core requirement for the design of a wind farm, as this is a large scale design problem involving hundreds of foundations. The optimisation process for a wind farm design (including foundation sizing, wind farm layout etc.) requires numerous iterations to obtain the optimal design solution. For a large wind farm project, the set of all feasible design solutions (termed the 'candidate space') may be very large. Thus, the time required to search through the candidate space for the optimal solution may be impractically long, if the design method for the foundation is slow.

This issue may be mitigated by applying some engineering judgment (e.g. consider only a small number of the foundation size possibilities) or using some fast but less accurate design methods to reduce the candidate space into a smaller set of shortlisted design solutions (termed the 'shortlisted space'). The shortlisted space represents the set of potentially optimal design solutions, which can then be explored using accurate but slow design methods (such as the three-dimensional finite element (3DFE) method) to obtain the final optimal design. The risk here is of course the inaccuracy of the judgment or design methods used in the shortlisting process, which may render the final solution obtained as suboptimal, resulting in lost opportunity costs. Thus, this research is motivated by the need for fast and accurate design methods to produce large scale, optimal designs for caisson-based offshore wind farms.

1.1.2 Proposed Solution

A family of computationally efficient design methods for suction caisson foundations called 'oxCaisson' is developed. These design methods are highly suited for time-critical applications such as large scale foundation design optimisation (hence the term 'time-critical design methods'). Unlike existing design methods that are fast but limited in accuracy, oxCaisson is more general and may be used to predict caisson behaviour in most ground conditions of practical importance (homogeneous, non-homogeneous, multi-layered) and for the complete six degrees-of-freedom (6DoF) loading. Furthermore, oxCaisson is both fast and accurate, offering approximately the same level of accuracy as rigorous 3DFE analyses. This is achieved by calibrating oxCaisson against the results of 3DFE analyses, making it effectively a surrogate model of the 3DFE method.

The key benefit of oxCaisson is that it is less likely for the true optimal design solution

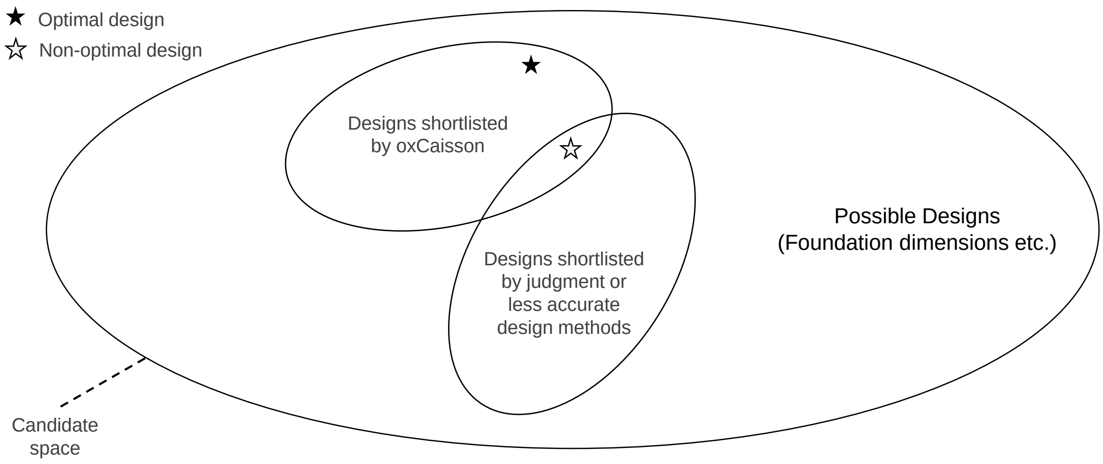

Figure 1.4: Potential miss of the true optimal design solution during the design process, due to the lack of availability of fast and accurate design methods.

to be missed in the shortlisting process (see Fig. 1.4), as the candidate space can be searched more thoroughly and accurately.

1.2 Design Methods

Definition 1.1 (Limit state) *A limit state is a condition beyond which a structure (or part of it) exceeds a specified design requirement.*

In general, the design process for a foundation (post-installation) encompasses satisfaction of three key limit states: fatigue limit state (FLS), serviceability limit state (SLS) and ultimate limit state (ULS). FLS corresponds to the cumulative damage in the structure due to repeated loads, SLS corresponds to the allowable displacement or deformation of the structure for normal use, and ULS corresponds to the ultimate resistance for carrying loads. Fig. 1.5 shows an idealised representation of the typical load-displacement behaviour of a foundation under the various limit states. Under FLS, the foundation behaviour is approximated as being linear elastic, as the applied loads on the foundation are in the lower ends of the range expected during its lifetime. Under SLS, the foundation behaviour starts exhibiting non-linearity, as the applied loads exceed the linear elastic range. Under ULS, the foundation reaches its ultimate load capacity and excessive displacements occur.

Analysis of suction caisson foundations in each of the limit states may be accomplished by various design methods, which range in complexity, accuracy and efficiency. This sec-

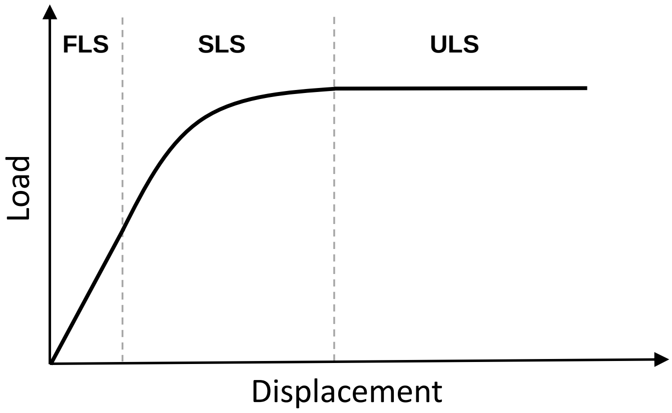

Figure 1.5: Idealised load-displacement behaviour of a foundation under the various limit states (FLS, SLS, ULS).

tion briefly reviews the existing design methods for caissons, before elaborating on the proposed oxCaisson approach. This review is not exhaustive and is restricted to existing design methods that can assess the foundation behaviour under FLS, SLS and ULS conditions. Thus, this excludes design methods such as limit analysis, which can only assess foundation behaviour under ULS conditions (Aubeny et al. 2003, Aubeny & Murff 2005).

1.2.1 Macro-element Model

The macro-element model (also known as the force resultant model) is widely used to describe the behaviour of shallow foundations, including suction caissons. In this model, the foundation behaviour is represented purely in terms of the resultant global forces and moments and the corresponding displacements. No attempt is made to model the elemental soil-foundation behaviour. Its main advantages are its simplicity (brought about by the parsimony of the model inputs and outputs), its computational efficiency (due to the small dimensionality of the model input space) and the ease of coupling with structural analysis programs. Over the years, elasto-plastic macro-element models for various types of shallow foundations (e.g. surface foundations, spudcan foundations) have been developed for clay (e.g. Martin 1994, Martin & Houlsby 2001) and sand (e.g. Byrne 2000, Houlsby & Cassidy 2002, Cassidy et al. 2002, 2004, Bienen et al. 2006). Macro-element models have been proposed by Cassidy et al. (2006) and Foglia et al. (2015) for suction caissons in clay and sand respectively. The key components of these models are:

1. A yield surface (or failure envelope) to define the maximum allowable load combinations. A hardening law is also usually defined to control the expansion or contraction of the yield surface.

2. A flow rule to define the plastic displacements during yielding.
3. A linear elastic stiffness matrix to define the elastic behaviour within the yield surface.

The macro-element model seems to be the ideal model, given its simplicity, efficiency and ease of coupling with structural analysis programs. However, it does have one key drawback: it tends to be 'overfitted' to the calibration data (which usually use highly idealised soil profiles that may not agree well with real-world soil profiles). While the model works well for inputs that are similar to that found in the calibration data, it tends to perform poorly for model inputs that are significantly different. For example, a macro-element model that had been calibrated for continuously varying, non-homogeneous soil profiles may not perform well for multi-layered, non-homogeneous soil profiles (e.g. see the performance of the Doherty et al. (2005) macro-element model in Suryasentana et al. (2017)). This disadvantage limits the use of macro-element models to selected situations where the foundation and soil properties are similar to that found in the calibration data.

1.2.2 Winkler Model

The Winkler model is widely used to describe the behaviour of deep foundations. For example, the *p*-*y* and *t*-*z* methods (e.g. Kraft et al. 1981, Murchison & O'Neill 1983, API 2002, DNV 2013) are commonly used to predict the behaviour of piles under lateral and axial loads respectively. The main attractions of the Winkler model are its simplicity and computational efficiency. This model essentially replaces the soil continuum with a series of independent 'springs' distributed along the foundation length, each of which represents the local soil reaction. In accordance to the Winkler hypothesis, the local soil reaction is defined to be a function of only the local soil displacement. For most existing Winkler models, the function is a non-linear one, where the soil reaction response is similar to that shown in Fig. 1.5 (i.e. there is a linear component, followed by a non-linear component and finally, an ultimate limit).

A key advantage of the Winkler model is that it tends to be more general than macro-element models. In other words, it may be used in a lot more situations than the macro-element model. Unlike macro-element models, the soil reactions in the Winkler models can be properly calibrated such that they are approximately decoupled from the foundation properties. In contrast, macro-element models tightly couple the soil and foundation properties in their calibrated parameters, as these parameters represent the combined deformation of the soil and foundation. Thus, a macro-element model that is calibrated using a rigid foundation would not be accurate for assessment of a flexible foundation. In contrast, a reasonably good approximation of the flexible foundation behaviour can be obtained using the Winkler model, simply by using appropriate deformable elements to represent the flexible foundation and leaving the soil reactions unchanged.

Furthermore, as the soil reactions of the Winkler model are calibrated on a local level, the Winkler model enables local optimisation of the foundation dimensions, such as varying wall thickness along the monopile foundation length (Kallehave et al. 2015). Another benefit is that the Winkler model can be applied directly for any arbitrary soil profile, although the predicted foundation behaviour may depart from its true behaviour in a continuum as the Winkler hypothesis ignores the interaction between each spring.

A four-spring Winkler model for laterally loaded caisson foundations was introduced in recent works (Gerolymos & Gazetas 2006*a*,*b*,*c*, Varun et al. 2009), which is similar to the PISA design method (Byrne et al. 2015, 2017) for laterally loaded monopile foundations with low length-to-diameter (L/D) ratios. However, this model is not directly applicable for suction caisson foundations, as it was calibrated using non-skirted, solid caisson foundations. Thus, the deformation of the soil plug within a suction caisson is not accounted for. At the time of writing, there is no existing Winkler model for suction caisson foundations.

1.2.3 3D Finite Element (3DFE) Method

The 3DFE method is commonly used to study the behaviour of suction caisson foundations for a variety of problems. For example, it has been used to determine the capacity of suction caisson foundations in clay and sand (Palix et al. 2010, Vulpe 2015, Achmus et al. 2013), and to evaluate the caisson behaviour in sand under transient vertical loads (Thieken et al. 2014, Cerfontaine et al. 2016). The 3DFE method is a versatile and rigorous design method that can solve complex geotechnical problems not readily tackled by other design methods, such as assessments of the influence of seepage flow during installation or extraction of suction caissons in sand (Erbrich & Tjelta 1999, Tran & Randolph 2008, Vásquez et al. 2010, Lehane et al. 2014). However, it has several disadvantages, such as complexity in setting up the model and low computational efficiency. Thus, this method is not suitable for time-critical

Table 1.1: Applicability of the different oxCaisson design methods for the different limit states.

	FLS	SLS	ULS
oxCaisson-LE	✓	-	-
oxCaisson-NLE	✓	✓	-
oxCaisson-LEPP	✓	✓	✓

applications such as large scale foundation design optimisation.

1.2.4 oxCaisson

As mentioned earlier, oxCaisson is not a single design method. Instead, it is a family of design methods, which are all based on the Winkler framework, in which the soil response is represented by Winkler-type soil reactions that are either distributed along the caisson skirt length or concentrated at the caisson base. The oxCaisson design methods are hierarchical in nature, where each subsequent design method builds upon previous ones.

First, a design method called 'oxCaisson-LE' was developed for a 'toy problem', in which the soil was idealised as a homogeneous, linear elastic material. Then, the assumption of homogeneous soil stiffness was relaxed as an energy-based design method was developed for non-homogeneous stiffness profiles. Thereafter, the assumption of a fully rigid caisson is relaxed as the caisson skirt is modelled using deformable frame elements, which allows predictions of flexible caisson behaviour (i.e. caissons with deformable skirts).

Next, a design method called 'oxCaisson-NLE' was developed to predict the caisson behaviour in small strain, non-linear elastic soil. Then, a new elasto-plastic design method called 'oxCaisson-LEPP' was developed to predict the caisson behaviour in linear elastic, perfectly plastic soil. oxCaisson-LEPP combines the previously developed linear elastic soil reactions with plastic yield surfaces, which were calibrated against 3DFE analyses using linear elastic, perfectly plastic soil with a von Mises yield criterion.

Table 1.1 shows the limit states for which the aforementioned design methods are appropriate. Notice how all the design methods are suitable for FLS assessments. This is because oxCaisson-NLE and oxCaisson-LEPP are extensions of oxCaisson-LE.

1.3 Limitations

First, this thesis focuses solely on the post-installation behaviour of the suction caisson foundation. The caisson is ‘wished in place’ and no attempt is made to model the suction installation process or its effect on the subsequent deformation response. Furthermore, the suction caisson lid is assumed to be rigid, which may not be true based on recent field measurements (Shonberg et al. 2017).

Second, previous studies have shown that the suction caisson behaviour under cyclic lateral (Zhu et al. 2013) and vertical (Kelly et al. 2006, Bienen et al. 2018*a*,*b*) loads are critical design criteria. Some key findings from these studies are that the accumulated settlement of the caisson increased with the number of cycles and cyclic amplitude, and that tensile loading is accompanied by large displacements. This suggests that SLS will govern the design for cyclic loading. However, this thesis is focused on monotonic 6DoF loading and does not consider the effects of cyclic loading (although oxCaisson-LEPP can be extended to model cyclic loading). Furthermore, dynamic effects are not considered.

Third, the constitutive models used to describe the soil behaviour may not fully capture its true behaviour in real life. Instead, these models describe a simplified version of the true soil behaviour. Furthermore, the analyses in this thesis cover cohesive soils only. No results were presented for frictional soils. Thus, the soil models used in this thesis may not apply for all situations. However, it was an intentional choice to not adopt an advanced soil constitutive model straightaway, but to increase the complexity of the soil model incrementally (starting from the basic linear elastic model), so that the mapping from the 3DFE model to the oxCaisson model for each additional complexity can be clearly understood.

1.4 Outline

This section gives brief summaries of the remaining chapters of the thesis.

Chapter 2 introduces the Winkler framework upon which the oxCaisson models are based upon and discusses its numerical implementation.

Chapter 3 derives the linear elastic soil reaction formulations for oxCaisson-LE.

Chapter 4 introduces an energy-based design method for non-homogeneous stiffness.

Chapter 5 assesses the accuracy of oxCaisson-LE (with deformable skirt elements) in predicting flexible caisson behaviour in non-homogeneous, linear elastic soil.

Chapter 6 derives the non-linear elastic soil reaction formulations for oxCaisson-NLE.

Chapter 7 assesses various numerical procedures for determining failure envelopes, which can also be used to determine the soil reaction yield surfaces.

Chapter 8 describes a systematic framework for formulating globally convex failure envelopes (or yield surfaces) and thermodynamically consistent plastic potentials.

Chapter 9 derives the formulations of the soil reaction yield surfaces in linear elastic, perfectly plastic soil with a von Mises yield criterion (which represents undrained clay).

Chapter 10 describes the use of the oxCaisson design methods in an example case study.

Chapter 11 details the contributions of this thesis and suggests future research directions.

1.5 Software

Unless otherwise stated, all finite element analyses in this thesis were carried out using the commercial finite element program Abaqus v6.13 (Dassault Systèmes 2014).

1.6 Conventions

The following conventions are used to make the presentation of material clearer.

Vectors are denoted by letters with an arrow on top, such as $\vec{x}$ or $\vec{X}$. All vectors are assumed to be column vectors, unless otherwise stated. Vector components are presented in square brackets (e.g. $\vec{x} = [x_1, x_2, x_3]^\intercal$).

Matrices are denoted by boldface letters, such as $\boldsymbol{k}$ or $\boldsymbol{K}$.

Normalised variables are denoted by letters with a tilde on top, such as $\tilde{x}$ or $\tilde{X}$. Normalised variables are also dimensionless variables.

Dot products between vectors are denoted interchangeably by the dot product operator $\cdot$ or by the standard matrix multiplication notation (i.e. $\vec{x} \cdot \vec{y}$ and $\vec{y}^\intercal \vec{x}$ are equivalent).

Displacements refer to both translations and rotations.

Loads refer to both forces and moments.

Chapter 2

Winkler Model

This chapter introduces the Winkler model underlying all the design methods proposed in this thesis. The basic model is first derived using the principle of virtual work, before extensions to it are proposed for the different design methods. Finally, the numerical implementation of the model is discussed in details.

2.1 Introduction

Definition 2.1 (Winkler model) *A model conforms to the Winkler hypothesis (Winkler 1867) if the reactions at any point depend only on the displacements (including rotations) at that point.*

The Winkler model is simple and computationally efficient. It may not be universally useful, but it forms the basis of many commonplace design methods for shallow and deep foundations. Mechanically, it is analogous to representing the soil volume as independent springs, which obviously misrepresents the continuum nature of the soil volume. Nevertheless, it remains an excellent basis for modelling due to its simplicity and efficiency.

2.2 Model Definitions

Definition 2.2 (6DoF) *Freedom of movement in three-dimensional space, comprising of six displacement components: translations along and rotations about three orthogonal axes.*

A Winkler model, called 'oxCaisson', is derived for a suction caisson foundation of diameter D and skirt length L under 6DoF kinematics $\vec{S} = [S_\mathrm{x}, S_\mathrm{y}, S_\mathrm{z}, \Theta_\mathrm{x}, \Theta_\mathrm{y}, \Theta_\mathrm{z}]^\intercal$ as defined in Fig. 2.1. Work conjugate loads $\vec{P} = [H_\mathrm{x}, H_\mathrm{y}, V, M_\mathrm{x}, M_\mathrm{y}, Q]^\intercal$ are applied onto the caisson at its reference point (RP), which is defined at the centre of the lid base (see Fig. 2.1a).

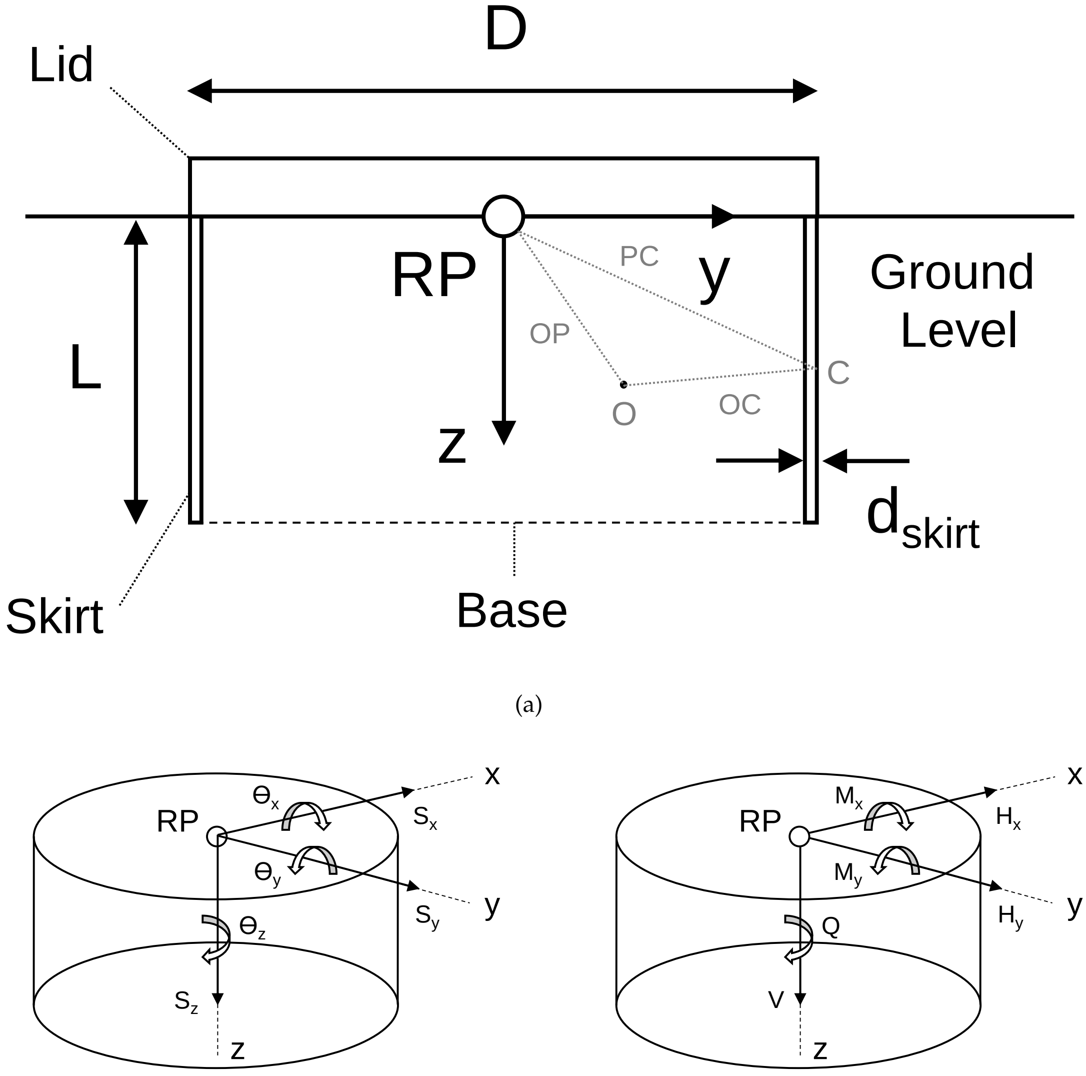

(a)

(b)

(c)

Figure 2.1: (a) Planar view of the caisson foundation and the adopted (b) kinematic and (c) load conventions. For clarity, the right hand rule applies for the rotations and moments. RP = reference point of the caisson, D = caisson diameter, L = skirt length, d_{skirt}= skirt thickness, S_x, S_y, S_z (H_x, H_y, V) = translations (applied forces) along the orthogonal x-y-z axes, $\Theta_x, \Theta_y, \Theta_z$ (M_x, M_y, Q) = rotations (applied moments) about the same x-y-z axes.

Before any displacement occurs, RP coincides with the origin of the global x-y-z coordinate system of the model.

Definition 2.3 (Skirt and base cross sections) *The skirt cross sections are the horizontal cross sections along the skirt length, while the base cross section is the horizontal cross section at the base of the caisson (including the soil plug), as shown in Fig. 2.1a.*

There are two types of cross sections defined in oxCaisson: skirt cross section and base cross section. The local soil reactions acting on the skirt and base cross sections are termed 'skirt soil reactions' and 'base soil reactions' respectively.

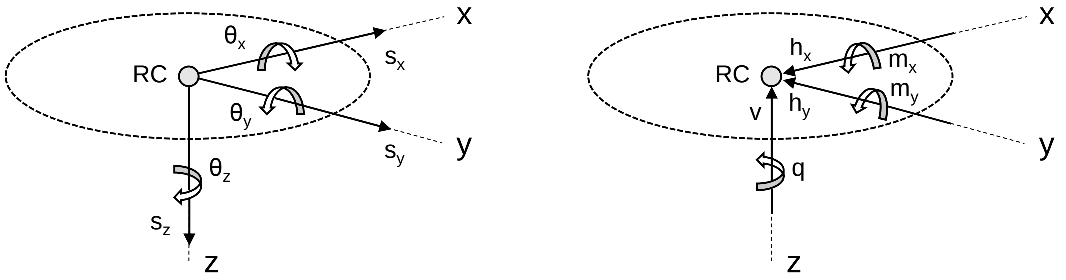

(a) (b)

Figure 2.2: Schematic diagram of a rigid caisson cross section and its (a) kinematic and (b) load conventions. RC = centre (and reference point) of the cross section, $s_{\mathrm{x}}, s_{\mathrm{y}}, s_{\mathrm{z}}$ $(h_{\mathrm{x}}, h_{\mathrm{y}}, v)$ = translations (applied forces) along the local orthogonal *x*-*y*-*z* axes (with the origin at RC), $\theta_{\mathrm{x}}, \theta_{\mathrm{y}}, \theta_{\mathrm{z}}$ $(m_{\mathrm{x}}, m_{\mathrm{y}}, q)$ = rotations (applied moments) about the same *x*-*y*-*z* axes. Note that the applied forces or moments have units of load per length for the cross sections along the skirt, and units of load for the base cross section.

Definition 2.4 (Soil reactions) *Soil reactions are the resultant forces or moments acting from the soil on each cross section of the caisson. The application of a soil traction on a cross section would result in a force (or moment about RC) on that cross section. The skirt soil reactions are the integration of these forces or moments along the external perimeter of the skirt cross section. Similarly, the base soil reactions are the integration of these forces or moments across the base cross-sectional area (including the soil plug). The units for the skirt and base soil reactions are loads per unit length and loads respectively.*

It is assumed that the cross sections of the caisson are in-plane rigid (i.e. no warping. The possible influence of warping was not investigated in this thesis). Each cross section has its own local kinematics $\vec{s} = [s_{\mathrm{x}}, s_{\mathrm{y}}, s_{\mathrm{z}}, \theta_{\mathrm{x}}, \theta_{\mathrm{y}}, \theta_{\mathrm{z}}]^{\mathsf{T}}$ and loads $\vec{p} = [h_{\mathrm{x}}, h_{\mathrm{y}}, v, m_{\mathrm{x}}, m_{\mathrm{y}}, q]^{\mathsf{T}}$ associated with it, with its centre (RC) acting as the reference point (as shown in Fig. 2.2). The local loads $\vec{p}$ correspond to the soil reactions acting on the cross sections. Note that the positive conventions for the local loads $\vec{p}$ are opposite to the positive conventions for the local kinematics $\vec{s}$ and the *x*-*y*-*z* coordinate system. This is to represent positive-valued soil reactions acting on the caisson due to positive displacements of the cross section.

To differentiate between the skirt and base soil reactions, the superscripts 'skirt' and 'base' are applied to the soil reactions $\vec{p}$ (i.e. $\vec{p}^{\mathrm{skirt}}$ = skirt soil reactions per unit length, $\vec{p}^{\mathrm{base}}$ = base soil reactions). The skirt soil reactions $\vec{p}^{\mathrm{skirt}} = [h_{\mathrm{x}}^{\mathrm{skirt}}, h_{\mathrm{y}}^{\mathrm{skirt}}, v^{\mathrm{skirt}}, m_{\mathrm{x}}^{\mathrm{skirt}}, m_{\mathrm{y}}^{\mathrm{skirt}}, q^{\mathrm{skirt}}]^{\mathsf{T}}$ are the distributed forces and moments per unit skirt length, while the base soil reactions $\vec{p}^{\mathrm{base}} = [h_{\mathrm{x}}^{\mathrm{base}}, h_{\mathrm{y}}^{\mathrm{base}}, v^{\mathrm{base}}, m_{\mathrm{x}}^{\mathrm{base}}, m_{\mathrm{y}}^{\mathrm{base}}, q^{\mathrm{base}}]^{\mathsf{T}}$ are the concentrated forces and moments acting on the base cross section. The skirt soil reactions per unit length are defined in terms of the soil tractions $\vec{t} = [t_\mathrm{x}, t_\mathrm{y}, t_\mathrm{z}]^\intercal$ (which follow the force conventions in Fig. 2.2b) as:

$$\begin{aligned}
h_\mathrm{x}^\mathrm{skirt} &= \int t_\mathrm{x}\, dl \\
h_\mathrm{y}^\mathrm{skirt} &= \int t_\mathrm{y}\, dl \\
v^\mathrm{skirt} &= \int t_\mathrm{z}\, dl \\
m_\mathrm{x}^\mathrm{skirt} &= \int y t_\mathrm{z}\, dl \\
m_\mathrm{y}^\mathrm{skirt} &= \int -x t_\mathrm{z}\, dl \\
q^\mathrm{skirt} &= \int x t_\mathrm{y} - y t_\mathrm{x}\, dl
\end{aligned} \tag{2.1}$$

where the integrations are evaluated over the external perimeter of the skirt cross section.

Similarly, the base soil reactions can be defined as:

$$\begin{aligned}
h_\mathrm{x}^\mathrm{base} &= \int t_\mathrm{x}\, dA \\
h_\mathrm{y}^\mathrm{base} &= \int t_\mathrm{y}\, dA \\
v^\mathrm{base} &= \int t_\mathrm{z}\, dA \\
m_\mathrm{x}^\mathrm{base} &= \int y t_\mathrm{z}\, dA \\
m_\mathrm{y}^\mathrm{base} &= \int -x t_\mathrm{z}\, dA \\
q^\mathrm{base} &= \int x t_\mathrm{y} - y t_\mathrm{x}\, dA
\end{aligned} \tag{2.2}$$

where the integrations are evaluated across the base cross-sectional area.

2.2.1 Fully Rigid Caisson

For a fully rigid caisson, the local kinematics $\vec{s}$ of each cross section are related to the global kinematics $\vec{S}$ of the caisson through:

$$\vec{s} = \boldsymbol{J}\vec{S} \tag{2.3}$$

where

$$\boldsymbol{J} = \begin{bmatrix} 1 & 0 & 0 & 0 & z & 0 \\ 0 & 1 & 0 & -z & 0 & 0 \\ 0 & 0 & 1 & 0 & 0 & 0 \\ 0 & 0 & 0 & 1 & 0 & 0 \\ 0 & 0 & 0 & 0 & 1 & 0 \\ 0 & 0 & 0 & 0 & 0 & 1 \end{bmatrix}$$

2.2.2 Flexible Caisson

A flexible caisson is defined as a suction caisson with a rigid lid, but a deformable skirt (although it is assumed that its cross sections remain in-plane rigid). For flexible caissons, Eq. 2.3 does not apply.

2.3 Principle of Virtual Work

The principle of virtual work is used to show the relationships between the global applied loads $\vec{P}$ and the soil reactions $\vec{p}$. Consider an arbitrary point C on the external surface of the skirt (see Fig. 2.1a). Let its coordinates relative to an arbitrary, fixed origin O and RP be $\overrightarrow{OC}$ and $\overrightarrow{PC}$ respectively. Ignoring any caisson deformation, its displacement $\vec{r} = \Delta\overrightarrow{OC}$ is:

$$\begin{aligned} \vec{r} &= \Delta\overrightarrow{OP} + \vec{\omega} \times \overrightarrow{PC} \\ \vec{r} &= \begin{pmatrix} S_\mathrm{x} + z\Theta_\mathrm{y} - y\Theta_\mathrm{z} \\ S_\mathrm{y} + x\Theta_\mathrm{z} - z\Theta_\mathrm{x} \\ S_\mathrm{z} + y\Theta_\mathrm{x} - x\Theta_\mathrm{y} \end{pmatrix} \end{aligned} \tag{2.4}$$

where $\Delta\overrightarrow{OP} = [S_\mathrm{x}, S_\mathrm{y}, S_\mathrm{z}]^\intercal$ is the translation vector of RP, $\vec{\omega} = [\Theta_\mathrm{x}, \Theta_\mathrm{y}, \Theta_\mathrm{z}]^\intercal$ is the rotation vector of RP and $\overrightarrow{PC} = [x, y, z]^\intercal$.

Definition 2.5 (Virtual displacement) *A virtual displacement of a point is any arbitrary infinitesimal change in the position of the point, that is consistent with the constraints imposed onto its motion. This displacement only needs to be kinematically admissible and need not relate to the real displacement.*

Using Eq. 2.4, the application of a virtual displacement $\delta\vec{S}$ at RP results in the following virtual displacement $\delta\vec{r}$ at point C:

$$\delta\vec{r} = \begin{pmatrix} \delta S_\mathrm{x} + z\delta\Theta_\mathrm{y} - y\delta\Theta_\mathrm{z} \\ \delta S_\mathrm{y} + x\delta\Theta_\mathrm{z} - z\delta\Theta_\mathrm{x} \\ \delta S_\mathrm{z} + y\delta\Theta_\mathrm{x} - x\delta\Theta_\mathrm{y} \end{pmatrix} \tag{2.5}$$

Eq. 2.5 applies for both rigid or flexible caissons, as the applied virtual displacement $\delta\vec{r}$ is kinematically admissible for both cases.

The virtual work $\delta W_{\text{soil}}^{\text{skirt}}$ done on the soil continuum (due to the soil tractions interacting with the caisson skirt exterior) is:

$$\begin{aligned}
\delta W_{\text{soil}}^{\text{skirt}} &= \int \vec{t} \cdot \delta \vec{r} \, dA \\
\delta W_{\text{soil}}^{\text{skirt}} &= \int_0^L \int \vec{t} \cdot \delta \vec{r} \, dl \, dz \\
\delta W_{\text{soil}}^{\text{skirt}} &= \int_0^L \int t_{\text{x}}(\delta S_{\text{x}} + z\delta\Theta_{\text{y}} - y\delta\Theta_{\text{z}}) + t_{\text{y}}(\delta S_{\text{y}} + x\delta\Theta_{\text{z}} - z\delta\Theta_{\text{x}}) \\
&\quad + t_{\text{z}}(\delta S_{\text{z}} + y\delta\Theta_{\text{x}} - x\delta\Theta_{\text{y}}) \, dl \, dz
\end{aligned} \tag{2.6}$$

where the integration is evaluated over the surface area of the caisson skirt exterior.

Substituting Eq. 2.3 into Eq. 2.6 gives:

$$\begin{aligned}
\delta W_{\text{soil}}^{\text{skirt}} &= \int_0^L \int t_{\text{x}}(\delta S_{\text{x}} + z\delta\Theta_{\text{y}}) + t_{\text{x}}(-y\delta\Theta_{\text{z}}) + t_{\text{y}}(\delta S_{\text{y}} - z\delta\Theta_{\text{x}}) + t_{\text{y}}(x\delta\Theta_{\text{z}}) \\
&\quad + t_{\text{z}}(\delta S_{\text{z}}) + t_{\text{z}}(y\delta\Theta_{\text{x}} - x\delta\Theta_{\text{y}}) \, dl \, dz \\
&= \int_0^L \int t_{\text{x}}(\delta s_{\text{x}}) + t_{\text{y}}(\delta s_{\text{y}}) + t_{\text{z}}(\delta s_{\text{z}}) \\
&\quad + (yt_{\text{z}})\delta\theta_{\text{x}} + (-xt_{\text{z}})\delta\theta_{\text{y}} + (xt_{\text{y}} - yt_{\text{x}})\delta\theta_{\text{z}} \, dl \, dz
\end{aligned} \tag{2.7}$$

Substituting Eq. 2.1 into Eq. 2.7 gives:

$$\begin{aligned}
\delta W_{\text{soil}}^{\text{skirt}} &= \int_0^L h_{\text{x}}^{\text{skirt}} \delta s_{\text{x}} + h_{\text{y}}^{\text{skirt}} \delta s_{\text{y}} + v^{\text{skirt}} \delta s_{\text{z}} \\
&\quad + m_{\text{x}}^{\text{skirt}} \delta\theta_{\text{x}} + m_{\text{y}}^{\text{skirt}} \delta\theta_{\text{y}} + q^{\text{skirt}} \delta\theta_{\text{z}} \, dz \\
&= \int_0^L \vec{p}^{\text{skirt}} \cdot \delta \vec{s} \, dz
\end{aligned} \tag{2.8}$$

Ignoring any caisson or soil plug deformation, a virtual displacement $\delta \vec{S}$ applied at RP will result in a virtual displacement $\delta \vec{r}^{\text{base}}$ at the base cross section. The virtual work $\delta W_{\text{soil}}^{\text{base}}$ done on the soil continuum (due to the soil tractions interacting with the base cross section) is:

$$\begin{aligned}
\delta W_{\text{soil}}^{\text{base}} &= \int \vec{t} \cdot \delta \vec{r}^{\text{base}} \, dA \\
&= \int t_{\text{x}}(\delta S_{\text{x}} + L\delta\Theta_{\text{y}} - y\delta\Theta_{\text{z}}) + t_{\text{y}}(\delta S_{\text{y}} + x\delta\Theta_{\text{z}} - L\delta\Theta_{\text{x}}) \\
&\quad + t_{\text{z}}(\delta S_{\text{z}} + y\delta\Theta_{\text{x}} - x\delta\Theta_{\text{y}}) \, dA
\end{aligned} \tag{2.9}$$

Substituting Eq. 2.3 into Eq. 2.9 gives:

$$\begin{aligned}\delta W_{\mathrm{soil}}^{\mathrm{base}} &= \int t_{\mathrm{x}}(\delta S_{\mathrm{x}} + L\delta\Theta_{\mathrm{y}}) + t_{\mathrm{x}}(-y\delta\Theta_{\mathrm{z}}) + t_{\mathrm{y}}(\delta S_{\mathrm{y}} - L\delta\Theta_{\mathrm{x}}) + t_{\mathrm{y}}(x\delta\Theta_{\mathrm{z}}) \\ &\quad + t_{\mathrm{z}}(\delta S_{\mathrm{z}}) + t_{\mathrm{z}}(y\delta\Theta_{\mathrm{x}} - x\delta\Theta_{\mathrm{y}})\, dA \\ &= \int t_{\mathrm{x}}(\delta s_{\mathrm{x}}^{\mathrm{base}}) + t_{\mathrm{y}}(\delta s_{\mathrm{y}}^{\mathrm{base}}) + t_{\mathrm{z}}(\delta s_{\mathrm{z}}^{\mathrm{base}}) \\ &\quad + (yt_{\mathrm{z}})\delta\theta_{\mathrm{x}}^{\mathrm{base}} + (-xt_{\mathrm{z}})\delta\theta_{\mathrm{y}}^{\mathrm{base}} + (xt_{\mathrm{y}} - yt_{\mathrm{x}})\delta\theta_{\mathrm{z}}^{\mathrm{base}}\, dA\end{aligned} \tag{2.10}$$

Substituting Eq. 2.2 into Eq. 2.10 gives:

$$\begin{aligned}\delta W_{\mathrm{soil}}^{\mathrm{base}} &= h_{\mathrm{x}}^{\mathrm{base}}\delta s_{\mathrm{x}}^{\mathrm{base}} + h_{\mathrm{y}}^{\mathrm{base}}\delta s_{\mathrm{y}}^{\mathrm{base}} + v^{\mathrm{base}}\delta s_{\mathrm{z}}^{\mathrm{base}} \\ &\quad + m_{\mathrm{x}}^{\mathrm{base}}\delta\theta_{\mathrm{x}}^{\mathrm{base}} + m_{\mathrm{y}}^{\mathrm{base}}\delta\theta_{\mathrm{y}}^{\mathrm{base}} + q^{\mathrm{base}}\delta\theta_{\mathrm{z}}^{\mathrm{base}} \\ \delta W_{\mathrm{soil}}^{\mathrm{base}} &= \overrightarrow{p}^{\mathrm{base}} \cdot \delta\overrightarrow{s}^{\mathrm{base}}\end{aligned} \tag{2.11}$$

Eq. 2.11 applies for rigid and flexible caissons, and for rigid and deformable soil plugs, as the applied virtual displacement $\delta\overrightarrow{r}^{\mathrm{base}}$ is kinematically admissible for all cases.

The total external virtual work δW^{ext} is the work done by the applied loads $\overrightarrow{P}$ at RP and the total internal virtual work δW^{int} is the sum of $\delta W_{\mathrm{soil}}^{\mathrm{skirt}}$ and $\delta W_{\mathrm{soil}}^{\mathrm{base}}$. The principle of virtual work then requires the total internal work to equal the total external virtual work:

$$\begin{aligned}\delta W^{\mathrm{int}} &= \delta W^{\mathrm{ext}} \\ (\overrightarrow{p}^{\mathrm{base}} \cdot \delta\overrightarrow{s}^{\mathrm{base}} + \int_0^L \overrightarrow{p}^{\mathrm{skirt}} \cdot \delta\overrightarrow{s}\, dz) &= (\overrightarrow{P} \cdot \delta\overrightarrow{S}) \\ \delta\overrightarrow{S}^{\intercal}\left(\boldsymbol{J}^{\mathrm{base}\intercal}\overrightarrow{p}^{\mathrm{base}} + \int_0^L \boldsymbol{J}^{\intercal}\overrightarrow{p}^{\mathrm{skirt}}\, dz - \overrightarrow{P}\right) &= 0\end{aligned} \tag{2.12}$$

where

$$\boldsymbol{J}^{\mathrm{base}} = \begin{bmatrix} 1 & 0 & 0 & 0 & L & 0 \\ 0 & 1 & 0 & -L & 0 & 0 \\ 0 & 0 & 1 & 0 & 0 & 0 \\ 0 & 0 & 0 & 1 & 0 & 0 \\ 0 & 0 & 0 & 0 & 1 & 0 \\ 0 & 0 & 0 & 0 & 0 & 1 \end{bmatrix}$$

Since $\delta\overrightarrow{S}$ is arbitrary, the expression within the brackets of the last line of Eq. 2.12 must be zero. Thus, the equilibrium equation of the system is obtained:

$$\overrightarrow{P} = \boldsymbol{J}^{\mathrm{base}\intercal}\overrightarrow{p}^{\mathrm{base}} + \int_0^L \boldsymbol{J}^{\intercal}\overrightarrow{p}^{\mathrm{skirt}}\, dz \tag{2.13}$$

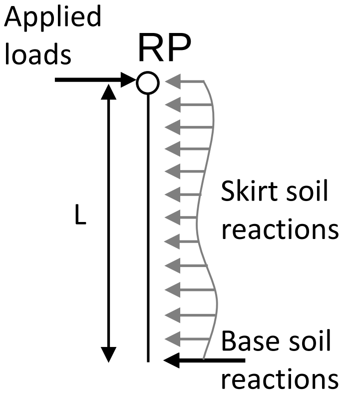

Figure 2.3: Schematic diagram of oxCaisson, with the skirt soil reactions distributed along the skirt length and the base soil reactions acting at the base. The skirt and base soil reactions can be any of $h_\mathrm{x}, h_\mathrm{y}, v, m_\mathrm{x}, m_\mathrm{y}, q$. The 3D caisson is replaced by a 1D structure representing the centre line (i.e. reference points) of the cross sections.

Definition 2.6 (Global and local stiffness matrices) *The global stiffness matrix* $\boldsymbol{K}$ *is defined as the instantaneous change in the global applied loads* $\vec{P}$ *per unit change in global displacements* $\vec{S}$ *(i.e.* $\boldsymbol{K} = \frac{\partial \vec{P}}{\partial \vec{S}}$*). The local stiffness matrix* $\boldsymbol{k}$ *is defined as the instantaneous change in the local applied loads* $\vec{p}$ *on a cross section per unit change in local displacements* $\vec{s}$ *(i.e.* $\boldsymbol{k} = \frac{\partial \vec{p}}{\partial \vec{s}}$*).*

Fully Rigid Caisson For a fully rigid caisson, the global stiffness matrix $\boldsymbol{K}$ is:

$$\begin{aligned}
\boldsymbol{K} &= \frac{\partial \vec{P}}{\partial \vec{S}} \\
&= \boldsymbol{J}^{\mathrm{base}\top} \frac{\partial \vec{p}^{\,\mathrm{base}}}{\partial \vec{s}^{\,\mathrm{base}}} \frac{\partial \vec{s}^{\,\mathrm{base}}}{\partial \vec{S}} + \int_0^L \boldsymbol{J}^\top \frac{\partial \vec{p}^{\,\mathrm{skirt}}}{\partial \vec{s}} \frac{\partial \vec{s}}{\partial \vec{S}} \, dz \\
&= \boldsymbol{J}^{\mathrm{base}\top} \frac{\partial \vec{p}^{\,\mathrm{base}}}{\partial \vec{s}^{\,\mathrm{base}}} \boldsymbol{J}^{\mathrm{base}} + \int_0^L \boldsymbol{J}^\top \frac{\partial \vec{p}^{\,\mathrm{skirt}}}{\partial \vec{s}} \boldsymbol{J} \, dz \\
&= \boldsymbol{J}^{\mathrm{base}\top} \boldsymbol{k}^{\mathrm{base}} \boldsymbol{J}^{\mathrm{base}} + \int_0^L \boldsymbol{J}^\top \boldsymbol{k}^{\mathrm{skirt}} \boldsymbol{J} \, dz
\end{aligned} \tag{2.14}$$

where Eq. 2.3 is used to define $\frac{\partial \vec{s}}{\partial \vec{S}}$, and $\boldsymbol{k}^{\mathrm{skirt}}$ and $\boldsymbol{k}^{\mathrm{base}}$ are the local stiffness matrices for the skirt and base soil reactions. Thus, oxCaisson computes the global behaviour of the caisson with a one-dimensional integration of the soil reactions along the skirt length (see Fig. 2.3). Despite the one-dimensional nature of oxCaisson, it is still solving a three-dimensional soil-caisson interaction problem as the three-dimensional soil tractions acting on each cross-section have been encapsulated within the soil reactions.

Flexible Caisson For a flexible caisson, Eq. 2.14 does not apply as the skirt deformation has to be accounted for in $\frac{\partial \vec{s}}{\partial \vec{S}}$. Thus, the global stiffness matrix $\boldsymbol{K}$ is computed using the finite element method, for which the numerical implementation is detailed in Section 2.6.

2.4 Elastic Winkler Models

2.4.1 Linear Elastic Model (LE)

If $\vec{p}$ are defined as linear functions of the local displacements $\vec{s}$, the caisson will behave linear elastically. The model with linear elastic $\vec{p}^{\text{skirt}}$ and $\vec{p}^{\text{base}}$ is termed 'oxCaisson-LE', and it is explored further in Chapter 3.

2.4.2 Non-linear Elastic Model (NLE)

If $\vec{p}$ are defined as explicit, path-independent, non-linear functions of the local displacements $\vec{s}$, the caisson will behave non-linear elastically. The model with non-linear elastic $\vec{p}^{\text{skirt}}$ and $\vec{p}^{\text{base}}$ is termed 'oxCaisson-NLE', and it is explored further in Chapter 6.

2.5 Elasto-plastic Winkler Models

The elastic Winkler models described in Section 2.2 cannot easily account for the influence of combined loading on failure states. Moreover, they are unsuited for cyclic loading, as they do not capture cyclic loading phenomena such as permanent displacement.

Definition 2.7 (Yield surface) *In the context of elasto-plastic Winkler models, a yield surface f is an n-dimensional hypersurface (where n is the number of soil reaction components i.e. six for 6DoF loading) in the soil reaction space, that restricts the allowable soil reaction states to within the yield surface. In other words, f represents the ultimate soil reactions. For soil reaction states within the yield surface, the model behaviour is linear elastic. For soil reactions states on the yield surface, the model behaviour is elasto-plastic. Soil reaction states outside the yield surface is inadmissible.*

To resolve these shortcomings, an elasto-plastic Winkler model for caissons is developed. The elasto-plastic Winkler model couples the soil reactions $\vec{p}$ with yield surfaces f to restrict the allowable $\vec{p}$ states. Intuitively, f represents the local yield states of the soil. When the soil reaction state reaches the yield surface, the soil deforms plastically. Further displacement causes the soil reaction state to remain on the yield surface, as plastic displacement accumulates. Soil reaction states outside the yield surface are not allowed.

The standard elasto-plasticity theory, as used in continuum mechanics, describes the behaviour of the elasto-plastic Winkler model. The main difference is that in continuum mechanics, the theory is applied in the stress-strain space (i.e. $\sigma_{\text{ij}}, \varepsilon_{\text{ij}}$) while in the Winkler model, the theory is applied in the soil reactions-displacement space (i.e. $\vec{p}$, $\vec{s}$). Most of the macro-element models described in Chapter 1 are based on the same elasto-plastic theory, but the theory is applied in the global loads-displacement space (i.e. $\vec{P}$, $\vec{S}$). A brief review of this theory, as applied to the Winkler model, is shown below.

2.5.1 Theory of Elasto-plasticity

By convention, the yield surface $f(\vec{p})$ is defined such that $f < 0$ represents states inside the yield surface, $f = 0$ represents states on the yield surface, and $f > 0$ represents inadmissible states outside the yield surface. For soil reaction states inside the yield surface, the soil response is linear elastic, and the incremental response is given by:

$$\delta\vec{p} = \boldsymbol{k}_{\mathrm{e}}\delta\vec{s} \tag{2.15}$$

where $\boldsymbol{k}_{\mathrm{e}}$ is the linear elastic stiffness matrix of the soil reactions.

When the soil reaction states reach the yield surface, elasto-plastic yielding occurs and plastic displacements accumulate. The total displacement increment $\delta\vec{s}$ can be decomposed into elastic $\vec{s}_{\mathrm{e}}$ and plastic $\vec{s}_{\mathrm{p}}$ parts:

$$\delta\vec{s} = \delta\vec{s}_{\mathrm{e}} + \delta\vec{s}_{\mathrm{p}} \tag{2.16}$$

The elastic displacement increment $\delta\vec{s}_{\mathrm{e}}$ is determined by the soil reaction increment:

$$\delta\vec{s}_{\mathrm{e}} = \boldsymbol{k}_{\mathrm{e}}^{-1}\delta\vec{p} \tag{2.17}$$

The plastic displacement increment $\delta\vec{s}_{\mathrm{p}}$ is determined by a plastic potential function $g(\vec{p})$ through the flow rule:

$$\delta\vec{s}_{\mathrm{p}} = \delta\lambda\frac{\partial g}{\partial\vec{p}} \tag{2.18}$$

which indicates that it is codirectional with the current gradient of g, with magnitude depending on a non-negative, scalar plastic multiplier $\delta\lambda$. When elasto-plastic behaviour is occurring, the incremental reaction $\delta\vec{p}$ must remain on the yield surface. This is enforced (for the case of a non-hardening yield surface) using the consistency condition:

$$\delta f = \left(\frac{\partial f}{\partial\vec{p}}\right)^{\mathsf{T}}\delta\vec{p} = 0 \tag{2.19}$$

Substituting Eqs. 2.17 and 2.18 into Eq. 2.16:

$$\delta\vec{s} = \boldsymbol{k}_{\mathrm{e}}^{-1}\delta\vec{p} + \delta\lambda\frac{\partial g}{\partial\vec{p}} \tag{2.20}$$

Premultiplying Eq. 2.20 by $\left(\frac{\partial f}{\partial \vec{p}}\right)^{\mathsf{T}} \boldsymbol{k}_{\mathrm{e}}$:

$$\left(\frac{\partial f}{\partial \vec{p}}\right)^{\mathsf{T}} \boldsymbol{k}_{\mathrm{e}} \delta \vec{s} = \left(\frac{\partial f}{\partial \vec{p}}\right)^{\mathsf{T}} \delta \vec{p} + \delta\lambda \left(\frac{\partial f}{\partial \vec{p}}\right)^{\mathsf{T}} \boldsymbol{k}_{\mathrm{e}} \frac{\partial g}{\partial \vec{p}} \tag{2.21}$$

Substituting Eq. 2.19 into Eq. 2.21:

$$\left(\frac{\partial f}{\partial \vec{p}}\right)^{\mathsf{T}} \boldsymbol{k}_{\mathrm{e}} \delta \vec{s} = \delta\lambda \left(\frac{\partial f}{\partial \vec{p}}\right)^{\mathsf{T}} \boldsymbol{k}_{\mathrm{e}} \frac{\partial g}{\partial \vec{p}} \tag{2.22}$$

Solving for $\delta\lambda$:

$$\delta\lambda = \frac{\left(\frac{\partial f}{\partial \vec{p}}\right)^{\mathsf{T}} \boldsymbol{k}_{\mathrm{e}} \delta \vec{s}}{\left(\frac{\partial f}{\partial \vec{p}}\right)^{\mathsf{T}} \boldsymbol{k}_{\mathrm{e}} \frac{\partial g}{\partial \vec{p}}} \tag{2.23}$$

Substituting Eq. 2.23 back into Eq. 2.20:

$$\delta \vec{s} = \boldsymbol{k}_{\mathrm{e}}{}^{-1} \delta \vec{p} + \frac{\frac{\partial g}{\partial \vec{p}} \left(\frac{\partial f}{\partial \vec{p}}\right)^{\mathsf{T}} \boldsymbol{k}_{\mathrm{e}} \delta \vec{s}}{\left(\frac{\partial f}{\partial \vec{p}}\right)^{\mathsf{T}} \boldsymbol{k}_{\mathrm{e}} \frac{\partial g}{\partial \vec{p}}} \tag{2.24}$$

Premultiplying Eq. 2.24 by $\boldsymbol{k}_{\mathrm{e}}$:

$$\boldsymbol{k}_{\mathrm{e}} \delta \vec{s} = \delta \vec{p} + \frac{\boldsymbol{k}_{\mathrm{e}} \frac{\partial g}{\partial \vec{p}} \left(\frac{\partial f}{\partial \vec{p}}\right)^{\mathsf{T}} \boldsymbol{k}_{\mathrm{e}} \delta \vec{s}}{\left(\frac{\partial f}{\partial \vec{p}}\right)^{\mathsf{T}} \boldsymbol{k}_{\mathrm{e}} \frac{\partial g}{\partial \vec{p}}} \tag{2.25}$$

Solving for $\vec{p}$:

$$\begin{aligned} \delta \vec{p} &= \left(\boldsymbol{k}_{\mathrm{e}} - \frac{\boldsymbol{k}_{\mathrm{e}} \frac{\partial g}{\partial \vec{p}} \left(\frac{\partial f}{\partial \vec{p}}\right)^{\mathsf{T}} \boldsymbol{k}_{\mathrm{e}}}{\left(\frac{\partial f}{\partial \vec{p}}\right)^{\mathsf{T}} \boldsymbol{k}_{\mathrm{e}} \frac{\partial g}{\partial \vec{p}}} \right) \delta \vec{s} \\ &= \boldsymbol{k}_{\mathrm{ep}} \delta \vec{s} \end{aligned} \tag{2.26}$$

where $\boldsymbol{k}_{\mathrm{ep}}$ is the elasto-plastic stiffness matrix of the soil reactions.

If associated flow rule is assumed (i.e. $g = f$):

$$\boldsymbol{k}_{\mathrm{ep}} = \boldsymbol{k}_{\mathrm{e}} - \frac{\boldsymbol{k}_{\mathrm{e}} \frac{\partial f}{\partial \vec{p}} \left(\frac{\partial f}{\partial \vec{p}}\right)^{\mathsf{T}} \boldsymbol{k}_{\mathrm{e}}}{\left(\frac{\partial f}{\partial \vec{p}}\right)^{\mathsf{T}} \boldsymbol{k}_{\mathrm{e}} \frac{\partial f}{\partial \vec{p}}} \tag{2.27}$$

For a fully rigid caisson, the global stiffness matrix $\boldsymbol{K}$ of the elasto-plastic Winkler model can be computed using Eq. 2.14, after setting the local stiffness matrices as $\boldsymbol{k}_{\mathrm{ep}}^{\mathrm{skirt}}$ and $\boldsymbol{k}_{\mathrm{ep}}^{\mathrm{base}}$.

2.5.2 Linear Elastic, Perfectly Plastic Model (LEPP)

The model that couples linear elastic soil reactions $\vec{p}^{\,\mathrm{skirt}}$ and $\vec{p}^{\,\mathrm{base}}$ with yield surfaces f^{skirt} and f^{base} is termed 'oxCaisson-LEPP', and it is explored further in Chapter 9.

2.6 Numerical Implementation

This section details the numerical implementation of the aforementioned Winkler models using the finite element method.

2.6.1 Step 1: Weak Form Formulation

Based on the principle of virtual work, the weak form formulation of the Winkler model for a flexible caisson (assuming zero body forces) is obtained as follows:

$$\begin{gathered}\delta W^{\mathrm{int}} = \delta W^{\mathrm{ext}} \\ \delta W_{\mathrm{caisson}} + \delta W^{\mathrm{skirt}}_{\mathrm{soil}} + \delta W^{\mathrm{base}}_{\mathrm{soil}} = \int_0^L \delta \vec{s}^{\mathsf{T}} \vec{t}\, dz\end{gathered} \tag{2.28}$$

where $\delta \vec{s}$ is a virtual displacement, $\vec{t}$ are external surface tractions and $\delta W_{\mathrm{caisson}}$ is the virtual work done by the caisson skirt deformation, which can be computed as:

$$\delta W_{\mathrm{caisson}} = \delta W^{\mathrm{a}}_{\mathrm{caisson}} + \delta W^{\mathrm{q}}_{\mathrm{caisson}} + \delta W^{\mathrm{b}}_{\mathrm{caisson}} + \delta W^{\mathrm{s}}_{\mathrm{caisson}} \tag{2.29}$$

where $\delta W^{\mathrm{a}}_{\mathrm{caisson}}, \delta W^{\mathrm{q}}_{\mathrm{caisson}}, \delta W^{\mathrm{b}}_{\mathrm{caisson}}, \delta W^{\mathrm{s}}_{\mathrm{caisson}}$ are the virtual work done by the axial, torsional, bending and shearing deformation of the caisson skirt (which is assumed to be linear elastic). Timoshenko beam theory is used to describe bending and shearing behaviour of the caisson skirt, while standard structural theory is used to describe its axial and torsional behaviour. $\delta W^{\mathrm{a}}_{\mathrm{caisson}}, \delta W^{\mathrm{q}}_{\mathrm{caisson}}, \delta W^{\mathrm{b}}_{\mathrm{caisson}}, \delta W^{\mathrm{s}}_{\mathrm{caisson}}$ can be computed as:

$$\delta W^{\mathrm{a}}_{\mathrm{caisson}} = \int_0^L \left(\frac{\partial(\delta s_{\mathrm{z}})}{\partial z}\right)^{\mathsf{T}} E_{\mathrm{s}} A_{\mathrm{s}} \frac{\partial s_{\mathrm{z}}}{\partial z}\, dz \tag{2.30}$$

$$\delta W^{\mathrm{q}}_{\mathrm{caisson}} = \int_0^L \left(\frac{\partial(\delta \theta_{\mathrm{z}})}{\partial z}\right)^{\mathsf{T}} G_{\mathrm{s}} J_{\mathrm{s}} \frac{\partial \theta_{\mathrm{z}}}{\partial z}\, dz \tag{2.31}$$

$$\delta W^{\mathrm{b}}_{\mathrm{caisson}} = \int_0^L \left(\frac{\partial(\delta \theta_{\mathrm{x}})}{\partial z}\right)^{\mathsf{T}} E_{\mathrm{s}} I_{\mathrm{s}} \frac{\partial \theta_{\mathrm{x}}}{\partial z}\, dz \tag{2.32}$$

$$\delta W^{\mathrm{s}}_{\mathrm{caisson}} = \int_0^L \left(\frac{\partial(\delta s_{\mathrm{y}})}{\partial z} + \delta\theta_{\mathrm{x}}\right)^{\mathsf{T}} G_{\mathrm{s}} A_{\mathrm{s}} \kappa \left(\frac{\partial s_{\mathrm{y}}}{\partial z} + \theta_{\mathrm{x}}\right) dz \tag{2.33}$$

where G_{s} and E_{s} are the shear modulus and Young's modulus of the caisson skirt material respectively. $A_{\mathrm{s}} = \pi({R_{\mathrm{ext}}}^2 - {R_{\mathrm{int}}}^2), J_{\mathrm{s}} = \frac{\pi}{2}({R_{\mathrm{ext}}}^4 - {R_{\mathrm{int}}}^4), I_{\mathrm{s}} = \frac{\pi}{4}({R_{\mathrm{ext}}}^4 - {R_{\mathrm{int}}}^4)$ are the area, polar moment of intertia and second moment of area of the caisson skirt annulus respectively, where R_{ext} and R_{int} are the external and internal radii of the annulus. κ is the Timoshenko shear correction factor, which is taken to be $\frac{1+\nu}{2+\nu}$ for an annulus (Hutchinson 2001). $\delta W^{\mathrm{b}}_{\mathrm{caisson}}$ and $\delta W^{\mathrm{s}}_{\mathrm{caisson}}$ may also be defined in terms of θ_{y} and s_{x}, by substituting $\theta_{\mathrm{y}} = -\theta_{\mathrm{x}}$ and $s_{\mathrm{x}} = s_{\mathrm{y}}$.

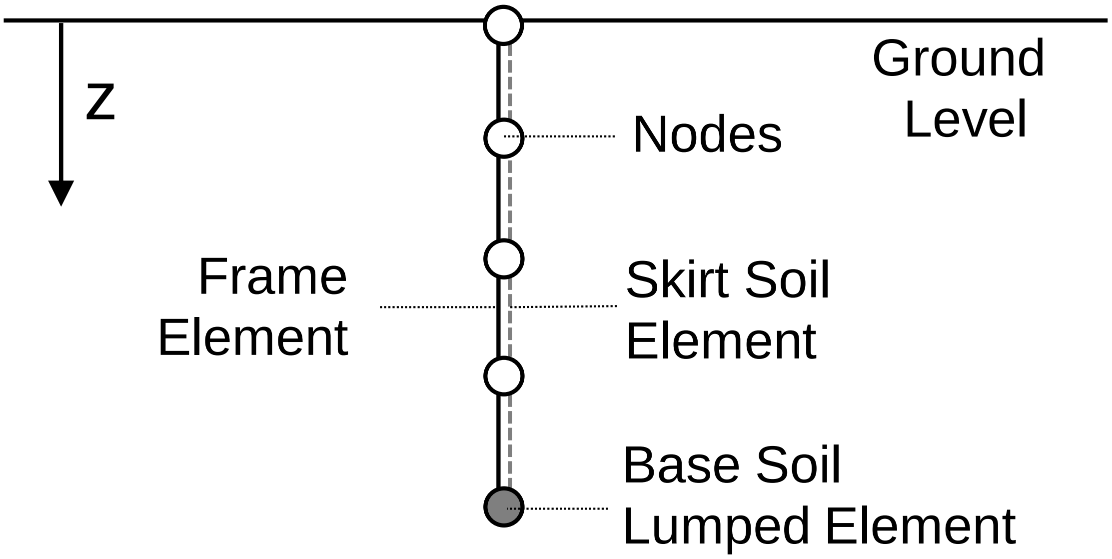

Figure 2.4: Schematic diagram of a typical finite element mesh of the Winkler model, where two-noded frame elements (representing the flexible caisson) share the same nodes as two-noded soil elements (representing the skirt soil reactions). Additionally, the base soil reactions are represented by a lumped element attached to the last node.

2.6.2 Step 2: Discretisation

The one-dimensional problem domain ($0 \leq z \leq L$) is discretised into a mesh of m (unless otherwise stated, $m = 20$ for the analyses in this thesis) equally sized two-noded finite elements. Note that there are two types of two-noded finite elements: frame elements (representing the flexible caisson) and skirt soil elements (representing the skirt soil reactions). As shown in Fig. 2.4, the frame and skirt soil elements share the same nodes. Furthermore, there is a lumped element (representing the base soil reaction) attached to the deepest node.

2.6.3 Step 3: Approximation

The displacements at the nodes are known as the nodal displacements $\vec{u}$. Let $\vec{u}_{\mathrm{el}} = [{s_{\mathrm{x}}}^{(1)}, {s_{\mathrm{y}}}^{(1)}, {s_{\mathrm{z}}}^{(1)}, {\theta_{\mathrm{x}}}^{(1)}, {\theta_{\mathrm{y}}}^{(1)}, {\theta_{\mathrm{z}}}^{(1)}, {s_{\mathrm{x}}}^{(2)}, {s_{\mathrm{y}}}^{(2)}, {s_{\mathrm{z}}}^{(2)}, {\theta_{\mathrm{x}}}^{(2)}, {\theta_{\mathrm{y}}}^{(2)}, {\theta_{\mathrm{z}}}^{(2)}]^{\intercal}$ be a vector containing the nodal displacements at the two nodes of an element (where the exponent (i) refers to the nodal displacements at node i). The displacements $\vec{s}_{\mathrm{el}} = [s_{\mathrm{x}}, s_{\mathrm{y}}, s_{\mathrm{z}}, \theta_{\mathrm{x}}, \theta_{\mathrm{y}}, \theta_{\mathrm{z}}]^{\intercal}$ at any point in an element is approximated as an interpolation of the element nodal displacements $\vec{u}_{\mathrm{el}}$. For example, the displacement s (which can be the vertical, torsional, lateral or rotational displacement) at a point in an element is approximated as:

$$s = N_1 u_1 + N_2 u_2 \tag{2.34}$$

where u_1, u_2 are the element nodal displacements and $N_1 = 1 - \xi, N_2 = \xi$ are linear shape functions (Hughes 2000, Reddy 2015). ξ is the local coordinate of the element such that the two element nodes are located at $\xi = 0$ and $\xi = 1$ respectively (Astley 1992).

The global coordinate z is approximated using the isoparametric mapping technique, where the same shape functions that are used to interpolate the nodal displacements are also used to interpolate the nodal coordinates. Thus, z is related to ξ through:

$$z = N_1 z_1 + N_2 z_2 \tag{2.35}$$

where z_1, z_2 are the global coordinates of the first (shallower) and second element nodes.

The displacement gradient at a point in the element can be approximated as:

$$\begin{aligned} \frac{\partial s}{\partial \xi} &= \frac{\partial N_1}{\partial \xi} u_1 + \frac{\partial N_2}{\partial \xi} u_2 \\ &= -u_1 + u_2 \end{aligned} \tag{2.36}$$

or in terms of the global coordinates:

$$\begin{aligned} \frac{\partial s}{\partial \xi} &= \frac{\partial s}{\partial z} \frac{\partial z}{\partial \xi} \\ &= \frac{\partial s}{\partial z}(z_2 - z_1) \\ \therefore \frac{\partial s}{\partial z} &= \frac{1}{L_\mathrm{e}}(-u_1 + u_2) \end{aligned} \tag{2.37}$$

where $L_\mathrm{e} = z_2 - z_1$ is the element length.

Combining the above, the displacements $\vec{s}_\mathrm{el}$ and displacement gradients $\frac{\partial \vec{s}_\mathrm{el}}{\partial z}$ at a point in an element are:

$$\vec{s}_\mathrm{el} = \boldsymbol{N} \vec{u}_\mathrm{el} \tag{2.38}$$

$$\frac{\partial \vec{s}_\mathrm{el}}{\partial z} = \frac{1}{L_\mathrm{e}} \boldsymbol{B} \vec{u}_\mathrm{el} \tag{2.39}$$

where

$$\boldsymbol{N} = \begin{bmatrix} N_1 & 0 & 0 & 0 & 0 & 0 & N_2 & 0 & 0 & 0 & 0 & 0 \\ 0 & N_1 & 0 & 0 & 0 & 0 & 0 & N_2 & 0 & 0 & 0 & 0 \\ 0 & 0 & N_1 & 0 & 0 & 0 & 0 & 0 & N_2 & 0 & 0 & 0 \\ 0 & 0 & 0 & N_1 & 0 & 0 & 0 & 0 & 0 & N_2 & 0 & 0 \\ 0 & 0 & 0 & 0 & N_1 & 0 & 0 & 0 & 0 & 0 & N_2 & 0 \\ 0 & 0 & 0 & 0 & 0 & N_1 & 0 & 0 & 0 & 0 & 0 & N_2 \end{bmatrix}$$

$$\boldsymbol{B} = \begin{bmatrix} -1 & 0 & 0 & 0 & 0 & 0 & 1 & 0 & 0 & 0 & 0 & 0 \\ 0 & -1 & 0 & 0 & 0 & 0 & 0 & 1 & 0 & 0 & 0 & 0 \\ 0 & 0 & -1 & 0 & 0 & 0 & 0 & 0 & 1 & 0 & 0 & 0 \\ 0 & 0 & 0 & -1 & 0 & 0 & 0 & 0 & 0 & 1 & 0 & 0 \\ 0 & 0 & 0 & 0 & -1 & 0 & 0 & 0 & 0 & 0 & 1 & 0 \\ 0 & 0 & 0 & 0 & 0 & -1 & 0 & 0 & 0 & 0 & 0 & 1 \end{bmatrix}$$

2.6.4 Step 4: Element Virtual Work

Using Eqs. 2.29 to 2.33, the virtual work done by the caisson skirt deformation $\delta W_{\mathrm{caisson}}$ in each element can be expressed as:

$$\delta W_{\mathrm{caisson}} = L_{\mathrm{e}} \int_0^1 \delta \vec{u}_{\mathrm{el}}{}^{\intercal} \boldsymbol{k}^{\mathrm{caisson}} \vec{u}_{\mathrm{el}} \, d\xi \tag{2.40}$$

where $\boldsymbol{k}^{\mathrm{caisson}} = \frac{1}{L_{\mathrm{e}}^2} \boldsymbol{B}^{\intercal} \boldsymbol{k}_{\mathrm{B}} \boldsymbol{B} + \boldsymbol{N}^{\intercal} \boldsymbol{k}_{\mathrm{N}} \boldsymbol{N} + \frac{1}{L_{\mathrm{e}}} \boldsymbol{B}^{\intercal} \boldsymbol{k}_{\mathrm{BN}} \boldsymbol{N} + \frac{1}{L_{\mathrm{e}}} \boldsymbol{N}^{\intercal} \boldsymbol{k}_{\mathrm{NB}} \boldsymbol{B}$

$$\boldsymbol{k}_{\mathrm{B}} = \begin{bmatrix} G_{\mathrm{s}} A_{\mathrm{s}} \kappa & 0 & 0 & 0 & 0 & 0 \\ 0 & G_{\mathrm{s}} A_{\mathrm{s}} \kappa & 0 & 0 & 0 & 0 \\ 0 & 0 & E_{\mathrm{s}} A_{\mathrm{s}} & 0 & 0 & 0 \\ 0 & 0 & 0 & E_{\mathrm{s}} I_{\mathrm{s}} & 0 & 0 \\ 0 & 0 & 0 & 0 & E_{\mathrm{s}} I_{\mathrm{s}} & 0 \\ 0 & 0 & 0 & 0 & 0 & G_{\mathrm{s}} J_{\mathrm{s}} \end{bmatrix} \quad \boldsymbol{k}_{\mathrm{N}} = \begin{bmatrix} 0 & 0 & 0 & 0 & 0 & 0 \\ 0 & 0 & 0 & 0 & 0 & 0 \\ 0 & 0 & 0 & 0 & 0 & 0 \\ 0 & 0 & 0 & G_{\mathrm{s}} A_{\mathrm{s}} \kappa & 0 & 0 \\ 0 & 0 & 0 & 0 & G_{\mathrm{s}} A_{\mathrm{s}} \kappa & 0 \\ 0 & 0 & 0 & 0 & 0 & 0 \end{bmatrix}$$

$$\boldsymbol{k}_{\mathrm{BN}} = \begin{bmatrix} 0 & 0 & 0 & 0 & -G_{\mathrm{s}} A_{\mathrm{s}} \kappa & 0 \\ 0 & 0 & 0 & G_{\mathrm{s}} A_{\mathrm{s}} \kappa & 0 & 0 \\ 0 & 0 & 0 & 0 & 0 & 0 \\ 0 & 0 & 0 & 0 & 0 & 0 \\ 0 & 0 & 0 & 0 & 0 & 0 \\ 0 & 0 & 0 & 0 & 0 & 0 \end{bmatrix} \quad \boldsymbol{k}_{\mathrm{NB}} = \begin{bmatrix} 0 & 0 & 0 & 0 & 0 & 0 \\ 0 & 0 & 0 & 0 & 0 & 0 \\ 0 & 0 & 0 & 0 & 0 & 0 \\ 0 & G_{\mathrm{s}} A_{\mathrm{s}} \kappa & 0 & 0 & 0 & 0 \\ -G_{\mathrm{s}} A_{\mathrm{s}} \kappa & 0 & 0 & 0 & 0 & 0 \\ 0 & 0 & 0 & 0 & 0 & 0 \end{bmatrix}$$

Substituting Eq. 2.38 into Eqs. 2.8 and 2.11, the virtual work done per element by the soil reactions is as follows:

$$\left(\delta W_{\text{soil}}^{\text{skirt}}\right)_{\text{elem}} = L_{\text{e}} \int_0^1 \delta \vec{u}_{\text{el}}{}^{\intercal} \boldsymbol{N}^{\intercal} \vec{p}^{\,\text{skirt}} \, d\xi \tag{2.41}$$

$$\left(\delta W_{\text{soil}}^{\text{base}}\right)_{\text{elem}} = \delta \vec{u}^{\,\text{base}\intercal} \vec{p}^{\,\text{base}} \tag{2.42}$$

where $\vec{u}^{\,\text{base}}$ is the nodal displacement at the deepest node. Similarly, the virtual work done per element by the external surface tractions is:

$$L_{\text{e}} \int_0^1 \delta \vec{s}_{\text{el}}^{\,\intercal} \vec{t} \, d\xi = L_{\text{e}} \int_0^1 \delta \vec{u}_{\text{el}}{}^{\intercal} \boldsymbol{N}^{\intercal} \vec{t} \, d\xi \tag{2.43}$$

Gaussian Quadrature

For the above virtual work integrations, the Gaussian quadrature scheme with two Gauss points is used, except for Eq. 2.40 where reduced integration (one Gauss point) is used to prevent shear locking (Hughes 2000, Reddy 2015).

2.6.5 Step 5: Assembly

Substituting Eqs. 2.40 to 2.43 into Eq. 2.28, the equivalent weak form formulation is:

$$\delta \vec{u}^{\,\text{base}\intercal} \vec{p}^{\,\text{base}} + \sum \delta \vec{u}_{\text{el}}{}^{\intercal} L_{\text{e}} \int_0^1 \left(\boldsymbol{k}^{\text{caisson}} \vec{u}_{\text{el}} + \boldsymbol{N}^{\intercal} \vec{p}^{\,\text{skirt}} \right) d\xi = \sum \delta \vec{u}_{\text{el}}{}^{\intercal} L_{\text{e}} \int_0^1 \boldsymbol{N}^{\intercal} \vec{t} \, d\xi \tag{2.44}$$

where the summation is taken over all the elements.

By carrying out the summation and assembly, Eq. 2.44 may be simplified into:

$$\begin{aligned} \delta \vec{u}_{\text{sys}}{}^{\intercal} \vec{F}_{\text{int}} &= \delta \vec{u}_{\text{sys}}{}^{\intercal} \vec{F}_{\text{ext}} \\ \delta \vec{u}_{\text{sys}}{}^{\intercal} \left(\vec{F}_{\text{ext}} - \vec{F}_{\text{int}} \right) &= 0 \end{aligned} \tag{2.45}$$

where $\delta \vec{u}_{\text{sys}}$ is the virtual system nodal displacements and $\vec{F}_{\text{ext}}$ and $\vec{F}_{\text{int}}$ are the external and internal system equivalent nodal forces, which may be computed as follows:

$$\vec{F}_{\text{int}} = \mathbb{A} \left(\vec{p}^{\,\text{base}} + \sum L_{\text{e}} \int_0^1 \boldsymbol{k}^{\text{caisson}} \vec{u}_{\text{el}} + \boldsymbol{N}^{\intercal} \vec{p}^{\,\text{skirt}} \, d\xi \right) \tag{2.46}$$

$$\vec{F}_{\text{ext}} = \mathbb{A} \left(\sum L_{\text{e}} \int_0^1 \boldsymbol{N}^{\intercal} \vec{t} \, d\xi \right) \tag{2.47}$$

where $\mathbb{A}$ is the assembly operator (which assembles the element force vectors into a global force vector). In this thesis, it is assumed that the external loads are applied at RP (see Fig. 2.1a), which is defined as the first (shallowest) node. Thus, the components of $\vec{F}_{\text{ext}}$ are set to zeros, except for the components of the first node which are set to $\vec{P}$.

Since Eq. 2.45 has to hold for any arbitrary $\delta \vec{u}_{\text{sys}}$, the following must be true:

$$\vec{F}_{\text{ext}} - \vec{F}_{\text{int}} = 0 \tag{2.48}$$

2.6.6 Step 6: Solve System

Let $\vec{F}_{\text{res}} = \vec{F}_{\text{ext}} - \vec{F}_{\text{int}}$ be the system residual. Before $\vec{F}_{\text{ext}}$ is applied, $\vec{F}_{\text{res}} = 0$. After $\vec{F}_{\text{ext}}$ is applied (either incrementally or entirely), the system is not in equilibrium as $\vec{F}_{\text{res}} \neq 0$. Taking the Taylor's series expansion of $\vec{F}_{\text{res}}$ in the neighbourhood of ${\vec{F}_{\text{res}}}^{(j)}$ and ignoring the second order terms and above, a linearised form of Eq. 2.48 is obtained as follows:

$$\begin{aligned} \vec{F}_{\text{res}} &= 0 \\ {\vec{F}_{\text{res}}}^{(j)} + \frac{\partial \vec{F}_{\text{res}}}{\partial \vec{u}_{\text{sys}}}^{(j)} \Delta \vec{u}_{\text{sys}} &= 0 \end{aligned} \tag{2.49}$$

where $\Delta \vec{u}_{\text{sys}}$ is the unknown system nodal displacements increment to solve for, ${\vec{F}_{\text{res}}}^{(j)} = \vec{F}_{\text{ext}} - {\vec{F}_{\text{int}}}^{(j)}$ is the unbalanced system residual and the superscript (j) represents the value of the corresponding variable at the start of iteration j.

Since $\vec{F}_{\text{ext}}$ is independent of $\vec{u}_{\text{sys}}$:

$$\frac{\partial \vec{F}_{\text{res}}}{\partial \vec{u}_{\text{sys}}} = -\frac{\partial \vec{F}_{\text{int}}}{\partial \vec{u}_{\text{sys}}} \tag{2.50}$$

Substituting Eq. 2.50 into Eq. 2.49 gives:

$$\begin{aligned} {\vec{F}_{\text{res}}}^{(j)} - \frac{\partial \vec{F}_{\text{int}}}{\partial \vec{u}_{\text{sys}}}^{(j)} \Delta \vec{u}_{\text{sys}} &= 0 \\ \frac{\partial \vec{F}_{\text{int}}}{\partial \vec{u}_{\text{sys}}}^{(j)} \Delta \vec{u}_{\text{sys}} &= {\vec{F}_{\text{res}}}^{(j)} \\ {\boldsymbol{K}_{\text{sys}}}^{(j)} \Delta \vec{u}_{\text{sys}} &= {\vec{F}_{\text{res}}}^{(j)} \end{aligned} \tag{2.51}$$

where $\boldsymbol{K}_{\text{sys}}$ is the system stiffness matrix.

For oxCaisson-LE, $\vec{F}_{\text{ext}}$ is applied entirely and Eq. 2.51 can be solved directly in one iteration. For oxCaisson-NLE or oxCaisson-LEPP, $\vec{F}_{\text{ext}}$ is applied in increments and the Newton-Raphson procedure is used to solve Eq. 2.51 iteratively. The pseudo code for this procedure is shown in Algorithm 1.

Update Procedures For Soil Reactions

Depending on the Winkler models deployed, different numerical procedures are used to update the values of $\vec{p}^{\text{skirt}}$ and $\vec{p}^{\text{base}}$ in Eq. 2.46 during the iteration process.

Algorithm 1 Newton-Raphson procedure

```
while $\vec{F}_{\text{ext}}$ has not been fully applied do
  Add the next increment to $\vec{F}_{\text{ext}}$
  while $\|\vec{F}_{\text{res}}\|_{\infty} \geq 10^{-4}\|\vec{F}_{\text{ext}}\|_{\infty}$ do
    Compute $\boldsymbol{K}_{\text{sys}}$
    $\Delta\vec{u}_{\text{sys}} = \boldsymbol{K}_{\text{sys}}{}^{-1}\vec{F}_{\text{res}}$
    Apply $\Delta\vec{u}_{\text{sys}}$ to elements
    $\vec{u}_{\text{sys}} = \vec{u}_{\text{sys}} + \Delta\vec{u}_{\text{sys}}$
    Update $\vec{F}_{\text{int}}$
    Update $\vec{F}_{\text{res}}$
  end while
end while
```

oxCaisson-LE and oxCaisson-NLE $\vec{p}^{\text{skirt}}$ and $\vec{p}^{\text{base}}$ are computed directly for any given displacements as they are explicit functions of the displacements.

oxCaisson-LEPP $\vec{p}^{\text{skirt}}$ and $\vec{p}^{\text{base}}$ have to be updated incrementally. Both the implicit closest point projection method (CPPM) (Simo & Taylor 1985, Huang & Griffiths 2009) algorithm and the explicit Runge-Kutta (4, 5) algorithm (Dormand & Prince 1980) have been implemented and can be used to integrate the elasto-plastic incremental relationships described in Section 2.5.1. By default, the CPPM algorithm is used.

Displacement Boundary Conditions

Displacement boundary conditions may be applied to node i, by replacing the ith row of $\boldsymbol{K}_{\text{sys}}$ with zeros (except for the ith column which is replaced with 1) and by replacing the ith row of $\vec{F}_{\text{ext}}$ and $\vec{F}_{\text{int}}$ to the prescribed displacement value and the current nodal displacement value at node i respectively.

Rigid Body Constraints

To model a fully rigid caisson where the only degrees of freedom are that of the reference point RP (see Fig. 2.1a), rigid body constraints are added to the weak form formulation in Eq. 2.45. These rigid body constraints are defined using a matrix $\boldsymbol{R}_{\text{sys}} = \frac{\partial \vec{u}_{\text{sys}}}{\partial \vec{S}}$ such that:

$$\vec{u}_{\text{sys}} = \boldsymbol{R}_{\text{sys}}\vec{S} \tag{2.52}$$

where the components of $\boldsymbol{R}_{\text{sys}}$ can be determined using Eq. 2.3.

Substituting Eq. 2.52 into Eq. 2.45, the updated weak form formulation is obtained:

$$\begin{aligned} \left(\boldsymbol{R}_{\text{sys}}\delta\vec{S}\right)^{\mathsf{T}}\left(\vec{F}_{\text{ext}}-\vec{F}_{\text{int}}\right)&=0\\ \delta\vec{S}^{\mathsf{T}}\boldsymbol{R}_{\text{sys}}{}^{\mathsf{T}}\left(\vec{F}_{\text{ext}}-\vec{F}_{\text{int}}\right)&=0 \end{aligned} \tag{2.53}$$

Since Eq. 2.53 has to hold for any arbitrary $\delta\vec{S}$, the following must be true:

$$\boldsymbol{R}_{\text{sys}}{}^{\mathsf{T}}\left(\vec{F}_{\text{ext}}-\vec{F}_{\text{int}}\right)=0 \tag{2.54}$$

Let $\vec{F}_{\text{res}}^{\text{rigid}}=\boldsymbol{R}_{\text{sys}}{}^{\mathsf{T}}\left(\vec{F}_{\text{ext}}-\vec{F}_{\text{int}}\right)$. Following the steps from Eq. 2.49 to 2.51:

$$\begin{aligned} \vec{F}_{\text{res}}^{\text{rigid}}&=0\\ \vec{F}_{\text{res}}^{\text{rigid}\,(j)}+\frac{\partial\vec{F}_{\text{res}}^{\text{rigid}}}{\partial\vec{u}_{\text{sys}}}^{(j)}\Delta\vec{u}_{\text{sys}}&=0\\ \vec{F}_{\text{res}}^{\text{rigid}\,(j)}-\boldsymbol{R}_{\text{sys}}{}^{\mathsf{T}}\frac{\partial\vec{F}_{\text{int}}}{\partial\vec{u}_{\text{sys}}}^{(j)}\left(\boldsymbol{R}_{\text{sys}}\Delta\vec{S}\right)&=0\\ \boldsymbol{R}_{\text{sys}}{}^{\mathsf{T}}\frac{\partial\vec{F}_{\text{int}}}{\partial\vec{u}_{\text{sys}}}^{(j)}\boldsymbol{R}_{\text{sys}}\Delta\vec{S}&=\vec{F}_{\text{res}}^{\text{rigid}\,(j)}\\ \left(\boldsymbol{R}_{\text{sys}}{}^{\mathsf{T}}\boldsymbol{K}_{\text{sys}}{}^{(j)}\boldsymbol{R}_{\text{sys}}\right)\Delta\vec{S}&=\vec{F}_{\text{res}}^{\text{rigid}\,(j)}\\ \boldsymbol{K}_{\text{sys}}^{\text{rigid}\,(j)}\Delta\vec{S}&=\vec{F}_{\text{res}}^{\text{rigid}\,(j)} \end{aligned} \tag{2.55}$$

where $\boldsymbol{K}_{\text{sys}}^{\text{rigid}}=\boldsymbol{R}_{\text{sys}}{}^{\mathsf{T}}\boldsymbol{K}_{\text{sys}}\boldsymbol{R}_{\text{sys}}$ and $\Delta\vec{S}$ is the displacement increment of RP to solve for.

Chapter 3

Linear Elastic Soil

In Chapter 2, the detailed workings of oxCaisson are outlined but the definitions of the soil reactions $\vec{p}$ are not addressed. In this chapter, the related work on suction caissons in linear elastic soil are first described before the formulations of linear elastic $\vec{p}$ are derived through calibration against 3DFE analyses of suction caissons in linear elastic soil.

Definition 3.1 (Stiffness Coefficient) *A stiffness coefficient is defined to be the ratio of a load (or load per unit length) to a displacement (which can be a translation or rotation). For example,* K_V *is the ratio of the global vertical force to the global vertical translation, while* $k_\mathrm{V}^\mathrm{skirt}$ *is the ratio of the vertical skirt soil reaction to the vertical translation of the skirt cross section. In the context of a Winkler model, the stiffness coefficient for a skirt soil reaction, such as* $k_\mathrm{V}^\mathrm{skirt}$*, is also known as 'modulus of subgrade reaction', 'subgrade modulus' or 'Winkler modulus' in previous literature.*

3.1 Introduction

The global stiffness matrix $\boldsymbol{K}_\mathrm{e}$ for a suction caisson in linear elastic soil is known from previous work (Doherty et al. 2005) as:

$$\vec{P} = \boldsymbol{K}_\mathrm{e}\vec{S} \tag{3.1}$$

where

$$\boldsymbol{K}_\mathrm{e} = \begin{bmatrix} K_\mathrm{H} & 0 & 0 & 0 & -K_\mathrm{CH} & 0 \\ 0 & K_\mathrm{H} & 0 & K_\mathrm{CH} & 0 & 0 \\ 0 & 0 & K_\mathrm{V} & 0 & 0 & 0 \\ 0 & K_\mathrm{CM} & 0 & K_\mathrm{M} & 0 & 0 \\ -K_\mathrm{CM} & 0 & 0 & 0 & K_\mathrm{M} & 0 \\ 0 & 0 & 0 & 0 & 0 & K_\mathrm{Q} \end{bmatrix}$$

and $K_{\mathrm{V}}, K_{\mathrm{Q}}, K_{\mathrm{H}}, K_{\mathrm{M}}, K_{\mathrm{CH}}, K_{\mathrm{CM}}$ are the global vertical, torsional, lateral, rotational, H-coupling and M-coupling stiffness coefficients respectively. For linear elastic soil, the H-coupling and M-coupling stiffness coefficients are identical (i.e. $K_{\mathrm{CH}} = K_{\mathrm{CM}} = K_{\mathrm{C}}$).

For a fully rigid caisson, these global stiffness coefficients can be related to the local stiffness coefficients of the soil reactions using Eq. 2.14. The local stiffness matrices for the skirt and base soil reactions $\boldsymbol{k}^{\mathrm{skirt}}$ and $\boldsymbol{k}^{\mathrm{base}}$ are defined as:

$$\vec{p}^{\,\mathrm{skirt}} = \boldsymbol{k}^{\mathrm{skirt}} \vec{s} \tag{3.2}$$

$$\vec{p}^{\,\mathrm{base}} = \boldsymbol{k}^{\mathrm{base}} \vec{s}^{\,\mathrm{base}} \tag{3.3}$$

where

$$\boldsymbol{k}^{\mathrm{skirt}} = \begin{bmatrix} k_{\mathrm{h}}^{\mathrm{skirt}} & 0 & 0 & 0 & -k_{\mathrm{ch}}^{\mathrm{skirt}} & 0 \\ 0 & k_{\mathrm{h}}^{\mathrm{skirt}} & 0 & k_{\mathrm{ch}}^{\mathrm{skirt}} & 0 & 0 \\ 0 & 0 & k_{\mathrm{v}}^{\mathrm{skirt}} & 0 & 0 & 0 \\ 0 & k_{\mathrm{cm}}^{\mathrm{skirt}} & 0 & k_{\mathrm{m}}^{\mathrm{skirt}} & 0 & 0 \\ -k_{\mathrm{cm}}^{\mathrm{skirt}} & 0 & 0 & 0 & k_{\mathrm{m}}^{\mathrm{skirt}} & 0 \\ 0 & 0 & 0 & 0 & 0 & k_{\mathrm{q}}^{\mathrm{skirt}} \end{bmatrix}$$

$$\boldsymbol{k}^{\mathrm{base}} = \begin{bmatrix} k_{\mathrm{h}}^{\mathrm{base}} & 0 & 0 & 0 & -k_{\mathrm{ch}}^{\mathrm{base}} & 0 \\ 0 & k_{\mathrm{h}}^{\mathrm{base}} & 0 & k_{\mathrm{ch}}^{\mathrm{base}} & 0 & 0 \\ 0 & 0 & k_{\mathrm{v}}^{\mathrm{base}} & 0 & 0 & 0 \\ 0 & k_{\mathrm{cm}}^{\mathrm{base}} & 0 & k_{\mathrm{m}}^{\mathrm{base}} & 0 & 0 \\ -k_{\mathrm{cm}}^{\mathrm{base}} & 0 & 0 & 0 & k_{\mathrm{m}}^{\mathrm{base}} & 0 \\ 0 & 0 & 0 & 0 & 0 & k_{\mathrm{q}}^{\mathrm{base}} \end{bmatrix}$$

Expanding the terms on the right-hand side of Eq. 2.14 and comparing the components of $\boldsymbol{K}$ with that of $\boldsymbol{K}_{\mathrm{e}}$, it can be shown that:

$$K_{\mathrm{V}} = \int_0^L k_{\mathrm{v}}^{\mathrm{skirt}}\, dz + k_{\mathrm{v}}^{\mathrm{base}} \tag{3.4}$$

$$K_{\mathrm{Q}} = \int_0^L k_{\mathrm{q}}^{\mathrm{skirt}}\, dz + k_{\mathrm{q}}^{\mathrm{base}} \tag{3.5}$$

$$K_{\mathrm{H}} = \int_0^L k_{\mathrm{h}}^{\mathrm{skirt}}\, dz + k_{\mathrm{h}}^{\mathrm{base}} \tag{3.6}$$

$$\begin{aligned} K_{\mathrm{M}} = &\int_0^L \left(k_{\mathrm{ch}}^{\mathrm{skirt}} + k_{\mathrm{h}}^{\mathrm{skirt}}(-z)\right)(-z) + k_{\mathrm{m}}^{\mathrm{skirt}} + k_{\mathrm{cm}}^{\mathrm{skirt}}(-z)\, dz \\ &+ \left(k_{\mathrm{ch}}^{\mathrm{base}} + k_{\mathrm{h}}^{\mathrm{base}}(-L)\right)(-L) + k_{\mathrm{m}}^{\mathrm{base}} + k_{\mathrm{cm}}^{\mathrm{base}}(-L) \end{aligned} \tag{3.7}$$

$$K_{\mathrm{CH}} = \int_0^L k_{\mathrm{ch}}^{\mathrm{skirt}} + k_{\mathrm{h}}^{\mathrm{skirt}}(-z)\,dz + k_{\mathrm{ch}}^{\mathrm{base}} + k_{\mathrm{h}}^{\mathrm{base}}(-L) \tag{3.8}$$

$$K_{\mathrm{CM}} = \int_0^L k_{\mathrm{cm}}^{\mathrm{skirt}} + k_{\mathrm{h}}^{\mathrm{skirt}}(-z)\,dz + k_{\mathrm{cm}}^{\mathrm{base}} + k_{\mathrm{h}}^{\mathrm{base}}(-L) \tag{3.9}$$

There currently exists two Winkler models (Gerolymos & Gazetas 2006*c*, Varun et al. 2009) for caissons in linear elastic soil under lateral and moment loads, which are similar to the PISA design method for laterally-loaded monopiles (Byrne et al. 2015, 2017). In these models, there are two distributed soil reactions (lateral force and rotational moment) acting along the foundation length and two concentrated soil reactions (shear force and rotational moment) acting on the foundation base. The key difference between each of these Winkler models is the definition of the soil reactions. Byrne et al. (2015, 2017) compute their soil reactions directly from the 3DFE local soil stress results, while Gerolymos & Gazetas (2006*c*) and Varun et al. (2009) back-calculated their soil reactions from published global stiffness solutions (Gazetas 1991) and 3DFE global stiffness results respectively.

However, there are some limitations with these existing Winkler models for caissons. First, they have been calibrated for non-skirted, fully solid caissons. Thus, they may not be used directly for suction caissons as the deformability of the soil plug has not been accounted for. Second, they are incomplete as they support only lateral and moment loads. Third, the adopted soil reactions are not representative of the true soil reactions. Instead, they are 'equivalent' soil reactions that have been back-calculated to match some target global caisson behaviour. This back-calculation approach is problematic as the back-calculated soil reactions can change significantly, depending on the assumptions of the Winkler model. For example, a Winkler model with just lateral soil reactions would lead to different values compared to one with lateral and rotational soil reactions, given the same target global caisson behaviour. As shown later in this chapter, this might cause a false understanding of how the soil interacts with the caisson.

To address the above limitations, a Winkler model for suction caissons under 6DoF loading is developed in this chapter. To avoid the aforementioned concerns with the back-calculation approach, the soil reactions are computed directly from the 3DFE local soil stress results. In general, the proposed methodology can be summarised as:

1. Run 3DFE analyses of a suction caisson under 6DoF loading in linear elastic soil.

2. Compute the soil reactions directly from the local soil stress results.
3. Use the computed soil reactions to derive the formulations of $\vec{p}$ in oxCaisson. For convenience, the calibrated oxCaisson is termed 'oxCaisson-LE'.
4. Compare the predictions of oxCaisson-LE with the 3DFE results.

3.2 Methodology

This section describes the 3DFE modelling that was performed to calibrate oxCaisson. The 3DFE model consists of a fully rigid suction caisson embedded in homogeneous linear elastic soil. The caisson diameter D was held constant at unit length, while six skirt lengths ($L/D = 0, 0.125, 0.25, 0.5, 1, 2$) and three skirt thickness ($d_{\text{skirt}}/D = 0.001, 0.005, 0.01$) were analysed. The variation in the skirt thickness is mainly to evaluate the geometry effect, rather than the stiffness effect (since the caissons are all fully rigid). Note that a suction caisson with zero skirt length is essentially a circular surface foundation.

3.2.1 Mesh

The mesh domain is set to $100D$ for both diameter and depth, which was large enough to avoid boundary effects. Mesh convergence analyses were carried out to determine the mesh fineness. A representative mesh of the 3DFE model is shown in Fig. 3.1.

3.2.2 Material Properties

The soil was defined as weightless and homogeneous isotropic linear elastic. The Young's modulus E of the soil was held constant at 100 MPa, while six Poisson's ratios ($\nu = 0, 0.1, 0.2, 0.3, 0.4, 0.49$) were analysed. First-order, fully-integrated, linear, brick elements C3D8 (or C3D8H for $\nu = 0.49$) were assigned to the soil elements. These elements were found to be adequate as comparisons with analyses using their higher-order (and more computationally expensive) counterparts (C3D20 or C3D20H) showed insignificant differences. The caisson was made entirely rigid using rigid body constraints. The reference point of the caisson was set at RP, as shown in Fig. 2.1a. Contact breaking between the soil and caisson was prevented using tie constraints at the soil-caisson interface.

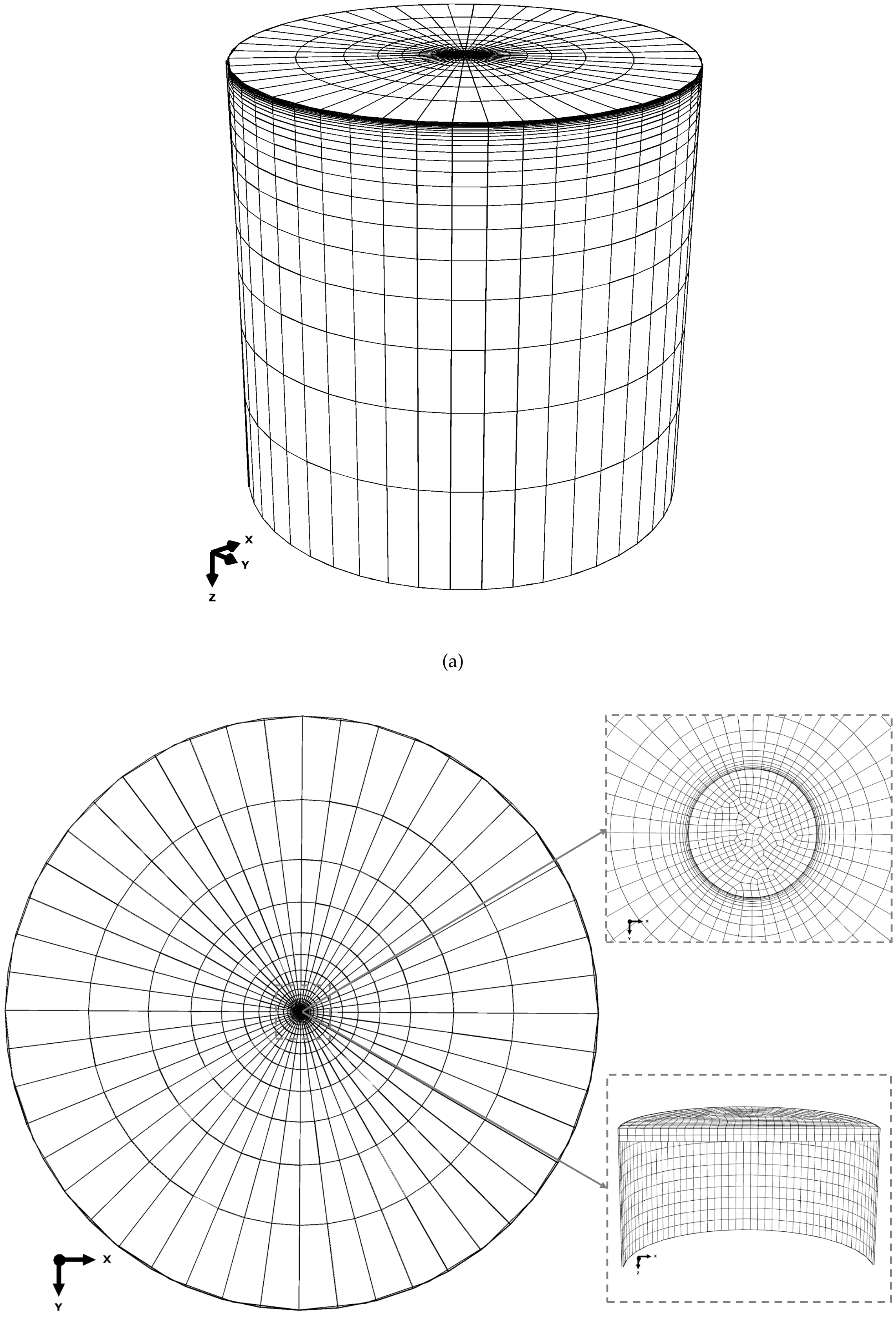

(a)

(b)

Figure 3.1: (a) Oblique view of the full 3DFE model. The depth and diameter of the mesh domain are both $100D$. (b) Plan view of the full 3DFE model, with enlarged partial views of the suction caisson foundation.

3.2.3 Boundary Conditions

Displacements were fixed in all directions at the bottom of the mesh domain and in the radial directions on its periphery. Due to symmetry in the lateral forces and rotational moments, only four displacement modes were required to compute the soil reactions under 6DoF loading. The displacement boundary conditions for these displacement modes, which are prescribed at RP, are shown in Table 3.1.

Table 3.1: Displacement boundary conditions applied at RP (see Fig. 2.1a) to determine the soil reactions under 6DoF loading. Note that the linear elastic nature of the soil permits any non-zero u_0 to be used for the analyses. For the analyses in this paper, u_0 was arbitrarily set to 0.1.

	S_x/D	S_y/D	S_z/D	Θ_x	Θ_y	Θ_z
Rigid Axial Translation	0	0	u_0	0	0	0
Rigid Lateral Translation	0	u_0	0	0	0	0
Rigid Rotation	0	0	0	u_0	0	0
Rigid Torsion	0	0	0	0	0	u_0

3.2.4 Validation

To validate the 3DFE model, the 3DFE global stiffness results were compared with previous work (Doherty et al. 2005). Examples of this comparison are shown in Table 3.2, which compares the results for a caisson of $L/D = 0.5$. Overall, there is excellent agreement between the 3DFE results and those reported by Doherty et al. (2005), with the maximum deviation being only 3.2%.

3.2.5 Computation of Soil Reactions

To compute the soil reactions from the 3DFE results, the contact nodal forces of the soil elements adjacent to the caisson are resolved into resultant forces and moments acting on each cross section. Contact nodal forces refer to nodal forces belonging to nodes at the interface between the caisson and soil elements (the soil plug is part of the caisson in this definition). For the skirt soil reactions, the contact nodal forces are from the soil elements in contact with the external surface of the skirt. For the base soil reactions, the contact nodal forces are from the soil elements directly below the caisson base, as shown in Fig. 3.2.

Table 3.2: Comparison of the normalised 3DFE global stiffness results in compressible ($\nu = 0.2$) and nearly incompressible ($\nu = 0.49$) soil with values reported in previous work (Doherty et al. 2005). The suction caisson used in this comparison has a skirt length of $0.5D$ and skirt thickness of $0.005D$.

Stiffness	ν	Doherty et al. (2005)	3DFE	Deviation (%)
K_{V}/GD	0.2	3.88	3.94	1.81
K_{Q}/GD^3	0.2	2.43	2.45	0.82
K_{H}/GD	0.2	4.55	4.66	2.42
K_{M}/GD^3	0.2	2.10	2.14	1.90
K_{C}/GD^2	0.2	-1.58	-1.63	3.16
K_{V}/GD	0.49	5.39	5.43	0.74
K_{Q}/GD^3	0.49	2.43	2.45	0.82
K_{H}/GD	0.49	5.45	5.56	2.02
K_{M}/GD^3	0.49	2.50	2.42	3.20
K_{C}/GD^2	0.49	-1.73	-1.73	0.00

For each soil element, the soil tractions are determined from the contact nodal forces by dividing the total contact nodal force by the contact surface area. This assumes that the stress within each soil element is constant, which is true if first-order, linear elements are used in the 3DFE analyses. Thereafter, the skirt and base soil reactions are computed from the soil tractions using Eqs. 2.1 and 2.2.

The skirt soil reactions represent the distributed forces and moments per metre skirt length (see Fig. 3.2 for a typical skirt soil reaction resolved from a 'ring' of soil elements in contact with the skirt exterior). The base soil reactions represent concentrated forces and moments acting on the caisson base.

3.2.6 Change of Variables

To determine the local stiffness coefficients (i.e. the components of $\frac{\partial \vec{p}}{\partial \vec{s}}$), the soil reactions $\vec{p}$ has to be defined in terms of the local displacements $\vec{s}$. However, since $\vec{p}$ are computed from analyses corresponding to the global displacements $\vec{S}$ (i.e. the results directly provide the components of $\frac{\partial \vec{p}}{\partial \vec{S}}$), there is a need to implement a change of variables. This can be

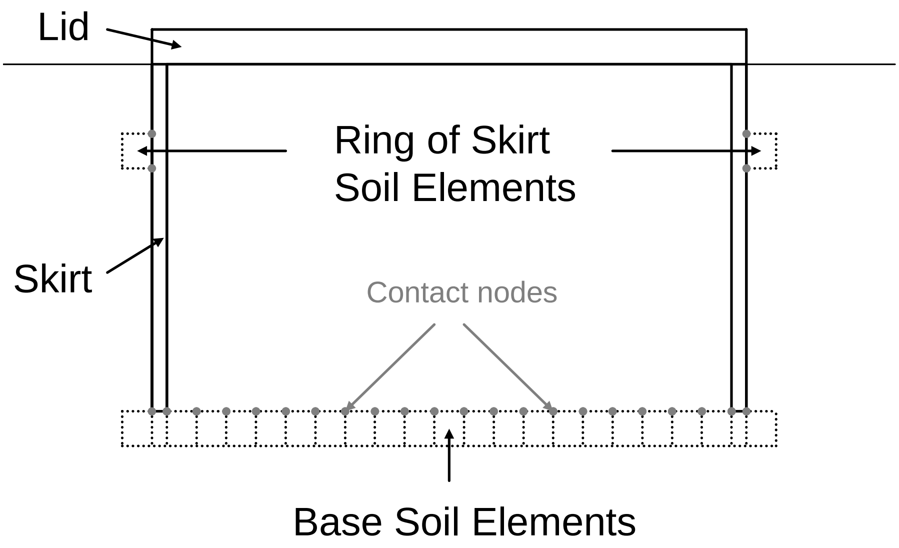

Figure 3.2: Plane view of the soil elements (not drawn to scale), from which the base and skirt soil reactions are derived from. Observe that the base soil reactions include both the soil response on the skirt tip and on the soil plug. The grey markers in the figure refer to the contact nodes from which the nodal forces are extracted from. Note that the ring of skirt soil elements shown in the figure is just one of many rings along the skirt from which the skirt soil reactions are derived from.

done by using Eq. 2.3 and the chain rule:

$$\begin{aligned} \frac{\partial \vec{p}}{\partial \vec{S}} &= \frac{\partial \vec{p}}{\partial \vec{s}} \frac{\partial \vec{s}}{\partial \vec{S}} \\ \frac{\partial \vec{p}}{\partial \vec{S}} &= \frac{\partial \vec{p}}{\partial \vec{s}} \boldsymbol{J} \\ \therefore \frac{\partial \vec{p}}{\partial \vec{s}} &= \frac{\partial \vec{p}}{\partial \vec{S}} \boldsymbol{J}^{-1} \end{aligned} \tag{3.10}$$

3.3 Results

The results presented are typically normalised by the soil shear modulus G and the caisson diameter D as the appropriate length dimension.

3.3.1 Effect of Skirt Thickness

Although 3DFE analyses were carried out for three skirt thickness (d_{skirt}/D = 0.001, 0.005, 0.01), only the results corresponding to one skirt thickness (d_{skirt}/D = 0.005) are presented, as the effect of skirt thickness is limited. The maximum deviation of the global stiffness results for the other skirt thicknesses (compared to that of d_{skirt}/D = 0.005) is only 0.81%. Further analysis indicates negligible effect on the skirt soil reactions and marginal effect on the base soil reactions, as shown in Fig. 3.3. Thus, for the range of skirt thicknesses analysed (0.001 $\leq d_{\text{skirt}}$/D $\leq$ 0.01), which is also the range expected for most operational caissons,

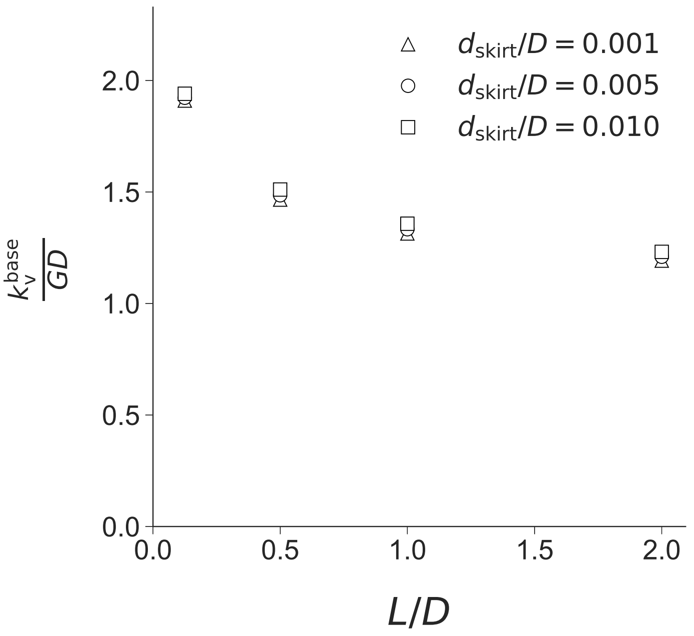

Figure 3.3: An example of the limited effect of skirt thickness on the base soil reactions for $\nu = 0.2$.

the skirt and base soil reactions are assumed to be independent of the skirt thickness and the results corresponding to d_{skirt}/D = 0.005 are considered as representative of this range.

3.3.2 Local Stiffness Coefficients

To determine the local stiffness coefficients, the procedure described in Section 3.2.6 is applied to the computed soil reactions $\vec{p}$. Fig. 3.4 shows the normalised local stiffness coefficients, for three skirt lengths ($L/D = 0.5, 1, 2$). Note the existence of the local coupling stiffness coefficients ($k_{\text{ch}}^{\text{skirt}}, k_{\text{cm}}^{\text{skirt}}, k_{\text{ch}}^{\text{base}}, k_{\text{cm}}^{\text{base}}$), which are ignored by the existing Winkler models for caissons (Gerolymos & Gazetas 2006*c*, Varun et al. 2009).

3.3.3 Idealised Local Stiffness Coefficients

To simplify the formulations of $\vec{p}$, the local stiffness coefficients for the skirt soil reactions were idealised as being either constant or linearly varying with depth, where the former represent the average stiffness of the skirt soil reactions. Fig. 3.5 compares the idealised and true normalised local stiffness coefficients for a caisson of $L/D = 1$, which shows that the idealisation tends to overestimate and underestimate the true soil reactions at shallow and deeper depths respectively. Moreover, it can be observed that there is a large increase in stiffness at the skirt tip depth, which is due to soil stress concentration. From Eqs. 3.4 to 3.6, it is evident that the overestimation and understimation of the idealised stiffness

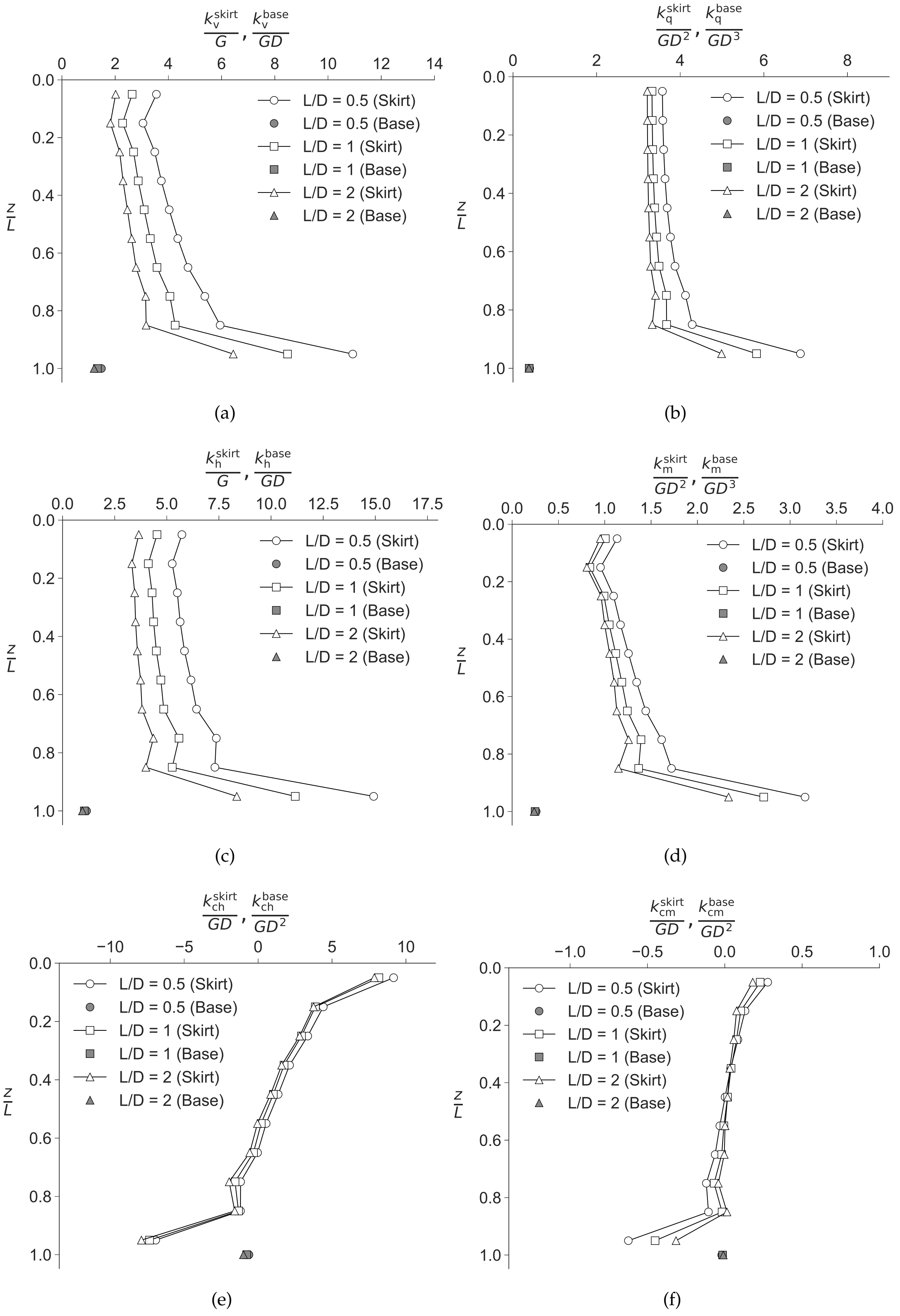

Figure 3.4: Profiles of normalised local stiffness coefficients for the skirt and base soil reactions for $\nu = 0.2$ and $d_{\text{skirt}}/D = 0.005$.

coefficients tend to cancel out when integrated over the skirt length (this is true only for a homogeneous elastic half-space). The additional complexity of linearly varying stiffness is required for $k_{\mathrm{ch}}^{\mathrm{skirt}}$, as a constant idealisation of $k_{\mathrm{ch}}^{\mathrm{skirt}}$ will underpredict the K_{M} prediction using Eq. 3.7. Interestingly, Fig. 3.5e,f show that $k_{\mathrm{ch}}^{\mathrm{skirt}} \neq k_{\mathrm{cm}}^{\mathrm{skirt}}$, which is not in line with the global behaviour where $K_{\mathrm{CH}} = K_{\mathrm{CM}}$. This will be discussed later in Section 3.4.

3.3.4 Effects of Caisson Dimensions and Soil Properties

To identify the effects of caisson dimensions and soil properties on the local stiffness coefficients, Figs. 3.6 and 3.7 show the variations of the normalised local stiffness coefficients for the skirt and base soil reactions with respect to L/D and ν. Note that in Fig. 3.6, each data point corresponds to the idealised, constant local stiffness coefficients along the skirt length (except for $k_{\mathrm{ch}}^{\mathrm{skirt}}$, which was idealised as linearly varying with depth). It is clear from Figs. 3.6 and 3.7 that the (absolute) magnitudes of the local stiffness coefficients tend to decrease and ultimately plateau with increasing L/D. Furthermore, they generally increase with increasing ν (except for $k_{\mathrm{q}}^{\mathrm{skirt}}$, which is independent of ν).

3.3.5 Calibration

Definition 3.2 (Function approximation) *Function approximation selects a function $\hat{h}$ that closely matches (or approximates) the output of some target function h. The explicit formulation of h is usually not known, but a finite set of data points generated by h are known. Techniques such as regression analysis may then be used to identify $\hat{h}$ using these data points. In this thesis, $\hat{h}$ is called an 'approximating function'.*

The objective of the calibration process is to identify functions that can approximate the local stiffness coefficients shown in Figs. 3.6 and 3.7. This is accomplished by carrying out function approximation, using the 3DFE local stiffness coefficients as training data.

This process involves two steps:

1. Select a form for the approximating function.
2. Learn the coefficients of the function from the training data.

This process is generally called parametric model learning (Russell & Norvig 2005). Since there is a multitude of functions that could fit the training data, simpler functional

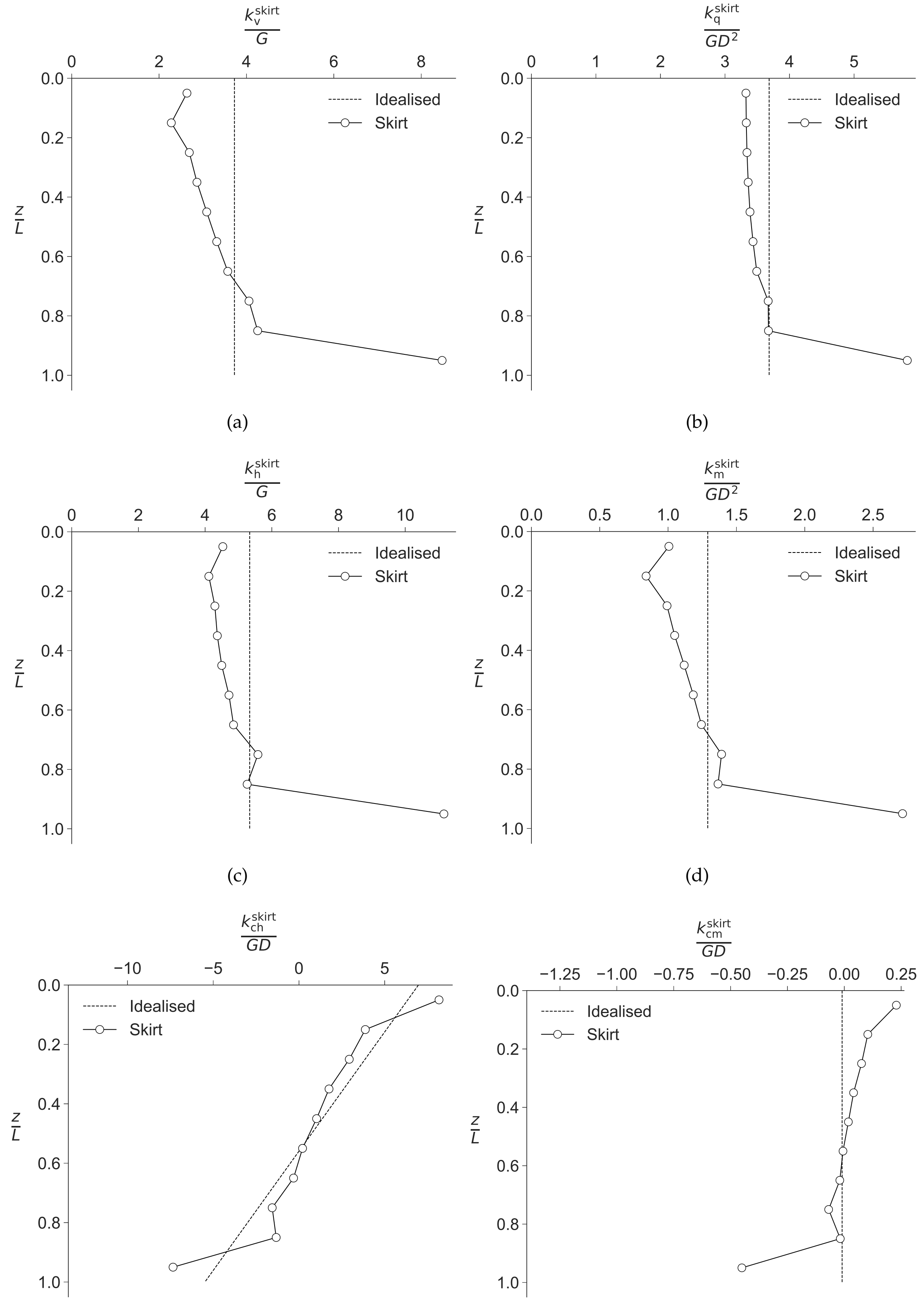

(a) (b)

(c) (d)

(e) (f)

Figure 3.5: Profiles of idealised and true normalised local stiffness coefficients for the skirt soil reactions for $\nu = 0.2$, $L/D = 1$ and $d_{\text{skirt}}/D = 0.005$.

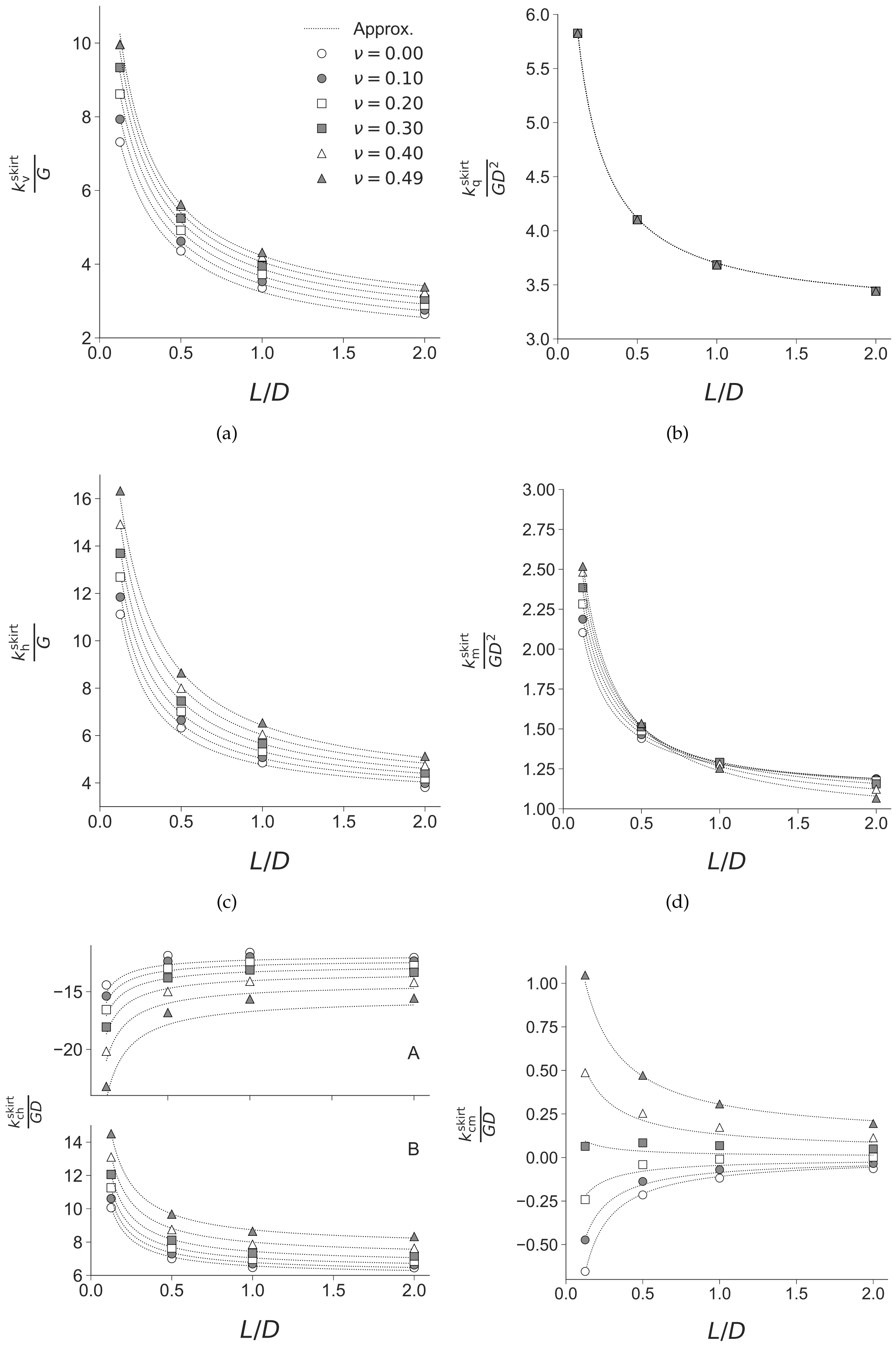

(a) (b)

(c) (d)

(e) (f)

Figure 3.6: Variations of the idealised local stiffness coefficients for the skirt soil reactions, with respect to L/D and ν for $d_{\text{skirt}}/D = 0.005$. All the local stiffness coefficients are idealised as being constant with depth, except for $k_{\text{ch}}^{\text{skirt}}/GD = A(z/L) + B$, as shown in (e). The dotted lines represent the predictions of the approximating functions (Eqs. 3.12 to 3.17). Note the non-zero y-axis origin.

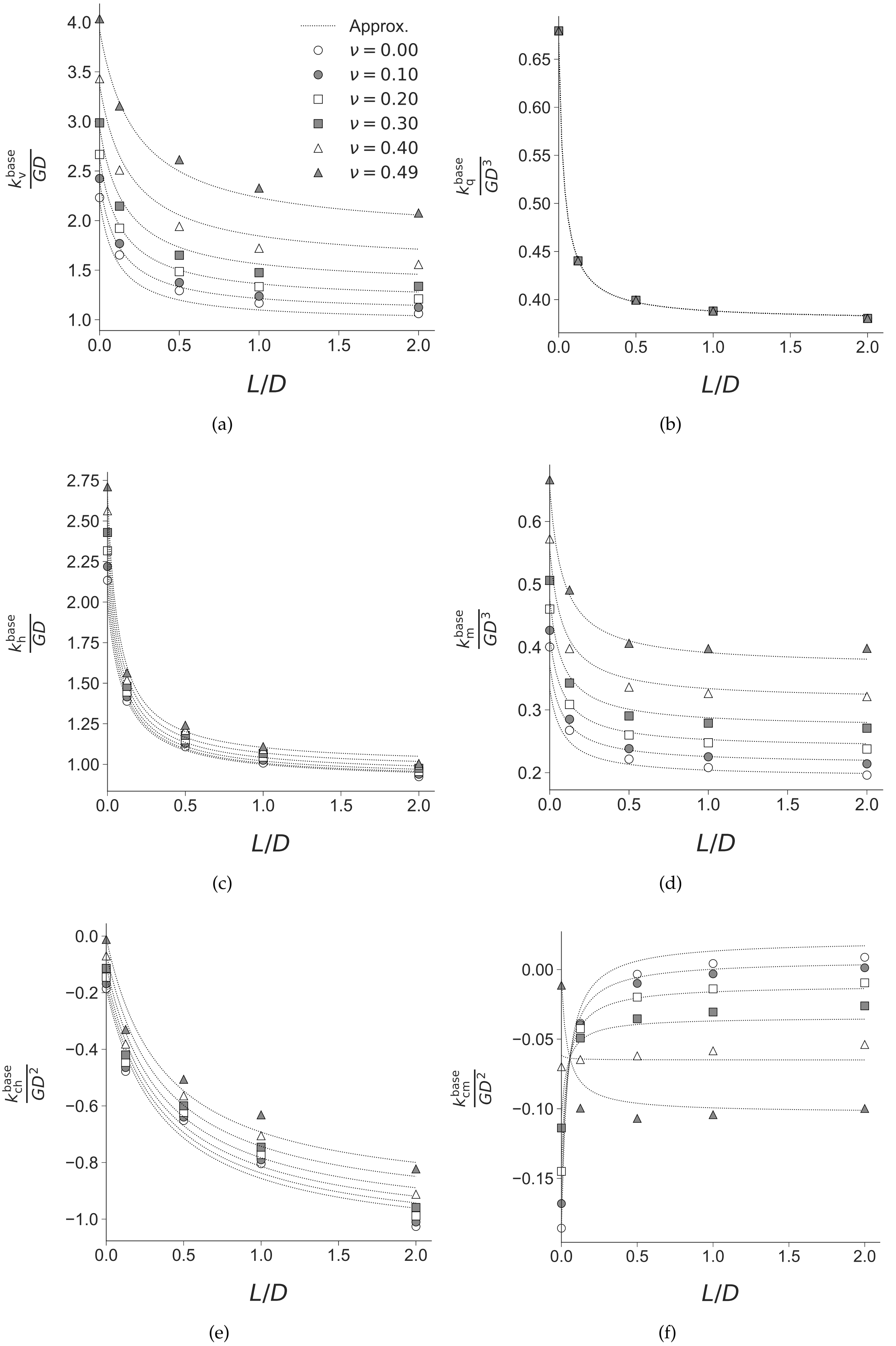

(a) (b)

(c) (d)

(e) (f)

Figure 3.7: Variations of the normalised local stiffness coefficients for the base soil reactions, with respect to L/D and ν for $d_{\text{skirt}}/D = 0.005$. The dotted lines represent the predictions of the approximating functions (Eqs. 3.20 to 3.25). Note the non-zero y-axis origin.

forms are favoured over complex ones, to minimise overfitting.

First, the focus is on finding approximating functions for the local stiffness coefficients for the skirt soil reactions. Surprisingly, a single functional form works well for all:

$$\hat{h}_1(a_1,\ldots,a_6) = (a_1 + a_2\nu)\left(1 - \frac{(a_3 + a_4\nu)\frac{L}{D}}{(a_5 + a_6\nu)\frac{L}{D} + 1}\right) \tag{3.11}$$

The unknown parameters $(a_1,\ldots,a_6)$ in Eq. 3.11 were identified by carrying out least squares (LS) regressions, which produced the following approximating functions:

$$\frac{k_{\mathrm{v}}^{\mathrm{skirt}}}{G} = \hat{h}_1(10.8, 14.4, 4.2, 5.2, 5, 5.8) \tag{3.12}$$

$$\frac{k_{\mathrm{q}}^{\mathrm{skirt}}}{GD^2} = \hat{h}_1(10.7, 0, 10.4, 0, 14.9, 0) \tag{3.13}$$

$$\frac{k_{\mathrm{h}}^{\mathrm{skirt}}}{G} = \hat{h}_1(23.3, 7.6, 10.5, -8.9, 12.2, -10.5) \tag{3.14}$$

$$\frac{k_{\mathrm{ch}}^{\mathrm{skirt}}}{GD} = \hat{h}_1(-170, -20, 360, -470, 387, -500)\frac{z}{L} + \hat{h}_1(51, -8.7, 71, -80.4, 80.5, -87) \tag{3.15}$$

$$\frac{k_{\mathrm{m}}^{\mathrm{skirt}}}{GD^2} = \hat{h}_1(3.8, 1.6, 9.55, -3, 13.4, -6.8) \tag{3.16}$$

$$\frac{k_{\mathrm{cm}}^{\mathrm{skirt}}}{GD} = \hat{h}_1(-2.4, 8.8, 21, -27.4, 21, -26.5) \tag{3.17}$$

Fig. 3.6 compares the predictions of Eqs. 3.12 to 3.17 with the 3DFE local stiffness coefficients. It is evident that the approximating functions closely matches the 3DFE results.

As for the base soil reactions, two functional forms were selected:

$$\hat{h}_2(k_0, a_1, a_2, a_3, a_4) = k_0\left(1 - \frac{(a_1 + a_2\nu)\frac{L}{D}}{(a_3 + a_4\nu)\frac{L}{D} + 1}\right) \tag{3.18}$$

$$\hat{h}_3(k_0, a_1, a_2, a_3) = k_0 + \left(a_1 + \frac{a_2}{1-\nu}\right)\left(1 - \frac{1}{a_3\frac{L}{D} + 1}\right) \tag{3.19}$$

The parameter k_0 in Eqs. 3.18 and 3.19 represents the corresponding stiffness of a rough, rigid, circular surface foundation on a homogeneous elastic half-space. Table 3.3 shows the solutions for k_0, all of which are analytical solutions except for the coupling stiffness K_{C}, which was approximated from the 3DFE results in this study.

Similarly, LS regressions were carried out to produce the following approximating

Table 3.3: Stiffness solutions for a rough (except for K_{M} which is for a smooth foundation), rigid, circular surface foundation on a homogeneous elastic half-space. All the stiffness solutions are analytical solutions, except for the coupling stiffness K_{C}, which is approximated from the 3DFE results. Most of the analytical solutions are conveniently summarised in Poulos & Davis (1974).

Stiffness	Formula	Source
$\frac{K_{\mathrm{V}}}{GD}$	$\frac{2\ln(3-4\nu)}{1-2\nu}$	Spence (1968)
$\frac{K_{\mathrm{H}}}{GD}$	$\frac{4}{2-\nu}$	Mindlin (1949)
$\frac{K_{\mathrm{M}}}{GD^3}$	$\frac{1}{3(1-\nu)}$	Borowicka (1943)
$\frac{K_{\mathrm{Q}}}{GD^3}$	$\frac{2}{3}$	Reissner (1944)
$\frac{K_{\mathrm{C}}}{GD^2}$	$\frac{0.185}{1-\nu} - 0.37$	3DFE results (this study)

functions for the local stiffness coefficients for the base soil reactions:

$$\frac{k_{\mathrm{v}}^{\mathrm{base}}}{GD} = \hat{h}_2(\frac{2\ln(3-4\nu)}{1-2\nu}, 5, -5.5, 9, -9.5) \tag{3.20}$$

$$\frac{k_{\mathrm{q}}^{\mathrm{base}}}{GD^3} = \hat{h}_2(\frac{2}{3}, 12.2, 0, 28.2, 0) \tag{3.21}$$

$$\frac{k_{\mathrm{h}}^{\mathrm{base}}}{GD} = \hat{h}_2(\frac{4}{2-\nu}, 5.3, 6.7, 9.6, 8.4) \tag{3.22}$$

$$\frac{k_{\mathrm{ch}}^{\mathrm{base}}}{GD^2} = \hat{h}_3(\frac{0.185}{1-\nu} - 0.37, -0.9, -0.02, 2.7) \tag{3.23}$$

$$\frac{k_{\mathrm{m}}^{\mathrm{base}}}{GD^3} = \hat{h}_3(\frac{1}{3(1-\nu)}, 0.01, -0.15, 12) \tag{3.24}$$

$$\frac{k_{\mathrm{cm}}^{\mathrm{base}}}{GD^2} = \hat{h}_3(\frac{0.185}{1-\nu} - 0.37, 0.52, -0.314, 25.7) \tag{3.25}$$

Fig. 3.7 compares the predictions of Eqs. 3.20 to 3.25 with the 3DFE local stiffness coefficients. Evidently, the predictions of the approximating functions agree well with the 3DFE results. Thus, Eqs. 3.12 to 3.17 define $\vec{p}^{\mathrm{skirt}}$ and Eqs. 3.20 to 3.25 define $\vec{p}^{\mathrm{base}}$, which complete the definition of oxCaisson for linear elastic soil (i.e. oxCaisson-LE).

3.3.6 Validation

To verify that oxCaisson-LE has been calibrated properly, Fig. 3.8 compares its global stiffness coefficient predictions (using Eqs. 3.4 to 3.9) against the 3DFE results for $L/D = 0, 0.125, 0.25, 0.5, 1, 2$ and $\nu = 0, 0.1, 0.2, 0.3, 0.4, 0.49$. It is clear that the oxCaisson-LE predictions agree very well with the 3DFE results. To quantify the prediction errors, Table 3.4 shows the average percentage differences (i.e. $\frac{1}{n}\sum_{i=1}^{n} PD_i$ where $PD_i = 100(K^{\mathrm{pred.(i)}}/K^{\mathrm{3DFE(i)}} - 1)$ and n is number of data points) and the root-mean-square percentage errors (RMSPE) of the global stiffness coefficient predictions. The RMSPE, which is computed as the root-mean-square of the percentage differences (i.e. $\sqrt{\frac{1}{n}\sum_{i=1}^{n} PD_i^2}$), approximates the average percentage deviation of the predictions. Looking at the RMSPE, it is clear that the oxCaisson-LE predictions for $K_{\mathrm{V}}, K_{\mathrm{Q}}, K_{\mathrm{H}}$ are relatively more accurate than that of $K_{\mathrm{M}}, K_{\mathrm{CH}}, K_{\mathrm{CM}}$.

On average, the percentage differences are minor, albeit less so for $K_{\mathrm{M}}, K_{\mathrm{CH}}, K_{\mathrm{CM}}$. Fig. 3.8d shows that oxCaisson-LE underpredicts K_{M} for $L/D = 0$ and for higher L/D. The former is due to the difference between the adopted analytical solution in Table 3.3 and the 3DFE results, while the latter is because $k_{\mathrm{h}}^{\mathrm{skirt}}$ has been idealised as being constant along the skirt. It is clear from Fig. 3.5c that doing so excludes a significant moment contribution from the large lateral soil reaction towards the end of the skirt length. Furthermore, it is evident from Table 3.4 and Fig 3.8e, f that, unlike the 3DFE results, the oxCaisson-LE predictions of the coupling stiffness K_{C} are not identical (i.e. $K_{\mathrm{CH}} \neq K_{\mathrm{CM}}$). This is an unfortunate limitation, which is addressed in the next section.

It should be highlighted that the validation process only indicates that the global stiffness is matched for a homogeneous elastic half-space. Fig. 3.5 suggests that this may be at the expense of overestimating the stiffness contribution of the shallower material and underestimating the stiffness contribution of the deeper material. This could have implications for applications to non-homogeneous soils.

Table 3.4: Average percentage differences and RMSPE of the global stiffness coefficients computed by oxCaisson-LE, relative to the 3DFE results.

Stiffness	Avg. Diff (%)	RMSPE (%)
${K_{\mathrm{V}}}^{\mathrm{pred.}}/{K_{\mathrm{V}}}^{\mathrm{3DFE}}$	-0.47	2.06
${K_{\mathrm{Q}}}^{\mathrm{pred.}}/{K_{\mathrm{Q}}}^{\mathrm{3DFE}}$	0.057	0.9
${K_{\mathrm{H}}}^{\mathrm{pred.}}/{K_{\mathrm{H}}}^{\mathrm{3DFE}}$	-0.37	2.62
${K_{\mathrm{M}}}^{\mathrm{pred.}}/{K_{\mathrm{M}}}^{\mathrm{3DFE}}$	-3.96	5.43
${K_{\mathrm{CH}}}^{\mathrm{pred.}}/{K_{\mathrm{CH}}}^{\mathrm{3DFE}}$	-0.98	6.47
${K_{\mathrm{CM}}}^{\mathrm{pred.}}/{K_{\mathrm{CM}}}^{\mathrm{3DFE}}$	-6.50	7.89

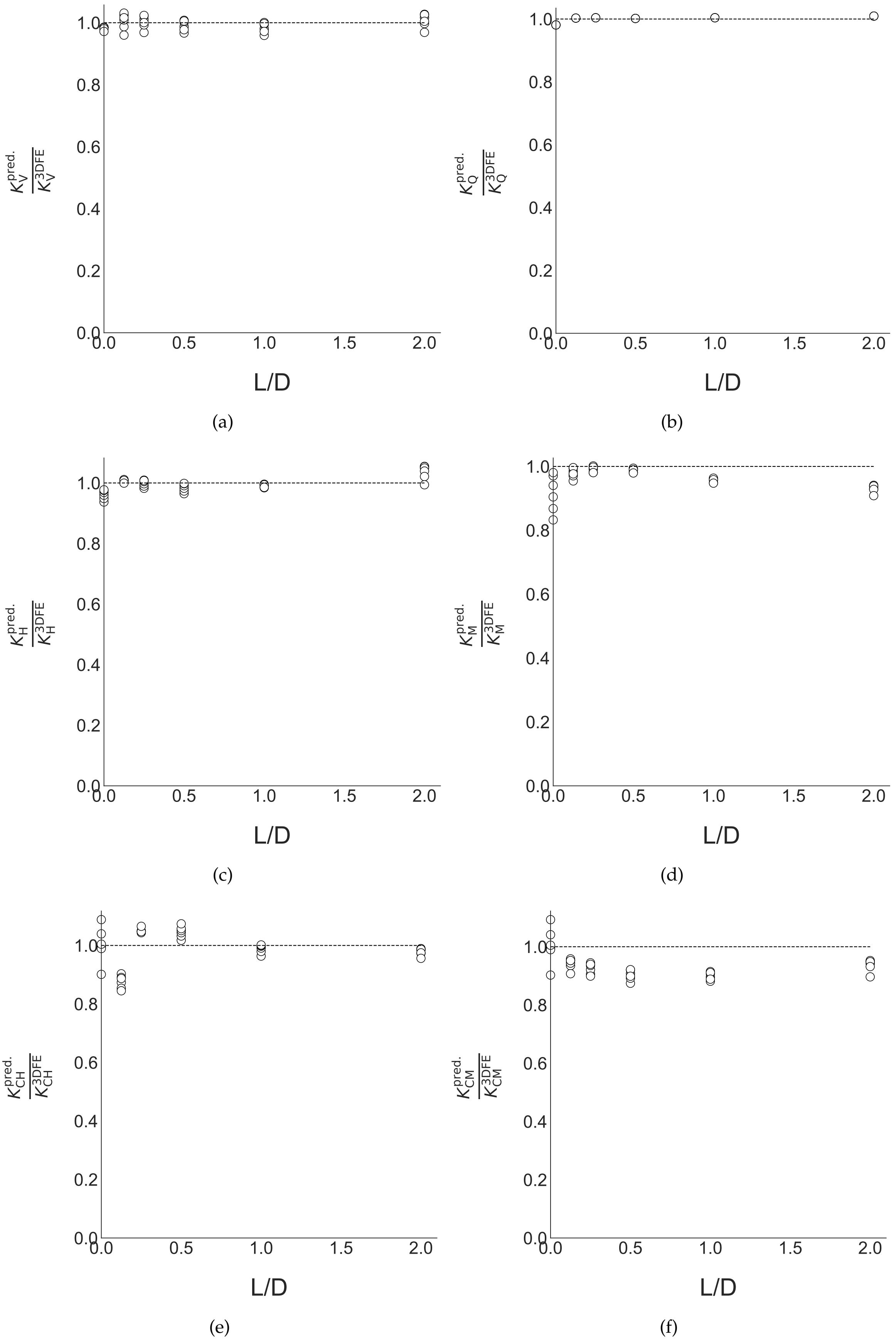

(a) (b) (c) (d) (e) (f)

Figure 3.8: Comparison of the global stiffness coefficients computed by oxCaisson-LE (normalised by the 3DFE results), for $L/D = 0, 0.125, 0.25, 0.5, 1, 2$ and $\nu = 0, 0.1, 0.2, 0.3, 0.4, 0.49$. Values of 1 represent perfect agreement between the oxCaisson-LE computations and the 3DFE results.

3.4 Discussion

oxCaisson-LE was found to be capable of closely reproducing the 3DFE global stiffness results. However, it was noticed that the oxCaisson-LE predictions for the coupling stiffness K_{C} were not identical (see Fig 3.8e, f). This violates energy considerations as the coupling terms for an elastic material with energy potential must be identical. The cause of this is the lack of symmetry between the local coupling stiffness coefficients for the skirt (compare Eq. 3.15 with Eq. 3.17) and base (compare Eq. 3.23 with Eq. 3.25) soil reactions. This is not an artefact of the idealisation process of the skirt soil reactions, as it is evident from Fig. 3.7e, f (which show the true base soil reactions) that $k_{\mathrm{ch}}^{\mathrm{base}}$ is not identical to $k_{\mathrm{cm}}^{\mathrm{base}}$ (unless $L/D = 0$). This reveals a limitation of the Winkler assumption: defining the true soil reactions in terms of only the local displacements results in energy non-compliant relationships. To enforce K_{C} symmetry in any arbitrary soil profile (where G may be non-homogeneous), the constraints $k_{\mathrm{ch}}^{\mathrm{skirt}} = k_{\mathrm{cm}}^{\mathrm{skirt}}$ and $k_{\mathrm{ch}}^{\mathrm{base}} = k_{\mathrm{cm}}^{\mathrm{base}}$ must be satisfied. This can be achieved by introducing symmetrical local coupling stiffness coefficients $k_{\mathrm{c}}^{\mathrm{skirt}}$ and $k_{\mathrm{c}}^{\mathrm{base}}$ such that $k_{\mathrm{c}}^{\mathrm{skirt}} = k_{\mathrm{ch}}^{\mathrm{skirt}} = k_{\mathrm{cm}}^{\mathrm{skirt}}$ and $k_{\mathrm{c}}^{\mathrm{base}} = k_{\mathrm{ch}}^{\mathrm{base}} = k_{\mathrm{cm}}^{\mathrm{base}}$, which will change Eqs. 3.7 to 3.9 to:

$$\begin{aligned} K_{\mathrm{M}} = &\int_0^L \left(k_{\mathrm{h}}^{\mathrm{skirt}}(-z)\right)(-z) + k_{\mathrm{m}}^{\mathrm{skirt}} + 2k_{\mathrm{c}}^{\mathrm{skirt}}(-z)\,dz \\ &+ \left(k_{\mathrm{h}}^{\mathrm{base}}(-L)\right)(-L) + k_{\mathrm{m}}^{\mathrm{base}} + 2k_{\mathrm{c}}^{\mathrm{base}}(-L) \end{aligned} \tag{3.26}$$

$$K_{\mathrm{C}} = K_{\mathrm{CH}} = K_{\mathrm{CM}} = \int_0^L k_{\mathrm{c}}^{\mathrm{skirt}} + k_{\mathrm{h}}^{\mathrm{skirt}}(-z)\,dz + k_{\mathrm{c}}^{\mathrm{base}} + k_{\mathrm{h}}^{\mathrm{base}}(-L) \tag{3.27}$$

The symmetrical local coupling stiffness coefficients $k_{\mathrm{c}}^{\mathrm{skirt}}$ and $k_{\mathrm{c}}^{\mathrm{base}}$ were determined by taking the average of the asymmetrical local coupling stiffness coefficients:

$$k_{\mathrm{c}}^{\mathrm{skirt}} = 0.5(k_{\mathrm{ch}}^{\mathrm{skirt}} + k_{\mathrm{cm}}^{\mathrm{skirt}}) \tag{3.28}$$

$$k_{\mathrm{c}}^{\mathrm{base}} = 0.5(k_{\mathrm{ch}}^{\mathrm{base}} + k_{\mathrm{cm}}^{\mathrm{base}}) \tag{3.29}$$

Fig. 3.9 shows the variations of $k_{\mathrm{c}}^{\mathrm{skirt}}$ and $k_{\mathrm{c}}^{\mathrm{base}}$ with L/D and ν. Comparing Fig. 3.9 with Figs. 3.6e, f and 3.7e, f, it is evident that the influence of $k_{\mathrm{ch}}^{\mathrm{skirt}}$ and $k_{\mathrm{ch}}^{\mathrm{base}}$ dominates. As for the global stiffness predictions, it is easy to see from Eq. 3.26 that K_{M} will remain unchanged, while K_{C} will now be the average of K_{CH} and K_{CM}. This results in a better match with the 3DFE results, as shown in Fig. 3.10. Table 3.5 compares the average percentage differences and RMSPE of the oxCaisson-LE predictions, with and without the symmetrical

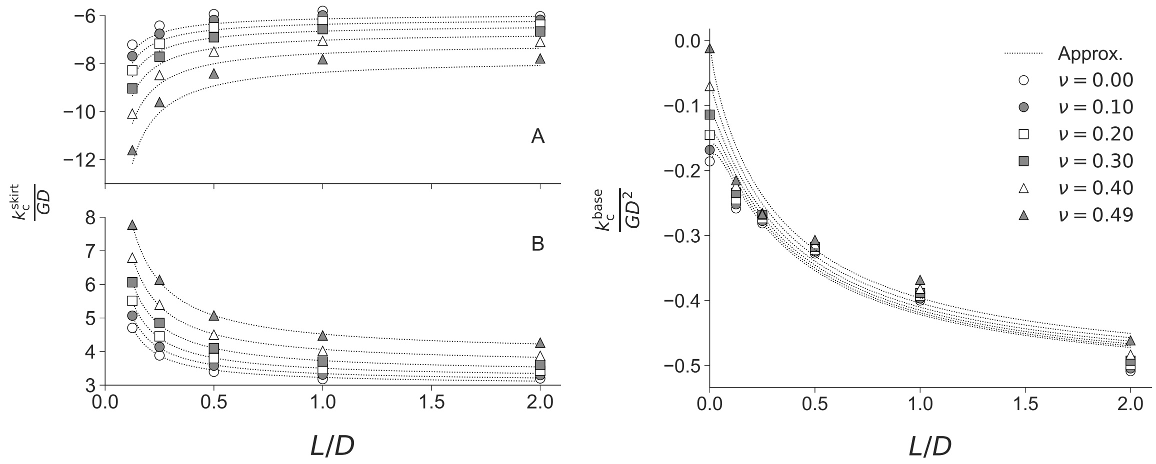

(a)

(b)

Figure 3.9: Variations of the average local coupling stiffness coefficients (k_c^{skirt} and k_c^{base}) with respect to L/D and ν for $d_{\text{skirt}}/D = 0.005$. The dotted lines represent the predictions of Eqs. 3.28 and 3.29.

coupling stiffness modifications. The RMSPE of the modified oxCaisson-LE prediction for K_C is now lower than that of oxCaisson-LE (asymm), which refers to the original model without the symmetrical coupling stiffness modifications.

3.4.1 Comparison with Previous Work

Fig. 3.10 also compares the global stiffness coefficients computed by the existing Winkler models for caissons (Gerolymos & Gazetas 2006*c*, Varun et al. 2009) (only for their calibrated range of $L/D \geq 0.5$) with the 3DFE results. The average percentage differences and RMSPE of these predictions are also listed in Table 3.5. Since the existing Winkler models are calibrated for non-skirted, solid caissons, instead of skirted caissons, higher RMSPE are expected for the predictions of these models.

For K_H, the predictions of Gerolymos & Gazetas (2006*c*) and Varun et al. (2009) are reasonably good, with RMSPE of 5.10% and 8.97% respectively. For K_M, the predictions of Varun et al. (2009) are satisfactory with RMSPE of 11.43%, but the predictions of Gerolymos & Gazetas (2006*c*) are too high, with an average percentage difference of 30.90% and RMSPE of 67.41%. Fig. 3.10b shows that there is a significant overprediction for $L/D = 0.5$. The main source of this overprediction is the k_m^{skirt} stiffness coefficient defined by Gerolymos & Gazetas (2006*c*), which tends to infinity as $L/D \to 0$ (see Fig. 3.11b). Lastly, for K_C, the predictions of Gerolymos & Gazetas (2006*c*) and Varun et al. (2009) were reasonable, with RMSPE of 9.41% and 10.77% respectively.

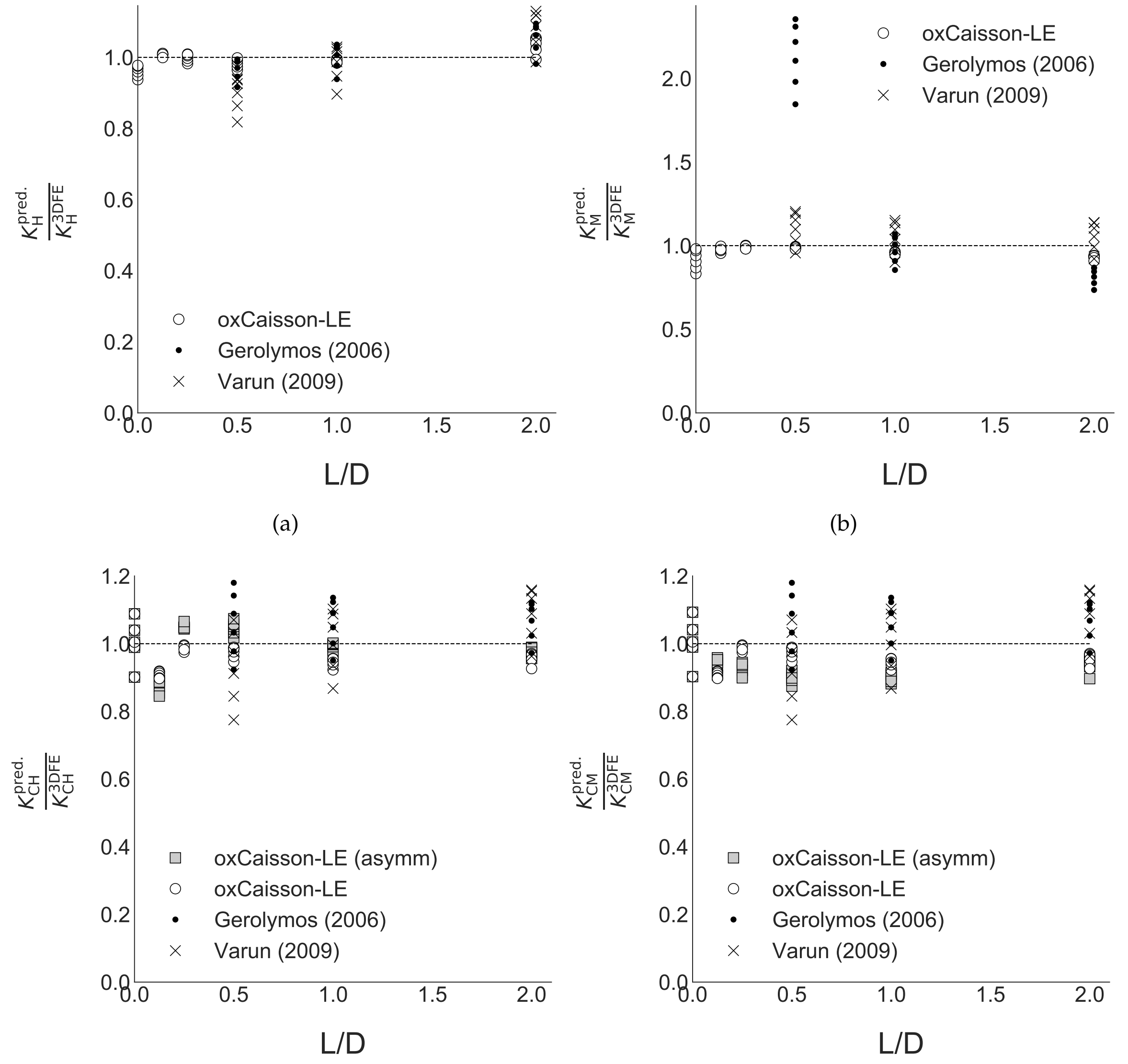

(a) (b) (c) (d)

Figure 3.10: Comparison of the global stiffness coefficients (normalised by their 3DFE counterparts) computed by oxCaisson-LE, oxCaisson-LE (asymm) and the existing Winkler models (Gerolymos & Gazetas 2006*c*, Varun et al. 2009), for $L/D = 0, 0.125, 0.25, 0.5, 1, 2$ and $\nu = 0, 0.1, 0.2, 0.3, 0.4, 0.49$. oxCaisson-LE refers to the updated oxCassion-LE using $k_c^{\text{skirt}}, k_c^{\text{base}}$, while oxCaisson-LE (asymm) refers to the original oxCaisson model using $k_{\text{ch}}^{\text{skirt}}, k_{\text{cm}}^{\text{skirt}}, k_{\text{ch}}^{\text{base}}, k_{\text{cm}}^{\text{base}}$. Note that the predictions of the existing Winkler models were only shown for their calibrated range of $L/D \geq 0.5$.

Table 3.5: Average percentage differences and RMSPE of the global stiffness coefficients computed by oxCaisson-LE, oxCaisson-LE (asymm), Gerolymos & Gazetas (2006*c*) and Varun et al. (2009), relative to the 3DFE results. oxCaisson-LE (asymm) refers to the original oxCaisson-LE with the asymmetrical local coupling stiffness coefficients, while oxCaisson-LE refers to the updated version with the symmetrical local coupling stiffness coefficients. For the symmetrical models (i.e. all except oxCaisson-LE (asymm)), $K_{\mathrm{C}} = K_{\mathrm{CH}} = K_{\mathrm{CM}}$.

Stiffness	Avg. Diff (%)	RMSPE (%)
${K_{\mathrm{CH}}}^{\text{oxCaisson-LE (asymm)}} / {K_{\mathrm{CH}}}^{\text{3DFE}}$	-0.98	6.47
${K_{\mathrm{CM}}}^{\text{oxCaisson-LE (asymm)}} / {K_{\mathrm{CM}}}^{\text{3DFE}}$	-6.50	7.89
${K_{\mathrm{C}}}^{\text{oxCaisson-LE}} / {K_{\mathrm{C}}}^{\text{3DFE}}$	-3.74	5.49
${K_{\mathrm{C}}}^{\text{Gerolymos}} / {K_{\mathrm{C}}}^{\text{3DFE}}$	6.10	9.41
${K_{\mathrm{C}}}^{\text{Varun}} / {K_{\mathrm{C}}}^{\text{3DFE}}$	1.00	10.77
${K_{\mathrm{H}}}^{\text{oxCaisson-LE}} / {K_{\mathrm{H}}}^{\text{3DFE}}$	-0.37	2.62
${K_{\mathrm{H}}}^{\text{Gerolymos}} / {K_{\mathrm{H}}}^{\text{3DFE}}$	0.85	5.10
${K_{\mathrm{H}}}^{\text{Varun}} / {K_{\mathrm{H}}}^{\text{3DFE}}$	-1.28	8.97
${K_{\mathrm{M}}}^{\text{oxCaisson-LE}} / {K_{\mathrm{M}}}^{\text{3DFE}}$	-3.96	5.43
${K_{\mathrm{M}}}^{\text{Gerolymos}} / {K_{\mathrm{M}}}^{\text{3DFE}}$	30.90	67.41
${K_{\mathrm{M}}}^{\text{Varun}} / {K_{\mathrm{M}}}^{\text{3DFE}}$	7.09	11.43

An interesting observation from Figs. 3.6 and 3.7 is that the sensitivity of the local stiffness coefficients with respect to L/D decreases with increasing L/D. This suggests that for L/D much greater than 2, these soil reactions may be largely independent of L/D. This agrees with the Winkler formulations used for the design of long, flexible monopiles (API 2002, DNV 2013), which are independent of the pile length. Furthermore, the results in Fig. 3.6a agree with the approach of Kraft et al. (1981) to approximate the base axial soil reaction for long piles as half of the elastic solution for a rigid punch at the surface. It should be highlighted that the soil reactions obtained in this study apply as much to the 'short' monopile problem ($0.5 \leq L/D \leq 2$) as they do to the caisson problem. This is because the soil reactions obtained would be similar if the foundation was modelled as a plugged open-ended monopile (confirmed by further 3DFE analyses not shown here). The absence of a lid has negligible effect on the soil response on the skirt exterior or caisson base, noting that the assumption of a short open-ended monopile being plugged is valid if the soil is linear elastic and contact breaking at the soil-pile interface is not allowed.

As mentioned earlier, there are issues with determining soil reactions through back-calculations. Fig. 3.11 compares the true $k_{\mathrm{h}}^{\mathrm{skirt}}$ and $k_{\mathrm{m}}^{\mathrm{skirt}}$ soil reactions for $\nu = 0.2$ (approximated by Eqs. 3.14, and 3.16) with the plane strain solutions of Novak et al. (1978) and those used in existing Winkler models for laterally-loaded caissons (Gerolymos & Gazetas 2006*c*, Varun et al. 2009). Observe how two vastly different $k_{\mathrm{m}}^{\mathrm{skirt}}$ values were back-calculated by Gerolymos & Gazetas (2006*c*) and Varun et al. (2009) in Fig. 3.11b, even though the same four soil reactions Winkler framework were adopted in both cases. Interestingly, Fig. 3.11b shows that the plane strain solution of Novak et al. (1978) is a better match to the true soil reaction than the back-calculated value from the 3DFE analyses by Varun et al. (2009).

Furthermore, Varun et al. (2009) back-calculated values for $k_{\mathrm{m}}^{\mathrm{skirt}}$ and $k_{\mathrm{h}}^{\mathrm{base}}$ that increase with L/D for $L/D \leq 2$ (see Fig. 3.11b, c), which they attributed to 'trench effect'. It is evident from Figs. 3.6d and 3.7c that no such increase is happening given the true physics of the problem. This shows the risk that spurious conclusions may arise from a back-calculation approach. To highlight this risk, alternative values of $k_{\mathrm{c}}^{\mathrm{skirt}}$ and $k_{\mathrm{c}}^{\mathrm{base}}$ are derived below using the back-calculation approach.

First, assuming that only the global caisson behaviour is known, the back-calculation approach requires *a priori* assumptions about the variation of $k_{\mathrm{c}}^{\mathrm{skirt}}$ with depth. As there are only two free equations (Eqs. 3.26 and 3.27) and two unknowns ($k_{\mathrm{c}}^{\mathrm{skirt}}$ and $k_{\mathrm{c}}^{\mathrm{base}}$), $k_{\mathrm{c}}^{\mathrm{skirt}}$ is assumed to be constant with depth. The integration in Eqs. 3.26 and 3.27 can be carried out to produce the following system of linear equations:

$$\left(\begin{array}{c} K_{\mathrm{M}} - k_{\mathrm{h}}^{\mathrm{skirt}} \left(\frac{L^3}{3} \right) - k_{\mathrm{m}}^{\mathrm{skirt}} \left(L \right) - k_{\mathrm{h}}^{\mathrm{base}} \left(L^2 \right) - k_{\mathrm{m}}^{\mathrm{base}} \\ K_{\mathrm{C}} + k_{\mathrm{h}}^{\mathrm{skirt}} \left(\frac{L^2}{2} \right) + k_{\mathrm{h}}^{\mathrm{base}} \left(L \right) \end{array} \right) = \begin{bmatrix} -L^2 & -2L \\ L & 1 \end{bmatrix} \left(\begin{array}{c} k_{\mathrm{c}}^{\mathrm{skirt}} \\ k_{\mathrm{c}}^{\mathrm{base}} \end{array} \right) \tag{3.30}$$

The resultant $k_{\mathrm{c}}^{\mathrm{skirt}}$ and $k_{\mathrm{c}}^{\mathrm{base}}$ are shown in Fig. 3.12. Evidently, there is now a larger contribution from the back-calculated $k_{\mathrm{c}}^{\mathrm{base}}$ than the true stiffness coefficients ($k_{\mathrm{ch}}^{\mathrm{base}}$ and $k_{\mathrm{cm}}^{\mathrm{base}}$) (compare Fig. 3.12b with Fig. 3.7e, f). Caution should therefore be exercised when trying to interpret any back-calculated stiffness coefficient. These stiffness coefficients were not obtained from the governing physics of the problem, but are artificial constructs that vary depending on the model assumptions. Although the adopted solution of taking the average of the true local coupling stiffness coefficients is not ideal, the average values agree better with the true values than the back-calculated values (compare Fig. 3.9b with Fig. 3.7e, f).

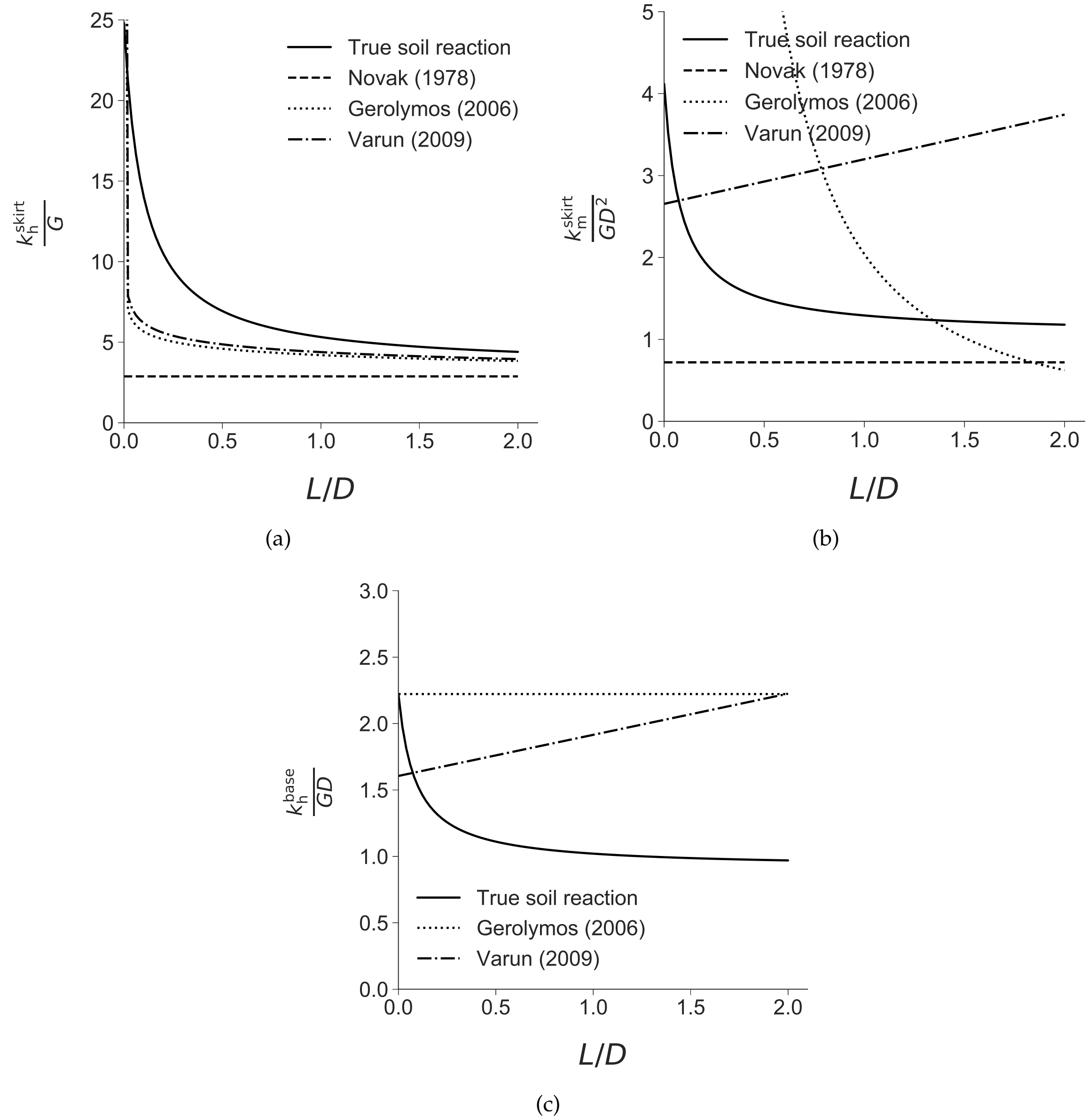

(a)

(b)

(c)

Figure 3.11: Comparison of the true k_h^{skirt}, k_m^{skirt},k_h^{base} local stiffness coefficients for $\nu = 0.2$ (approximated by Eqs. 3.14, 3.16 and 3.22) with the plane strain solution of Novak et al. (1978) and those from existing Winkler models for laterally-loaded caisson foundations (Gerolymos & Gazetas 2006*c*, Varun et al. 2009). In spite of the plane strain assumption, the solution of Novak et al. (1978) is the closest match to the true k_m^{skirt} soil reaction.

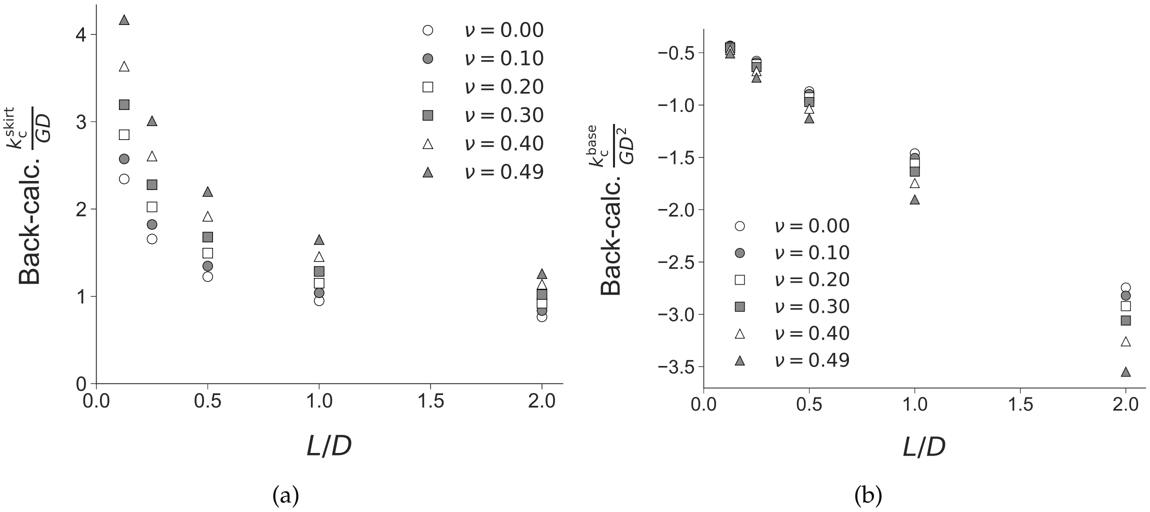

(a)

(b)

Figure 3.12: Variation of the normalised back-calculated k_c^{skirt} and k_c^{base} with L/D and ν.

3.4.2 Strengths and Limitations

The key advantage of oxCaisson-LE is its combination of high efficiency and high accuracy. While the 3DFE model took 36 hours to run 144 analyses to compute all the global stiffness coefficients shown in Fig. 3.8, oxCaisson-LE took less than a second in total to do the same. This is a major leap in computational efficiency as it allows a rapid turnover of design evaluations, which is crucial for many time-critical design jobs such as optimisation of large scale foundation design.

Nevertheless, oxCaisson-LE has some limitations. In particular, the model has only been validated for homogeneous elastic soil but real soil profiles tend to be non-homogeneous or multi-layered. Although oxCaisson-LE may be used with non-homogeneous soil properties in its current form, the accuracy of its predictions for such input has not been validated.

Chapter 4

Non-homogeneous, Linear Elastic Soil

Definition 4.1 (Non-homogeneous, linear elastic soil) *Non-homogeneous, linear elastic soil refers to linear elastic soil with a shear modulus that varies with depth z, but is uniform in the x-y plane. Furthermore, the Poisson's ratio of the soil is assumed to be uniform everywhere.*

In Chapter 3, a model for suction caissons in linear elastic soil, oxCaisson-LE, was developed and shown to be capable of producing highly efficient and accurate global stiffness predictions. However, oxCaisson-LE is only validated for homogeneous, linear elastic soil and its performance in non-homogeneous, linear elastic soil has not been addressed. This is a significant limitation, as grounds with non-homogeneous shear modulus G are commonplace; even homogeneous deposits of clay or sand have non-homogeneous G that varies continuously with depth. Empirical studies have shown that the initial shear modulus G_0 of soil varies with the mean effective stress p' (which increases with depth) as follows:

$$\frac{G_0}{p_r} \propto \left(\frac{p'}{p_r}\right)^m \tag{4.1}$$

where p_r is a reference stress (usually taken to be the atmospheric pressure) and $m = 0.5$ was found to be applicable for most clays (Hardin & Black 1968, Shibuya et al. 1997) and sands (Hardin & Black 1966, Wroth et al. 1979); some researchers (e.g. Gourvenec 2007) argue that $m = 1$ is more suitable for normally consolidated clays.

In this chapter, the previous work on Winkler models in non-homogeneous, linear elastic soil is reviewed, before an energy-based design method is introduced to improve the accuracy of oxCaisson-LE in non-homogeneous, linear elastic soil. However, as a circular surface foundation is a degenerate form of a suction caisson when $L/D = 0$, the classic problem of predicting the vertical stiffness of a surface foundation on non-homogeneous, linear elastic soil is revisited before looking at the general suction caisson problem.

4.1 Surface Foundations

This section revisits the classic problem of predicting the vertical stiffness of a rigid, circular surface foundation on linear elastic soil with continuously varying or multi-layered, piecewise constant shear modulus G. For homogeneous, linear elastic soil, the reference vertical stiffness solution (Boussinesq 1885, Poulos & Davis 1974) for a smooth, rigid, circular surface foundation is:

$$K_{\mathrm{V}} = \frac{V}{S_{\mathrm{z}}} = \frac{2DG}{1-\nu} \tag{4.2}$$

where V is the applied vertical load, S_{z} is the vertical displacement, D is the foundation diameter and ν is the Poisson's ratio of the soil.

4.1.1 Introduction

There has been much research (e.g. Gibson 1967, Carrier & Christian 1973, Kassir & Chuaprasert 1974, Boswell & Scott 1975, Vrettos 1991, Selvadurai 1996) into the vertical stiffness problem for rigid circular surface foundations on elastic half-spaces with different types of non-homogeneity. This chapter does not intend to provide an exhaustive review of these research, which vary in complexity and rigour, but focuses on the most widely cited design methods for such problems. One widely cited design method for predicting the vertical stiffness of a rigid, circular surface foundation on non-homogeneous soil is that proposed by Mayne & Poulos (1999):

$$K_{\mathrm{V}} = \frac{2D}{1-\nu} G_{\mathrm{mayne}} \tag{4.3}$$

where

$$\begin{aligned}
G_{\mathrm{mayne}} &= \frac{1-\nu^2}{\int_0^{\infty} \frac{1}{G}\left(\tilde{\sigma}_{\mathrm{z}} - 2\nu\tilde{\sigma}_{\mathrm{r}}\right) d\tilde{z}} \\
\tilde{\sigma}_{\mathrm{z}} &= 1 - \frac{1}{\left(1 + (0.5/\tilde{z})^2\right)^{1.5}} \\
\tilde{\sigma}_{\mathrm{r}} &= \frac{1}{2} + \nu - \frac{1+\nu}{\left((0.5/\tilde{z})^2 + 1\right)^{0.5}} + \frac{0.5}{\left((0.5/\tilde{z})^2 + 1\right)^{1.5}} \\
\tilde{z} &= z/D
\end{aligned}$$

z is the depth below ground level, $\tilde{\sigma}_{\mathrm{z}} = \sigma_{\mathrm{z}}/q_{\mathrm{z}}$ is a normalised stress distribution derived from the Boussinesq stress distribution (Boussinesq 1885), $\tilde{\sigma}_{\mathrm{r}} = \sigma_{\mathrm{r}}/q_{\mathrm{z}}$ is a normalised stress distribution derived from the horizontal stress distribution for axisymmetrical, uniform loading (Poulos & Davis 1974) and q_{z} is the average vertical stress at the soil-foundation interface. This design method was derived by assuming that the vertical displacement at the centre of the foundation base is equal to the integration of the vertical strains directly beneath it. As Eq. 4.3 is of a different and more general form than that proposed by Mayne & Poulos (1999), the derivations are included in Appendix A.1 for interested readers.

Another solution to the vertical stiffness problem is found in the field of contact mechanics, where Gao et al. (1992) proposed the following design method to predict the vertical stiffness of a rigid, cylindrical punch on a non-homogeneous elastic half-space:

$$K_{\mathrm{V}} = \frac{2D}{1-\nu} G_{\mathrm{gao}} \tag{4.4}$$

where

$$\begin{aligned} G_{\mathrm{gao}} &= \int_0^\infty G \frac{dI_0}{d\tilde{z}}\, d\tilde{z} \\ I_0 &= \frac{2}{\pi} \arctan(2\tilde{z}) + \frac{(1-2\nu)(2\tilde{z}) \ln\left(\frac{1+(2\tilde{z})^2}{(2\tilde{z})^2}\right) - \frac{(2\tilde{z})}{1+(2\tilde{z})^2}}{2\pi(1-\nu)} \end{aligned}$$

Eq. 4.4 was derived using a first-order accurate moduli-perturbation method, in which the displacement and stresses in a non-homogeneous body are determined based on the known solutions to a reference homogeneous body.

Despite the different derivation methods for Eqs. 4.3 and 4.4, they are quite similar conceptually (as can be observed from the form of the equations), with both involving a weighting of the shear modulus profile. However, the weighting methodology in Eqs. 4.3 and 4.4 can be shown to be based on somewhat opposite assumptions. This contradiction leads to uncertainty for industry practitioners when they use either design method for vertical stiffness predictions. This is not aided by the fact that there is little guidance in the design codes (API 2002) on how to predict the vertical stiffness of surface foundations on non-homogeneous soil.

To address the above uncertainty, the two design methods were interpreted using an energy-based theoretical framework, which provides a unified basis to compare the two design methods and allow discovery of their underlying, implicit assumptions. The validity of these assumptions were then examined by comparing them against the reference solutions provided by rigorous 3DFE analyses.

4.1.2 Theoretical Framework

Definition 4.2 (Work-equivalence) *Work-equivalence between two half-spaces means that it takes the same amount of work (or load) to produce the same amount of uniaxial displacement (e.g. vertical displacement only) on both half-spaces. For linear elastic half-spaces, work-equivalence is synonymous with strain energy equivalence.*

Assume there exists a non-homogeneous elastic half-space H_1. Suppose it is necessary to find a homogeneous elastic half-space H_2 that is equivalent to H_1. Two questions arise: what defines equivalence and what would be the equivalent shear modulus of H_2? For the first question, two half-spaces are defined to be equivalent if they are work-equivalent. For the second question, an examination of the elastic strain energy of the half-spaces is required. The elastic strain energy U of a half-space can be calculated as:

$$U = \iiint \sum_{i,j} \frac{1}{2} \sigma_{\mathrm{ij}} \varepsilon_{\mathrm{ij}} \, dx \, dy \, dz \tag{4.5}$$

where σ_{ij}, $\varepsilon_{\mathrm{ij}}$ are the stress and strain components of the half-space and the integration is carried out over the entire volume of the half-space.

Case 1: Stress-based Propositions

From linear elasticity theory, it is known that:

$$\varepsilon_{\mathrm{ij}} = \frac{(1+\nu)\sigma_{\mathrm{ij}} - \nu \delta_{\mathrm{ij}} \sum_k \sigma_{\mathrm{kk}}}{2(1+\nu)G} \tag{4.6}$$

where δ_{ij} is the Kronecker delta. Substituting Eq. 4.6 into Eq. 4.5 gives:

$$U = \iiint \sum_{i,j} \frac{1}{2} \sigma_{\mathrm{ij}} \left(\frac{(1+\nu)\sigma_{\mathrm{ij}} - \nu \delta_{\mathrm{ij}} \sum_k \sigma_{\mathrm{kk}}}{2(1+\nu)G} \right) dx \, dy \, dz \tag{4.7}$$

Since G is assumed to vary with depth only, Eq. 4.7 may be simplified to:

$$U = \int_0^\infty \frac{1}{G} u_\sigma \, dz \tag{4.8}$$

where

$$u_\sigma = \iint \sum_{i,j} \frac{1}{2} \sigma_{\mathrm{ij}} \left(\frac{(1+\nu)\sigma_{\mathrm{ij}} - \nu \delta_{\mathrm{ij}} \sum_k \sigma_{\mathrm{kk}}}{2(1+\nu)} \right) dx \, dy$$

Let U_1 and U_2 be the elastic strain energy of H_1 and H_2 respectively:

$$U_1 = \int_0^\infty \frac{1}{G} \left(u_\sigma\right)_1 dz \tag{4.9}$$

$$U_2 = \frac{1}{G_{\text{eq}}} \int_0^\infty \left(u_\sigma\right)_2 dz \tag{4.10}$$

where G_{eq} is the equivalent shear modulus of the homogeneous half-space.

Since H_1 and H_2 are work-equivalent, $U_1 = U_2$:

$$\frac{1}{G_{\text{eq}}} \int_0^\infty \left(u_\sigma\right)_2 dz = \int_0^\infty \frac{1}{G} \left(u_\sigma\right)_1 dz \tag{4.11}$$

Proposition 1a $\int_o^\infty u_\sigma \, dz$ is equal for any work-equivalent half-space.

Under this proposition, $\int_o^\infty \left(u_\sigma\right)_1 dz = \int_o^\infty \left(u_\sigma\right)_2 dz$. Thus, Eq. 4.11 simplifies to:

$$\frac{1}{G_{\text{eq}}} \int_0^\infty \left(u_\sigma\right)_1 dz = \int_0^\infty \frac{1}{G} \left(u_\sigma\right)_1 dz \tag{4.12}$$

Without loss of generality, let $u_\sigma = \left(u_\sigma\right)_1$. Therefore,

$$\begin{aligned} \frac{1}{G_{\text{eq}}} &= \int_0^\infty \frac{1}{G} \frac{u_\sigma}{\int_o^\infty u_\sigma \, dz} dz \\ &= \int_0^\infty \frac{1}{G} w_\sigma \, d\tilde{z} \end{aligned} \tag{4.13}$$

where

$$w_\sigma = \frac{u_\sigma}{\int_0^\infty u_\sigma \, d\tilde{z}} \tag{4.14}$$

Proposition 1b w_σ is invariant to G.

Under this proposition, there exists a unique w_σ for every ν, that can be used to convert any non-homogeneous half-spaces into work-equivalent homogeneous half-spaces. It can be observed that w_σ is a normalised weight function (that sums up to 1 like a probability density function) and G_{eq} is simply the weighted average shear modulus after treating the x-y planes of the half-space like springs in series.

G_{mayne} in Eq. 4.3 can be manipulated into the form of Eq. 4.13 as follows:

$$\begin{aligned} G_{\text{mayne}} &= \frac{1 - \nu^2}{\int_0^\infty \frac{1}{G} \left(\tilde{\sigma}_z - 2\nu\tilde{\sigma}_r\right) d\tilde{z}} \\ \frac{1}{G_{\text{mayne}}} &= \int_0^\infty \frac{1}{G} w_{\text{mayne}} \, d\tilde{z} \end{aligned} \tag{4.15}$$

where

$$w_{\text{mayne}} = \frac{\tilde{\sigma}_{\text{z}} - 2\nu\tilde{\sigma}_{\text{r}}}{1-\nu^2}$$
$$1-\nu^2 = \int_0^{\infty} \tilde{\sigma}_{\text{z}} - 2\nu\tilde{\sigma}_{\text{r}}\, d\tilde{z}$$

It can be observed that w_{mayne} has the same functional form as w_{σ}. This implies that the design method of Mayne & Poulos (1999) implicitly assumes Propositions 1a and 1b are approximately true under the work-equivalence framework. Indeed, Mayne & Poulos (1999) assume in their derivations that the normalised stress distribution is invariant to changes in G (i.e. it is always 'Boussinesq-based'). Since the average vertical stress q_{z} is equivalent for two work-equivalent half-spaces, this implies that $(u_{\sigma})_1 = (u_{\sigma})_2$, which is a stronger assumption than Proposition 1a (i.e. normalised stress distribution invariance implies Proposition 1a, but not necessarily the other way round).

Case 2: Strain-based Propositions

From linear elasticity theory, it is also known that:

$$\sigma_{\text{ij}} = 2G\left(\frac{\nu}{1-2\nu}\delta_{\text{ij}}\sum_k \varepsilon_{\text{kk}} + \varepsilon_{\text{ij}}\right) \tag{4.16}$$

Substituting Eq. 4.16 into Eq. 4.5, the following expression is obtained:

$$U = \iiint \sum_{i,j} \frac{1}{2}\varepsilon_{\text{ij}}\left(2G\left(\frac{\nu}{1-2\nu}\delta_{\text{ij}}\sum_k \varepsilon_{\text{kk}} + \varepsilon_{\text{ij}}\right)\right) dx\, dy\, dz \tag{4.17}$$

Since G is assumed to vary with depth only, Eq. 4.17 may be simplified to:

$$U = \int_0^{\infty} G u_{\varepsilon}\, dz \tag{4.18}$$

where

$$u_{\varepsilon} = \iint \sum_{i,j} \frac{1}{2}\varepsilon_{\text{ij}}\left(\frac{2\nu}{1-2\nu}\delta_{\text{ij}}\sum_k \varepsilon_{\text{kk}} + 2\varepsilon_{\text{ij}}\right) dx\, dy$$

The elastic strain energy U_1 and U_2 can be defined in the following alternative forms:

$$U_1 = \int_0^{\infty} G\,(u_{\varepsilon})_1\, dz \tag{4.19}$$

$$U_2 = G_{\text{eq}} \int_0^{\infty} (u_{\varepsilon})_2\, dz \tag{4.20}$$

Since H_1 and H_2 are work-equivalent, $U_1 = U_2$:

$$G_{\text{eq}} \int_0^{\infty} (u_{\varepsilon})_2\, dz = \int_0^{\infty} G\,(u_{\varepsilon})_1\, dz \tag{4.21}$$

Proposition 2a $\int_o^\infty u_\varepsilon \, dz$ is equal for any work-equivalent half-space.

Under this proposition, $\int_o^\infty (u_\varepsilon)_1 \, dz = \int_o^\infty (u_\varepsilon)_2 \, dz$. Thus, Eq. 4.21 simplifies to:

$$G_{\text{eq}} \int_0^\infty (u_\varepsilon)_1 \, dz = \int_0^\infty G \, (u_\varepsilon)_1 \, dz \tag{4.22}$$

Without loss of generality, let $u_\varepsilon = (u_\varepsilon)_1$. Therefore,

$$\begin{aligned} G_{\text{eq}} &= \int_0^\infty G \frac{u_\varepsilon}{\int_o^\infty u_\varepsilon \, dz} \, dz \\ G_{\text{eq}} &= \int_0^\infty G w_\varepsilon \, d\tilde{z} \end{aligned} \tag{4.23}$$

where

$$w_\varepsilon = \frac{u_\varepsilon}{\int_0^\infty u_\varepsilon \, d\tilde{z}} \tag{4.24}$$

Proposition 2b w_ε is invariant to G.

Under this proposition, there exists a unique weight function w_ε for every ν, that can be used to convert any non-homogeneous half-spaces into work-equivalent homogeneous half-spaces. Like w_σ, w_ε is a normalised weight function but G_{eq} is now the weighted average shear modulus after treating the x-y planes of the half-space like springs in parallel.

G_{gao} in Eq. 4.4 can be manipulated into the form of Eq. 4.23 as follows:

$$\begin{aligned} G_{\text{gao}} &= \int_0^\infty G \frac{dI_0}{d\tilde{z}} \, d\tilde{z} \\ &= \int_0^\infty G w_{\text{gao}} \, d\tilde{z} \end{aligned} \tag{4.25}$$

where

$$w_{\text{gao}} = \frac{dI_0}{dz} \tag{4.26}$$

Like w_ε, w_{gao} is a normalised weight function that sums up to 1. This implies that the design method of Gao et al. (1992) implicitly assumes that Propositions 2a and 2b are approximately true under the work-equivalence framework.

Summary

Finding work-equivalent homogeneous half-spaces involves finding the weighted average of the shear modulus after treating the x-y planes of the half-space as springs in series (if w_σ invariance is assumed) or springs in parallel (if w_ε invariance is assumed).

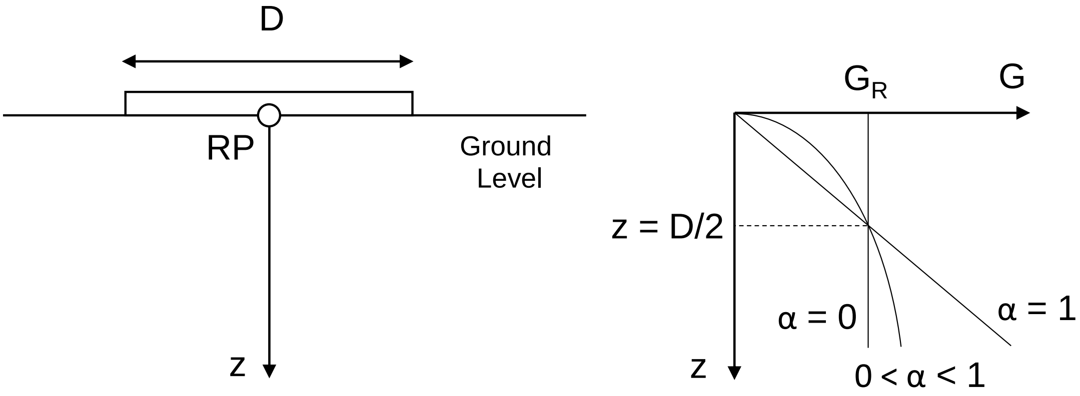

Figure 4.1: Schematic diagram of a surface foundation bearing on a non-homogeneous elastic half-space (after Doherty et al. 2005).

Despite the different derivation techniques, it is obvious within this work-equivalence framework that both design methods belong to the same family of weighted shear modulus methods, albeit with different ways of applying the weights depending on the assumptions. To investigate which set of assumptions are more valid, 3DFE analyses of the vertical stiffness problem for a rigid, circular surface foundation on non-homogeneous soil were carried out and the 3DFE results were used to test the validity of Propositions 1 and 2.

4.1.3 Methodology

This section describes the 3DFE modelling carried out in this study. The 3DFE model consists of a circular surface foundation of diameter D on non-homogeneous soil with continuously varying shear modulus (see Fig. 4.1). The same shear modulus profile used in Doherty et al. (2005) is adopted here:

$$G = G_R \left(\frac{2z}{D} \right)^{\alpha} \tag{4.27}$$

where α is a factor controlling the rate of increase of the shear modulus with depth ($\alpha = 0$ represents homogeneous G). This profile was adopted as it is expressive enough to represent most of the continuously varying shear modulus profiles that exist in real life.

Mesh

The 3DFE mesh used in this study is similar to that used in Chapter 3, except that a half model was used here due to symmetry of the problem. A typical mesh of the 3DFE model

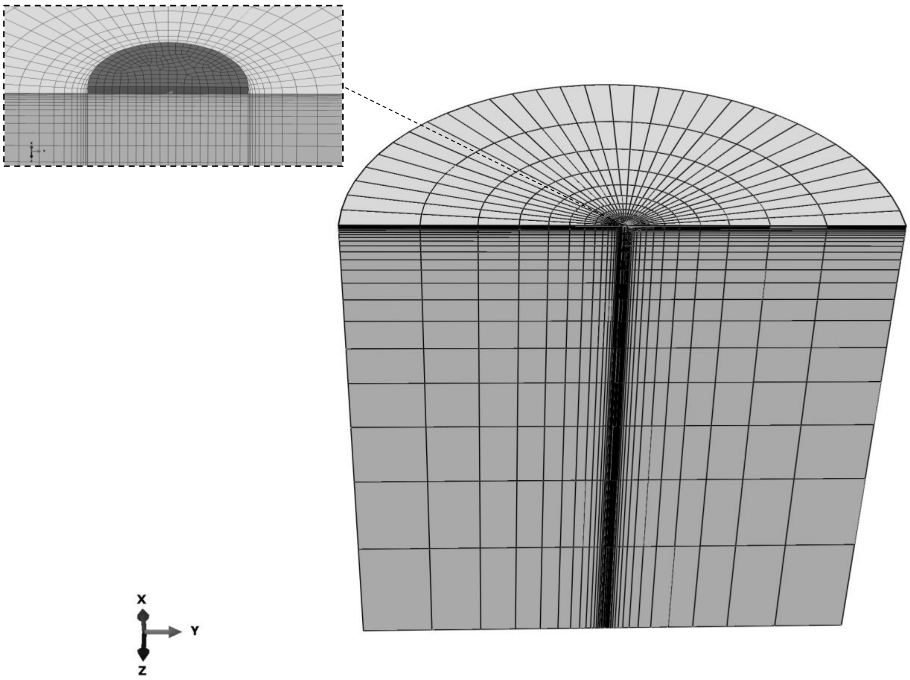

Figure 4.2: 3DFE mesh for the computation of the vertical stiffness of a rigid, circular surface foundation.

is shown in Fig. 4.2.

Materials

The soil volume was defined as weightless and linear elastic. Four shear modulus profiles ($\alpha = 0, 0.2, 0.6, 1$) and two Poisson's ratios ($\nu = 0.2, 0.49$) were analysed for the soil. The variation in G was implemented in Abaqus using a user-defined material model (UMAT).

Boundary Conditions

Displacements were fixed in all directions at the bottom of the mesh domain and in the radial directions on its periphery. Vertical displacement was prescribed at RP (see Fig. 4.1) to obtain the applied vertical load, which is used to compute the vertical stiffness.

Validation

To verify that the 3DFE model has been set up correctly, the stiffness predictions were compared with the results from previous work (Doherty et al. 2005), as shown in Table 4.1. Overall, the 3DFE results agree fairly well with those reported by Doherty et al. (2005), except when $\nu = 0.49$. This is because Doherty et al. (2005) used $\nu = 0.499$ in their analyses, while this study uses $\nu = 0.49$. The results from 3DFE analyses using $\nu = 0.499$ are also

Table 4.1: Comparison of the normalised 3DFE vertical stiffness predictions with the results of Doherty et al. (2005).

ν	α	$\frac{K_V}{G_R D}$ (Doherty)	$\frac{K_V}{G_R D}$ (3DFE)	Deviation (%)
0.2	0	2.65	2.67	0.75
0.2	0.2	2.5	2.5	0
0.2	0.6	1.63	1.61	1.23
0.2	1	0	0.58	-
0.49	0	4.04	4.04	0
0.49	0.2	4.37	4.26	2.52
0.49	0.6	4.39	3.99	9.11
0.49	1	3.72	2.71	27.15
0.499	0	4.04	4.11	1.73
0.499	0.2	4.37	4.37	0
0.499	0.6	4.39	4.26	2.96
0.499	1	3.72	3.34	10.21

shown in Table 4.1, which shows better agreement with the results of Doherty et al. (2005). For the case of $\nu = 0.499$ and $\alpha = 1$, the 3DFE result agrees better than Doherty et al. (2005), when compared with the analytical solution (Booker et al. 1985) as shown below:

$$\begin{aligned} S_z &= \frac{3q_z}{2(2(1+\nu))m} \\ \frac{V}{S_z} &= \frac{2(2(1+0.5))}{3}\left(\frac{2G_R}{D}\right)\left(\frac{\pi D^2}{4}\right) \\ \frac{K_V}{G_R D} &= \pi \end{aligned} \tag{4.28}$$

where m = gradient of the shear modulus profile (i.e. $2G_R/D$).

4.1.4 Results

Comparison of Stiffness Predictions

To assess the accuracy of the design methods of Mayne & Poulos (1999) and Gao et al. (1992), a comparison of their normalised stiffness predictions with the 3DFE results are

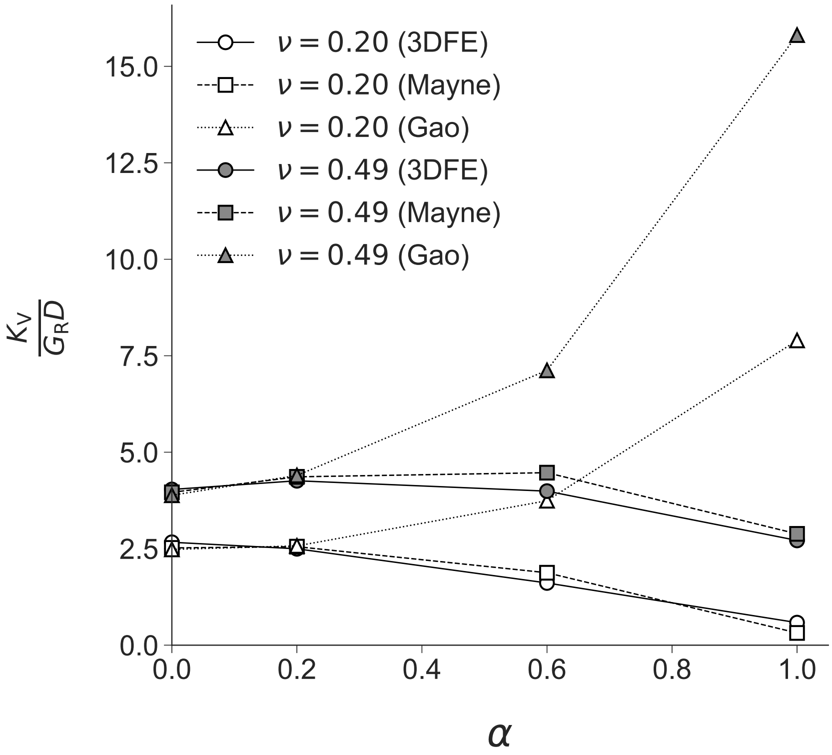

Figure 4.3: Comparison of the normalised vertical stiffness predicted by the design methods of Mayne & Poulos (1999) and Gao et al. (1992) with the 3DFE results.

presented in Fig. 4.3. It can be observed that the predictions of Mayne & Poulos (1999) agree remarkably well with the 3DFE results, while the predictions of Gao et al. (1992) agree well with the 3DFE results at low levels of non-homogeneity (i.e. low α) but perform poorly at higher α. Furthermore, the design method of Gao et al. (1992) surprisingly predicted increasing stiffness with increasing α, in contrast to the 3DFE trend of decreasing stiffness with increasing α. To investigate the reason behind the diverging performance of the two design methods, their underlying assumptions were examined.

Assessment of Propositions 1a and 2a

First, Propositions 1a and 2a were assessed by comparing the values of $\int_0^\infty u_\sigma \, dz$ and $\int_0^\infty u_\varepsilon \, dz$ for different α values. u_σ and u_ε may be directly computed from the stress or strain components of each soil element in accordance to Eqs. 4.7 and 4.17. However, as the elastic strain energy for each soil element is available in the 3DFE results, the following alternative forms of Eqs. 4.8 and 4.18 were used to compute u_σ and u_ε instead:

$$u_\sigma = \frac{\partial U}{\partial z} G \tag{4.29}$$

$$u_\varepsilon = \frac{\partial U}{\partial z} \frac{1}{G} \tag{4.30}$$

where $\frac{\partial U}{\partial z}$ can be approximated from the 3DFE results by dividing the sum of the elastic strain energy of every soil element at a given depth by the height of a soil element at that depth (every soil element at that depth has the same height as a structured mesh was used).

The values of u_σ and u_ε computed from Eqs. 4.29 and 4.30 cannot be used directly to assess Propositions 1a and 2a, as these u_σ and u_ε values were not obtained from work-equivalent half-spaces (notice that the 3DFE stiffness predictions in Fig. 4.3 are different from one another). Thus, the following transformations had to be applied to compute the values of u_σ for a unit amount of work. By noting that the applied load (and hence the applied work) is linearly dependent on G for a linear elastic half-space (i.e. $U \propto G$):

$$\begin{aligned}(u_\sigma)_{\text{unit}} &= \frac{\partial (kU)}{\partial z} kG \\ &= k^2 \frac{\partial U}{\partial z} G\end{aligned} \tag{4.31}$$

where

$$k = \frac{1}{U}$$

Thus, u_σ for a unit work can be obtained by applying a factor of $(1/U)^2$. No transformation is required for u_ε, as shown below:

$$\begin{aligned}(u_\varepsilon)_{\text{unit}} &= \frac{\partial (kU)}{\partial z} \frac{1}{kG} \\ &= \frac{\partial U}{\partial z} G\end{aligned} \tag{4.32}$$

Fig. 4.4 shows the variations $\int_0^\infty u_\sigma \, dz$ and $\int_0^\infty u_\varepsilon \, dz$ for different α values, where u_σ and u_ε here refer to the corresponding values for unit work. For clarity, the computed values are normalised by their corresponding values for the homogeneous case (i.e. $\alpha = 0$). It can be observed that $\int_0^\infty u_\sigma \, dz$ for unit work does not vary much for different G profiles, while $\int_0^\infty u_\varepsilon \, dz$ for unit work varies greatly for different G profiles, especially for $\alpha = 1$ where the computed $\int_0^\infty u_\varepsilon \, dz$ is about 30 times greater than the homogeneous case. Thus, this suggests that Proposition 1a is approximately true, while Proposition 2a is not.

Assessment of Propositions 1b and 2b

Next, to assess Propositions 1b and 2b, the values of w_σ and w_ε were computed from the 3DFE results in accordance to Eqs. 4.14 and 4.24, and compared for the different G profiles.

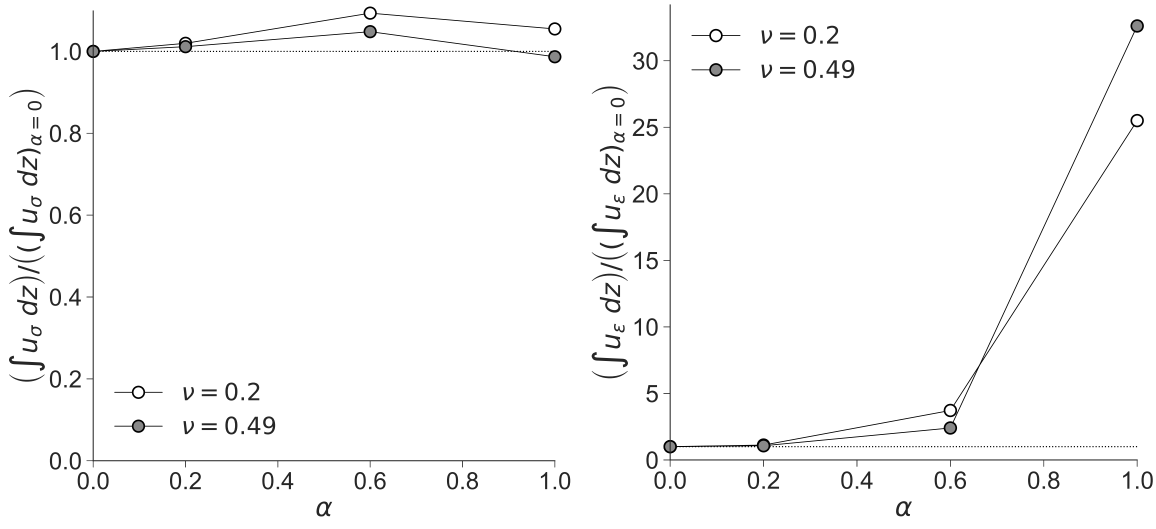

(a) (b)

Figure 4.4: Comparison of the normalised $\int_0^\infty u_\sigma\,dz$ and $\int_0^\infty u_\varepsilon\,dz$ computed from 3DFE results for $\nu = 0.2, 0.49$ and $\alpha = 0, 0.2, 0.6, 1$. Note that $\alpha = 0$ represents the homogeneous elastic half-space case.

Fig. 4.5 shows the profiles of the computed w_σ and w_ε for different values of α. It is evident that for different G profiles, w_σ stays largely the same, while w_ε changes significantly. This suggests that Proposition 1b is approximately true, while Proposition 2b is not. Furthermore, w_ε tends to be concentrated near the surface as α increases, which implies that the soil deformation is concentrated near the surface for higher α.

For more insights into the two design methods, their weight functions w_{mayne} and w_{gao} are included in Fig. 4.5 for comparison. It can be observed that w_{mayne} matches w_σ (and w_{gao} matches w_ε) for $\alpha = 0$. This explains why the design method of Gao et al. (1992) predicts increasing stiffness with increasing α, as there is a larger weighting of the higher shear modulus at greater depths (as α increases) compared to the true weight function, which results in an overestimated equivalent modulus.

4.1.5 Discussion

The comparison of the vertical stiffness in Fig. 4.3 indicates that the design method proposed by Mayne & Poulos (1999) is more accurate than that of Gao et al. (1992). This is because the underlying model assumptions of Mayne & Poulos (1999) (Propositions 1a and 1b) were found to be more valid than that of Gao et al. (1992) (Propositions 2a and 2b), making the design method of Mayne & Poulos (1999) theoretically more realistic. This highlights the strong interplay between model accuracy and model assumptions.

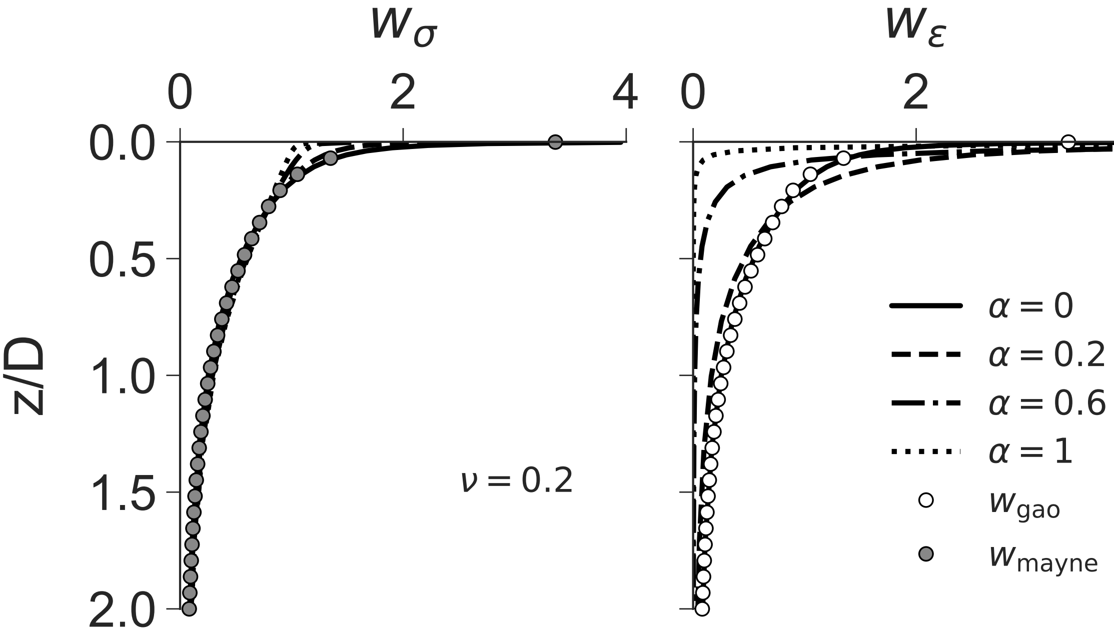

(a)

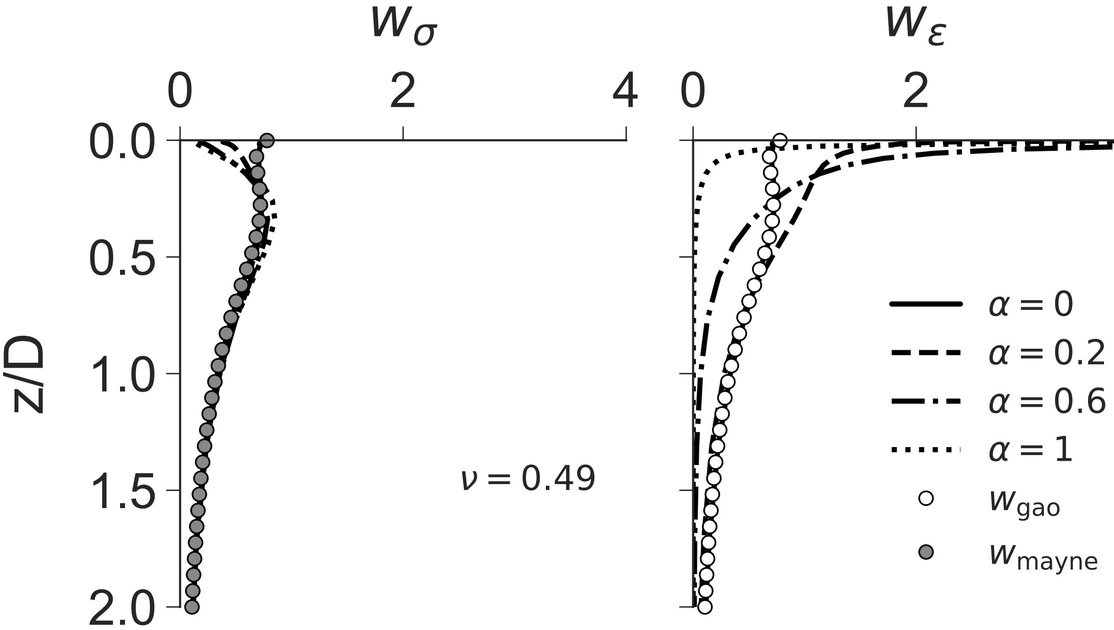

(b)

Figure 4.5: Comparison of w_σ and w_ε under different α values for (a) $\nu = 0.2$ (b) $\nu = 0.49$. Note that $\alpha = 0$ represents the homogeneous elastic half-space case.

4.2 Suction Caisson Foundations

The previous section has shown that there exists a design method (Mayne & Poulos 1999) that allows accurate vertical stiffness predictions of surface foundations in non-homogeneous soil. While not explicitly defined as so, the design method involves finding some equivalent, weighted average, homogeneous shear modulus G_{eq} for the non-homogeneous soil. As will be shown later, the work-equivalence framework described in the previous section serves as a key tool for improving the accuracy of oxCaisson-LE in non-homogeneous soil.

4.2.1 Introduction

Given the relative novelty of Winkler models for caissons (Gerolymos & Gazetas 2006*c*, Varun et al. 2009), there has been limited research exploring the effect of shear modulus non-homogeneity on the soil reactions. However, there are some related works that looked at this problem for piles. Guo & Randolph (1996, 1997) derived closed-form solutions for the soil reactions along the pile shaft for axially and torsionally loaded piles in non-homogeneous, linear elastic soil with a shear modulus profile similar to Eq. 4.27. The solutions are explicit functions of the non-homogeneity factor (i.e. α in Eq. 4.27), and cannot be used for arbitrary, multi-layered soils. Karatzia & Mylonakis (2017) recently proposed analytical procedures for determining the dynamic stiffness and damping of a laterally loaded pile in soil exhibiting different types of non-homogeneity with depth.

Poulos (1979) suggested two solutions for dealing with shear modulus non-homogeneity for axially loaded piles. The first solution involves taking the average G of the influenced layer and the influencing layer as input into Mindlin's stress equations (Mindlin 1936). The second solution involves converting the non-homogeneous soil into a two-layer system. The first layer is along the pile shaft and has a constant shear modulus equivalent to the average G along the pile shaft. The second layer is below the pile base and has a constant shear modulus equivalent to the average G from the base depth to $5D$ below the base. A key advantage of these two solutions are that they are general enough to be applicable for arbitrary, multi-layered soils.

Nevertheless, there are still some gaps in the understanding of the effect of shear modulus non-homogeneity. Most of the previous works on piles look at just axial and torsional loading, and it has not been demonstrated that effects found previously for axial and torsional loading apply for lateral and moment loading too. Moreover, there has been no research done on the effect of non-homogeneity on the pile base soil reactions. This is particularly important as the base soil reactions contribute significantly to the overall soil response on caissons. The design codes (API 2002, DNV 2013) provide little guidance on the effect of shear modulus non-homogeneity on their recommended Winkler-based design methods such as the *p-y*, *t-z* methods for laterally and axially loaded piles. It is implicitly assumed that the Winkler soil reactions are dependent only on the local soil properties and thus, are valid for both homogeneous and non-homogeneous soil. This assumption, however, has not been validated robustly.

To address the above gaps, 3DFE analyses of suction caisson behaviour under 6DoF loading in non-homogeneous, linear elastic soil were carried out to establish the effect of non-homogeneity on the soil reactions. Thereafter, oxCaisson-LE was used in its existing form to predict the suction caisson behaviour in non-homogeneous soil. As the predictions were found to differ significantly from the 3DFE results, a new design method was developed to address the inaccuracies.

4.2.2 Methodology

This section describes the 3DFE modelling carried out in this study. The 3DFE model implemented in this study is the same as that described in Chapter 3, except for the shear modulus profile of the soil, which now varies with depth in accordance to Eq. 4.27. In summary, a range of caisson dimensions ($L/D = 0, 0.25, 0.5, 1, 2$) and soil properties ($\nu = 0, 0.1, 0.2, 0.3, 0.4, 0.49$ and $\alpha = 0, 0.2, 0.4, 0.6, 0.8, 1$) were assessed in this study. The same displacements as detailed in Table 3.1 were prescribed at RP (see Fig. 2.1a).

To validate that the 3DFE model has been implemented correctly, Fig. 4.6 compares the 3DFE stiffness results with that of Doherty et al. (2005). Evidently, the 3DFE results agree very well with the results of Doherty et al. (2005).

4.2.3 Results

Effect of Shear Modulus Non-homogeneity on Local Stiffness Coefficients

Fig. 4.7 shows the local stiffness coefficient profiles for the skirt and base soil reactions for $L/D = 1$, $\nu = 0.2$ and $\alpha = 0, 0.2, 0.6, 1$. To examine the validity of the ‘naive assumption’

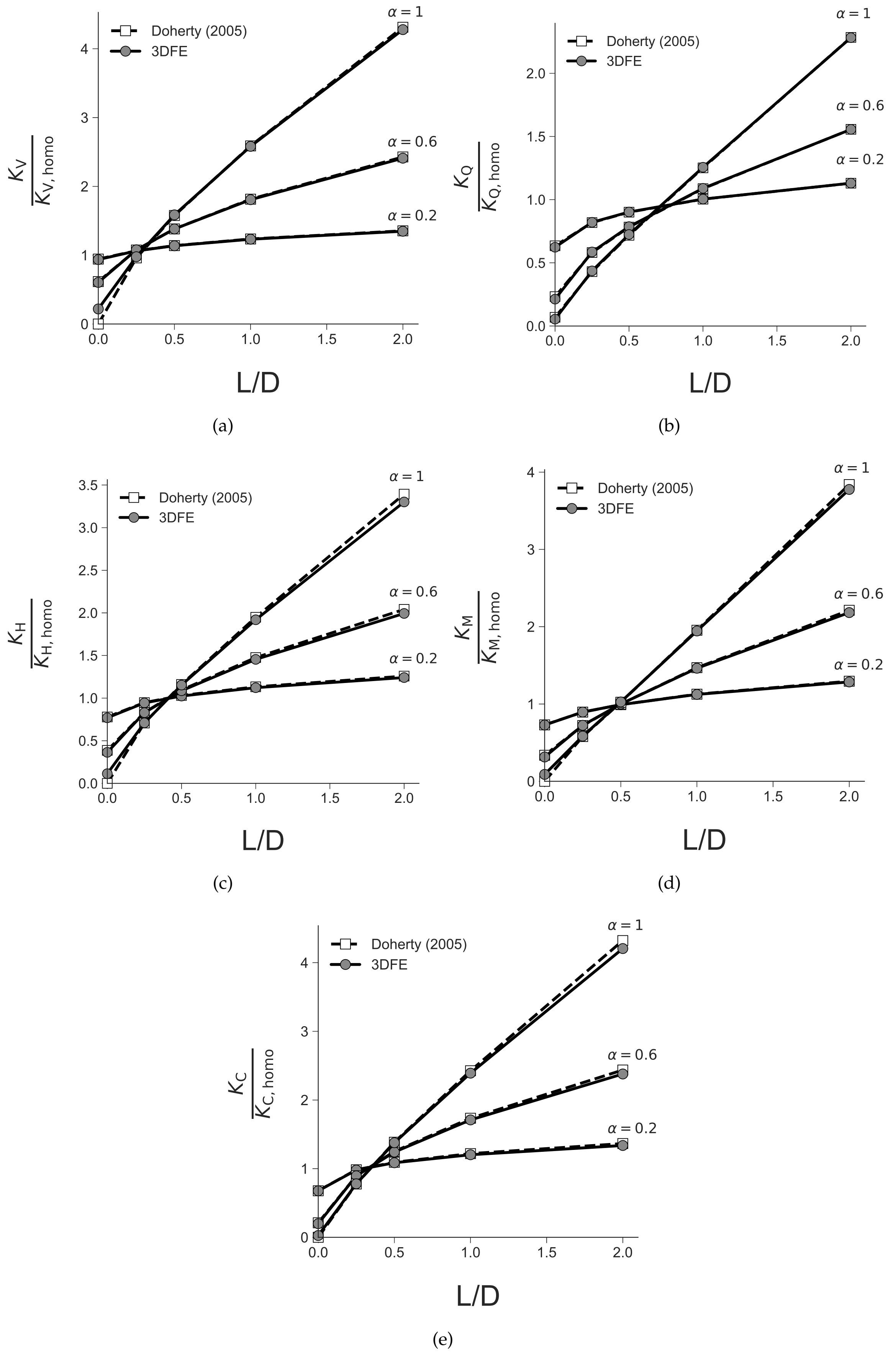

(a)

(b)

(c)

(d)

(e)

Figure 4.6: Comparison of the global stiffness coefficients (normalised by their homogeneous counterparts) predicted by the 3DFE model and Doherty et al. (2005) for $\alpha = 0.2, 0.6, 1$ and $\nu = 0.2$.

that the Winkler soil reactions are dependent only on the local soil properties, these local stiffness coefficients were normalised by the local shear modulus G_z. If the naive assumption is approximately true, the normalised local stiffness coefficient profiles for different α should be close to one another. However, it is clear from Fig. 4.7 that this assumption is approximately true for only $k_\mathrm{q}^\mathrm{skirt}$ and $k_\mathrm{q}^\mathrm{base}$. Comparing the profiles for $\alpha = 0$ and $\alpha = 1$, it can be observed that adopting the naive assumption will underpredict $k_\mathrm{v}^\mathrm{skirt}$ by two-thirds. The effect of the shear modulus non-homogeneity on the other local stiffness coefficients are relatively less significant, especially for the coupling stiffness coefficients. This suggests that the naive assumption will cause the biggest error for the vertical stiffness predictions.

Naive Predictions

Three Winkler models for caissons (oxCaisson-LE, Gerolymos & Gazetas 2006*c* and Varun et al. 2009) were used (in their existing forms) to predict the caisson behaviour in non-homogeneous soil. These predictions shall be referred to as 'naive predictions', as the naive assumption was adopted for the Winkler soil reactions.

Fig. 4.8 compares the naive predictions of the Winkler models with the 3DFE results for $L/D = 0, 0.125, 0.25, 0.5, 1, 2$, $\nu = 0.2$ and $\alpha = 0, 0.2, 0.6, 1$. As expected, the naive predictions of K_Q by oxCaisson-LE agree fairly well with the 3DFE results, while the naive predictions of K_V are most erroneous. The predictions of $K_\mathrm{H}, K_\mathrm{M}, K_\mathrm{C}$ by all the Winkler models are lower than the 3DFE results, especially for $\alpha = 1$. Overall, Fig. 4.8 suggests that the naive assumption is acceptable for predictions of K_Q but not for the others. Caution should therefore be exercised when using these Winkler models in non-homogeneous soil.

4.2.4 Work-Equivalence Framework

Given how poor the naive predictions are in Fig. 4.8, a new design method is proposed to improve the accuracy of the Winkler model predictions in non-homogeneous soil. This design method, termed the 'modulus weighting method', is based on the work-equivalence framework described in the Section 4.1. The main principle of the framework is that any non-homogeneous soil can be converted into a work-equivalent homogeneous soil, if the stress-based propositions (Propositions 1a and 1b) or strain-based propositions (Propositions 2a and 2b) are true.

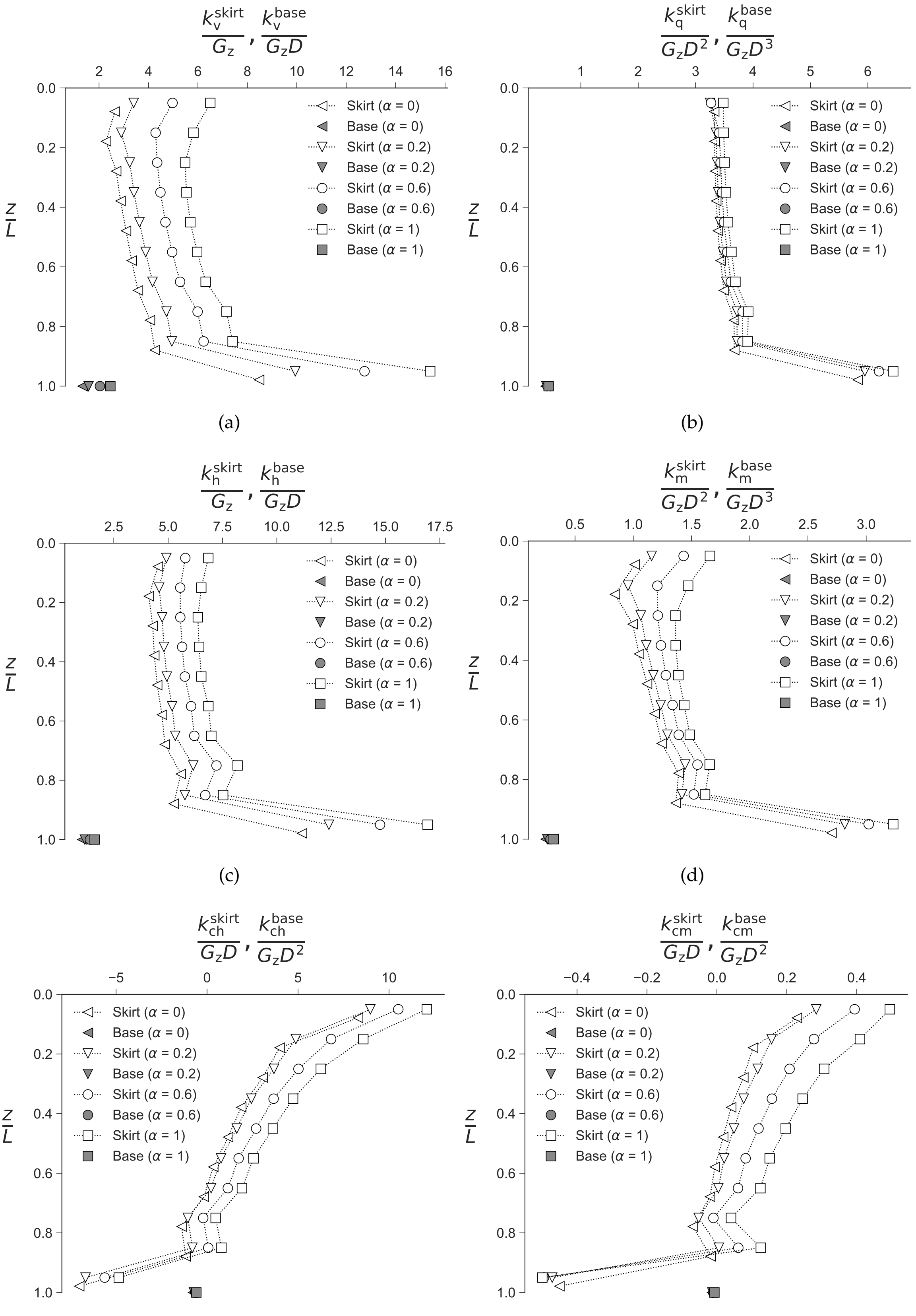

(a) (b)

(c) (d)

(e) (f)

Figure 4.7: Profiles of the local stiffness coefficients (normalised by the local shear modulus $G_z = G_R(2z/D)^\alpha$) for the skirt and base soil reactions, for $L/D = 1$, $\nu = 0.2$ and $\alpha = 0, 0.2, 0.6, 1$.

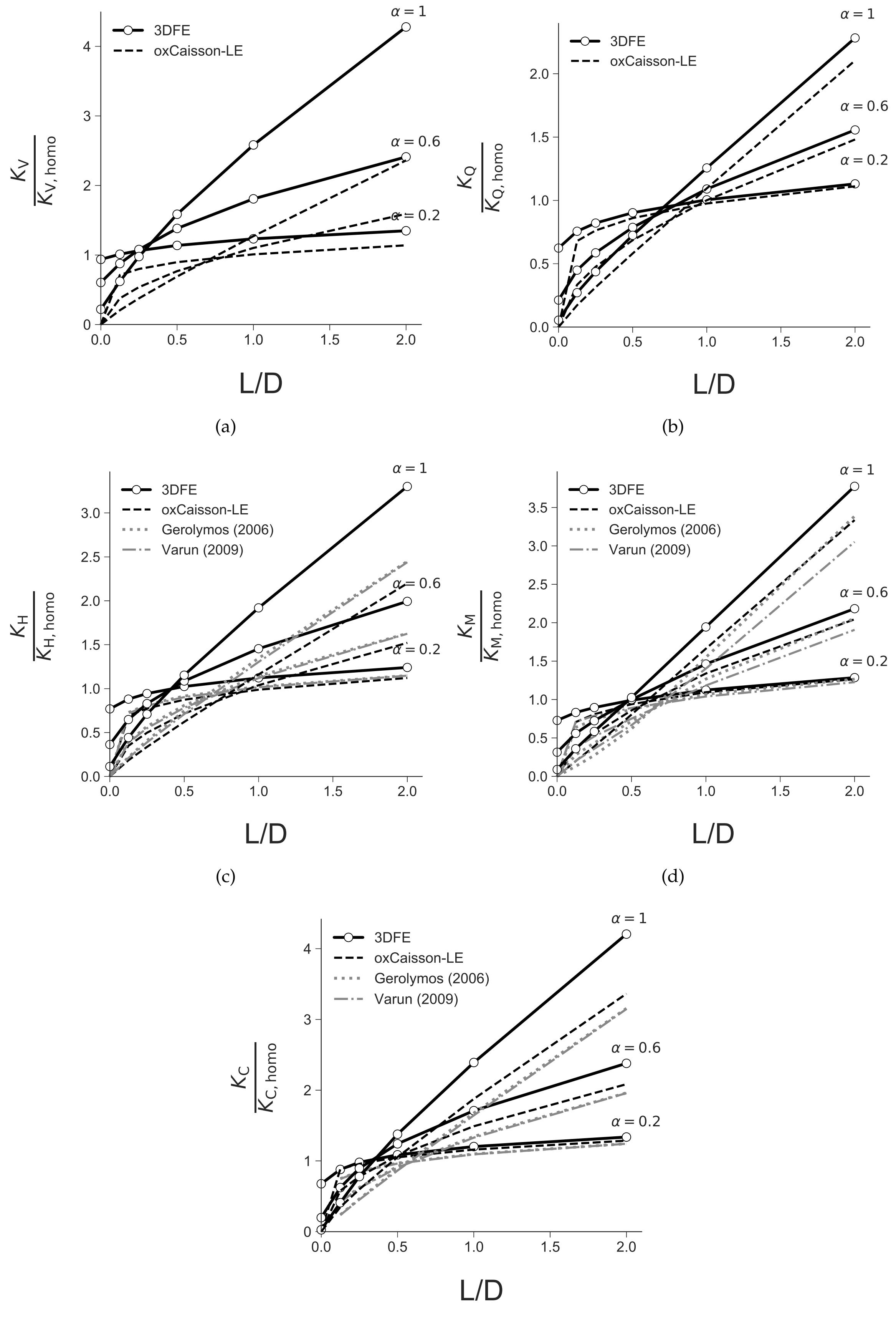

(a)

(b)

(c)

(d)

(e)

Figure 4.8: Comparison of the global stiffness coefficients (normalised by their corresponding stiffness for the homogeneous soil case) predicted by oxCaisson-LE, Gerolymos & Gazetas (2006*c*) and Varun et al. (2009) with the 3DFE results, for $\alpha = 0.2, 0.6, 1$ and $\nu = 0.2$.

The results of Section 4.1 validated the stress-based propositions for vertical loading on a surface foundation. This section follows up on those results by assessing the validity of the stress-based and strain-based propositions for 6DoF loading on suction caissons. However, there is a notable difference between the assessments carried out in this section and that in Section 4.1. As there are two soil reaction types (skirt and base soil reactions) for suction caissons, the propositions were assessed under the independent application of the skirt and base soil reactions. This was implemented in the 3DFE model by removing the tie constraints between the caisson skirt exterior and the soil elements in contact with it or the caisson base (including the soil plug) and the soil elements beneath it. Removal of the tie constraints means that the untied soil elements would not provide any direct resistance to the prescribed displacement of the caisson.

Assessment of Propositions 1a and 2a

First, Propositions 1a and 2a were assessed under the application of only the base soil reactions. Figs. 4.9 and 4.10 compare the resulting $\int_0^\infty u_\sigma \, dz$ and $\int_0^\infty u_\varepsilon \, dz$ per unit work under independent applications of vertical, lateral, rotational and torsional displacements, for $L/D = 0, 1$, $\nu = 0.2, 0.49$ and $\alpha = 0, 0.2, 0.6, 1$. For clarity, they are normalised by their corresponding values for the homogeneous soil case (i.e. $\alpha = 0$). It is evident that $\int_0^\infty u_\sigma \, dz$ per unit work stays largely the same for different values of $L/D, v$ and α, while $\int_0^\infty u_\varepsilon \, dz$ varies widely; although the variations of $\int_0^\infty u_\varepsilon \, dz$ are much less for higher L/D ratios. In general, the results show that Proposition 1a is more valid than Proposition 2a for the base soil reactions.

Next, Propositions 1a and 2a were assessed under the application of only the skirt soil reactions. Like Figs. 4.9 and 4.10, Figs. 4.11 and 4.12 compare the resulting $\int_0^\infty u_\sigma \, dz$ and $\int_0^\infty u_\varepsilon \, dz$ per unit work under independent applications of vertical, lateral, rotational and torsional displacements. The results show that $\int_0^\infty u_\sigma \, dz$ generally varies more than $\int_0^\infty u_\varepsilon \, dz$ for different values of α, although the variations were minor for both cases. This suggests that Proposition 2a is generally more valid than Proposition 1a for the skirt soil reactions.

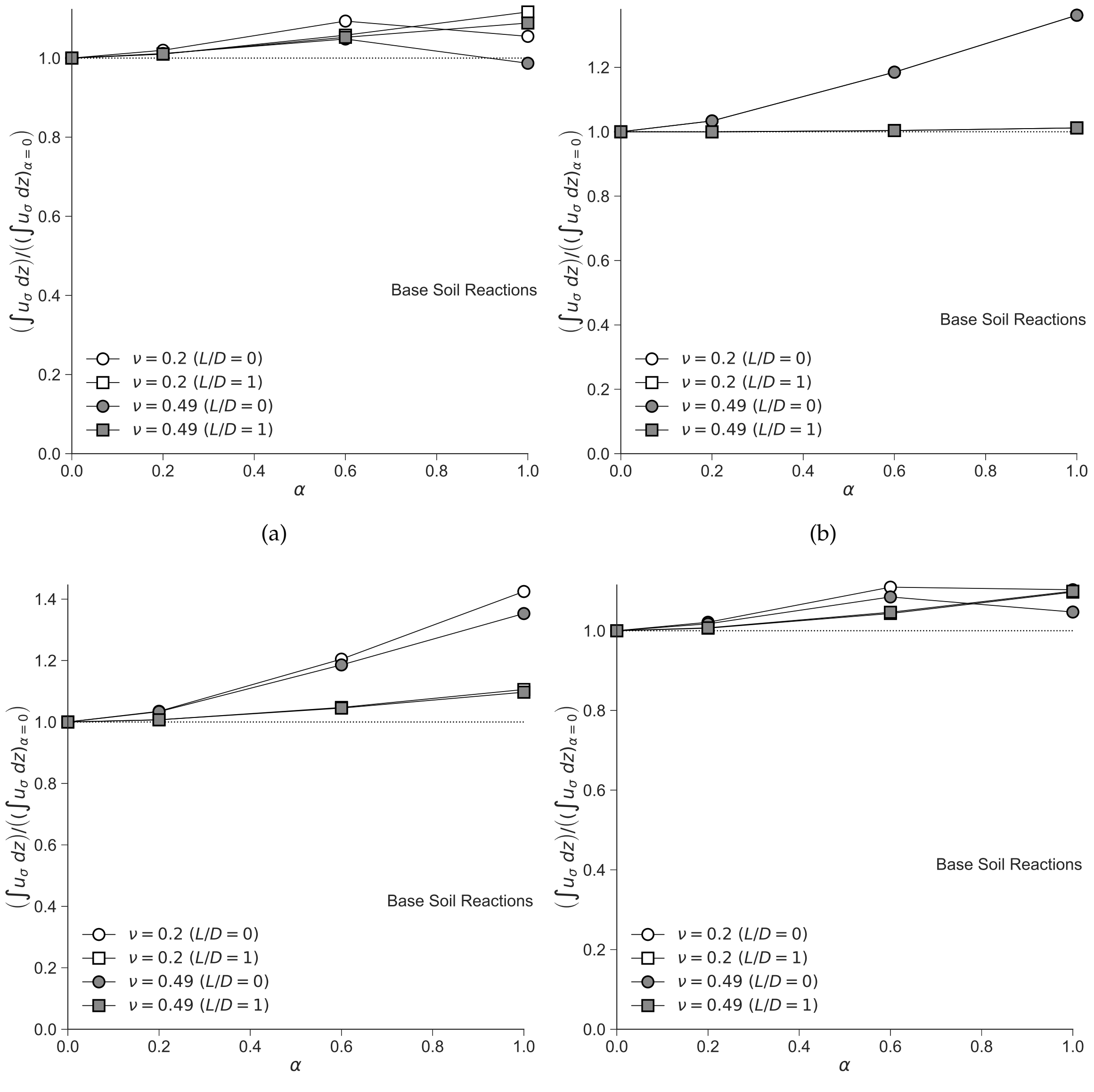

(a) (b)

(c) (d)

Figure 4.9: Comparison of the normalised $\int_0^\infty u_\sigma\, dz$ due to base soil reactions only, for $\alpha = 0, 0.2, 0.6, 1$ and $\nu = 0.2, 0.49$ under the following displacements: (a) Vertical (b) Torsional (c) Lateral (d) Rotational.

Assessment of Propositions 1b and 2b

Figs. 4.13 and 4.14 compare w_σ and w_ε under the application of only the base and skirt soil reactions respectively, for different L/D and α values. To allow for direct comparisons of w_σ below the caisson base for different L/D values, the results for $L/D = 0$ are shifted downwards to start at a depth of $L/D = 1$. Fig. 4.13 shows that w_σ is more invariant to G than w_ε, while Fig. 4.14 indicates the opposite. This suggests that Proposition 1b is more valid than Proposition 2b for the base soil reactions, while Proposition 2b is more valid than Proposition 1b for the skirt soil reactions.

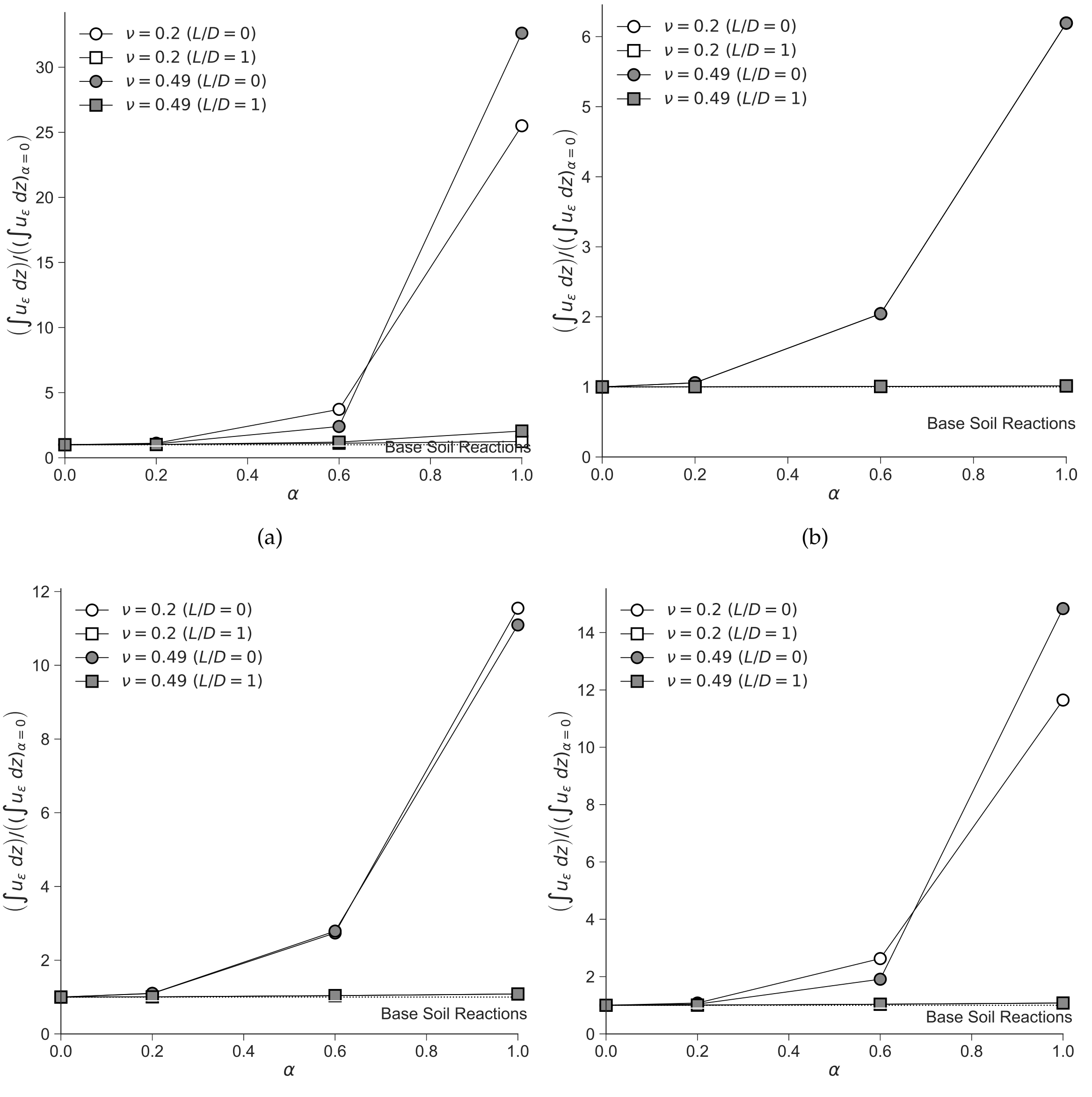

(a)

(b)

(c)

(d)

Figure 4.10: Comparison of the normalised $\int_0^\infty u_\varepsilon \, dz$ due to base soil reactions only, for $\alpha = 0, 0.2, 0.6, 1$ and $\nu = 0.2, 0.49$ under the following displacements: (a) Vertical (b) Torsional (c) Lateral (d) Rotational.

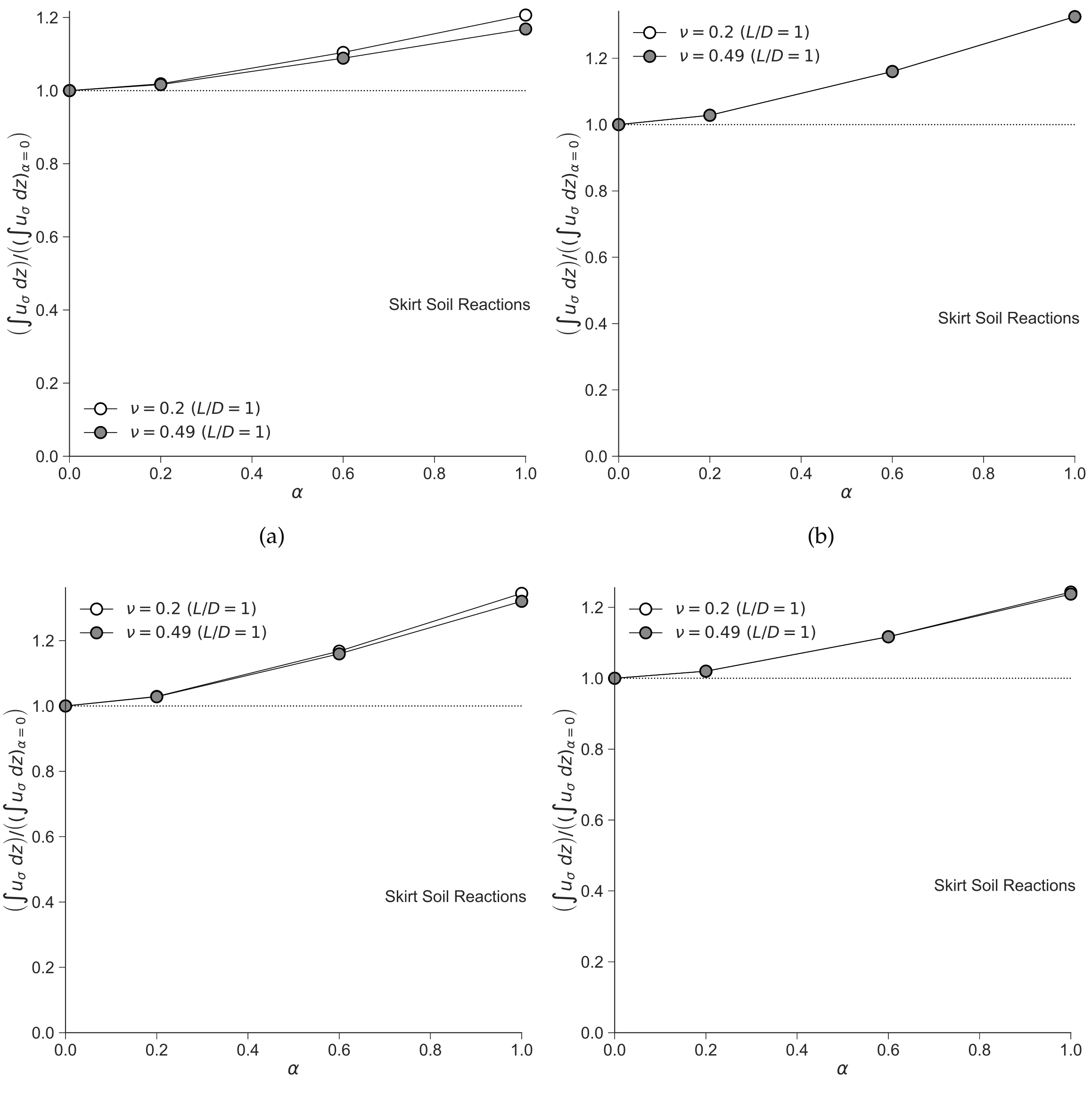

(a) (b)

(c) (d)

Figure 4.11: Comparison of the normalised $\int_0^\infty u_\sigma\,dz$ due to skirt soil reactions only, for $\alpha = 0, 0.2, 0.6, 1$ and $\nu = 0.2, 0.49$ under the following displacements: (a) Vertical (b) Torsional (c) Lateral (d) Rotational.

It is assumed that the previous assessments of Propositions 1 and 2 remain true under the combined application of skirt and base soil reactions. Fig. 4.15 shows the comparisons of w_σ and w_ε for $L/D = 1$ under the combined application of the skirt and base soil reactions. The results suggests that the principle of superposition approximately applies.

In summary, the assessments suggest that the stress-based propositions (Propositions 1a and 1b) apply for the base soil reactions, while the strain-based propositions (Propositions 2a and 2b) apply for the skirt soil reactions.

In his two-layer solution for axially loaded piles in non-homogeneous soil, Poulos

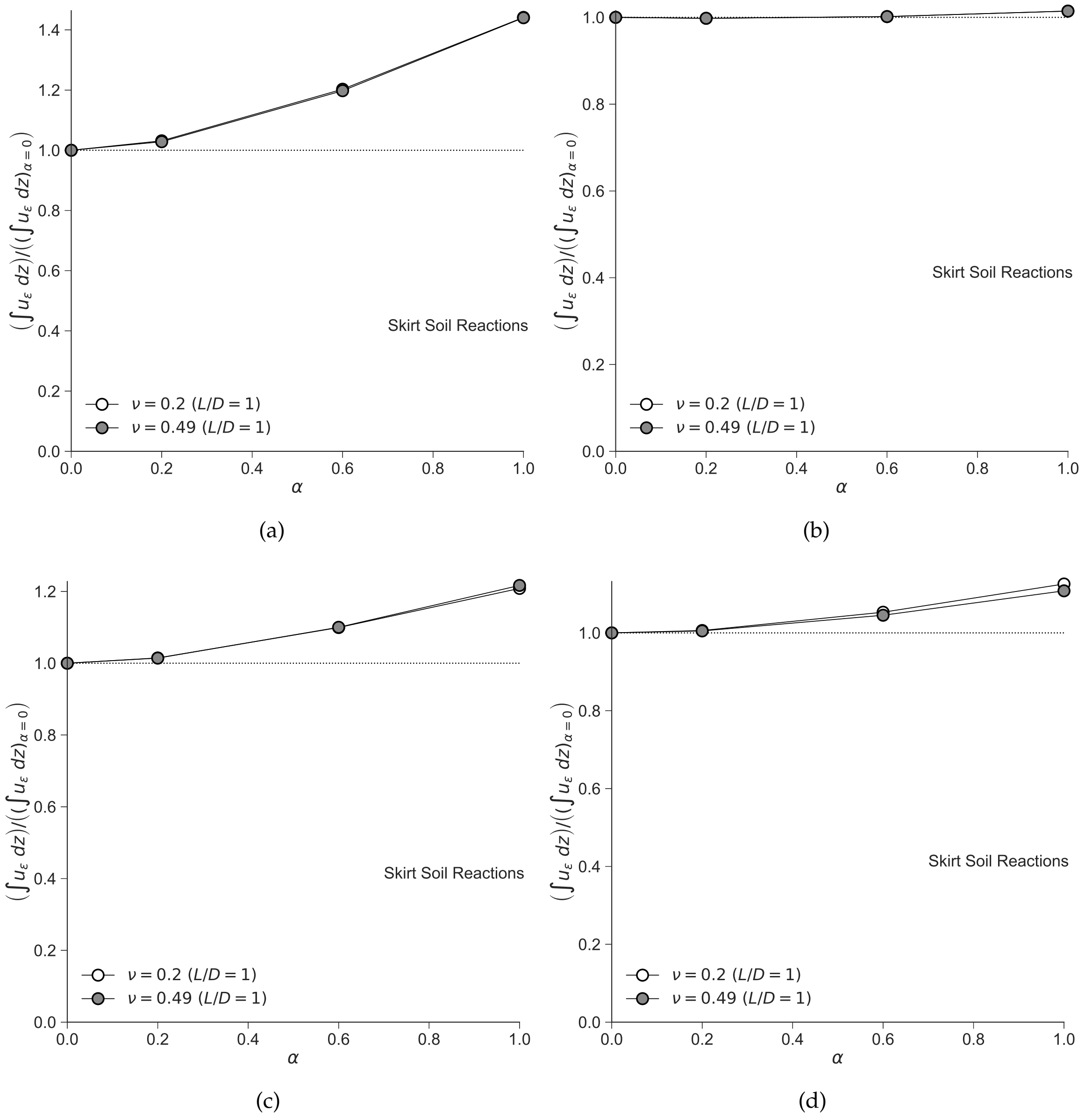

(a)

(b)

(c)

(d)

Figure 4.12: Comparison of the normalised $\int_o^\infty u_\varepsilon \, dz$ due to skirt soil reactions only, for $\alpha = 0, 0.2, 0.6, 1$ and $\nu = 0.2, 0.49$ under the following displacements: (a) Vertical (b) Torsional (c) Lateral (d) Rotational.

(1979) implicitly suggests that the practical influence of w_ε extends to a depth of $5D$ below the base depth. This is corroborated by Fig. 4.16, which shows that the influence of w_ε is insignificant after that depth. However, the recommendation of uniformly weighting the shear modulus from the base depth till $5D$ below it would overestimate the influence of the deeper layers, resulting in an overestimated, equivalent shear modulus G_{eq}.

4.2.5 Modulus Weighting Method

Now that the propositions of the work-equivalence framework have been assessed for the skirt and base soil reactions, a new design method, termed the 'modulus weighting

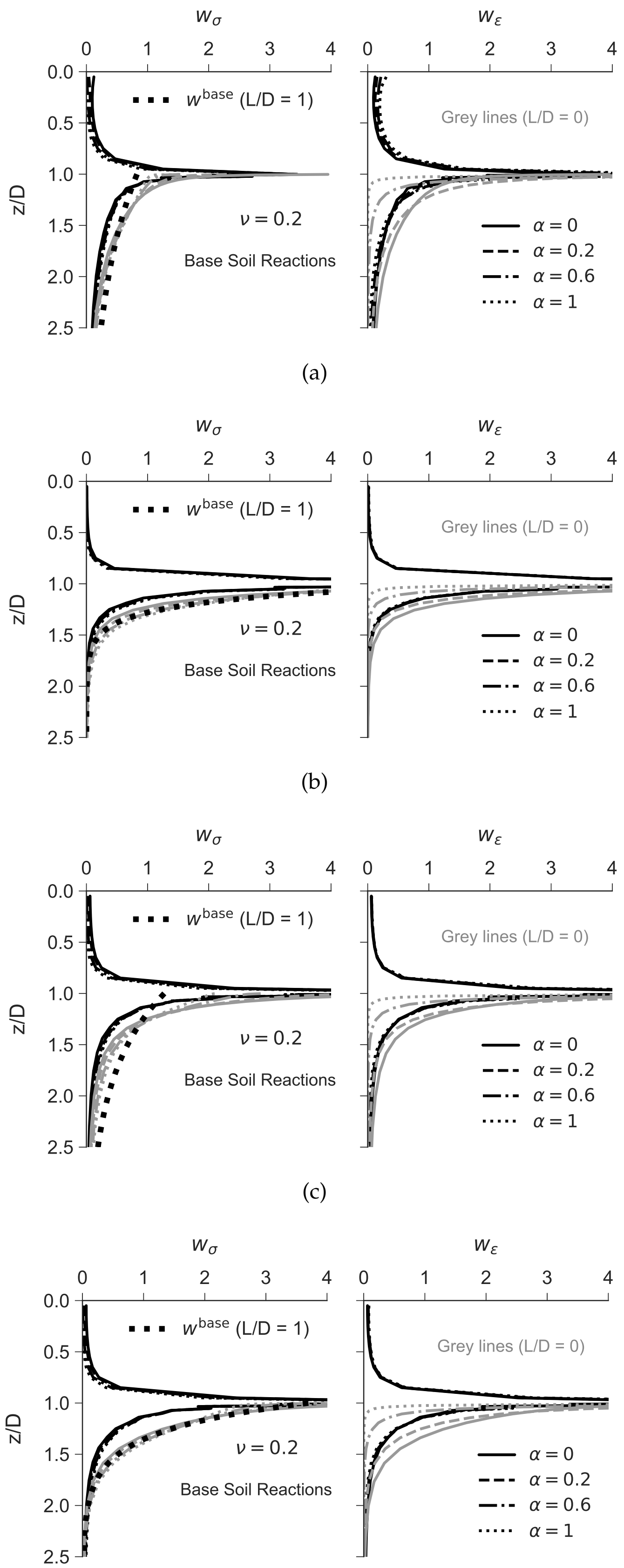

(a)

(b)

(c)

(d)

Figure 4.13: Comparison of w_σ and w_ε due to base soil reactions only, for $L/D = 0, 1$, $\nu = 0.2$ and $\alpha = 0, 0.2, 0.6, 1$ under the following displacements: (a) Vertical (b) Torsional (c) Lateral (d) Rotational. The grey and black lines correspond to $L/D = 0$ and $L/D = 1$ respectively. The thick dashed lines w^{base} represent the weight functions used in the modulus weighting method (Eq. 4.35) for the base soil reactions (for $L/D = 1$).

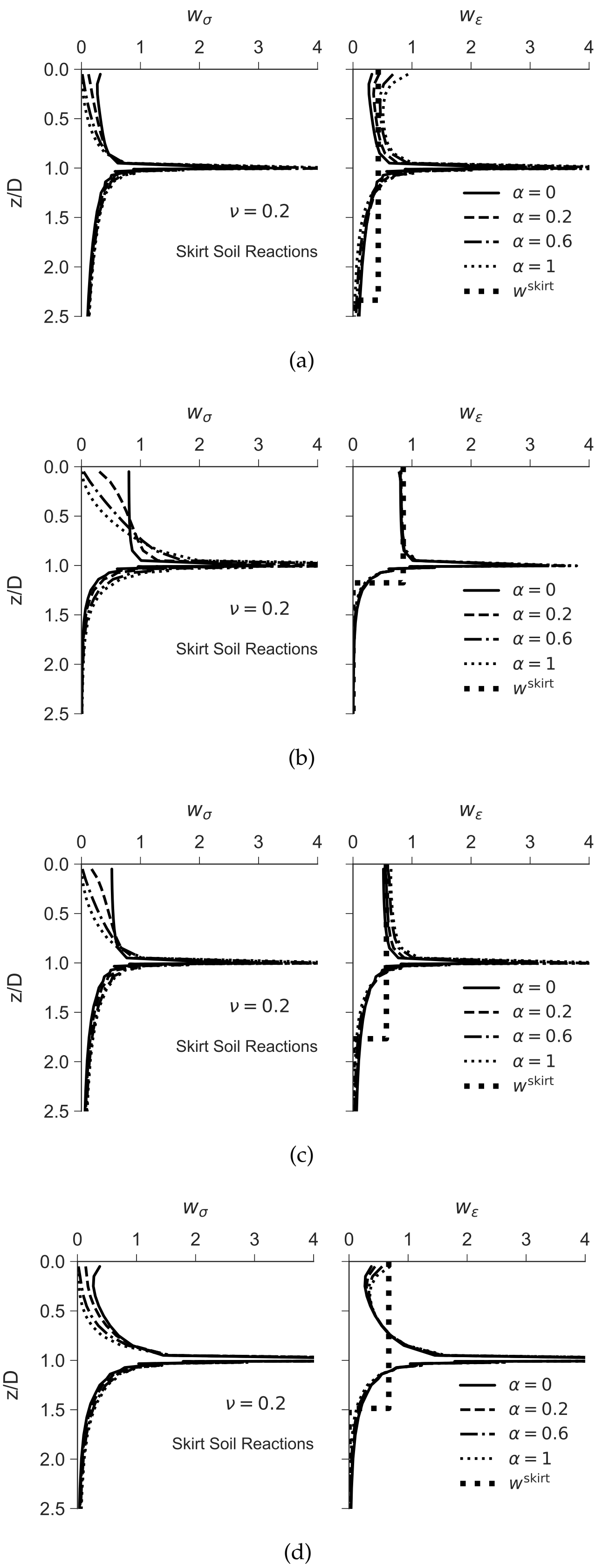

(a)

(b)

(c)

(d)

Figure 4.14: Comparison of w_σ and w_ε due to skirt soil reactions only, for $L/D = 1$, $\nu = 0.2$ and $\alpha = 0, 0.2, 0.6, 1$ under the following displacements: (a) Vertical (b) Torsional (c) Lateral (d) Rotational. The thick dashed lines w^{skirt} represent the weight functions used in the modulus weighting method (Eq. 4.36) for the skirt soil reactions (for $L/D = 1$). Note that the weight functions may extend beyond the skirt length, as the equivalent shear modulus may be affected by the soil stiffness below the skirt length. The uniform distribution assumed by Eq. 4.36 underestimates the true weighting at the skirt tip level, but overestimates the true weighting below the skirt tip.

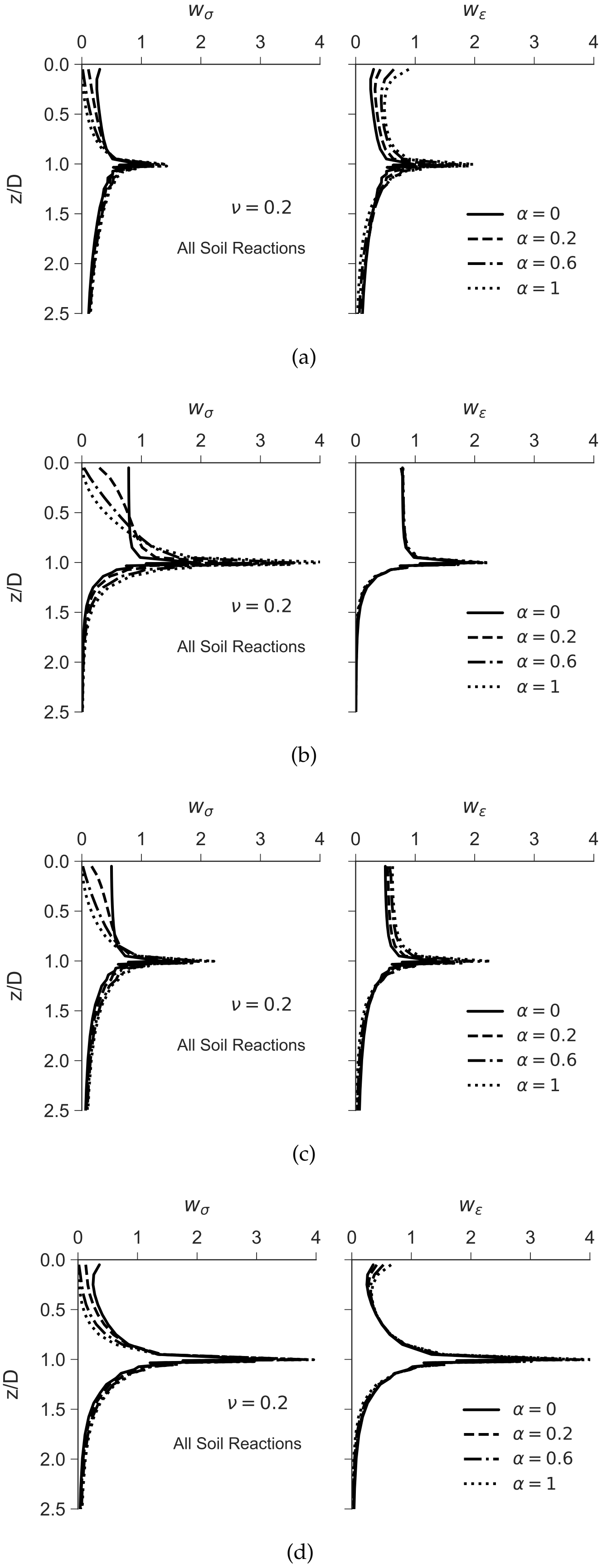

(a)

(b)

(c)

(d)

Figure 4.15: Comparison of w_σ and w_ε under the combined application of the skirt and base soil reactions, for $L/D = 1$, $\nu = 0.2$ and $\alpha = 0, 0.2, 0.6, 1$ for (a) Vertical displacement (b) Torsion (c) Horizontal displacement (d) Rotation.

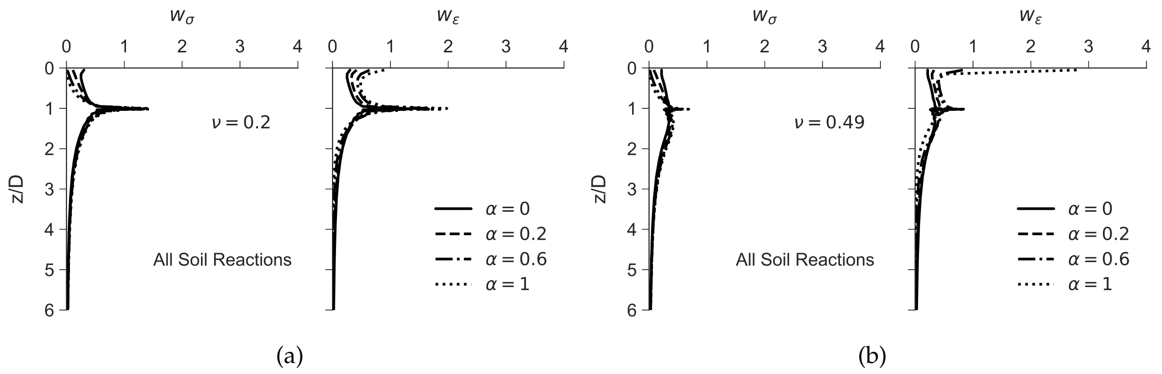

(a)

(b)

Figure 4.16: Comparison of w_σ and w_ε under the combined application of the skirt and base soil reactions for vertical displacement, for $L/D = 1$ and $\alpha = 0, 0.2, 0.6, 1$ (a) $\nu = 0.2$ (b) $\nu = 0.49$.

method', is introduced to deal with non-homogeneous soil. This modulus weighting method is similar to the two-layer solution of Poulos (1979) in that two equivalent, homogeneous shear modulus G_{eq} are identified: one for the skirt soil reactions and one for the base soil reactions. However, what differs is the weighting methodology.

Based on the results in the previous section, w_ε is used to find the equivalent shear modulus $G_{\text{eq}}^{\text{skirt}}$ for the skirt soil reactions, while w_σ is used to find the equivalent shear modulus $G_{\text{eq}}^{\text{base}}$ for the base soil reactions. The equations to calculate $G_{\text{eq}}^{\text{skirt}}$ and $G_{\text{eq}}^{\text{base}}$ are:

$$G_{\text{eq}}^{\text{base}} = 1/\left(\int_{L/D}^{\infty} \frac{1}{G} w_\sigma \, d\tilde{z}\right) \tag{4.33}$$

$$G_{\text{eq}}^{\text{skirt}} = \int_{0}^{\infty} G w_\varepsilon \, d\tilde{z} \tag{4.34}$$

where w_σ and w_ε are unknown weight functions. Due to the nature of the weight functions (which reduces in magnitude rapidly when far from the caisson base), numerically integrating the above equations to a depth of $30D$ below caisson base is sufficient.

It can be observed from Figs. 4.13 to 4.14 that w_σ is exponential below the caisson base, while w_ε tends to be uniform along the skirt length. Noting that w_σ and w_ε sums up to 1 like a probability density function, the modulus weighting method adopts the Weibull and uniform probability density functions to approximate w_σ and w_ε respectively:

$$\hat{w}_\sigma = \begin{cases} \frac{\kappa}{\lambda}\left(\frac{\tilde{z}-L/D}{\lambda}\right)^{\kappa-1} \exp\left(-(\frac{\tilde{z}-L/D}{\lambda})^{\kappa}\right) & \text{for } \tilde{z} \geq L/D \\ 0 & \text{for } \tilde{z} < L/D \end{cases} \tag{4.35}$$

$$\hat{w}_\varepsilon = \begin{cases} \frac{1}{b} & \text{for } 0 \leq \tilde{z} \leq b \\ 0 & \text{for } \tilde{z} < 0 \text{ or } \tilde{z} > b \end{cases} \tag{4.36}$$

Table 4.2: Best-fit parameters $a_1, \ldots, a_6$ in Eqs. 4.38 and 4.39 for each base soil reaction stiffness coefficient.

Stiffness	a_1	a_2	a_3	a_4	a_5	a_6
$k_{\mathrm{v}}^{\mathrm{base}}$	0.265	0.489	27.3	5	0.711	0.914
$k_{\mathrm{q}}^{\mathrm{base}}$	0.459	0.076	0	0	0.069	0.346
$k_{\mathrm{h}}^{\mathrm{base}}$	0.269	0.237	-0.049	0.988	0.558	0.68
$k_{\mathrm{m}}^{\mathrm{base}}$	0.388	0.144	5.10	4.34	0.122	0.549
$k_{\mathrm{c}}^{\mathrm{base}}$	0.197	0.19	-0.37	1	0	0

where $\kappa > 0$ is the shape parameter and $\lambda > 0$ is the scale parameter of the Weibull distribution, and $b > 0$ is the end boundary of the uniform distribution.

To identify the unknown parameters (κ, λ) in Eq. 4.35, the 3DFE local stiffness coefficient results for $L/D = 0, 0.125, 0.25, 0.5, 1, 2$, $\nu = 0.2, 0.49$ and $\alpha = 0, 0.2, 0.6, 1$ were used as calibration data for the LS regression. The LS regression was carried out in terms of the normalised local stiffness coefficients for the base soil reactions (normalised by their corresponding values for the homogeneous soil case):

$$\begin{aligned}\frac{\chi^{\mathrm{base}}}{\chi^{\mathrm{base}}_{\mathrm{homo}}} &= \frac{G^{\mathrm{base}}_{\mathrm{eq}} f^{\mathrm{base}}_{\mathrm{k}}(L, D, \nu)}{G_{\mathrm{R}} f^{\mathrm{base}}_{\mathrm{k}}(L, D, \nu)} \\ &= \frac{1/\left(\int_0^\infty \frac{1}{G_{\mathrm{R}}(2\tilde{z})^\alpha} \hat{w}_\sigma \, d\tilde{z}\right)}{G_{\mathrm{R}}} \\ &= 1/\left(\int_0^\infty \frac{1}{(2\tilde{z})^\alpha} \hat{w}_\sigma \, d\tilde{z}\right)\end{aligned} \tag{4.37}$$

where Eq. 4.33 was used to evaluate $G^{\mathrm{base}}_{\mathrm{eq}}$, χ^{base} can be any base soil reaction stiffness coefficient (e.g. $k^{\mathrm{base}}_{\mathrm{v}}$) and $f^{\mathrm{base}}_{\mathrm{k}}$ is its corresponding normalised stiffness function (e.g. Eq. 3.20). The best-fit κ, λ in Eq. 4.35 were identified by carrying out LS regression between the left hand side (i.e. 3DFE results) and right-hand side (i.e. predictions) of Eq. 4.37. Based on the regression results, the following approximating functions for κ and λ were obtained:

$$\hat{\kappa} = 1 + a_1 \exp(-1000L/D) \tag{4.38}$$

$$\hat{\lambda} = a_2 + a_3 \nu^{a_4} + a_5 (L/D)^{a_6} \tag{4.39}$$

where the best-fit $a_1, \ldots, a_6$ for each base soil reaction stiffness coefficient are listed in Table 4.2.

Table 4.3: Best-fit parameters a_1, a_2, a_3 in Eq. 4.41 for each skirt soil reaction stiffness coefficient.

Stiffness	a_1	a_2	a_3
$k_{\mathrm{v}}^{\mathrm{skirt}}$	2.28	0.272	0.720
$k_{\mathrm{q}}^{\mathrm{skirt}}$	1.18	0	0.877
$k_{\mathrm{h}}^{\mathrm{skirt}}$	1.77	0	0.791
$k_{\mathrm{m}}^{\mathrm{skirt}}$	1.44	0.23	0.8

A similar process was followed to compute the best-fit b in Eq. 4.36 for the skirt soil reactions. For example:

$$\begin{aligned}\frac{\chi^{\mathrm{skirt}}}{\chi^{\mathrm{skirt}}_{\mathrm{homo}}} &= \frac{G^{\mathrm{skirt}}_{\mathrm{eq}} f^{\mathrm{skirt}}_{\mathrm{k}}(L,D,\nu)}{G_{\mathrm{R}} f^{\mathrm{skirt}}_{\mathrm{k}}(L,D,\nu)} \\ &= \frac{\int_0^\infty G_{\mathrm{R}}(2\tilde{z})^\alpha \hat{w}_\varepsilon \, d\tilde{z}}{G_{\mathrm{R}}} \\ &= \int_0^\infty (2\tilde{z})^\alpha \hat{w}_\varepsilon \, d\tilde{z}\end{aligned} \tag{4.40}$$

where Eq. 4.34 was used to evaluate $G^{\mathrm{skirt}}_{\mathrm{eq}}$, χ^{skirt} can be any skirt soil reaction stiffness coefficient (except $k^{\mathrm{skirt}}_{\mathrm{c}}$) and $f^{\mathrm{skirt}}_{\mathrm{k}}$ is its corresponding normalised stiffness function (e.g. Eq. 3.12).

The best-fit b in Eq. 4.36 were identified by carrying out LS regression between the left hand side (i.e. 3DFE results) and right-hand side (i.e. predictions) of Eq. 4.40. Based on the regression results, the following approximating function for b was obtained:

$$\hat{b} = (a_1 + a_2\nu)(L/D)^{a_3} \tag{4.41}$$

where the best-fit $a_1, \ldots, a_3$ for each skirt soil reaction stiffness coefficient are listed in Table 4.3.

To visualise what the numbers in Tables 4.2 and 4.3 represent, the resultant w^{base} and w^{skirt} using these numbers are included in Figs. 4.13 and 4.14 for $L/D = 1$. Evidently, w^{base} and w^{skirt} are somewhat crude approximations of the true w_σ and w_ε. For example, the uniform distribution assumed by Eq. 4.36 tends to underestimate the true weighting at the skirt tip level, but overestimate the true weighting at depths below the skirt tip. However, they still match the salient features of the distribution.

Non-homogeneity Factors

Using a constant $G_{\mathrm{eq}}^{\mathrm{skirt}}$ implies that the skirt soil reactions are constant along the skirt, which is not true for non-homogeneous soil. Thus, constant, non-homogeneity factors η^{skirt} were derived for the skirt soil reactions, such that the work done by the factored skirt reactions is equal to the work done when $G_{\mathrm{eq}}^{\mathrm{skirt}}$ is applied i.e.

$$\begin{aligned} \frac{1}{2} G_{\mathrm{eq}}^{\mathrm{skirt}} \int_0^{L/D} f_{\mathrm{k}}^{\mathrm{skirt}}(L, D, \nu)(\Delta s)^2 \, d\tilde{z} &= \frac{1}{2} \int_0^{L/D} \eta^{\mathrm{skirt}} G f_{\mathrm{k}}^{\mathrm{skirt}}(L, D, \nu)(\Delta s)^2 \, d\tilde{z} \\ \therefore \eta^{\mathrm{skirt}} &= G_{\mathrm{eq}}^{\mathrm{skirt}} \frac{\int_0^{L/D} f_{\mathrm{k}}^{\mathrm{skirt}}(L, D, \nu) \, d\tilde{z}}{\int_0^{L/D} G f_{\mathrm{k}}^{\mathrm{skirt}}(L, D, \nu) \, d\tilde{z}} \end{aligned} \tag{4.42}$$

where Δs is the work conjugate displacement (e.g. vertical displacement for $k_{\mathrm{v}}^{\mathrm{skirt}}$).

As $f_{\mathrm{k}}^{\mathrm{skirt}}$ does not vary with depth (except for $k_{\mathrm{c}}^{\mathrm{skirt}}$), Eq. 4.42 simplifies to:

$$\begin{aligned} \eta^{\mathrm{skirt}} &= G_{\mathrm{eq}}^{\mathrm{skirt}} \frac{f_{\mathrm{k}}^{\mathrm{skirt}}(L, D, \nu) \int_0^{L/D} d\tilde{z}}{f_{\mathrm{k}}^{\mathrm{skirt}}(L, D, \nu) \int_0^{L/D} G \, d\tilde{z}} \\ &= \frac{G_{\mathrm{eq}}^{\mathrm{skirt}}}{G_{\mathrm{sk}}} \end{aligned} \tag{4.43}$$

where G_{sk} is the average shear modulus along the skirt length.

Therefore, by applying η^{skirt} to the local shear modulus (i.e. use $G_{\mathrm{fac}}(z) = \eta^{\mathrm{skirt}} G(z)$) and using the factored local shear modulus to predict the skirt soil reactions at depth z, the skirt soil reactions in non-homogeneous soil are obtained. This can be directly observed from Fig. 4.17, which shows that the factored stiffness profiles converge to the profile corresponding to the homogeneous soil case. Note that $\eta^{\mathrm{skirt}} = 1$ for $k_{\mathrm{c}}^{\mathrm{skirt}}$ as there is no w_ε defined for it in Table 4.3. This is because no sensible w_ε could be obtained for it during the regression analysis. Thus, the local G is used for $k_{\mathrm{c}}^{\mathrm{skirt}}$.

Summary

The modulus weighting method involves the following steps:

1. Calculate non-homogeneity factors η^{skirt} for the skirt soil reactions, where $\eta^{\mathrm{skirt}} = G_{\mathrm{eq}}^{\mathrm{skirt}} / G_{\mathrm{sk}}$. $G_{\mathrm{eq}}^{\mathrm{skirt}}$ can be computed using Eqs. 4.34, 4.36, 4.41 and Table 4.3. G_{sk} is the average shear modulus along the skirt length. Let $\eta^{\mathrm{skirt}} = 1$ for $k_{\mathrm{c}}^{\mathrm{skirt}}$.
2. Calculate the equivalent shear modulus $G_{\mathrm{eq}}^{\mathrm{base}}$ for the base soil reactions, where $G_{\mathrm{eq}}^{\mathrm{base}}$ can be computed using Eqs. 4.33, 4.35, 4.38, 4.39 and Table 4.2.

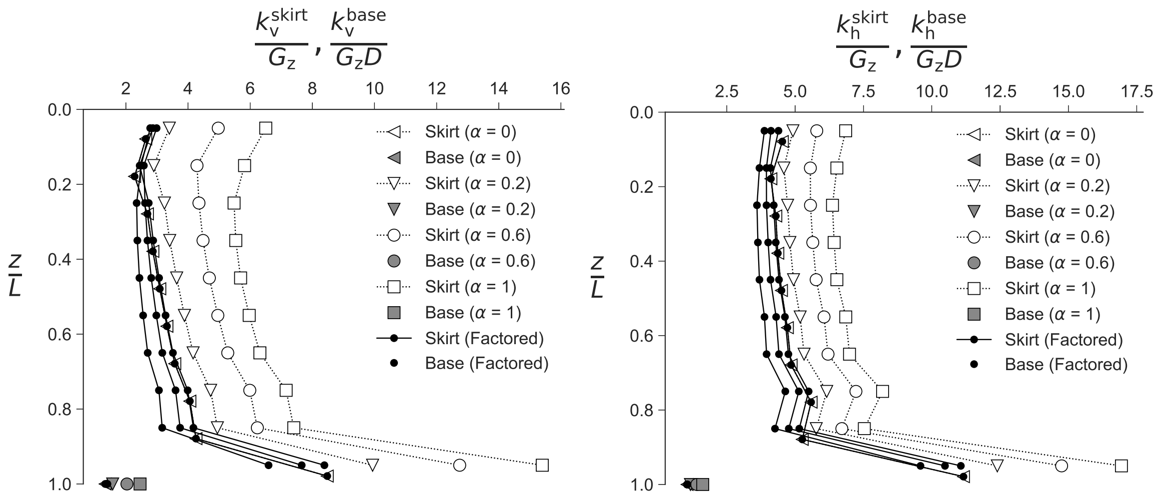

(a) (b)

Figure 4.17: Comparison of the vertical and lateral skirt soil reaction stiffness profiles, normalised by the local shear modulus $G_z = G_R(2\tilde{z})^\alpha$, for $L/D = 1$, $\nu = 0.2$ and $\alpha = 0, 0.2, 0.6, 1$. The factored profiles are the results of normalising the stiffness profiles by the factored local shear modulus $G_{fac} = \eta^{skirt} G_z$.

3. Predict the skirt soil reactions using Eqs. 3.12 to 3.17 with the factored local shear modulus (i.e. $G_{fac}(z) = \eta^{skirt} G(z)$).
4. Predict the base soil reactions using Eqs. 3.20 to 3.25 with G_{eq}^{base}.

Validation

To validate the modulus weighting method, Fig. 4.18 updates Fig. 4.8 by replacing the naive predictions with the weighted predictions using the modulus weighting method. Clearly, the weighted predictions are huge improvements over the naive predictions. There is some overestimation for K_M and K_C at higher α but overall, the modulus weighting method works very well. Notably, the modulus weighting method not only improves the predictions of oxCaisson-LE, but also that of Gerolymos & Gazetas (2006*c*) and Varun et al. (2009).

Next, oxCaisson-LE was tested in multi-layered soil. The modulus weighting method for a surface foundation on multi-layered soil has been considered by Suryasentana et al. (2017) with positive results. This study looks at the performance of the modulus weighting method for suction caissons in a three-layer system, similar to that used in Poulos (1979). The Young's modulus profile of this three-layer system is shown in Table 4.4 and three cases were evaluated in total. Fig. 4.19 compares the naive and weighted stiffness predictions of oxCaisson-LE with the 3DFE results for a caisson of $L/D = 1$. The modulus weighting method improves the accuracy of K_V, K_Q, K_H, but not for K_M and K_C. This is cor-

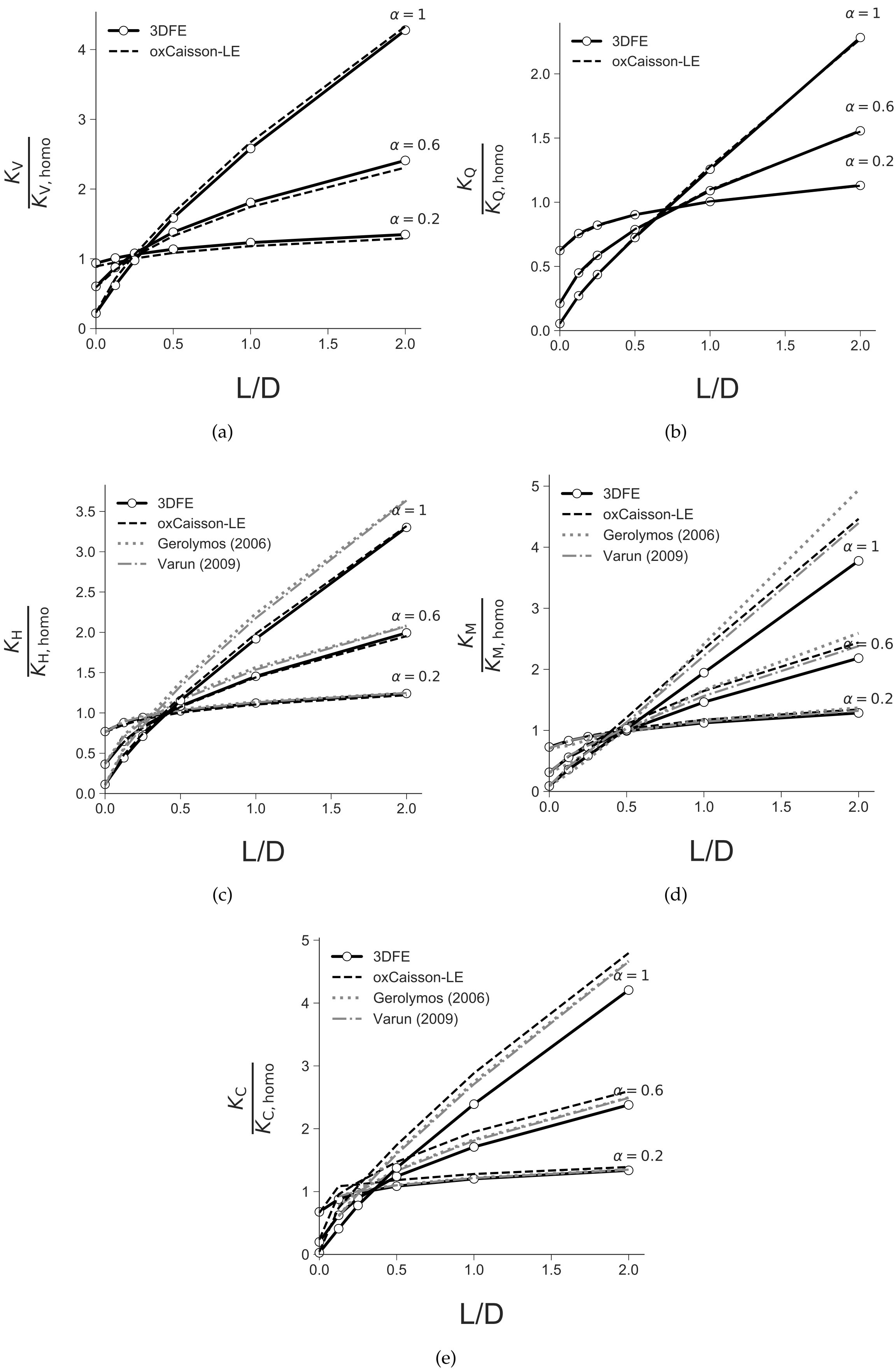

(a)

(b)

(c)

(d)

(e)

Figure 4.18: Comparison of the global stiffness coefficients (normalised by their corresponding stiffness for the homogeneous soil case) predicted by oxCaisson-LE, Gerolymos & Gazetas (2006*c*) and Varun et al. (2009) (using the modulus weighting method) with the 3DFE results, for $\alpha = 0.2, 0.6, 1$ and $\nu = 0.2$.

Table 4.4: Young's Modulus profiles for a three-layer, non-homogeneous soil system, where $E_\mathrm{R} = 100$ MPa is the reference Young's Modulus.

Depth	Case 1	Case 2	Case 3
$0 \leq z/L \leq 0.3$	$1E_\mathrm{R}$	$4E_\mathrm{R}$	$2E_\mathrm{R}$
$0.3 < z/L \leq 0.7$	$2E_\mathrm{R}$	$2E_\mathrm{R}$	$1E_\mathrm{R}$
$z/L > 0.7$	$4E_\mathrm{R}$	$1E_\mathrm{R}$	$4E_\mathrm{R}$

roborated by Table 4.5, which shows that the RMSPE of the stiffness predictions decrease for $K_\mathrm{V}, K_\mathrm{Q}, K_\mathrm{H}$ after the modulus weighting method is used, but not for K_M and K_C. Nevertheless, the predictions of oxCaisson-LE (with the modulus weighting method) generally agree well with the 3DFE results.

Table 4.5: Average percentage differences and RMSPE of the global stiffness coefficients predicted by oxCaisson-LE (naive and weighted) relative to the 3DFE results, for a three-layer, non-homogeneous soil system as per Table 4.4.

	Naive Predictions		Weighted Predictions	
Stiffness	Avg. Diff (%)	RMSPE (%)	Avg. Diff (%)	RMSPE (%)
${K_\mathrm{V}}^\mathrm{pred.}/{K_\mathrm{V}}^\mathrm{3DFE}$	5.59	38.42	4.87	8.67
${K_\mathrm{Q}}^\mathrm{pred.}/{K_\mathrm{Q}}^\mathrm{3DFE}$	-4.88	13.37	-2.28	4.84
${K_\mathrm{H}}^\mathrm{pred.}/{K_\mathrm{H}}^\mathrm{3DFE}$	-3.10	26.18	-0.01	2.45
${K_\mathrm{M}}^\mathrm{pred.}/{K_\mathrm{M}}^\mathrm{3DFE}$	-2.50	2.72	0.77	12.25
${K_\mathrm{C}}^\mathrm{pred.}/{K_\mathrm{C}}^\mathrm{3DFE}$	-13.98	16.93	-11.27	30.09

4.2.6 Discussion

The results in the previous section have shown that the modulus weighting method works reasonably well for non-homogeneous linear elastic soil with continuously varying or multi-layered, piecewise constant shear modulus profiles. A key advantage of the modulus weighting method is its transferability. Unlike other solutions for dealing with non-homogeneous soil (e.g. Guo & Randolph 1996, 1997), the modulus weighting method is not tightly coupled to oxCaisson-LE and can be easily used with other Winkler models with good effect, as shown in Fig. 4.18.

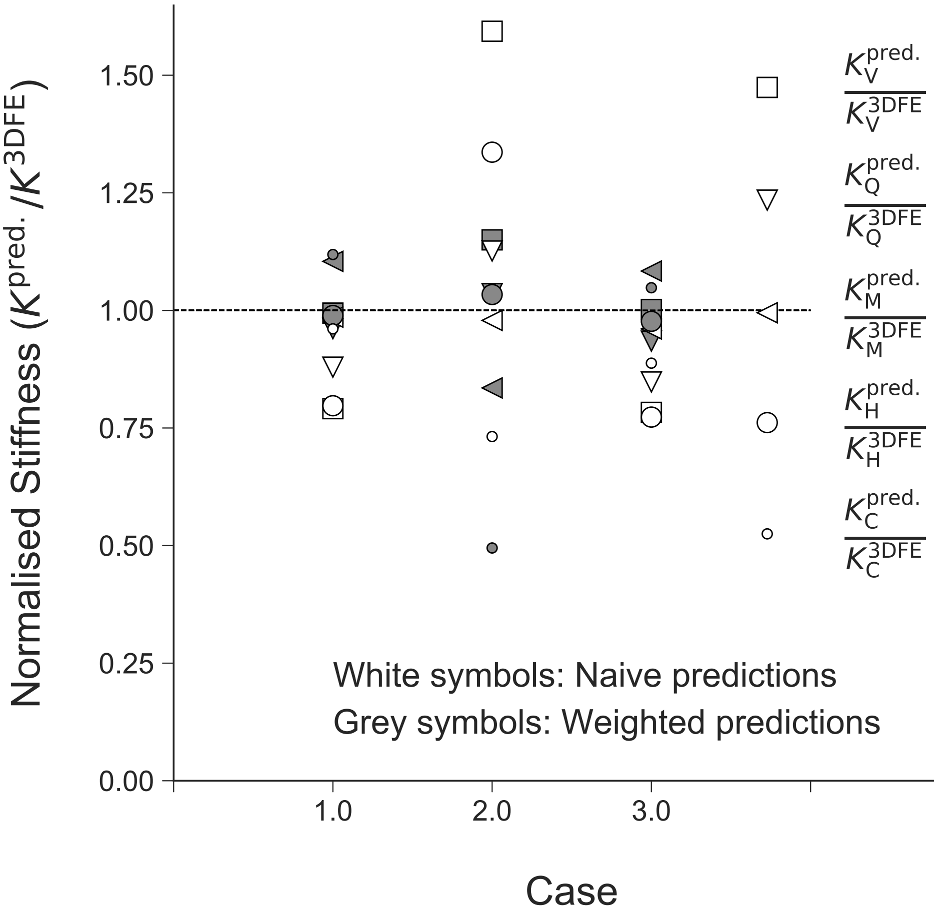

Figure 4.19: Comparison of the global stiffness coefficients computed by oxCaisson-LE (normalised by the 3DFE results), for a suction caisson of $L/D = 1$ in a three-layer, non-homogeneous system as per Table 4.4. The grey and white symbols represent the oxCaisson-LE predictions, with and without the application of the modulus weighting method respectively.

Chapter 5

Flexible Caisson Behaviour

In Chapters 3 and 4, oxCaisson-LE has been shown to be capable of approximating the 3DFE results for a fully rigid caisson. However, a fully rigid suction caisson is an idealised representation of an actual suction caisson, where the skirt is highly deformable. In this chapter, the set of linear elastic soil reactions derived in Chapters 3 and 4 are used to represent the soil reactions acting on a flexible caisson, which is defined as a suction caisson with a deformable skirt. The predictions of oxCaisson-LE with deformable skirt elements are then compared with published results for a flexible caisson in linear elastic soil.

5.1 Introduction

In previous numerical studies involving suction caissons (Bransby & Yun 2009, Hung & Kim 2014, Vulpe 2015, Mehravar et al. 2016), the caisson is usually modelled as being entirely rigid, which improves the efficiency of the numerical analyses. A flexible caisson is modelled only in a few numerical studies (Doherty et al. 2005, Thieken et al. 2014). Thieken et al. (2014) focus on the tensile behaviour of flexible caissons in sand under different loading rates, while Doherty et al. (2005) focus on determining the global stiffness coefficients of rigid and flexible caissons in non-homogeneous, linear elastic soil as per Eq. 4.27.

Doherty et al. (2005) found that the flexible caisson behaves in a manner that is intermediate to that of a fully rigid caisson and a rigid, circular surface foundation. In an example in homogeneous undrained clay, Doherty et al. (2005) showed that the rotational stiffness of a flexible caisson with $d_{\text{skirt}}/D = 0.00375$ and $L/D = 1$ is 29% less than that of a rigid caisson with the same dimensions.

Doherty et al. (2005) propose that the normalised global stiffness coefficient $K(J)$ (which can be $K_V/G_R D$, $K_H/G_R D$, $K_M/G_R D^3$, $K_Q/G_R D^3$ or $K_C/G_R D^2$) for a flexible caisson is:

$$K(J) = \frac{K_0 + (J/J_m)^p K_\infty}{1 + (J/J_m)^p} \tag{5.1}$$

where $J = 2(E_{skirt}/G_R)(d_{skirt}/D)$, E_{skirt} is the Young's modulus of the caisson skirt, G_R is the reference shear modulus as per Eq. 4.27, K_0 and K_∞ are the corresponding stiffness for a rigid surface foundation and a rigid caisson foundation respectively, and J_m, p are best-fit parameters. Although not directly applicable for caissons, there are related research (Dobry et al. 1982, Karatzia & Mylonakis 2017) on piles that propose procedures (based on the principle of virtual work) to estimate the global stiffness at the pile head, due to contributions from the pile flexural stiffness and the soil stiffness.

Eq. 5.1 suggests that the deformation of a caisson depends on two main factors: the relative foundation-soil stiffness ratio (E_{skirt}/G_R) and the normalised skirt thickness (d_{skirt}/D). Typically, the deformation of the caisson skirt can be ignored if $J > 1000$. Careful analysis must therefore be carried out before ignoring the skirt deformation. For example, consider a caisson with $d_{skirt}/D = 0.002$ in soft clay where $G_R = 2$ MPa. Its computed J is $2(210000/2)(0.002) = 420$ and ignoring the skirt deformation would overestimate the global stiffness. In contrast, if the caisson had a thicker skirt (e.g. $d_{skirt}/D = 0.005$), its computed J would be 1050 and the caisson skirt deformation can be ignored.

Given the significant influence of skirt deformation on the overall caisson behaviour, some measures of skirt deformation must be incorporated within oxCaisson for more realistic predictions. This is accomplished by representing the caisson skirt with deformable frame elements in oxCaisson. It is hypothesised that the soil reactions acting on the flexible caisson are similar to that of a rigid caisson. Thus, the same set of soil reactions derived in Chapters 3 and 4 are used to represent the soil reactions acting on the flexible caisson. The main objective of this chapter is to evaluate if this approach of modelling a flexible caisson is reasonable, via comparison with the results of Doherty et al. (2005).

5.2 Methodology

In this study, the global stiffness coefficients for a flexible caisson in non-homogeneous, linear elastic soil are predicted by oxCaisson-LE (with deformable skirt elements) and they are compared with the results of Doherty et al. (2005).

Table 5.1: Comparison of global stiffness coefficients for a flexible caisson, for $L/D = 1, \nu = 0.49, \alpha = 0$.

	Doherty et al. (2005)	oxCaisson-LE	Deviation (%)
$K_\mathrm{V}/G_\mathrm{R}D$	6.39	6.29	1.55
$K_\mathrm{H}/G_\mathrm{R}D$	6.34	6.45	1.8
$K_\mathrm{M}/G_\mathrm{R}D^3$	5.26	5.25	0.31
$K_\mathrm{Q}/G_\mathrm{R}D^3$	3.58	3.63	1.38
$K_\mathrm{C}/G_\mathrm{R}D^2$	-3.19	-3.18	0.26

Both a flexible caisson and a rigid caisson are modelled using deformable skirt elements in the Winkler framework. However, for the oxCaisson analyses in Chapters 3 to 6, a rigid body constraint was applied to the skirt elements to prevent deformation (as described in Section 2.6). In this chapter, the rigid body constraint was not applied and thus, the skirt elements were free to deform.

5.2.1 Material Properties

The flexible caisson properties are as follows: $D = 8$ m, $d_\mathrm{skirt}/D = 0.00375$, $L/D = 0.25, 0.5, 1, 2$, $E_\mathrm{skirt} = 200$ GPa (steel) and $\nu_\mathrm{skirt} = 0.25$. The soil properties are as follows: $G_\mathrm{R} = 20$ MPa, $\nu = 0.2, 0.499$ and $\alpha = 0, 0.2, 0.6, 1$ (as per Eq. 4.27).

5.3 Results

First, Table 5.1 compares the predictions of oxCaisson-LE with that of Doherty et al. (2005), for the homogeneous undrained clay example in their paper (i.e. $L/D = 1, \nu = 0.49, \alpha = 0$). There is excellent agreement between the two sets of predictions, with the maximum deviation being only 1.8%.

Next, Fig. 5.1 compares the normalised stiffness predictions of oxCaisson-LE and Doherty et al. (2005) for $L/D = 0.25, 0.5, 1, 2$, $\nu = 0.2, 0.499$ and $\alpha = 0, 0.2, 0.6, 1$. Looking at the homogeneous case (i.e. $\alpha = 0$), it is evident that the predictions of oxCaisson-LE agree very well with that of Doherty et al. (2005), especially for K_Q. For the non-homogeneous case (i.e. $\alpha \neq 0$), the agreement is still reasonably good, except for K_C. Since the agreement for K_C is excellent for the homogeneous case and the modulus weighting method overestimates

K_C for rigid caissons in non-homogeneous soil (see Fig. 4.18e), it is likely that the prediction errors in Fig. 5.1e are mainly attributable to the modulus weighting method. Indeed, Table 5.2 shows that the average percentage differences and RMSPE for the K_C predictions jumped from 1.71% and 7.09% for the homogeneous case to 17.58% and 24.20% after the non-homogeneous cases are included.

Table 5.2: Average percentage differences and RMSPE of the global stiffness coefficients predicted by oxCaisson-LE (with deformable skirt elements), relative to the results of Doherty et al. (2005). Two sets of results are presented: the first includes only the results for the homogeneous case ($\alpha = 0$) and the second includes all the results ($\alpha \geq 0$).

	Homogeneous Soil Profiles		All Soil Profiles	
Stiffness	Avg. Diff (%)	RMSPE (%)	Avg. Diff (%)	RMSPE (%)
${K_V}^{\text{oxCaisson-LE}} / {K_V}^{\text{Doherty}}$	1.07	2.38	-2.37	6.10
${K_Q}^{\text{oxCaisson-LE}} / {K_Q}^{\text{Doherty}}$	1.50	1.64	1.72	2.60
${K_H}^{\text{oxCaisson-LE}} / {K_H}^{\text{Doherty}}$	0.17	3.82	1.64	7.69
${K_M}^{\text{oxCaisson-LE}} / {K_M}^{\text{Doherty}}$	2.92	3.61	-0.29	4.79
${K_C}^{\text{oxCaisson-LE}} / {K_C}^{\text{Doherty}}$	1.71	7.09	17.58	24.20

5.4 Discussion

In general, Table 5.2 shows that oxCaisson-LE can predict the stiffness of flexible caissons reasonably well, simply by representing the skirt elements with deformable frame elements. This positive result is likely due to the fact that the soil reactions had been calibrated based on the true local soil stress results. If they had been back-calculated instead, the distribution of the soil response may not be correct, and the deformation of the flexible caisson may be inaccurate.

Moreover, the hypothesis that the soil reactions acting on flexible caissons are similar to that acting on rigid caissons is indirectly found to be approximately true. This is a remarkably useful result, as it implies that the soil reactions derived from 3DFE analyses of rigid caissons are fairly independent of the caisson stiffness and may be used to predict caissons of arbitrary stiffness. However, a closer look at the soil reactions from 3DFE analyses of flexible caissons is needed to confirm this hypothesis.

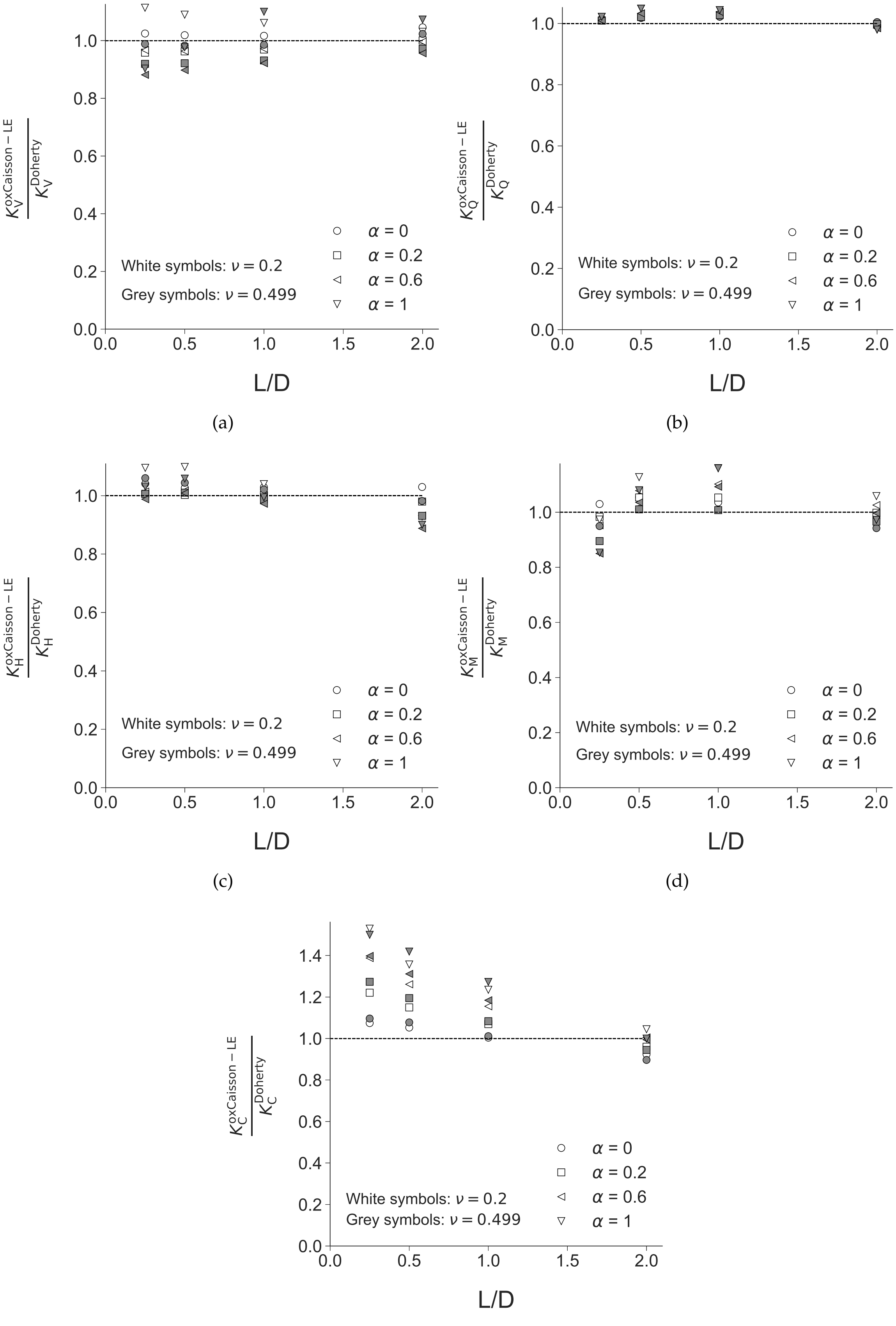

(a)

(b)

(c)

(d)

(e)

Figure 5.1: Comparison of the stiffness predictions of oxCaisson-LE (with deformable skirt elements) relative to the results of Doherty et al. (2005), for $L/D = 0.25, 0.5, 1, 2$, $\alpha = 0, 0.2, 0.6, 1$ and $\nu = 0.2, 0.499$.

Chapter 6

Small-strain, Non-linear Elastic Soil

Definition 6.1 (Small-strain) *The small-strain range for soil is defined as* $\varepsilon_{\mathrm{e}} \leq \varepsilon \leq 10^{-3}$*, where* $\varepsilon_{\mathrm{e}} \approx 10^{-6}$ *is the elastic strain limit (Atkinson 2000). This is the range within which the stiffness of the soil usually decreases the most.*

In Chapter 3 and 4, the complete definitions of oxCaisson-LE for homogeneous and non-homogeneous, linear elastic soil were provided. However, real soil response can only be approximated as being linear elastic at low levels of loading. In this chapter, oxCaisson-LE is extended to allow for non-linear, elastic predictions. Specifically, a set of small-strain, non-linear elastic soil reactions are defined to better correspond to the observed soil behaviour in laboratory tests.

6.1 Introduction

It is widely known that real soils exhibit non-linear stress-strain behaviour, where the soil stiffness decreases with increasing strain (Atkinson 2000). There has been a lot of work done to describe the non-linear stress-strain behaviour of soil (Hardin & Drnevich 1972, Fahey & Carter 1993, Vardanega & Bolton 2013, Oztoprak & Bolton 2013) and this is most commonly described in terms of the variation of the secant shear modulus G with strain. For example, Hardin & Drnevich (1972) proposed the following one-parameter model to describe the reduction of G with increasing shear strain γ for sand and clay:

$$\frac{G}{G_0} = \frac{1}{1 + \left(\frac{\gamma}{\gamma_{\mathrm{ref}}}\right)} \tag{6.1}$$

where G_0 (also known as G_{max}) is the initial shear modulus and γ_{ref} is the reference shear strain, which governs the shape of the stiffness degradation curve.

Darendeli (2001) proposed a two-parameter variant of Eq. 6.1 to better match his laboratory test data on sand and clay:

$$\frac{G}{G_0} = \frac{1}{1 + \left(\frac{\gamma}{\gamma_{\mathrm{ref}}}\right)^{\kappa}} \tag{6.2}$$

where the reference shear strain γ_{ref} and the non-linearity parameter κ governs the shape of the stiffness degradation curve. Based on his analyses, Darendeli (2001) obtained a best-fit value for κ that ranges from 0.8 to 0.9 for sand and 0.9 to 1.0 for clay and silt. Furthermore, γ_{ref}, which is the shear strain at which $G/G_0 = 0.5$, was found to be dependent on the plasticity index (PI), overconsolidation ratio (OCR) and the mean confining stress.

Eq. 6.2 was later adopted by Vardanega & Bolton (2013) to describe the stiffness degradation of a large database of clay and silts. Based on their analyses, the best-fit value for κ ranges from 0.5 to 0.88 for clay (excluding the London Clay outliers) and 0.73 to 0.94 for silt. As for γ_{ref},Vardanega & Bolton (2013) define it as being solely dependent on PI. In a follow-up work, Vardanega & Bolton (2014) found insignificant influence of OCR on γ_{ref}, which contrasts with the findings of Darendeli (2001). Oztoprak & Bolton (2013) also used a similar equation to Eq. 6.2 to describe a large database of laboratory test results for sand.

Given that soil stiffness starts to degrade at small strains, it is important to consider the non-linear soil behaviour for soil–structure interaction problems. For soil-pile interaction problems, the non-linear soil behaviour is considered by incorporating some form of non-linearity within the design methods used for pile designs. For example, the commonly used *p*-*y* design method (API 2002, DNV 2013) for laterally loaded piles define a non-linear elastic relationship between the lateral soil reaction p and the local displacement y, which approximates the non-linear stress-strain response of the soil.

Previous numerical studies (Bransby 1999, Zhang & Andersen 2017) on laterally loaded piles found that the *p*-*y* response is a scaled version of the stress-strain behaviour of a soil element. This finding was first made by Bransby (1999) through comparison of the *p*-*y* response (from plane strain finite element analyses of a laterally loaded pile slice) with the stress-strain constitutive relationship of the soil model, which is based on a power law:

$$q = a\varepsilon_{\mathrm{q}}^{\mathrm{b}} \tag{6.3}$$

where q is the deviatoric stress, ε_{q} is the deviatoric strain and a and b are constants. In this study, Bransby (1999) found that the *p*-*y* response is identical to the stress-strain relationship, after the normalised displacement (y/D) has been suitably scaled:

$$\frac{y}{D} = \beta \varepsilon_{\mathrm{q}} \tag{6.4}$$

where D is the pile diameter and β is some scaling factor. This means that site-specific p-y curves can be generated directly from the stress-strain behaviour of soil samples in laboratory tests through a simple change of variables. Using Eqs. 6.3, 6.4 and the assumed relationship $p/D = q$, the site-specific p-y response for a laterally loaded pile in this soil is:

$$\frac{p}{D} = a\left(\frac{y}{D}\frac{1}{\beta}\right)^{b} \tag{6.5}$$

Similarly, Zhang & Andersen (2017) found that the p-y response obtained from their 3DFE analyses of a laterally loaded pile slice in an elasto-plastic soil can be scaled to match the stress-strain behaviour of a soil element. In their study, the scaling relationships obtained were $p/p_{\mathrm{u}} = \tau/s_{\mathrm{u}}$ and $y/D = \xi_1\gamma_{\mathrm{e}} + \xi_2\gamma_{\mathrm{p}}$, where $p_{\mathrm{u}}, s_{\mathrm{u}}, \gamma_{\mathrm{e}}, \gamma_{\mathrm{p}}$ are the maximum value of p, undrained shear strength, elastic shear strain and plastic shear strain respectively and ξ_1, ξ_2 are scaling factors.

The existence of scaling relationships is not exclusive to deep foundations or numerical studies. For example, Atkinson (2000) found scaling relationships between the stress-strain behaviour of soil samples in laboratory tests and the load-settlement behaviour of surface foundations in field tests. Osman et al. (2007) also obtained scaling relationships between the stress-strain behaviour of a soil element and the load-displacement behaviour of a surface foundation bearing on Tresca soil in their 3DFE analyses.

As past research has shown that soil stiffness decreases with increasing strain, this limits the applicability of oxCaisson-LE to low load levels where the soil response can be approximated as linear elastic or for cases where a representative G can be assumed. To extend the applicability of oxCaisson-LE to higher load levels, the model must consider the non-linear soil behaviour for more realistic predictions. While there are scaling relationships derived in previous work, they are not directly applicable for oxCaisson-LE as they were derived assuming plane strain conditions, which do not apply for caissons with low L/D ratios. Furthermore, these relationships are restricted to the lateral soil reactions only.

To address this issue, this chapter derives a set of non-linear soil reactions, that were calibrated against 3DFE analyses of rigid caissons in small-strain, non-linear elastic soil.

These non-linear soil reactions were derived by finding mapping relationships between the soil reactions displacement space and the soil element strain space. These non-linear soil reactions are incorporated in a new, non-linear elastic Winkler model, called 'oxCaisson-NLE', for more realistic predictions of caisson behaviour at higher load levels.

6.2 Methodology

This section describes the 3DFE modelling carried out in this study. The 3DFE model implemented in this study is the same as that described in Chapter 3 (including the boundary conditions), except for the soil model, which is small-strain, non-linear elastic here. The foundation diameter D and skirt thickness d_{skirt} were held constant at unit length and $0.005D$ respectively, while five skirt lengths ($L/D = 0, 0.25, 0.5, 1, 2$) were analysed.

6.2.1 Material Properties

The soil model used for the 3DFE analyses is a custom, non-linear elastic constitutive model based on the small-strain, non-linear behaviour described by Eq. 6.2. This empirical relationship was adopted as it is widely used to model the non-linear stress-strain behaviour of a large variety of soil types, including clay and sand (Darendeli 2001, Vardanega & Bolton 2013). However, it is not ideal to use Eq. 6.2 in its original form as it is expressed in the one-dimensional stress-strain space. Thus, it was generalized to the three-dimensional stress-strain space by redefining it in terms of the deviatoric strain ε_{q} and the deviatoric stress q (in some literature, q and ε_{q} are also known as the von Mises stress and equivalent strain respectively):

$$q = \sqrt{3J_2} \tag{6.6}$$

$$\varepsilon_{\text{q}} = \sqrt{\frac{4}{3}J_2^{\text{e}}} \tag{6.7}$$

where J_2 and J_2^{e} are the second deviatoric stress and strain invariant respectively.

It is straightforward to convert the strain results of the triaxial and simple shear tests into ε_{q}. For a triaxial test, $\varepsilon_{\text{q}} = (2/3)\left|\varepsilon_{\text{a}} - \varepsilon_{\text{r}}\right|$ and for a simple shear test, $\varepsilon_{\text{q}} = \left|\gamma\right| / \sqrt{3}$. Interested readers may refer to Appendix A.2 for the derivations. A key benefit of making G dependent on ε_{q}, instead of γ, is that ε_{q} is an objective strain measure (i.e. independent of the coordinate system adopted). Hence, the adopted, generalised form of Eq. 6.2 for the three-dimensional stress-strain space is:

$$\frac{G}{G_0} = \frac{1}{1 + \left(\frac{\varepsilon_{\mathrm{q}}}{\varepsilon_{\mathrm{q,ref}}}\right)^{\kappa}} \tag{6.8}$$

Besides the strain-dependency of the shear (and bulk) modulus, the other aspects of the soil model is identical to an isotropic, linear hypoelastic constitutive model, with ν being constant.

In the 3DFE model, the soil volume was defined as weightless and homogeneous. The initial shear modulus G_0 of the soil was held constant, while four Poisson's ratios ($\nu = 0, 0.2, 0.4, 0.49$), three $\varepsilon_{\mathrm{q,ref}}$ (0.0001, 0.0005, 0.002) and three κ (0.4, 0.7, 1) were analysed. The three $\varepsilon_{\mathrm{q,ref}}$ and κ values were selected as they approximate the corresponding minimum, mean and maximum values obtained by Vardanega & Bolton (2013).

6.2.2 Validation

To validate that the soil constitutive model has been implemented correctly, a 3DFE model was set up to simulate a triaxial test and an unconsolidated simple shear test. For these analyses, a cubic finite element (first-order, fully-integrated, linear element C3D8) subjected to triaxial or simple shear boundary conditions was simulated and the stress-strain behaviour for that element was computed. Fig. 6.1 shows the stiffness behaviour that resulted from the triaxial test and simple shear test simulations for $\varepsilon_{\mathrm{q,ref}}$ = 0.0005 and κ = 1. Evidently, the computed stress-strain behaviour agrees well with that predicted by Eq. 6.8.

6.3 Results

6.3.1 Effect On Global Caisson Behaviour

Fig. 6.2 shows the 3DFE results for the normalised, global load-displacement behaviour under the displacement boundary conditions shown in Table 3.1, for $L/D = 0.5$, $\nu = 0.2$, $\varepsilon_{\mathrm{q,ref}} = 0.0005$ and $\kappa = 0.7$. As expected, the responses are non-linear. Furthermore, Fig. 6.2e, f shows that the HM-coupling responses, which are symmetric for an elastic soil, deviate at increasing displacements. This is because the same amount of rotation or lateral displacement induce different amounts of ε_{q}, which results in different current shear and bulk moduli.

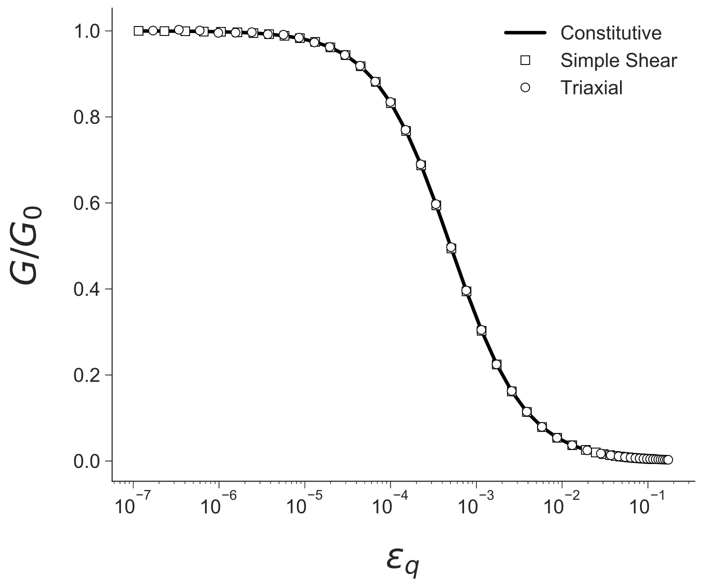

Figure 6.1: Comparison of 3DFE simulation results of triaxial and simple shear tests (for $\varepsilon_{\mathrm{q,ref}} = 0.0005$ and $\kappa = 1$) with the soil constitutive relationship (Eq. 6.8).

6.3.2 Effect On Soil Reactions

Fig. 6.3 shows the soil reactions for $L/D = 0.5$, $\nu = 0.2$, $\varepsilon_{\mathrm{q,ref}} = 0.0005$, $\kappa = 0.7$. Similar to the global responses, both the skirt and base soil reactions are non-linear, with their secant stiffness decreasing with increasing displacement. Fig. 6.4 normalises the secant stiffness of the soil reactions shown in Fig. 6.3 by their linear elastic counterparts (using the 3DFE results of Chapter 3). The normalised secant stiffness in Fig. 6.4 can be observed to decrease with increasing displacement, in a similar manner to the decrease in G/G_0 with increasing strain. However, this does not apply to the hm-coupling soil reactions. For example, Fig. 6.5 shows that $k_{\mathrm{cm}}^{\mathrm{skirt}}$ and $k_{\mathrm{cm}}^{\mathrm{base}}$ do not degrade in a similar manner as G/G_0.

6.3.3 Small-strain, Non-linear Elastic Soil Reactions

Fig. 6.4 suggests that scaling factors may be applied in the displacement space to achieve agreement between the curves. Thus, suitable displacement scaling factors ($\beta_{\mathrm{v}}, \beta_{\mathrm{q}}, \beta_{\mathrm{h}}, \beta_{\mathrm{m}}$) were identified for each soil reaction in Fig. 6.4 using LS regression, where $\beta_{\mathrm{v}}, \beta_{\mathrm{q}}, \beta_{\mathrm{h}}, \beta_{\mathrm{m}}$ represent the scaling factors for $s_{\mathrm{z}}, \theta_{\mathrm{z}}, s_{\mathrm{y}}$ (and s_{x}), θ_{x} (and θ_{y}) respectively. Note that different displacement scaling factors were identified for the skirt and base soil reactions (i.e. the displacement scaling factor β_{v} for $k_{\mathrm{v}}^{\mathrm{skirt}}$ is different from that of $k_{\mathrm{v}}^{\mathrm{base}}$). Fig. 6.6 compares the normalised secant stiffness of the soil reactions with G/G_0, after applying these scaling factors. Evidently, there is now excellent agreement between the curves. This shows that

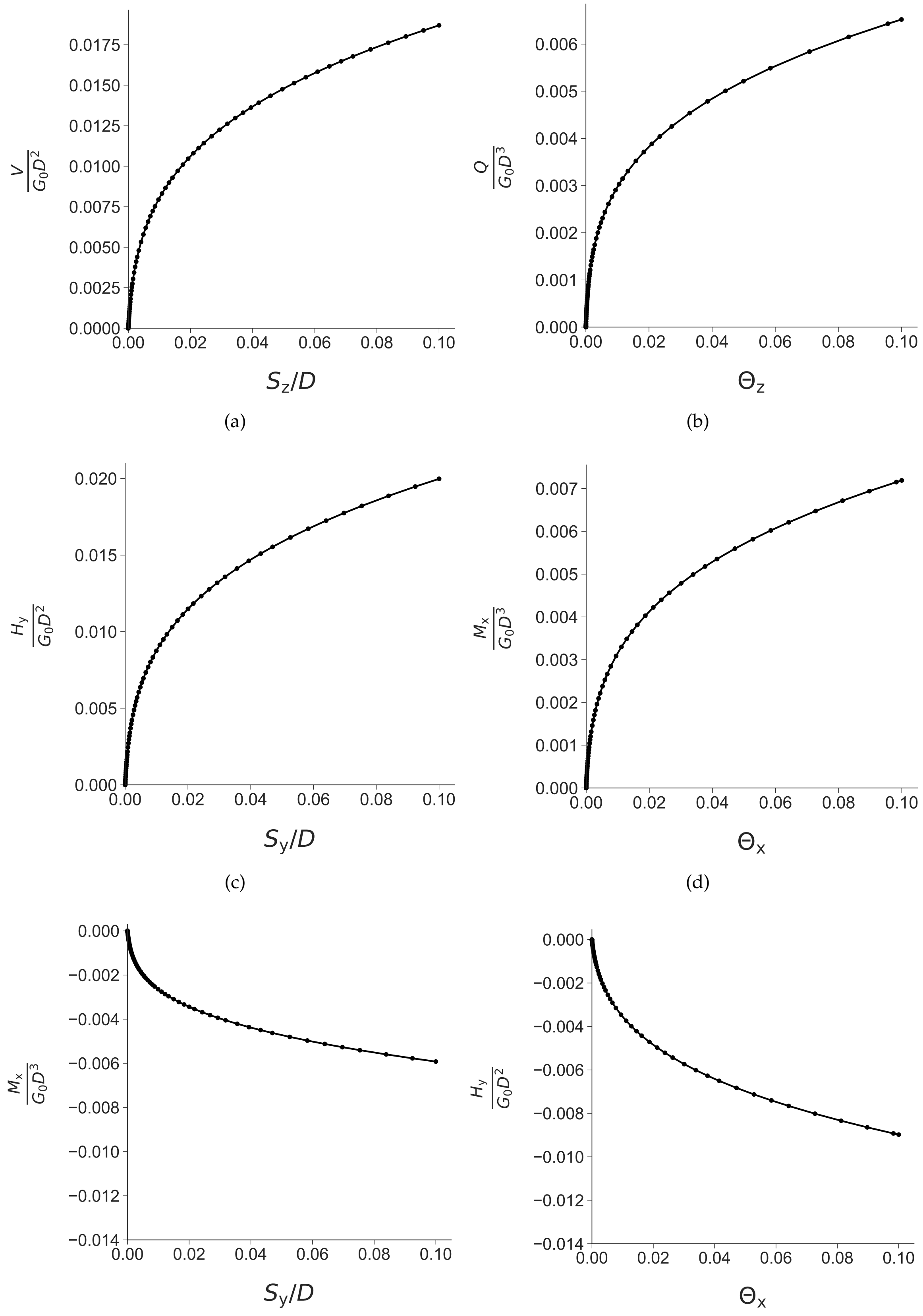

(a) (b)

(c) (d)

(e) (f)

Figure 6.2: The 3DFE results for the normalised, global load-displacement behaviour of suction caissons in small-strain, non-linear elastic soil under the displacement boundary conditions shown in Table 3.1, for $\nu = 0.2$, $\varepsilon_{q,\text{ref}} = 0.0005$, $\kappa = 0.7$ and $L/D = 0.5$. Note the non-zero y-axis origin for (e) and (f).

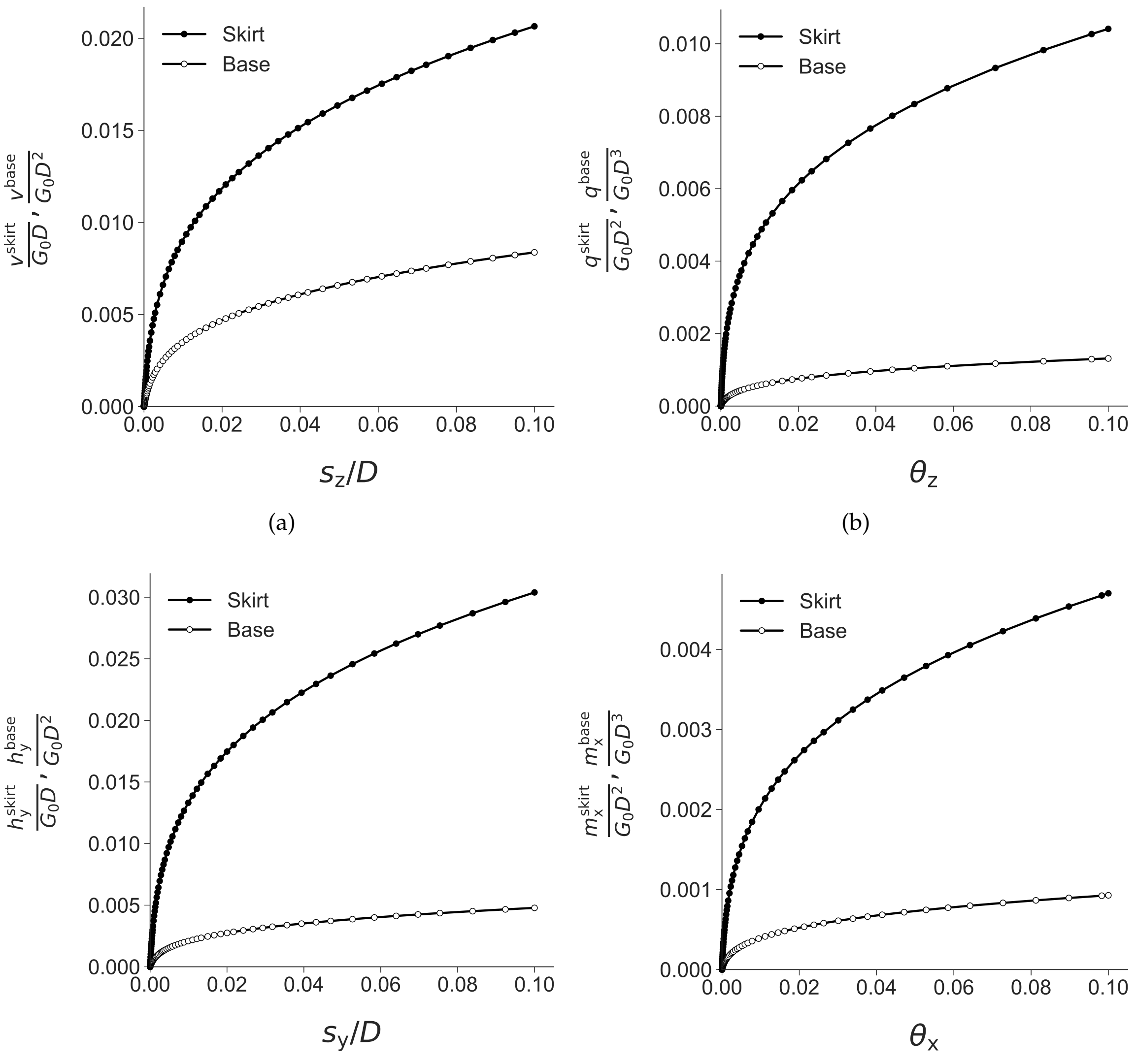

(a)

(b)

(c)

(d)

Figure 6.3: Normalised load-displacement behaviour of the skirt and base soil reactions for $\nu = 0.2$, $\varepsilon_{\text{q,ref}} = 0.0005$, $\kappa = 0.7$ and $L/D = 0.5$.

the normalised secant stiffness are just scaled versions of G/G_0.

Definition 6.2 (Equivalent deviatoric strain) *Equivalent deviatoric strain* $\varepsilon_{\text{q,eq}}$ *refers to the equivalent amount of deviatoric strain induced by a normalised displacement (e.g.* s_z/D*). This can be found by applying displacement scaling factors* β *to the normalised displacements. For vertical or torsional displacements,* $\varepsilon_{\text{q,eq}} = \beta_{\text{v}} \, |s_z/D|$ *or* $\beta_{\text{q}} \, |\theta_z|$ *respectively. For lateral or rotational displacements,* $\varepsilon_{\text{q,eq}} = \beta_{\text{h}} \sqrt{{s_x}^2 + {s_y}^2}/D$ *or* $\beta_{\text{m}} \sqrt{{\theta_x}^2 + {\theta_y}^2}$ *respectively.*

Therefore, the behaviour of the soil reactions for small-strain, non-linear elastic soil can

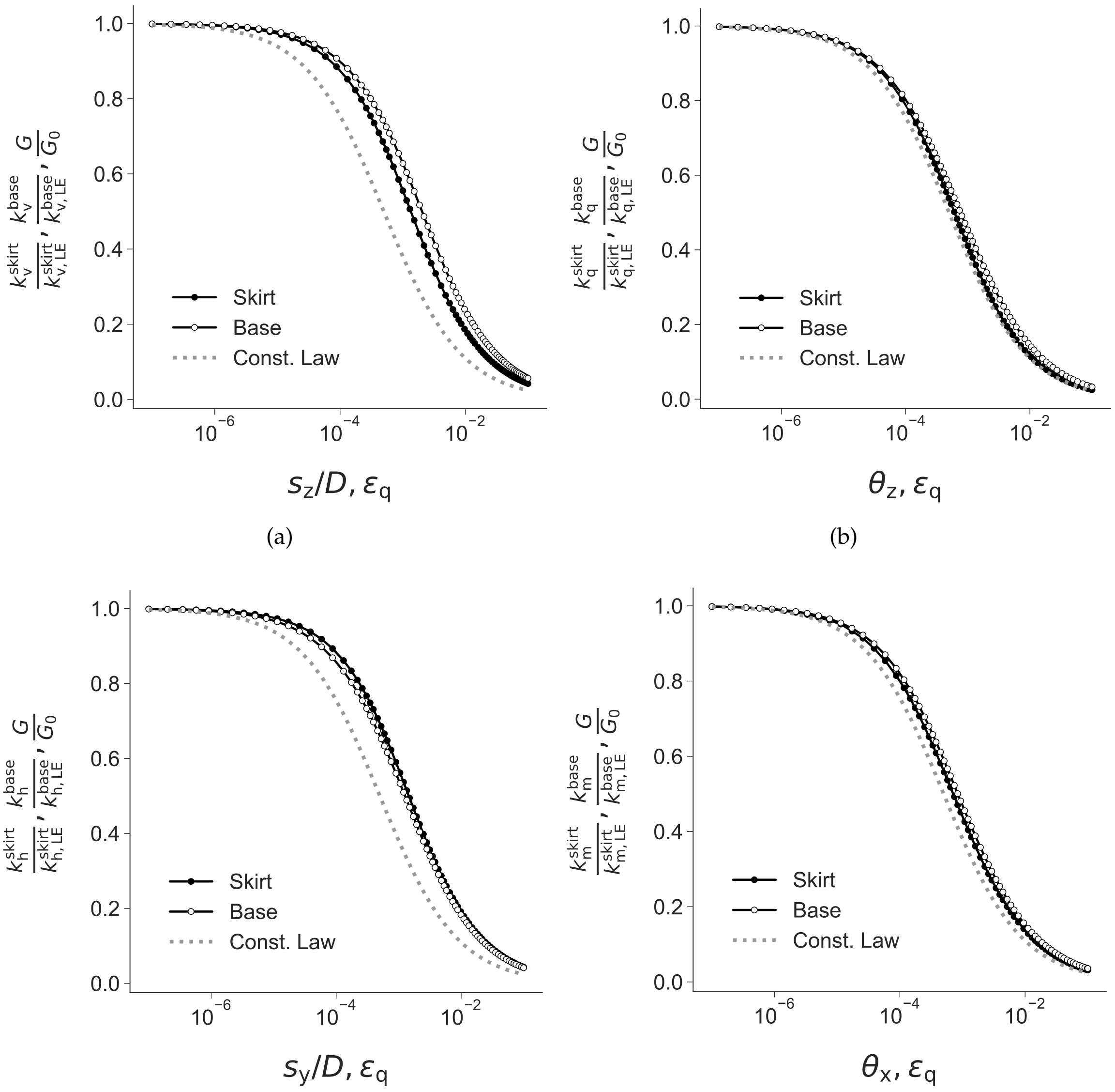

(a) (b)

(c) (d)

Figure 6.4: Secant stiffness of the skirt and base soil reactions, normalised by their linear elastic counterparts, for $\nu = 0.2$, $\varepsilon_{\text{q,ref}} = 0.0005$, $\kappa = 0.7$ and $L/D = 0.5$. The soil constitutive relationship (Eq. 6.8) is also plotted here.

be described using Eq. 6.8 with a simple change of variables ($\frac{G}{G_0} \rightarrow \frac{\chi}{\chi_{\text{LE}}}$ and $\varepsilon_{\text{q}} \rightarrow \varepsilon_{\text{q,eq}}$):

$$\frac{\chi}{\chi_{\text{LE}}} = \frac{1}{1 + \left(\frac{\varepsilon_{\text{q,eq}}}{\varepsilon_{\text{q,ref}}}\right)^{\kappa}} \tag{6.9}$$

where χ, χ_{LE} are the secant stiffness of the non-linear and linear soil reactions respectively.

With a slight manipulation of Eq. 6.9, the secant stiffness of the soil reactions for small-strain, non-linear elastic soil can be defined as:

$$\chi = \frac{\chi_{\text{LE}}}{1 + \left(\frac{\varepsilon_{\text{q,eq}}}{\varepsilon_{\text{q,ref}}}\right)^{\kappa}} \tag{6.10}$$

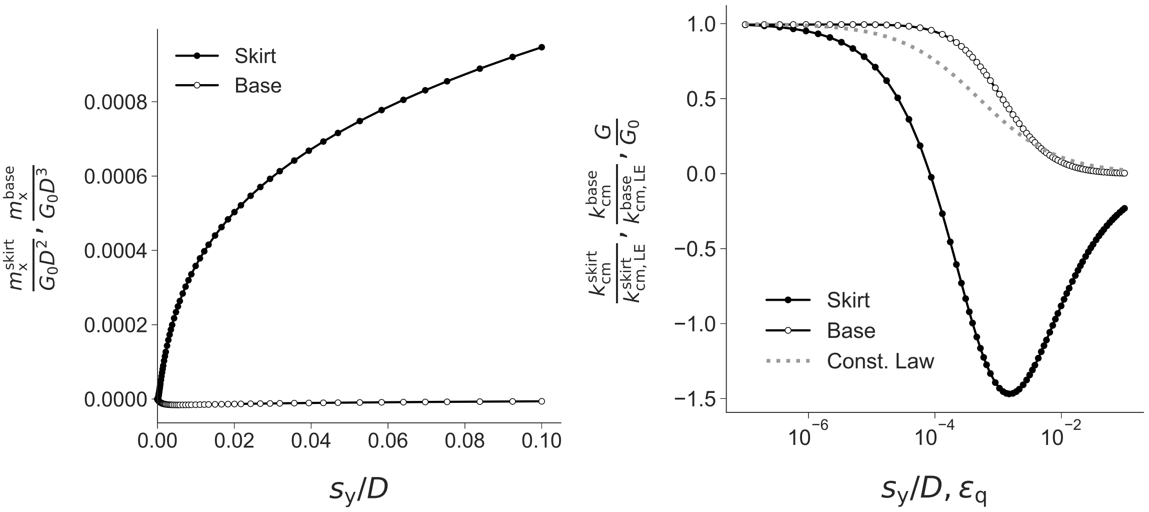

(a)

(b)

Figure 6.5: (a) Normalised, load-displacement behaviour of the skirt and base moment coupling soil reactions (b) Secant stiffness of the skirt and base moment coupling soil reactions, normalised by their linear elastic counterparts, for $\nu = 0.2$, $\varepsilon_{q,ref} = 0.0005$, $\kappa = 0.7$ and $L/D = 0.5$. The soil constitutive relationship (Eq. 6.8) is plotted in (b).

where χ_{LE} can be obtained from Eqs. 3.12 to 3.17 and Eqs. 3.20 to 3.25. For example, using Eq. 3.12, the secant stiffness for the linear and non-linear vertical skirt soil reactions are:

$$k_{v,LE}^{skirt} = \hat{h}_1(10.8, 14.4, 4.2, 5.2, 5, 5.8)G_0 \tag{6.11}$$

$$k_{v}^{skirt} = \hat{h}_1(10.8, 14.4, 4.2, 5.2, 5, 5.8)\frac{G_0}{1 + \left(\frac{\beta_v |s_z/D|}{\varepsilon_{q,ref}}\right)^{\kappa}} \tag{6.12}$$

The key insight of Eq. 6.10 is that the secant stiffness of the soil reactions for small-strain, non-linear elastic soil can be obtained directly from the stiffness formulations for linear elastic soil reactions, simply by replacing the linear elastic G with the strain dependent G (using Eq. 6.8) and finding the equivalent deviatoric strain $\varepsilon_{q,eq}$ using the displacement scaling factors β. For simplicity, the secant stiffness of the *hm*-coupling soil reactions (i.e. k_c^{skirt} and k_c^{base} in Eqs. 3.28 and 3.29) are degraded rapidly such that they have negligible contributions at increasing displacements. Thus, the displacement scaling factor β_c is set to a high value of 1000 for k_c^{skirt} and k_c^{base}. It will be shown later in the validation section that this assumption results in reasonably accurate global load-displacement predictions.

6.3.4 Displacement Scaling Factors β

LS regression was carried out to determine the best-fit displacement scaling factors β for the 3DFE results corresponding to the inputs in Table 6.1. It was found that $\varepsilon_{q,ref}$ has negligible effect on the resultant β. Thus, β are dependent only on L/D, ν and κ.

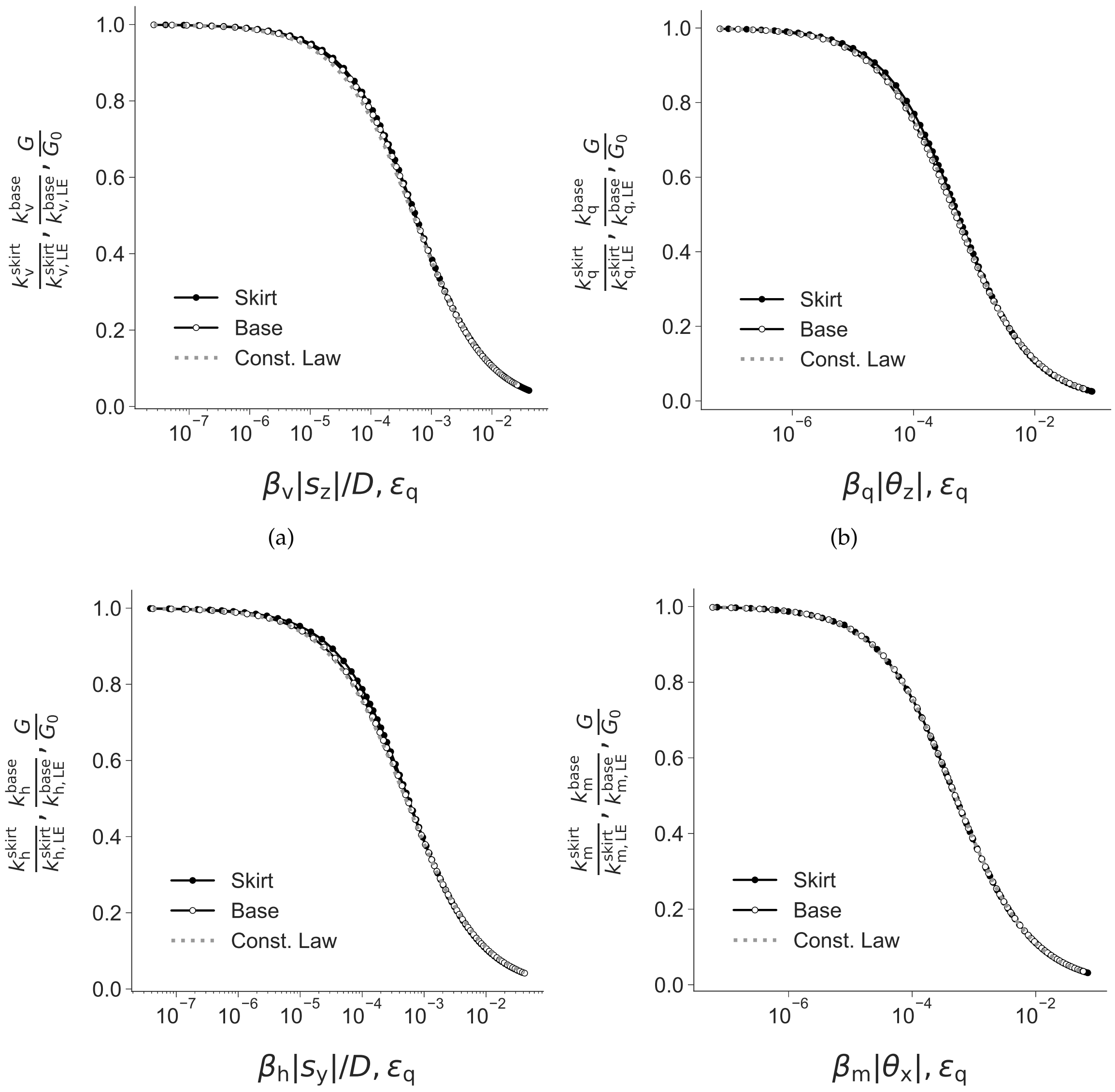

(a) (b)

(c) (d)

Figure 6.6: Secant stiffness of the skirt and base soil reactions, normalised by their linear elastic counterparts, after applying the displacement scaling factors $(\beta_v, \beta_q, \beta_h, \beta_m)$, for $\nu = 0.2$, $\varepsilon_{q,ref} = 0.0005$, $\kappa = 0.7$ and $L/D = 0.5$. The soil constitutive relationship (Eq. 6.8) is also plotted here.

Table 6.1: 3DFE input parameters for the dataset used for the computation of best-fit displacement scaling factors for the skirt and base soil reactions

	Values analysed
L/D	0, 0.25, 0.5, 1, 2
ν	0, 0.2, 0.4, 0.49
α	0.4, 0.7, 1
$\varepsilon_{q,ref}$	0.0001, 0.0005, 0.002

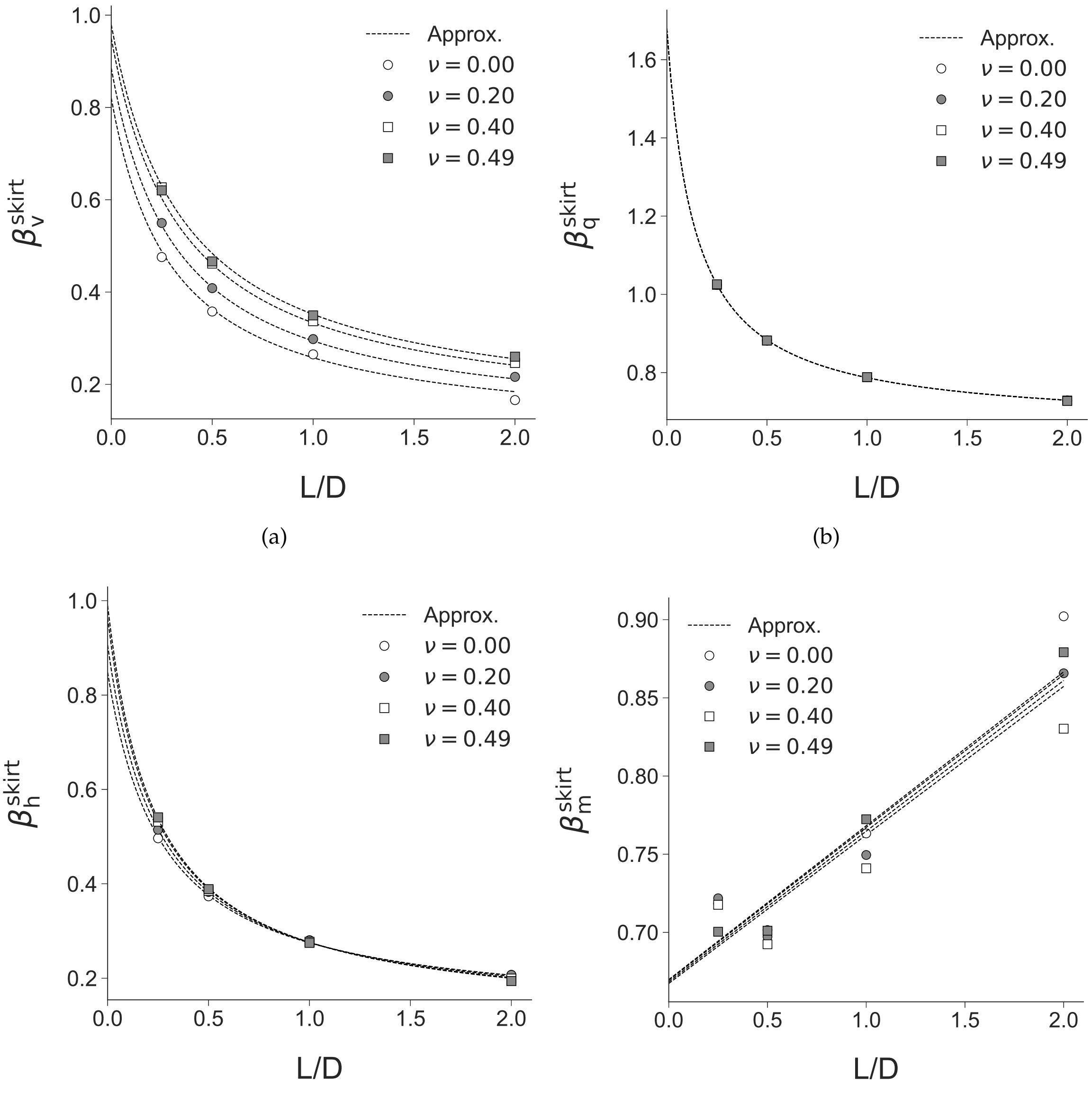

(a) (b)

(c) (d)

Figure 6.7: Variations of best-fit displacement scaling factors ($\beta_{\mathrm{v}}^{\mathrm{skirt}}, \beta_{\mathrm{q}}^{\mathrm{skirt}}, \beta_{\mathrm{h}}^{\mathrm{skirt}}, \beta_{\mathrm{m}}^{\mathrm{skirt}}$) for the skirt soil reactions with respect to ν and L/D for $\kappa = 0.7$. The dotted lines represent the predictions of the approximating functions.

Fig. 6.7 shows the variations of the best-fit displacement scaling factors for the skirt soil reactions ($\beta_{\mathrm{v}}^{\mathrm{skirt}}, \beta_{\mathrm{q}}^{\mathrm{skirt}}, \beta_{\mathrm{h}}^{\mathrm{skirt}}, \beta_{\mathrm{m}}^{\mathrm{skirt}}$) with L/D and ν for $\kappa = 0.7$. $\beta_{\mathrm{v}}^{\mathrm{skirt}}, \beta_{\mathrm{q}}^{\mathrm{skirt}}, \beta_{\mathrm{h}}^{\mathrm{skirt}}$ tend to decrease with L/D, while $\beta_{\mathrm{m}}^{\mathrm{skirt}}$ increases with L/D. $\beta_{\mathrm{v}}^{\mathrm{skirt}}, \beta_{\mathrm{h}}^{\mathrm{skirt}}$ generally increase with ν, $\beta_{\mathrm{q}}^{\mathrm{skirt}}$ is independent of ν and no consistent trend with ν was found for $\beta_{\mathrm{m}}^{\mathrm{skirt}}$.

Similarly, Fig. 6.8 shows the variations of the best-fit scaling factors for the base soil reactions ($\beta_{\mathrm{v}}^{\mathrm{base}}, \beta_{\mathrm{q}}^{\mathrm{base}}, \beta_{\mathrm{h}}^{\mathrm{base}}, \beta_{\mathrm{m}}^{\mathrm{base}}$) with L/D and ν for $\kappa = 0.7$. Like their skirt counterparts, $\beta_{\mathrm{v}}^{\mathrm{base}}, \beta_{\mathrm{q}}^{\mathrm{base}}, \beta_{\mathrm{h}}^{\mathrm{base}}$ were found to decrease with L/D, while $\beta_{\mathrm{m}}^{\mathrm{base}}$ tend to increase with L/D. $\beta_{\mathrm{v}}^{\mathrm{base}}$ decreases with ν, $\beta_{\mathrm{q}}^{\mathrm{base}}$ is independent of ν, $\beta_{\mathrm{h}}^{\mathrm{skirt}}$ increases with ν (albeit marginally) and no consistent trend with ν was found for $\beta_{\mathrm{m}}^{\mathrm{base}}$.

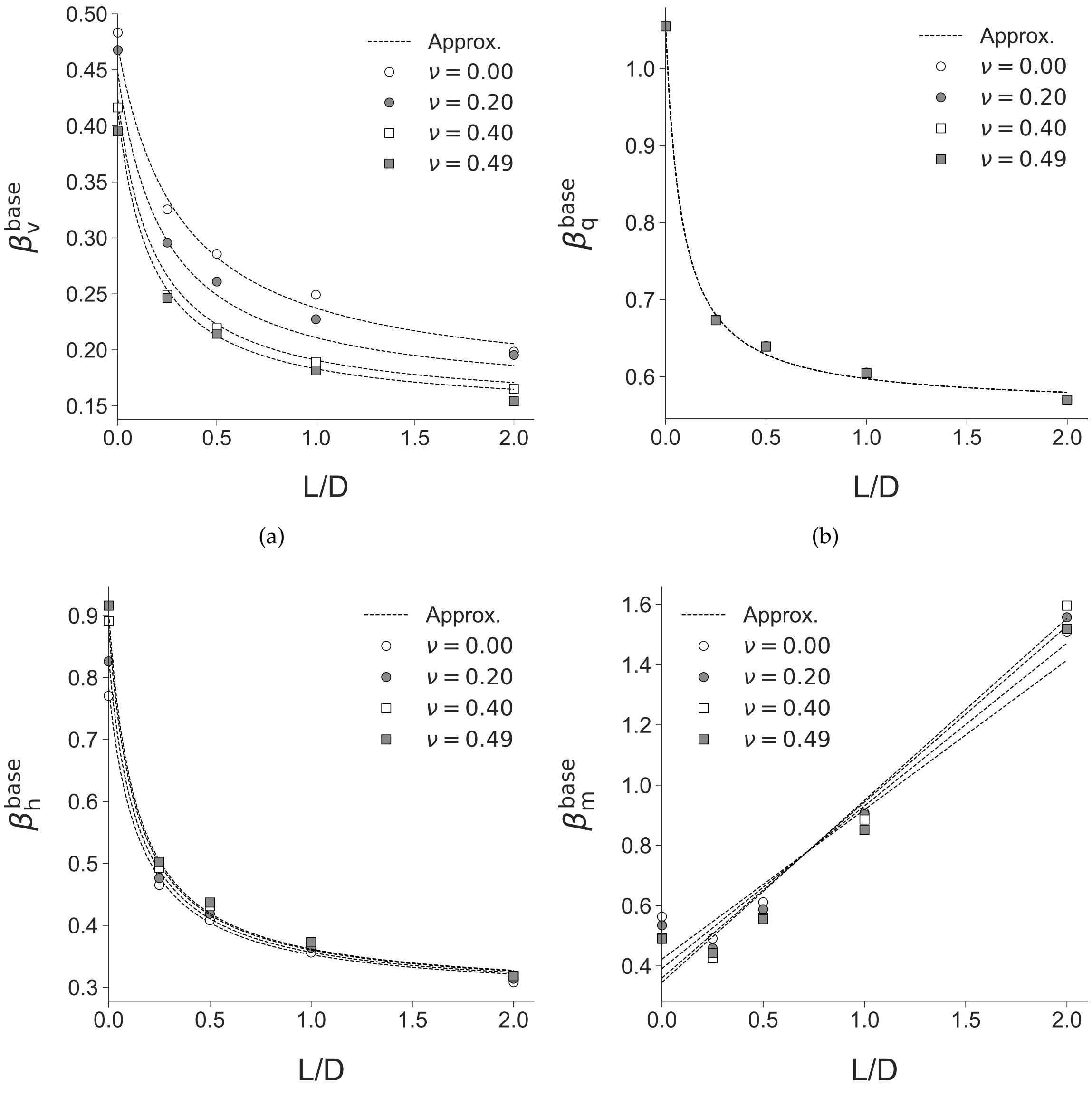

(a) (b)

(c) (d)

Figure 6.8: Variations of best-fit displacement scaling factors ($\beta_v^{base}, \beta_q^{base}, \beta_h^{base}, \beta_m^{base}$) for the base soil reactions with respect to ν and L/D for $\kappa = 0.7$. The dotted lines represent the predictions of the approximating functions.

Figs. 6.9 and 6.10 show the variations of the best-fit displacement scaling factors for the skirt and base soil reactions with L/D and κ for $\nu = 0.2$. For both the skirt and base displacement scaling factors, $\beta_v, \beta_q, \beta_h$ were found to decrease with L/D, while β_m tends to increase with L/D. Furthermore, $\beta_v, \beta_q, \beta_h, \beta_m$ all increase with κ.

To identify approximating functions to predict these displacement scaling factors, two functional forms were found to be suitable for all of the displacement scaling factors:

$$\hat{\beta}_1(L, D, \nu, \alpha, a_1, \ldots, a_9) = (a_1 + a_2\nu + a_3\kappa) + \frac{a_4 + a_5\nu + a_6\kappa}{(a_7 + a_8\nu + a_9\kappa)\frac{L}{D} + 1} \tag{6.13}$$

$$\hat{\beta}_2(L, D, \nu, \alpha, a_1, \ldots, a_6) = (a_1 + a_2\nu + a_3\kappa) + (a_4 + a_5\nu + a_6\kappa)\frac{L}{D} \tag{6.14}$$

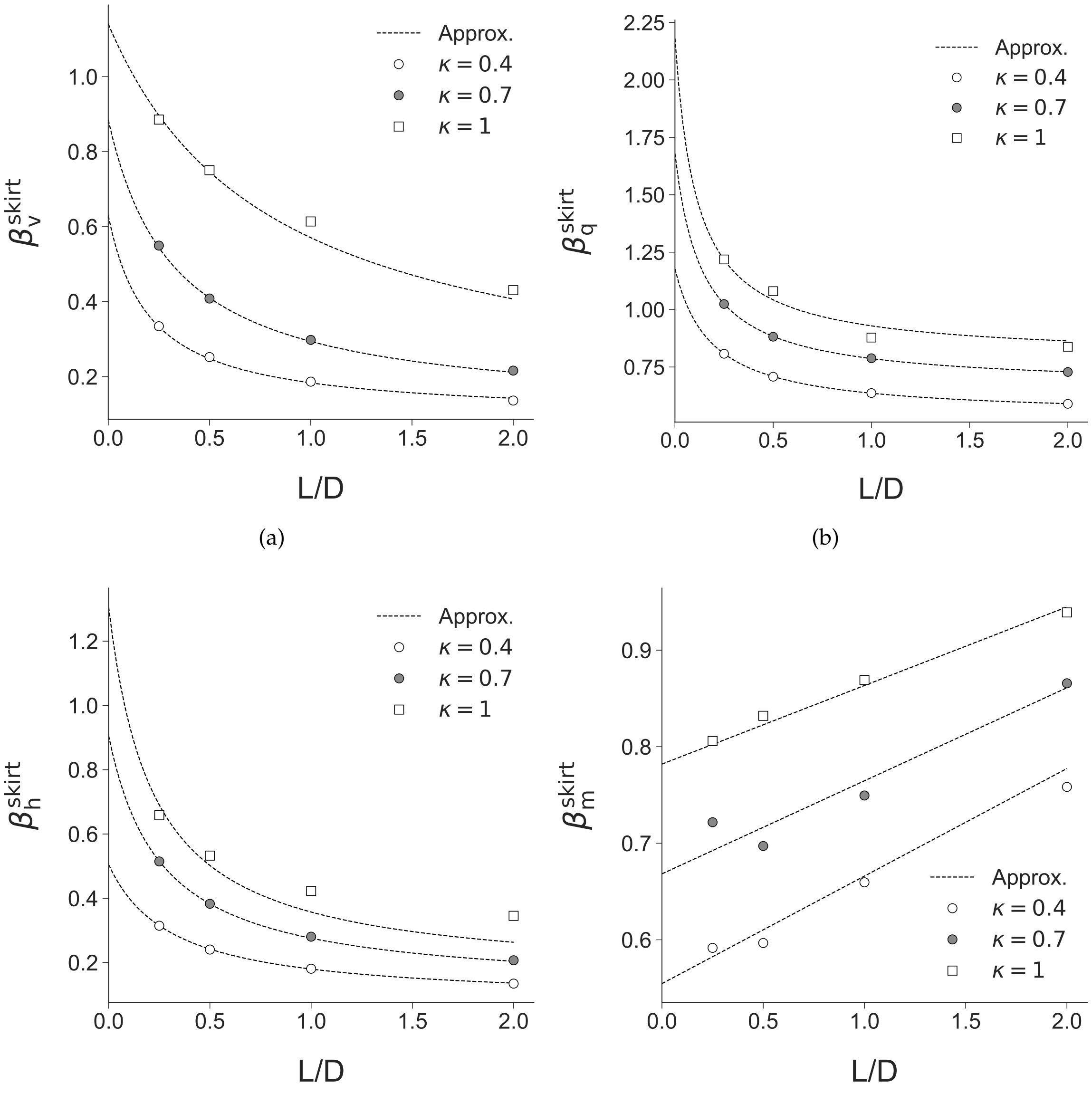

(a) (b)

(c) (d)

Figure 6.9: Variations of best-fit displacement scaling factors (β_v^{skirt}, β_q^{skirt}, β_h^{skirt}, β_m^{skirt}) for the skirt soil reactions with respect to κ and L/D for $\nu = 0.2$. The dotted lines represent the predictions of the approximating functions.

where Eq. 6.14 is used for β_m and β_m^{base}, while Eq. 6.13 is used for the rest.

The unknown parameters in Eqs. 6.13 and 6.14 were identified by carrying out LS regression against the computed displacement scaling factors. From the regression results, the best-fit parameters for the skirt and base soil reactions were identified and listed in Tables 6.2 and 6.3. For comparison, the displacement scaling factors approximated by Eqs. 6.13 and 6.14 using the best-fit parameters in Tables 6.2 and 6.3 are also shown in Figs 6.7 to 6.10 as dashed lines. It is evident that the approximating functions match the computed displacement scaling factors reasonably well.

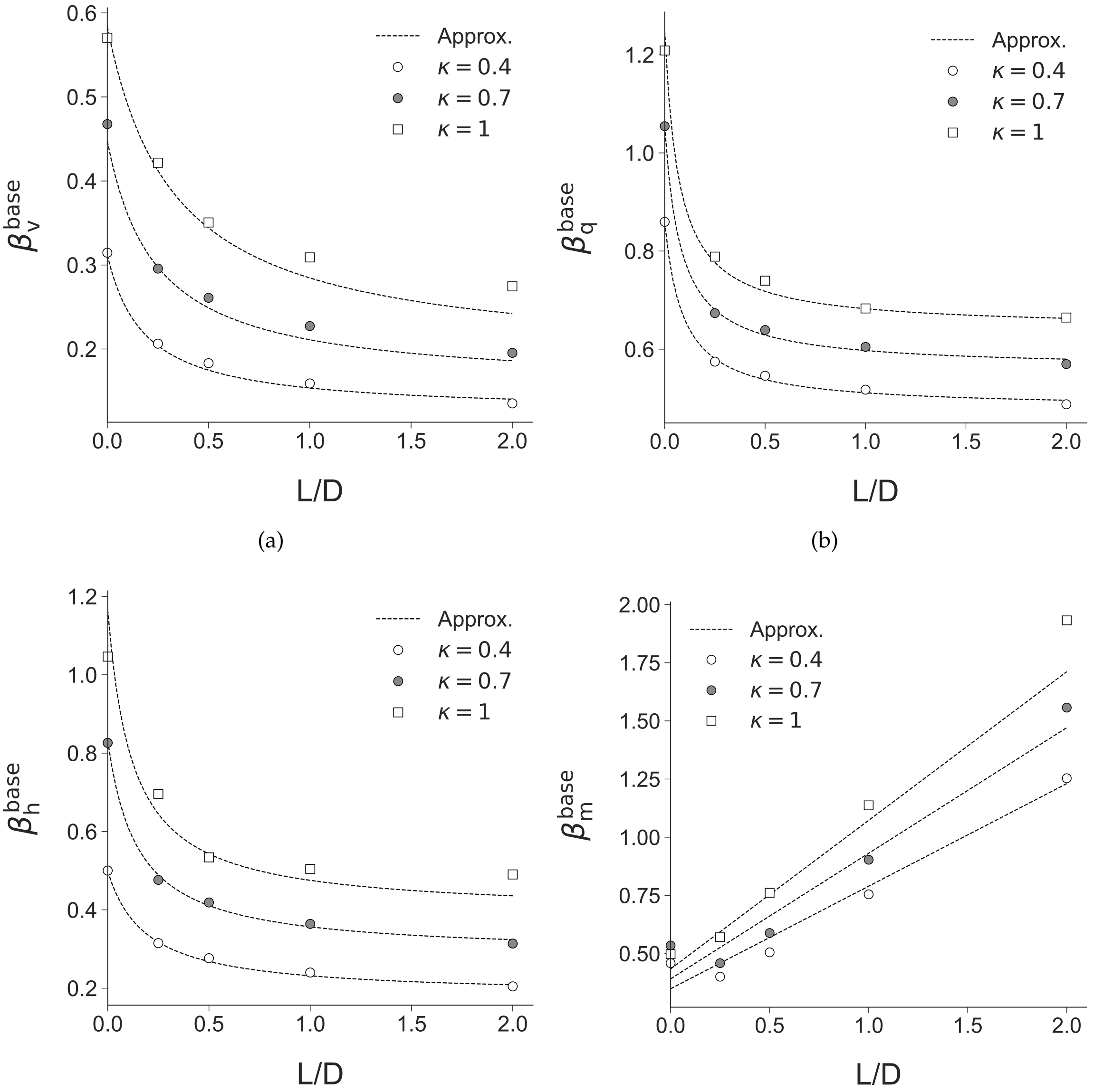

(a) (b) (c) (d)

Figure 6.10: Variations of best-fit displacement scaling factors ($\beta_v^{base}, \beta_q^{base}, \beta_h^{base}, \beta_m^{base}$) for the base soil reactions with respect to κ and L/D for $\nu = 0.2$. The dotted lines represent the predictions of the approximating functions.

6.3.5 Validation

A new, non-linear elastic version of oxCaisson, called 'oxCaisson-NLE', has been developed, where its non-linear elastic soil reactions are determined using Eq. 6.10 and the equivalent deviatoric strains are computed using the displacement scaling factors approximated by Eqs. 6.13 and 6.14 (using the best-fit parameters in Tables 6.2 and 6.3).

To verify if oxCaisson-NLE can reproduce the 3DFE global response, Fig. 6.11 compares the global responses predicted by oxCaisson-NLE, with the 3DFE results shown in Fig. 6.2. It is clear that they agree very well, albeit less so for the H-coupling response (see Fig. 6.11f).

Table 6.2: Best-fit parameters in Eq. 6.13 for the displacement scaling factors for the skirt and base soil reactions

	a_1	a_2	a_3	a_4	a_5	a_6	a_7	a_8	a_9
$\beta_{\mathrm{v}}^{\mathrm{skirt}}$	0.066	0.072	0.032	0.158	0.252	0.82	7.63	-1.17	-6.16
$\beta_{\mathrm{q}}^{\mathrm{skirt}}$	0.367	0	0.424	0.141	0	1.25	3.04	0	6.01
$\beta_{\mathrm{h}}^{\mathrm{skirt}}$	0.038	-0.028	0.116	-0.125	0.316	1.22	2.13	1.03	2.21
$\beta_{\mathrm{v}}^{\mathrm{base}}$	0.092	-0.041	0.1	0.062	-0.076	0.351	5.99	5.40	-4.04
$\beta_{\mathrm{q}}^{\mathrm{base}}$	0.371	0	0.271	0.228	0	0.379	8.97	0	5.03
$\beta_{\mathrm{h}}^{\mathrm{base}}$	0.04	0.007	0.35	-0.035	0.238	0.762	2.96	2.09	4.85

Table 6.3: Best-fit parameters in Eq. 6.14 for the displacement scaling factors for the skirt and base soil reactions

	a_1	a_2	a_3	a_4	a_5	a_6
$\beta_{\mathrm{m}}^{\mathrm{skirt}}$	0.402	0.005	0.379	0.13	0.007	-0.05
$\beta_{\mathrm{m}}^{\mathrm{base}}$	0.323	-0.157	0.142	0.265	0.22	0.33

The key advantage of oxCaisson-NLE is its efficiency. The total time taken to produce the 3DFE results in Fig. 6.11 is 5 hours, while it took only 2 seconds for the oxCaisson-NLE predictions, yielding a computational time savings of 99.99%.

6.4 Discussion

The results show that the non-linear elastic soil reactions are simply scaled versions of the soil element stress-strain behaviour. This is clear from the similarity in functional form between Eqs. 6.8 and 6.9. This similarity allows convenient derivations of site-specific soil reactions that better correspond to soil sample behaviour in laboratory tests, which should result in more realistic predictions of suction caisson behaviour in the field.

6.4.1 Comparison with Previous Work

In previous numerical studies on laterally loaded piles in undrained soil ($\nu = 0.49$), Bransby (1999) proposed a scaling factor for lateral displacement $\beta_{\mathrm{h}}^{\mathrm{skirt}}$ that ranges from 0.14 to 0.5 (depending on the non-linearity of the soil constitutive relationship), while Zhang & Andersen (2017) proposed a constant value of $1/2.8 = 0.36$ (assuming only elastic displacement).

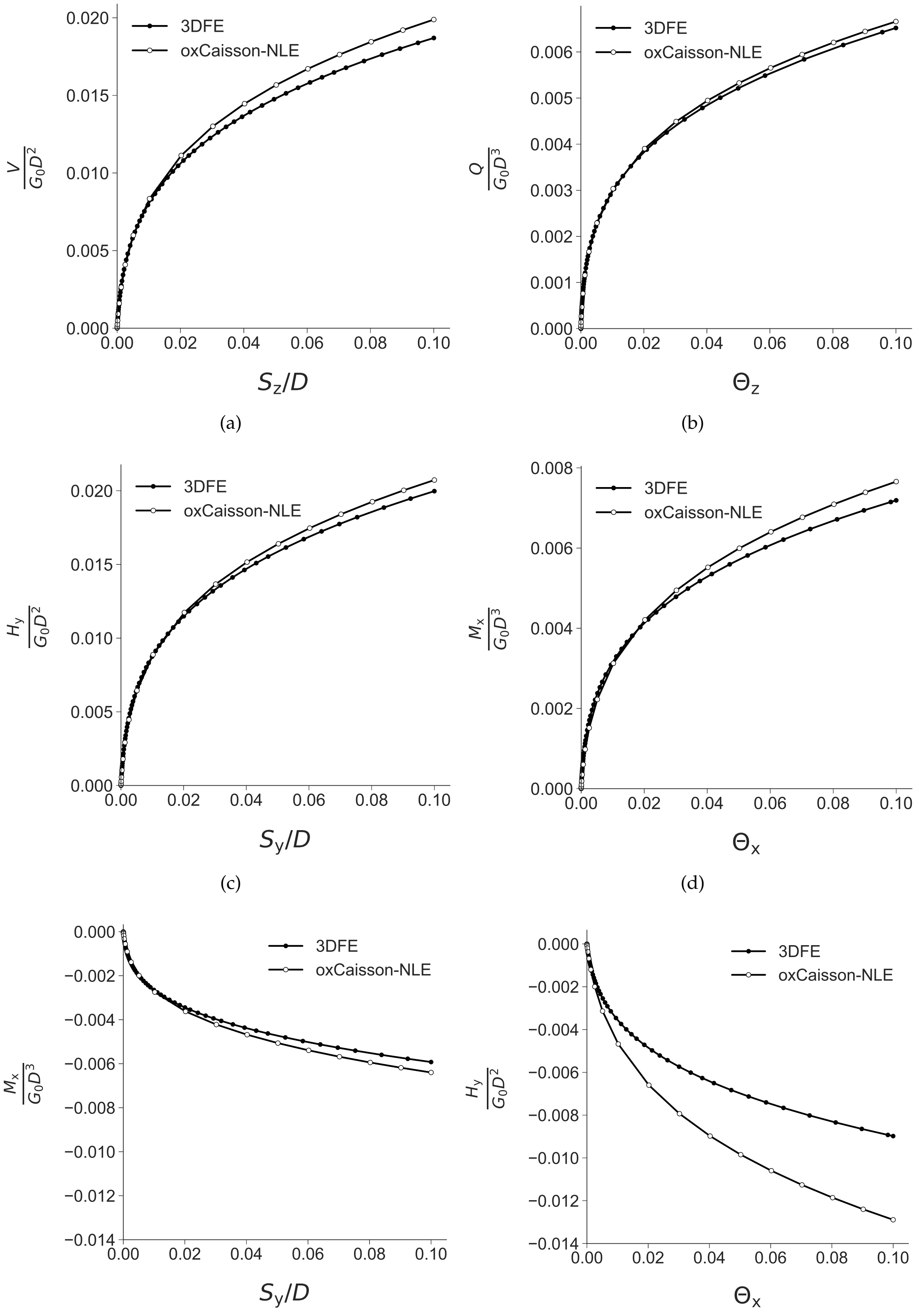

(a)

(b)

(c)

(d)

(e)

(f)

Figure 6.11: Comparison of the normalised, global load-displacement predictions of oxCaisson-NLE with the 3DFE results for $\nu = 0.2$, $\varepsilon_{\mathrm{q,ref}} = 0.0005$, $\kappa = 0.7$ and $L/D = 0.5$. Note the non-zero y-axis origin for (e) and (f).

By comparison, Eq. 6.13 and the best-fit parameters in Table 6.2 suggests a $\beta_{\mathrm{h}}^{\mathrm{skirt}}$ value (for $\nu = 0.49$ and $L/D = 2$) that ranges from 0.13 to 0.26 (depending on κ), which is a closer match to the values proposed by Bransby (1999). The disparity between the suggested $\beta_{\mathrm{h}}^{\mathrm{skirt}}$ values is probably due to the different constitutive relationships employed in the soil model, which differ greatly between this study and those employed by Bransby (1999) and Zhang & Andersen (2017).

6.4.2 Strengths And Limitations

To use the displacement scaling factors in this study or previous studies, the soil stress-strain behaviour in laboratory tests must be described in terms of the employed soil constitutive relationship. For example, the soil stress-strain behaviour must be first described in terms of Eq. 6.3 to get the best-fit a, b parameters, before using the displacement scaling factors proposed by Bransby (1999). A key advantage of the displacement scaling factors proposed in this study is that the soil constitutive relationship employed (Eq. 6.8) is similar to that commonly used to describe the soil stress-strain behaviour in laboratory tests (Eq. 6.2). Only a simple conversion from the triaxial or simple shear strain results to deviatoric strain ε_{q} is needed (see Appendix A.2). If the stress-strain results have been described in terms of Eq. 6.2, the conversion is straightforward. For example, if the best-fit parameters for Eq. 6.2 are $\kappa = 0.7, \gamma_{\mathrm{ref}} = 0.0006$ for simple shear stress-strain results, the corresponding parameters for the non-linear soil reactions are $\kappa = 0.7, \varepsilon_{\mathrm{q,ref}} = 0.0006/\sqrt{3}$. Furthermore, as Eq. 6.2 is used to describe sand and clay laboratory test results, the non-linear soil reaction formulations (Eq. 6.10) can be used for both sand and clay soil profiles.

Nevertheless, there are some limitations with oxCaisson-NLE. First, the displacement scaling factors are appropriate only for individual (or uniaxial) loading. Second, oxCaisson-NLE can only be used to assess monotonic loading, and not cyclic loading. Lastly, oxCaisson-NLE does not have an upper bound response and cannot be used to assess ultimate limit state (ULS) conditions. It should be noted that the bulk of the data used to calibrate Eq. 6.2 in previous work is in the small strain range, which is usually well before failure occurs.

To address the inability of oxCaisson-NLE to assess ULS conditions, the next few chapters explore a new class of Winkler models, where the linear elastic soil reactions are coupled with plastic yield surfaces (which represent the local failure states of the soil).

Chapter 7

Assessment of Numerical Procedures for Determining Failure Envelopes

While Chapters 3 to 6 explored the behaviour of suction caissons in elastic soil, Chapters 7 to 9 deal with caisson behaviour in linear elastic, perfectly plastic soil. The focus is now on determining the elasto-plastic soil reactions that correspond to this representative soil behaviour. Before exploring the derivation of the elasto-plastic soil reactions, the tools that are required for this task are discussed in Chapters 7 and 8. This chapter focuses on the numerical procedures for determining failure envelopes.

Definition 7.1 (Sublevel set) *The m-sublevel set of a function is the set where the function evaluates to less than or equal to a given constant value m. In other words, the m-sublevel set of a function* $f(x_1, \dots, x_n) : \mathbb{R}^n \to \mathbb{R}$ *is defined as the set* C_m *(Boyd & Vandenberghe 2004):*

$$C_m = \{x_1, \dots, x_n \mid f(x_1, \dots, x_n) \leq m\}$$

In the context of conventional elasto-plasticity theory, the 0-sublevel set of a yield function f represents the set of stress states that are within the yield surface (i.e. elastic behaviour).

Definition 7.2 (Level set) *The m-level set of a function is the set where the function takes on a given constant value m. In other words, the m-level set of a function* $f(x_1, \dots, x_n) : \mathbb{R}^n \to \mathbb{R}$ *is defined as the set* C_m^**:*

$$C_m^* = \{x_1, \dots, x_n \mid f(x_1, \dots, x_n) = m\}$$

In the context of conventional elasto-plasticity theory, the 0-level set of a yield function f represents the set of stress states that lie on the yield surface.

Definition 7.3 (Failure envelope) *A failure envelope is a hypersurface that defines the combination of n-dimensional loads ($n \geq 1$) that results in the ultimate limit state (or 'plastic failure' of a foundation). For the special case of a non-hardening plastic material, it is equivalent to the yield surface in the global load $\vec{P}$ space. By convention, a failure envelope is defined as the 0-level set of the yield function f (i.e. $\{\vec{P} \mid f(\vec{P}) = 0\}$).*

This section explores several numerical procedures available for determining failure envelopes. The procedures used to determine failure envelopes and yield surfaces are equivalent for a non-hardening plastic model.

7.1 Introduction

Over the past two decades, there has been significant interest in the failure envelope approach for assessing the ultimate capacity of foundations under combined loading. The advantages of this approach over the classical bearing capacity methods (Terzaghi 1943, Meyerhof 1951, Vesić 1973) are manifold and have been widely discussed (Tan 1990, Nova & Montrasio 1991, Gottardi & Butterfield 1993, Bransby & Randolph 1998, Martin & Houlsby 2000, Houlsby & Byrne 2001, Gourvenec 2007).

The failure envelope approach was first introduced by Roscoe & Schofield (1957) to analyse the interaction between a steel frame and its foundations using envelopes of normalised forces. Since then, it has been widely adopted to represent the results of numerical studies on foundation bearing capacity, for a broad range of foundation types. For example, failure envelopes have been determined for surface foundations (Bell 1991, Gourvenec 2007, Taiebat & Carter 2000, 2010, Vulpe et al. 2014, Shen et al. 2016, 2017), skirted or caisson foundations (Bransby & Yun 2009, Gourvenec & Barnett 2011, Hung & Kim 2014, Karapiperis & Gerolymos 2014, Gerolymos et al. 2015, Vulpe 2015, Mehravar et al. 2016), spudcan foundations (Zhang et al. 2011) and mudmat foundations (Nouri et al. 2014, Fu et al. 2014, Feng et al. 2014, Dunne & Martin 2017).

However, surprisingly little attention has been paid to the performance of the numerical procedures used to determine these failure envelopes. For example, the displacement probe test is the most widely used procedure to determine these failure envelopes but it is unclear whether it is better than the other procedures. Given recent trends towards bespoke design methods (Byrne et al. 2015), more problem specific failure envelopes may be required and thus, the performance of these numerical procedures becomes important.

This issue is addressed by running a comparative study that evaluates the performance of various numerical procedures for determining undrained failure envelopes of shallow foundations in linear elastic, perfectly plastic (von Mises) soil under total stress conditions.

7.2 Acknowledgements

The author wishes to acknowledge and thank Dr. Helen Dunne for computing the FELA results presented in this chapter. These FELA results are included here for comparison purposes. In addition, the author gratefully acknowledges the valuable feedback from Prof. Chris Martin on the contents of this chapter.

7.3 Numerical Procedures for Determination of Failure Envelopes

The numerical procedures explored in this paper can be categorised into two main groups: displacement-controlled and load-controlled. The displacement-controlled analyses (i.e. displacement probe test, single swipe test, and sequential swipe test) are performed using the three-dimensional (3D) finite element analysis (FEA) software, Abaqus version 6.13 (Dassault Systèmes 2014). The load-controlled analyses (i.e. load probe test) are performed using the 3D finite element limit analysis (FELA) software, OxLim (Makrodimopoulos & Martin 2006, 2007, Martin 2011), which has been used to analyse various bearing capacity problems in plane strain (Martin & White 2012, Mana et al. 2013, Dunne et al. 2015), and more recently in 3D (Dunne & Martin 2017).

In this study, V, H, M refer to vertical, horizontal and moment loading respectively, and S_{z}, S_{y}, Θ_{x} refer to the corresponding vertical, horizontal and rotational displacements (refer to Fig. 7.1 for the adopted sign conventions). Note that H and M refers to H_{y} and M_{x}, but the subscripts are removed for brevity since this chapter looks at planar loading only. Failure envelopes are presented in terms of the normalised loads ($\tilde{V} = \frac{V}{V_0}, \tilde{H} = \frac{H}{H_0}, \tilde{M} = \frac{M}{M_0}$), which refer to the loads normalised by their respective uniaxial capacities (V_0, H_0, M_0), as determined using the same numerical procedure.

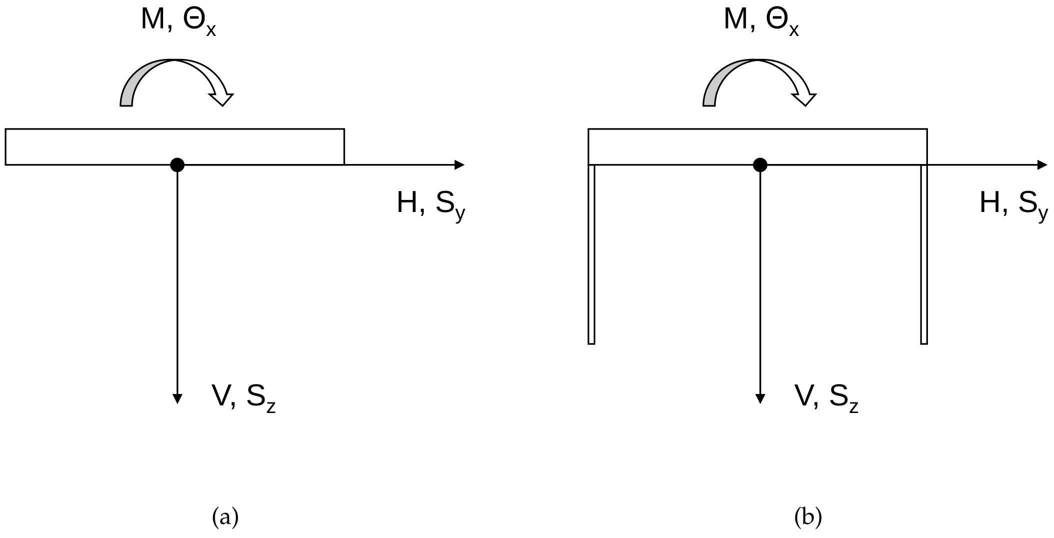

(a) (b)

Figure 7.1: Sign conventions for loads (V, H, M) and displacements (S_y, S_z, Θ_x) (a) Surface foundation (b) Caisson foundation.

7.3.1 Displacement Probe Test

In the displacement probe test, a displacement increment in a prescribed direction is applied to the foundation from a zero load state, with the final (steady) load state determining a single point on the failure envelope. To find the full failure envelope, a series of these probe tests with varying displacement directions must be completed. The displacement probe test has robust convergence properties, and provided that the prescribed displacement magnitude is sufficiently large, a well-defined failure load can be obtained.

However, this approach is relatively inefficient as it only determines a single point on the failure envelope. Furthermore, it does not allow a systematic investigation of the failure envelope, as the load path followed during a displacement probe test is typically non-linear and difficult to predict. For example, the schematic diagram in Fig. 7.2 shows a representative, non-linear load path that occurs during a displacement probe. The initial load path is determined by the elastic foundation stiffness. However, as soil yielding occurs, the foundation stiffness varies and the load path changes direction before arriving at the failure envelope and settling to a steady load state as the displacements continue to increase.

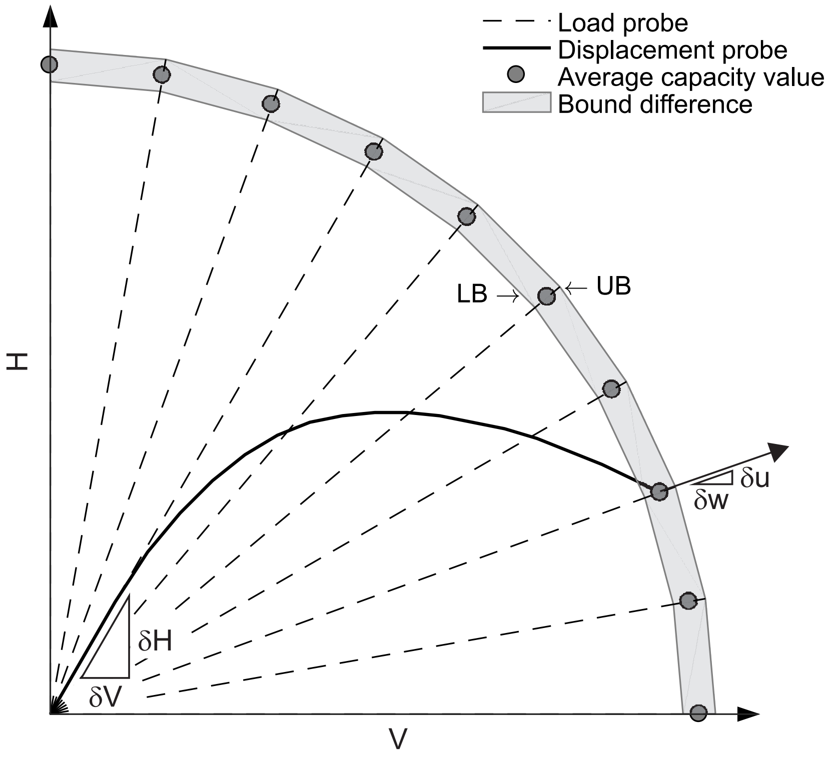

Figure 7.2: Load paths during displacement and load probe tests in VH space. For a displacement probe test, the initial load path is determined by its elastic properties i.e. $\frac{\delta H}{\delta V} = \left(\frac{k^e_H}{k^e_V}\right)\left(\frac{\delta S_y}{\delta S_z}\right)$, where k^e_H, k^e_V are the elastic horizontal and vertical stiffness and $\delta S_y, \delta S_z$ are the horizontal and vertical displacement respectively. As the soil starts yielding, the load path changes non-linearly until it reaches the failure envelope. In this figure, associated flow is assumed and the load path ends on the failure envelope where the gradient is codirectional with the displacement probe direction. For a load probe test, the load path is always codirectional with the load probe direction.

7.3.2 Load Probe Test

In the load probe test, combined loading components in a prescribed ratio are applied to the foundation until failure occurs. It is more difficult to determine failure loads with load control in FEA, as convergence cannot be obtained if the final prescribed load exceeds the foundation capacity. A series of trial and error load cases, or a careful approach to the failure envelope, is therefore required to determine the maximum load that can converge. However, the FELA technique does not suffer from such issues and hence, FELA was adopted for the load probe tests in this study. Furthermore, the use of combined lower bound (LB) and upper bound (UB) FELA provides a rigorous bracket on the theoretical failure load. A key advantage of the load probe test is that the pre-defined direction is followed throughout the analysis, which enables a more systematic approach to determination of the entire failure envelope. Fig. 7.2 shows the process of determining a VH failure envelope by probing in load space. Once a loading ratio is defined, each of the load paths travels from the origin in the prescribed direction until the failure envelope is reached.

7.3.3 Single Swipe Test

The original form of the single swipe test, also known as the sideswipe test, was introduced by Tan (1990) to find the VH failure envelope for a surface foundation in physical experiments. In a sideswipe test, the foundation is first pushed vertically to a prescribed embedment, after which the vertical displacement is held constant while the foundation is 'swiped' horizontally. This test was generalised to VHM loading by Martin (1994) and Gottardi et al. (1999), amongst others. Subsequent numerical studies (e.g. Bransby & Randolph 1998, Gourvenec & Randolph 2003) then applied this technique to a range of load spaces by following the same principle of applying displacement in one degree of freedom (DoF), followed by a displacement in another DoF (while the displacement in the first DoF is held constant). This process is essentially two displacement probe tests applied in sequence.

A fundamental assumption underpinning this type of test is that the swipe phase results in a load path that is close to the failure envelope, using analogies with hardening plasticity theory applied to soil mechanics problems (e.g. see discussion in Tan 1990, Martin 1994). Unfortunately, this assumption does not always hold in numerical studies, as the load path may underpredict the failure envelope significantly (Bransby & Randolph 1998). Several explanations for this underprediction have been proposed. For example, when discussing their numerical study on Tresca soil, Taiebat & Carter (2010) suggest that the load path moves inside the failure envelope when the magnitude of the elastic displacement in the first DoF exceeds the corresponding plastic displacement during the swipe phase. However, this contradicts other researchers (Bransby & Randolph 1998, Gourvenec & Randolph 2003) who suggest that the elastic displacement in the first DoF is equal in magnitude but opposite in sign to the corresponding plastic displacement during the swipe phase (since zero additional displacement in the first DoF is enforced during the swipe phase) but yet, the load path still move inside the failure envelope.

7.3.4 Sequential Swipe Test

The sequential swipe test is a rarely used procedure for determining failure envelopes, which resolves the potential underprediction behaviour of the single swipe test. A sequential swipe test is a multi-swipe test, which applies a more gradual change in displacement direction via a series of steps, compared with the abrupt directional change that occurs in the single swipe test. It first appeared in physical experiments (Martin 1994, Byrne 2000, Martin & Houlsby 2000), under the term 'loop test', as a closed loop path applied in the displacement space. More recently, Taiebat & Carter (2010) and Shen et al. (2017) used a similar approach, called the 'modified swipe test', in which the displacement increment in the first DoF is reduced gradually using a sine function while the displacement increment(s) in the other DoF is gradually increased using a cosine function at the same time.

Regardless of the different names (loop test, modified swipe test, sequential swipe test) given to these tests, the key principle behind these tests is the same, which is that changes in displacement direction should be applied gradually. It might be useful to consider the sequential swipe test as a 'discrete' version of the loop or modified swipe test, in which the user can control how gradual the displacement direction changes through the number of discrete swipe sequences. This is made clearer in the following exposition.

Suppose that the directional change in the displacement space is controlled by ψ, the angle between the current and previous displacement increments. In this paper, the sequential swipe test is implemented by keeping ψ constant for all steps of the swipe sequence. For example, a 2-swipe sequential swipe test in the first quadrant of the S_z-S_y displacement space (assuming the initial pre-swipe displacement is in the S_z direction) applies $\psi = \frac{\pi}{4}$ for all swipes, resulting in $\frac{\delta S_\mathrm{y}}{\delta S_\mathrm{z}} = \tan(\frac{\pi}{4})$ followed by $\frac{\delta S_\mathrm{y}}{\delta S_\mathrm{z}} = \tan(\frac{\pi}{2})$, where δS_y and δS_z are the horizontal and vertical displacement increments respectively. Correspondingly, an m-swipe sequential swipe test applies $\psi = \frac{\pi}{2m}$ for all swipes, where the direction of the displacement increment in the ith swipe is given in Eq. 7.1 (ψ_t is the total directional change in the displacement space during the swipe phase e.g. $\psi_\mathrm{t} = \frac{\pi}{2}$ for the above swipe).

$$\left(\frac{\delta S_\mathrm{y}}{\delta S_\mathrm{z}}\right)_i = \tan\left(\frac{i\psi_\mathrm{t}}{m}\right) \qquad \text{for } 1 \leq i \leq m \tag{7.1}$$

Obviously, the larger m is, the more gradually the displacement direction changes. A single swipe test can be obtained as a special case of the sequential swipe test by letting $m = 1$. To illustrate the effect of m, different m-valued sequential swipe tests were carried out for a surface strip foundation on von Mises soil.

Fig. 7.3 shows the 2D FEA mesh for the surface strip foundation, which comprised of 7200 quadratic quadrilateral elements (CPE8H). The von Mises soil yield strength in pure shear k was equated with the undrained shear strength of the clay s_u and was modelled as

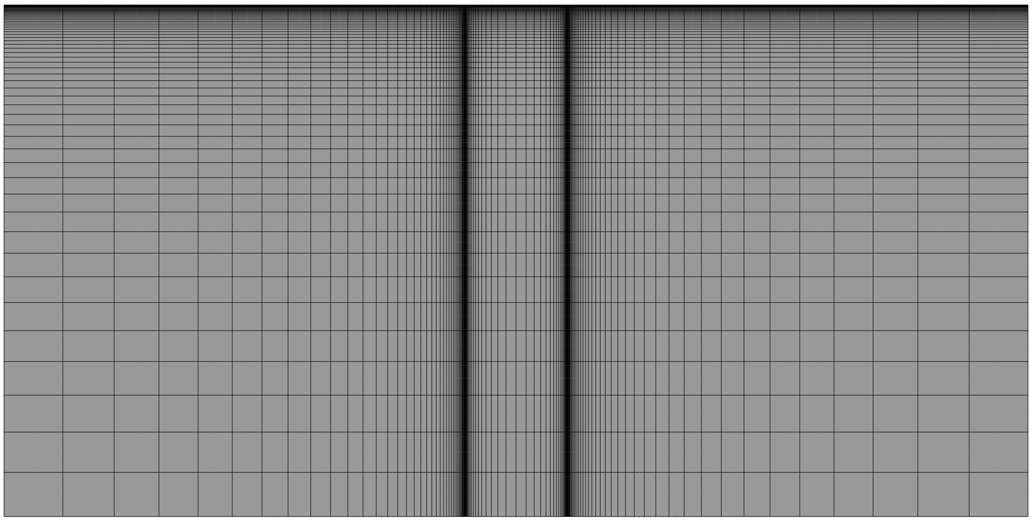

(a)

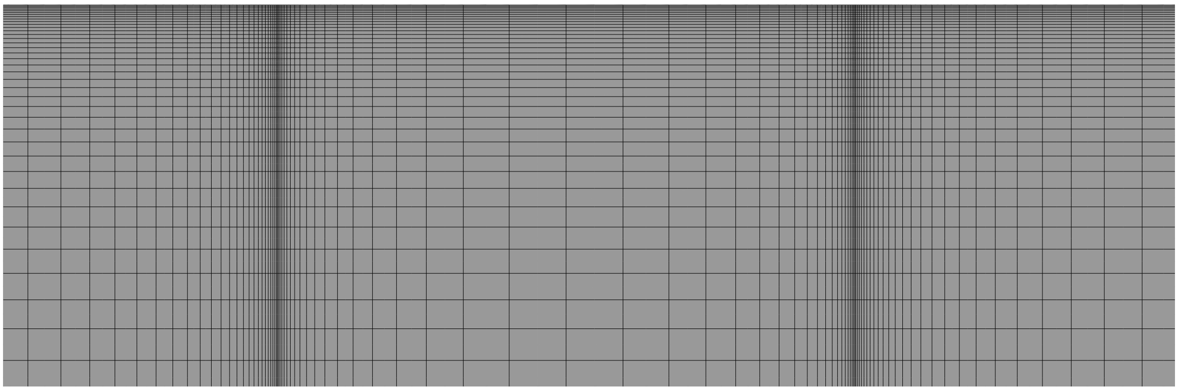

(b)

Figure 7.3: Finite element mesh for sequential swipe tests of a surface strip foundation of diameter D (Domain: $5D$ in depth and $10D$ in width) (a) Full mesh domain (b) Close-up view of the mesh area around the foundation.

homogeneous throughout the soil domain. The Poisson's ratio ν of the soil was set to 0.49, while its Young's modulus E was set to $1000\sqrt{3}s_\mathrm{u}$. The soil was modelled as a weightless material, as soil weight does not affect the capacity for the problems considered here. The surface strip foundation was modelled indirectly by applying a rigid body constraint to the soil element nodes where the foundation is supposed to bear on.

Fig. 7.4 compares the VH failure envelopes for a surface strip foundation on von Mises soil obtained from different m-valued sequential swipe tests with the analytical solution (Green 1954). Two types of swipe analysis were carried out, with one reaching maximum

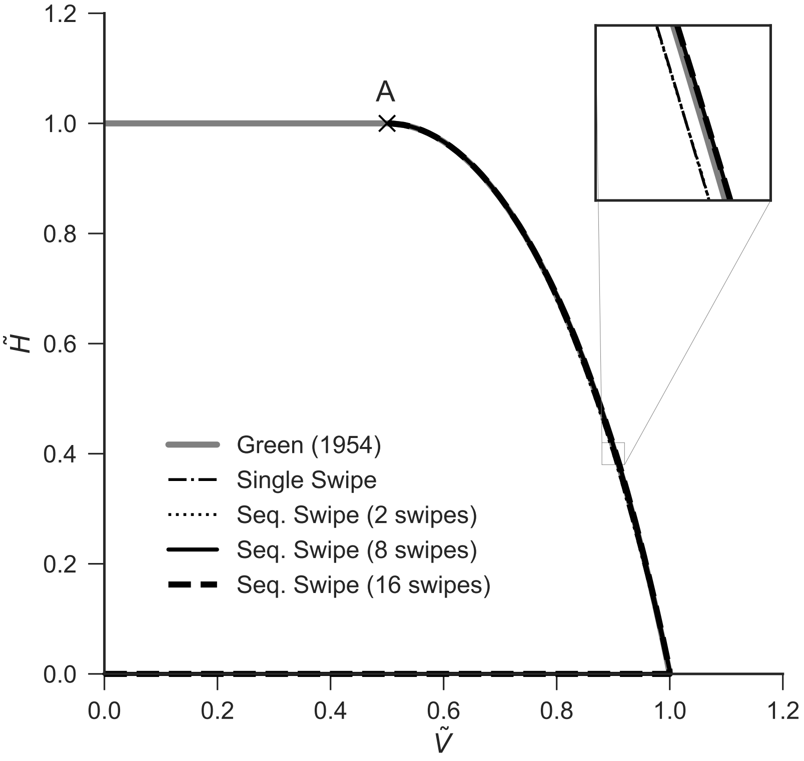

(a)

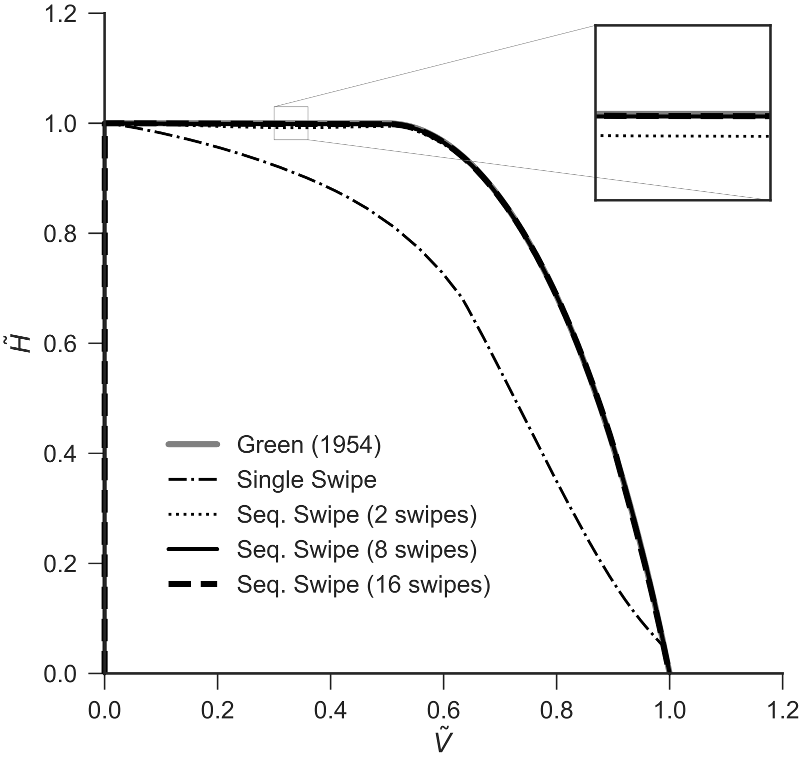

(b)

Figure 7.4: Comparison of various swipe tests in the VH load space for a surface strip foundation with the analytical Green (1954) solution. The swipe test results were obtained using plane strain finite element analyses: (a) swipe tests first reach maximum V capacity before swiping to maximum H capacity (b) swipe tests first reach maximum H capacity before swiping to maximum V capacity.

V before swiping to maximum H and the other taking the opposite route. For each analysis, three sequential swipe tests were carried out, with m ranging from 2 to 16. Key observations from Fig. 7.4 are:

1. It is evident from Fig. 7.4a that all the tests swiping to maximum H end at point A, where the analytical solution indicates no further change in failure envelope gradient.
2. The single swipe test marginally underpredicts the failure envelope in Fig. 7.4a but significantly underpredicts it in Fig. 7.4b. In contrast, the sequential swipe tests show accurate tracking of the failure envelope regardless of the starting point of the swipe phase.
3. It can be observed that the load paths of the sequential swipe tests are essentially indistinguishable from the analytical failure envelope when $m \geq 8$. This suggests that if ψ is below some critical value, the load path will track the failure envelope with negligible deviation.

When completing the analyses for Fig. 7.4, it was observed that the rate of increase in the total computational time decreased as the number of swipes increased (this is because FEA requires fewer incrementation cutbacks and equilibrium iterations for smaller ψ than for larger ψ). For example, the extra increases in total computational time (relative to the single swipe test) taken for the 2-swipe, 8-swipe and 16-swipe tests were approximately 19%, 24% and 28% respectively. This indicates a marginal penalty in choosing a higher number of swipes for the sequential swipe test. Hence, it is more practical to select an arbitrary, high number of swipes (corresponding to an arbitrary, small ψ) than to waste computational resources finding the optimal ψ, which in any case is likely to vary with the problem type and the current load state.

Nevertheless, the sequential swipe test has some limitations. Taiebat & Carter (2010) used full displacement control to find the VHM failure envelope for a surface foundation. Unfortunately, this did not provide control over the load paths and hence, there were segments of the failure envelope that were not mapped (this was later rectified using supplementary load-controlled tests). Thus, it is recommended that the sequential swipe test be restricted to two dimensions, while load boundary conditions are applied for the other dimensions (if any). In other words, the sequential swipe test should be used primarily to find two-dimensional contours of a failure envelope with dimensionality $n \geq 3$.

7.4 Application of Numerical Procedures

To evaluate the numerical procedures described above, each procedure was used to find the failure envelopes for planar VHM loading of two types of shallow foundation (circular surface and caisson foundations) bearing on undrained clay.

7.4.1 Foundation and Soil Properties

Both the surface and caisson foundations were modelled as fully rigid, with a diameter D. The caisson foundations were modelled as having a skirt of thickness $t_\mathrm{s} = 0.005D$ and length $L = D$. The undrained clay was modelled in the FEA as a linear elastic, perfectly plastic material and in the FELA as a rigid, perfectly plastic material. For both sets of analyses, the von Mises yield criterion with an associated flow rule was adopted. The von Mises yield strength in pure shear, k, was equated with the undrained shear strength of the clay, s_u, and was modelled as homogeneous throughout the soil domain. The Poisson's ratio ν of the soil was set to 0.49, while its Young's modulus E was set to $1000\sqrt{3}s_\mathrm{u}$. The soil and foundations were modelled as weightless materials, as soil weight does not affect the capacity for the problems considered here.

7.4.2 3D Finite Element (FEA) Model

First-order, fully integrated brick elements (C3D8R) were used for the foundation, while their hybrid counterparts (C3D8RH) were used for the soil as these are generally recommended for modelling near-incompressible materials (Dassault Systèmes 2014). The foundation was made fully rigid by the application of a rigid body constraint. Contact breaking between the foundation and soil was not allowed.

Fig. 7.5 shows the 3D FEA meshes for the surface and caisson foundations, with symmetry exploited. Displacement boundary conditions were set to prevent radial displacements at the circumferential faces and out-of-plane displacements at the plane of symmetry. In addition, the base of the mesh was fixed in all directions. The meshes were sufficiently large that boundary effects on the failure response of the foundation were verified to be negligible (increasing the mesh domain has negligible effect on the uniaxial capacities computed). The meshes for the surface foundation and caisson foundation comprised approximately 40,000 and 44,000 elements respectively.

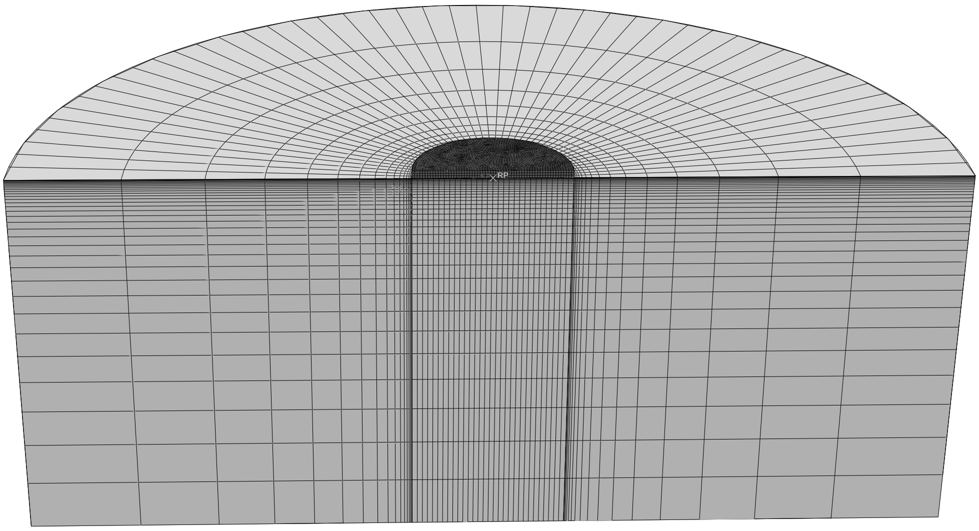

(a)

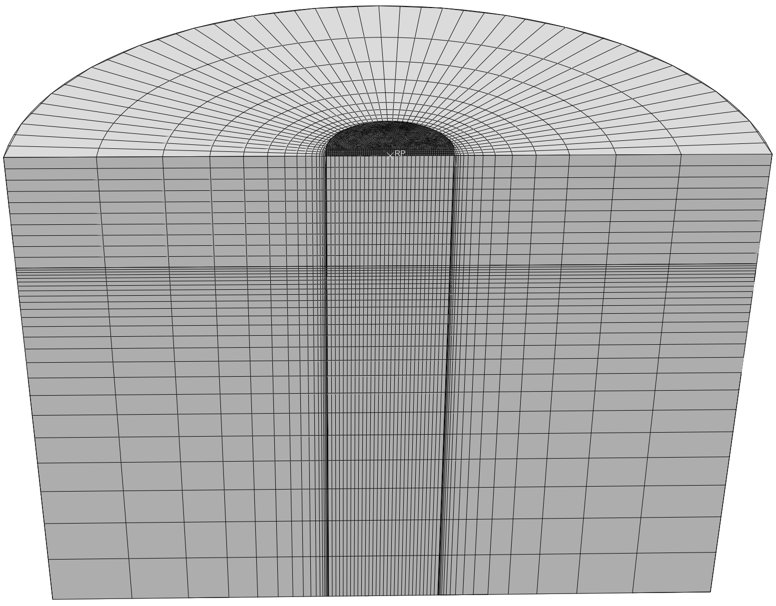

(b)

Figure 7.5: Finite element meshes for displacement probe and swipe tests: (a) Surface foundation of diameter D (Domain: $2.5D$ in depth and $3D$ in radius) (b) Caisson foundation of diameter D and skirt length L = D (Domain: $4.5D$ in depth and $3D$ in radius)

7.4.3 3D Finite Element Limit Analysis (FELA) Model

The FELA software OxLim first discretises the soil domain into a mesh of tetrahedral elements using TetGen (Si 2015) and applies the boundary conditions. Then, it sets up two constrained optimisation problems that together bound the load multiplier (i.e. the factor by which the specified live loads must be increased by to cause failure). For this study, the lower bound (LB) analyses used a piecewise linear stress field, and the upper bound (UB) analyses used a piecewise linear velocity field. The average of the bounds, $(LB + UB)/2$, is used as the best estimate solution for the load multiplier. Both the LB and UB analyses were cast as standard second-order cone programming problems and solved using specialised optimisation software (Mosek 2014).

OxLim uses adaptive mesh refinement to improve the bracketing of the exact collapse load multiplier, where the adaptivity is based on the spatial variation of the maximum shear strain rate in the UB velocity field. For the surface foundation, a mostly unstructured mesh was used, although auxiliary 'singularity facets' (see Fig. 7.6a) were added around the foundation base perimeter to improve convergence of the bounds. The initial mesh was adaptively refined twice to increase the number of elements from approximately 6,500 to 25,000, as illustrated in Fig. 7.6b. For the caisson, the initial mesh was adaptively refined once to increase the number of elements from approximately 14,000 to 30,000, as shown in Fig. 7.6c, d. To keep the number of elements comparable with the FEA mesh, a second refinement was not undertaken for the caisson. It should be noted, however, that the average of the collapse load bounds (which is the main measure of comparison with the FEA results) typically does not vary much as the bounds converge. The mesh domain was sufficiently large to render boundary effects negligible. Fixed boundary conditions were applied to the base and sides of the domain (excluding the symmetric plane).

7.4.4 Loading Methodology

For this study, the failure envelopes were explored in increasing dimensionality of load components. A failure envelope for one-dimensional loading defines a uniaxial capacity. Hence, these were first identified for pure V, H and M loading.

Failure envelopes for two-dimensional loading (combined VH, VM and HM loading) were then found. Due to symmetry in the VH and VM load spaces, only one quadrant of

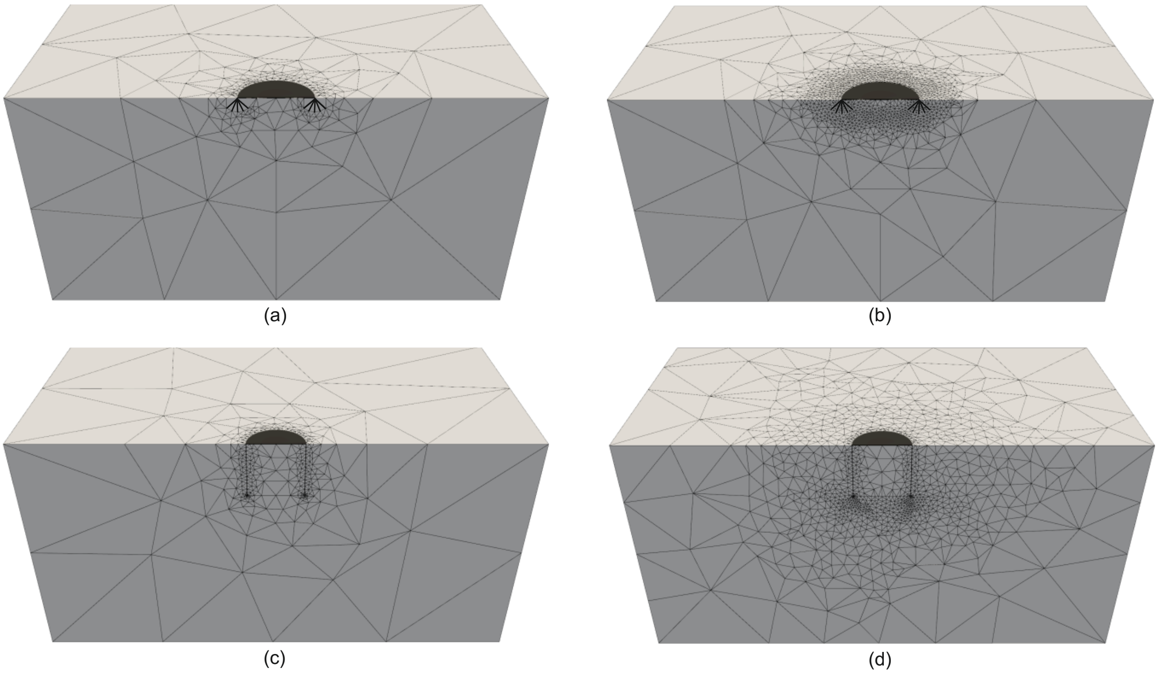

Figure 7.6: FELA mesh exploiting symmetry. Prescribed 'singularity facets' in the mesh are shown in bold. For surface foundation of diameter D, mesh domain is $3.5D$ deep, $7D$ wide and $3.5D$ thick. For caisson of diameter D and skirt length L = D, mesh domain is $4.5D$ deep, $9D$ wide and $4.5D$ thick. (a) Surface foundation, initial mesh; (b) Surface foundation, refined mesh under vertical loading; (c) Caisson, initial mesh; (d) Caisson, refined mesh under vertical loading.

the failure envelope needs to be determined. Similarly, symmetry in the HM load space dictates that only two adjoining quadrants are needed to define the full failure envelope. For the displacement probe test, nine equally spaced displacement probe directions were used in each quadrant. For comparison purposes, an 8-swipe sequence (using the same set of displacement probe directions in each quadrant) was adopted for the sequential swipe test. The displacement probe directions can be identified from Eq. 7.1 by replacing δS_{y} and δS_{z} with the displacement/rotation increments corresponding to the load spaces (e.g. in the HM load space, $\frac{\delta S_{\mathrm{y}}}{\delta S_{\mathrm{z}}}$ will be replaced by $\frac{\delta D\Theta_{\mathrm{x}}}{\delta S_{\mathrm{y}}}$). Thereafter, let $m = 8$ and $\psi_{\mathrm{t}} = \frac{\pi}{2}$ (for VH and VM) or $m = 16$ and $\psi_{\mathrm{t}} = \pi$ (for HM). Single swipe tests were also implemented for the study, with the probe directions similarly identified from Eq. 7.1 by letting $m = 1$ and $\psi_{\mathrm{t}} = \frac{\pi}{2}$ (for VH and VM) or $m = 2$ and $\psi_{\mathrm{t}} = \pi$ (for HM). With regards to the magnitude of the displacement increments used in the displacement probe, sequential swipe and single swipe tests, they were arbitrarily chosen to be sufficiently large that the load will reach steady state by the end of each displacement increment. For this study, each displacement increment was set to a constant magnitude of $0.1D$. For the load probe tests, nine equally spaced loading directions were used in each quadrant.

Finally, the full VHM failure envelope was determined. Mixed load and displacement controls were used for the FEA-based tests. Load control was used for V, while displacement control was used in the HM load space, i.e. the VHM failure envelope was explored by determining HM contours of the failure envelope at fixed levels of V. Five vertical load levels were considered: $\tilde{V}$ = 0.25, 0.5, 0.625, 0.75 and 0.875. A similar procedure was followed for the load probe tests performed using FELA, with the HM contours being determined by probing in HM load space under the same set of fixed V loads.

7.5 Results

Definition 7.4 (Uniaxial capacity) *The uniaxial capacity of a foundation is its capacity under individual loading (i.e. only one of Q, V, H, M is applied). The uniaxial capacities under torsional, vertical, lateral and moment loading are defined as Q_0, V_0, H_0 and M_0 respectively.*

7.5.1 Pure V, H and M Loading

Table 7.1 lists the results obtained for the uniaxial foundation capacities (V_0, H_0 and M_0), which shows that the results from the FEA-based displacement probe tests are within the bounds obtained using the 3D FELA load probe tests, except for pure H loading. For the vertical capacity, the 3DFE computed value of 5.63 compares well with the known exact solutions (albeit for Tresca soil) of 5.69 (Shield 1955) and 6.05 (Eason & Shield 1960) for a smooth and rough surface foundation respectively.

7.5.2 Combined VH, VM and HM Loading

An important note about displacement-controlled tests is that probes from one quadrant of the displacement space do not necessarily map to loads in the same quadrant of the load space. Fig. 7.7 shows the HM failure envelope for the caisson, as predicted by the displacement probe and sequential swipe tests, where symmetry is used to recover the full envelope. The applied HM displacement directions (as depicted by the arrows in the figure) are from the top two quadrants (i.e. $D\Theta_x \geq 0$) of the S_y-$D\Theta_x$ displacement space, but the resultant failure loads are spread amongst three quadrants in the HM load space.

The small black markers represent the intermediate equilibrium load states during each step of the sequential swipe, which are determined by Abaqus's automatic step size

Table 7.1: Uniaxial capacities of surface and caisson foundations. $A = \pi D^2/4$ refers to the foundation base area. Note that the procedure, and therefore the results, for the displacement probe, single swipe and sequential swipe tests are identical for one-dimensional loading.

		$\frac{V_0}{As_\mathrm{u}}$	$\frac{H_0}{As_\mathrm{u}}$	$\frac{M_0}{ADs_\mathrm{u}}$
Surface	Displacement Probe	5.63	1.02	0.714
	Load Probe (LB)	5.45	1.00	0.667
	Load Probe (UB)	5.77	1.00	0.715
	Load Probe (Average)	5.61	1.00	0.691
Caisson	Displacement Probe	13.12	5.86	3.64
	Load Probe (LB)	12.52	5.52	3.36
	Load Probe (UB)	13.68	6.28	3.96
	Load Probe (Average)	13.10	5.90	3.66

incrementation scheme. The density of the black markers (i.e. resolution of the failure envelope) can be controlled by changing the step size incrementation scheme.

Figs. 7.8 and 7.10 show the VH, VM and HM failure envelopes for both foundations. Because of symmetry, only one or two quadrants are shown in these figures, as appropriate. As discussed above, the small black markers on the sequential swipe load paths represent equilibrium load states during the steps of each swipe. The discrete load states from the displacement probe tests and the continuous load paths from the sequential swipe tests were all within the bounds obtained from the load probe tests. In fact, there are no significant differences between these two sets of FEA-generated results and the FELA load probe (average) results. In contrast, there is consistent underprediction of the failure envelope by the single swipe test, especially for the caisson. Moreover, Fig. 7.10 shows that the single swipe test predictions of the HM failure envelope for the surface foundation are particularly poor.

Finally, by comparing the load probe (average) results with the sequential swipe results in Figs. 7.8, 7.9 and 7.10, there is strong evidence that the sequential swipe load path is tracking on or close to the relevant failure envelope. Hence, the intermediate data points obtained during each swipe of the sequence, as shown by the black markers in the load paths, can be regarded as fairly accurate failure loads.

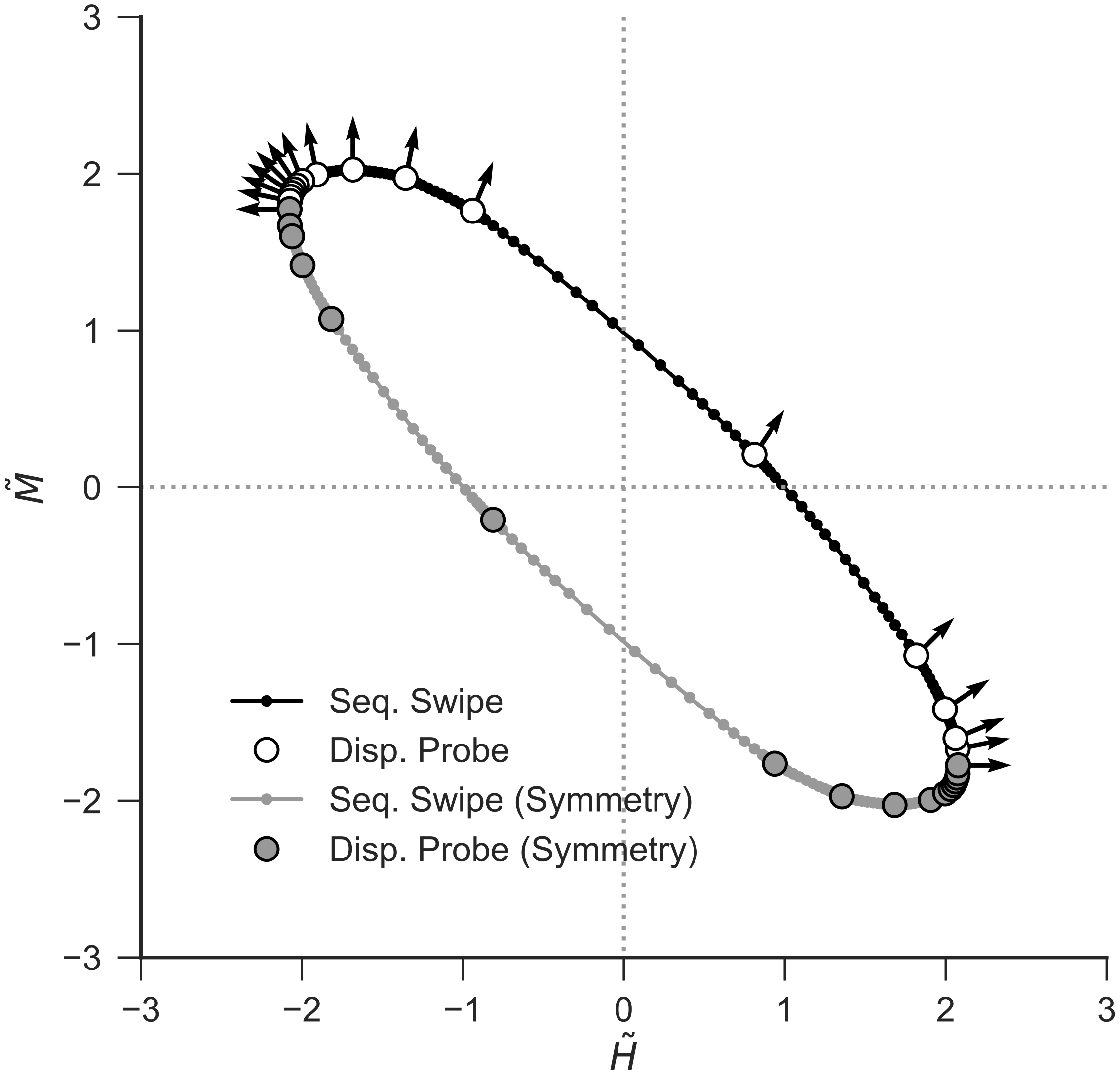

Figure 7.7: Recovery of the complete HM failure envelope for the caisson after application of symmetry principles. The arrows represent the direction of the displacement probes in the conjugate S_y-$D\Theta_x$ displacement space.

7.5.3 Combined VHM Loading

Fig. 7.11 shows the HM failure envelopes obtained for both foundations under three selected levels of the normalised vertical load $\tilde{V}$. Again, the results of the displacement probe and sequential swipe tests are all within the lower and upper bounds obtained using FELA. Furthermore, Fig. 7.12 shows the HM failure envelopes obtained from both the single swipe and sequential swipe tests for all of the normalised vertical load levels considered. It is clear that the single swipe test performs poorly relative to the sequential swipe test, with the latter providing the additional benefit of higher resolution predictions.

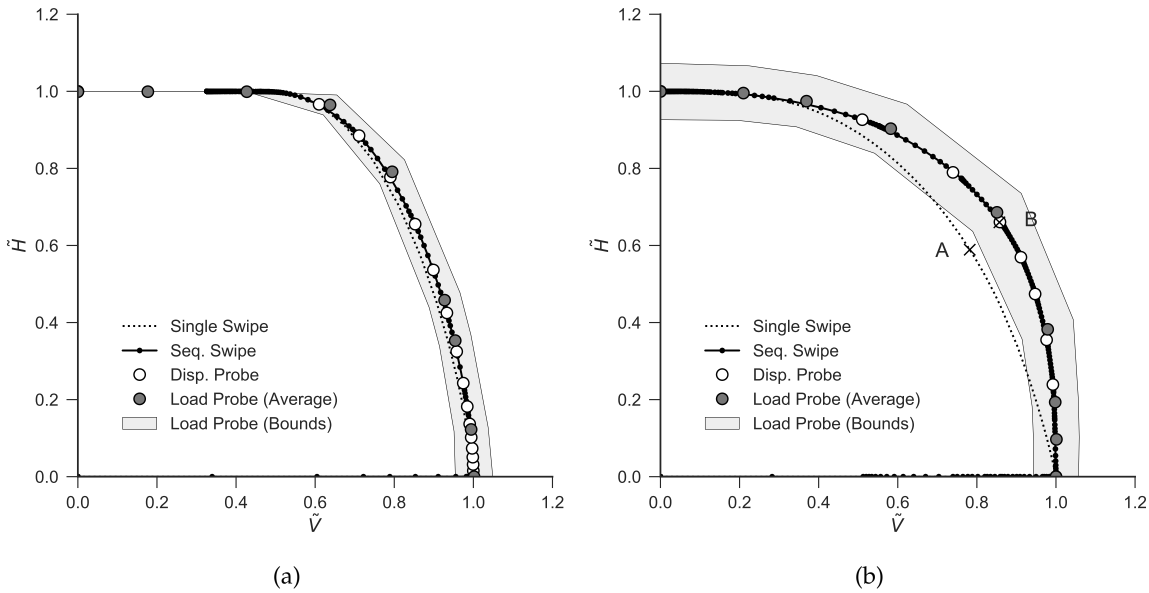

Figure 7.8: Dimensionless VH failure envelopes: (a) Surface foundation (b) Caisson foundation.

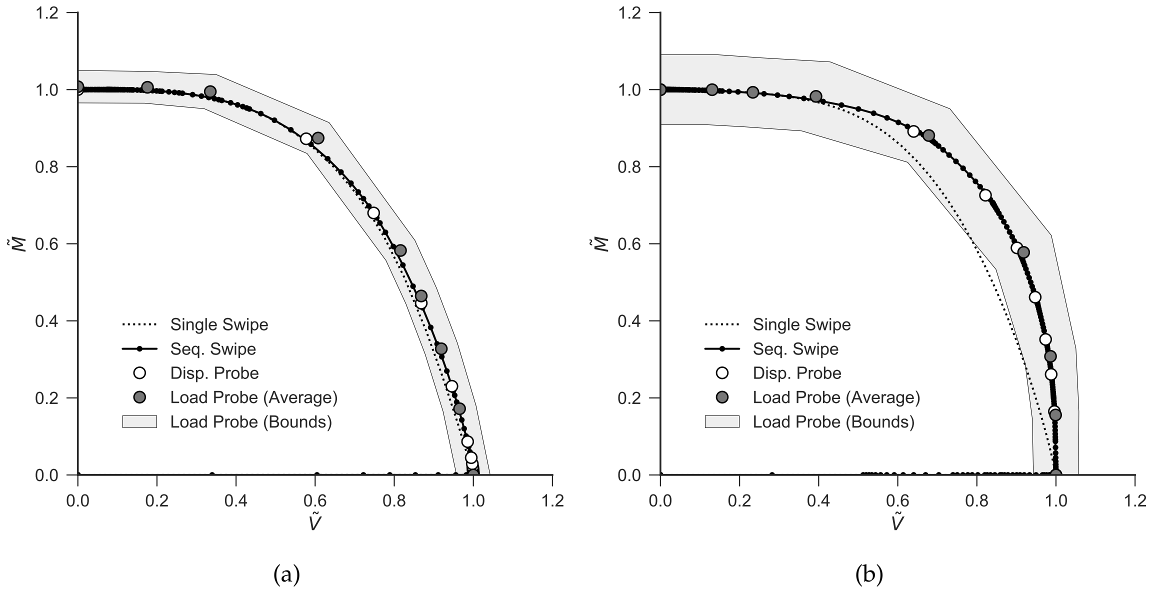

Figure 7.9: Dimensionless VM failure envelopes: (c) Surface foundation (d) Caisson foundation.

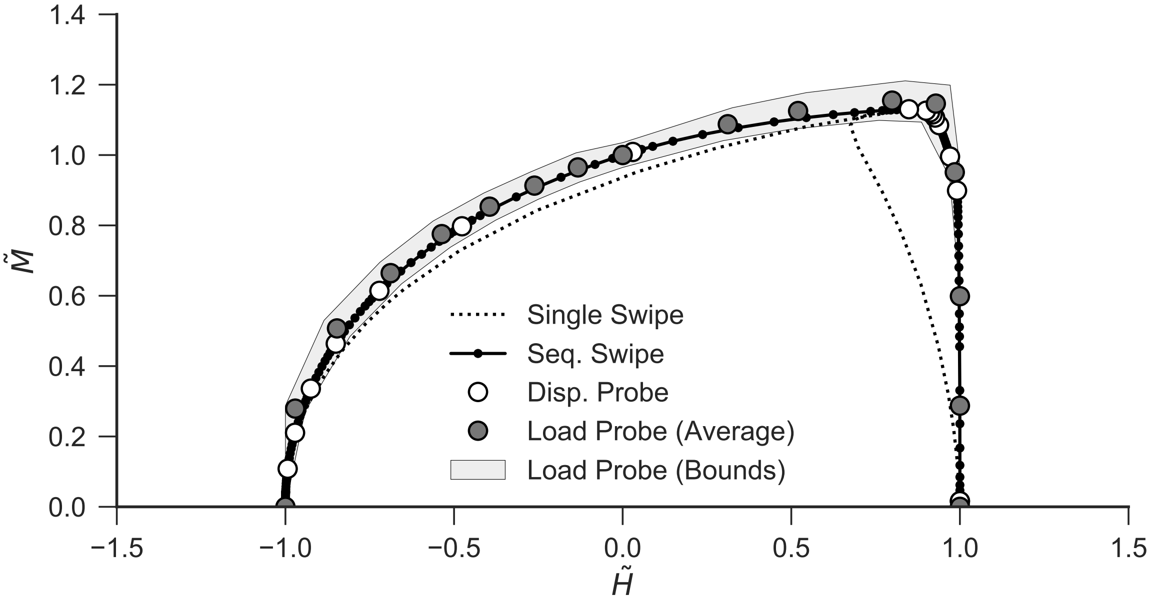

(a)

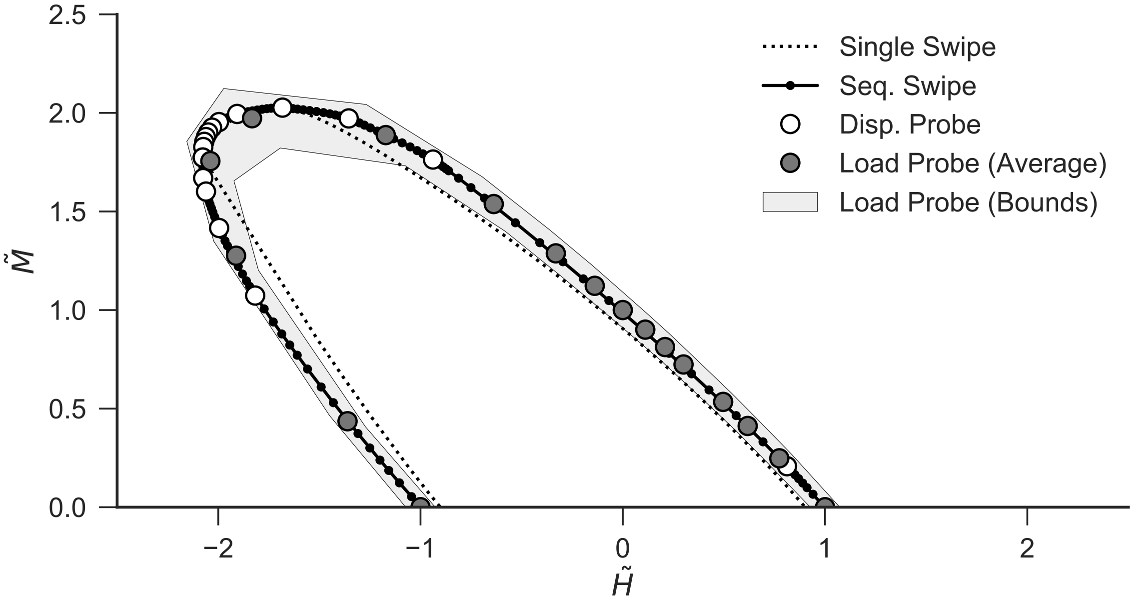

(b)

Figure 7.10: Dimensionless HM failure envelopes: (a) Surface foundation (b) Caisson foundation.

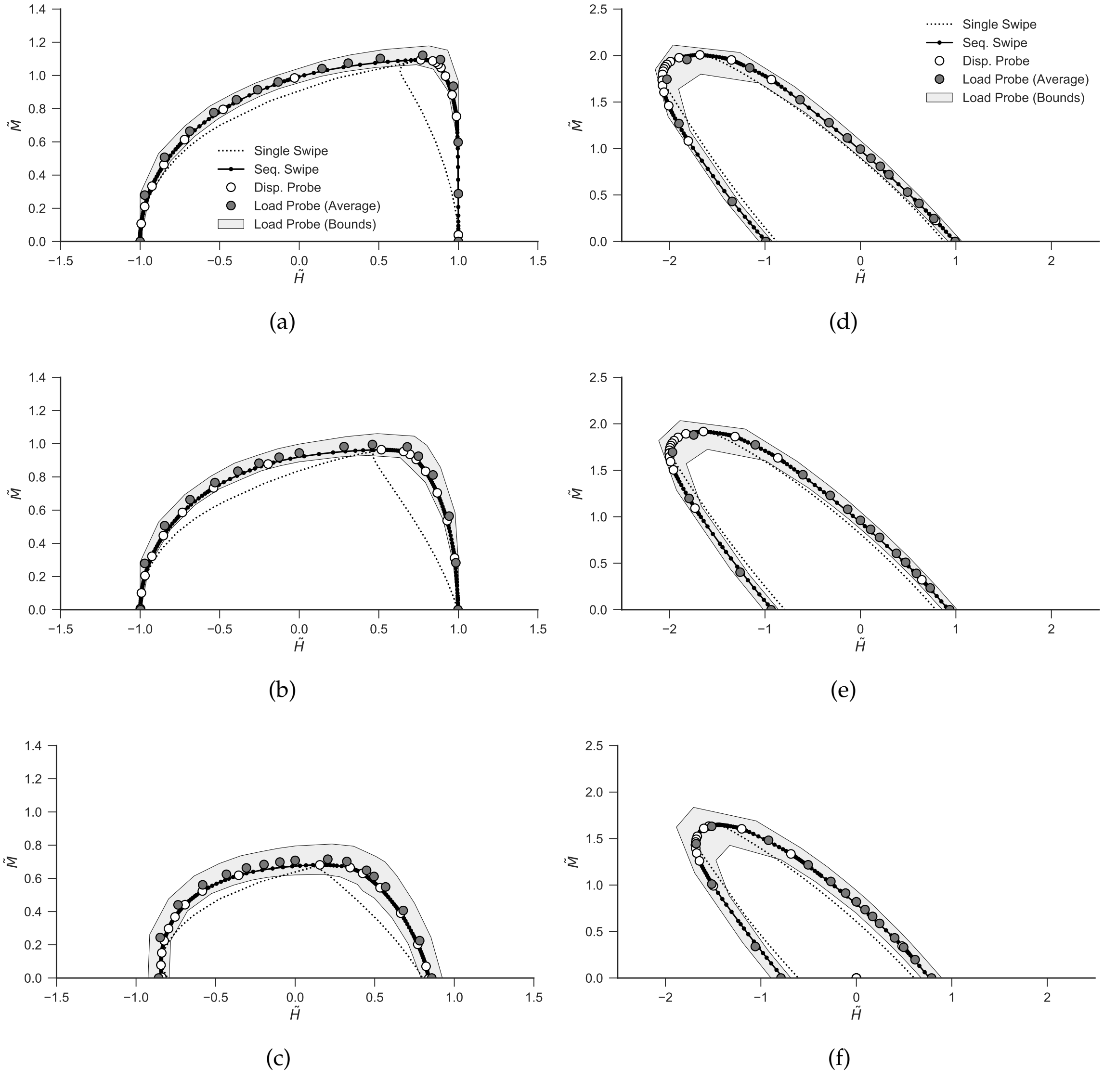

(a) (d)

(b) (e)

(c) (f)

Figure 7.11: Dimensionless HM failure envelopes at selected $\tilde{V}$ levels for surface foundations: (a) $\tilde{V} = 0.25$ (b) $\tilde{V} = 0.5$ (c) $\tilde{V} = 0.75$ and caisson foundations: (d) $\tilde{V} = 0.25$ (e) $\tilde{V} = 0.5$ (f) $\tilde{V} = 0.75$

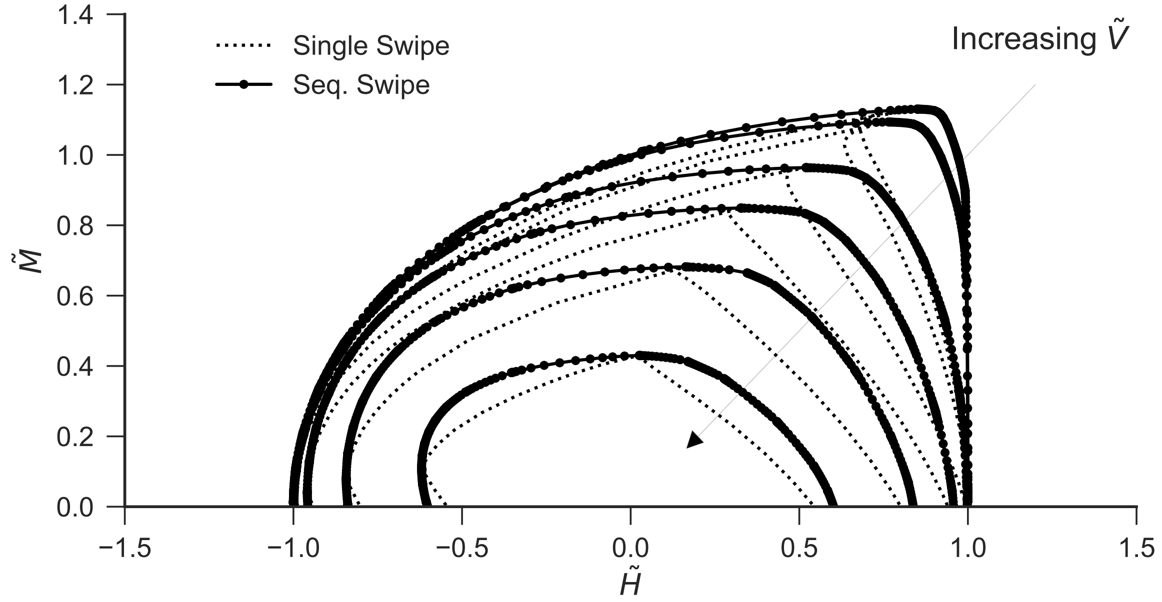

(a)

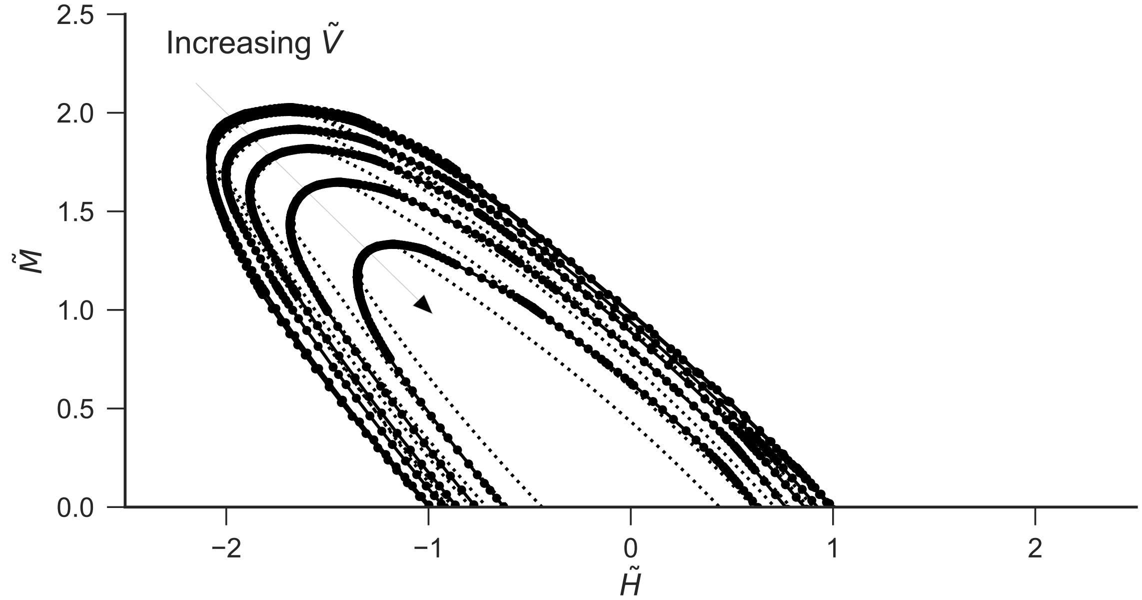

(b)

Figure 7.12: Dimensionless HM failure envelopes under increasing $\tilde{V}$ load levels ($\tilde{V}$ = 0, 0.25, 0.5, 0.625, 0.75, 0.875): (a) Surface foundation (b) Caisson foundation.

7.6 Discussion

To assess the performance of the various numerical procedures for determining failure envelopes, two foundation types with significantly different failure envelopes were evaluated. The performance criteria of interest are accuracy, computational efficiency and resolution.

In terms of accuracy, the results indicate that the single swipe test generally underpredicts the failure envelope (often significantly), while the other procedures provide similar levels of accuracy. In terms of computational efficiency, Table 7.2 shows the total and average (per probe) computational time taken by each procedure to find the VH, VM, HM and VHM failure envelopes presented in the previous section. Using FEA, 120 displacement probe tests were performed for each foundation. For the sequential swipe tests, the same probe directions were used consecutively as displacement increments for the swipes. In contrast, only 22 displacement increments (corresponding to the first and last probe directions in each quadrant of the displacement space) were performed for the single swipe tests. Using FELA, 120 load probes tests were performed to identify 120 failure loads. The computer used to run the analyses had an Intel Xeon 3.60 GHz processor (8 CPUs core) with 16 GB RAM.

Table 7.2 is revealing in several ways. First, the sequential swipe test is the most efficient amongst the FEA-based procedures, as judged by the average (clock) time required to analyse one probe direction. Second, the load probe test using FELA is the most efficient procedure. Although it might seem somewhat surprising that the load probe analyses took longer for the surface foundation than for the caisson foundation, this is due to the additional adaptive mesh iteration used when analysing the surface foundation, which yielded tighter bounds (compare the bound differences for the two foundations in Figs. 7.8, 7.9 and 7.10).

For both foundations, the sequential swipe test is nearly three times faster than the displacement probe test. This is a striking result as it shows the existence of a numerical procedure that can provide failure envelope predictions that are as accurate as the displacement probe test, but with greater efficiency. The single swipe test, on the other hand, has relatively poor efficiency when evaluated on a per probe basis. Although the intermediate load states obtained during the single swipe tests have been disregarded when evaluating the performance on a per probe basis, the results provided in the previous section have

Table 7.2: Time taken by each numerical procedure to find the failure envelopes of the surface and caisson foundations: evaluated on a total time and average time per probe basis

		No. of probes	Total time (hrs)	Average time per probe (hrs)
Surface	Disp. Probe	120	68.6	0.571
	Single Swipe	22	21.4	0.971
	Seq. Swipe	120	25.5	0.212
	Load Probe (FELA)	120	31.2	0.260
Caisson	Disp. Probe	120	152.8	1.27
	Single Swipe	22	23.0	1.05
	Seq. Swipe	120	59.5	0.496
	Load Probe (FELA)	120	22.3	0.186

shown that these intermediate data points are unreliable as they may be far from the failure envelope. In contrast, the intermediate load states obtained during a sequential swipe test have been shown to be sufficiently close to the failure envelope to be acceptable as reliable failure loads. Thus, in terms of failure envelope resolution, the sequential swipe test outperforms the other procedures.

Overall, the sequential swipe test is the best option amongst the FEA-based procedures in terms of accuracy, efficiency and resolution. Therefore, the sequential swipe test is used to determine the soil reaction yield surfaces in Chapter 9.

Chapter 8

Systematic Framework To Formulate Convex Failure Envelopes

In Chapter 7, the numerical procedures for determining failure envelopes were assessed, with the sequential swipe test being the most efficient amongst the finite element based procedures. Failure envelope formulations are usually derived to approximate the failure envelopes determined using the numerical procedures. In this chapter, a systematic framework for formulating globally convex failure envelopes (or yield surfaces) and thermodynamically consistent plastic potentials is introduced.

8.1 Introduction

Definition 8.1 (Polynomial) *A polynomial* $f(x_1, \ldots, x_n) : \mathbb{R}^{\mathrm{n}} \to \mathbb{R}$ *is a function that is a finite linear combination of monomials:*

$$f(x_1, \ldots, x_n) = \sum_{a_1, \ldots, a_n} b_{a_1, \ldots, a_n} x_1^{a_1} \cdots x_n^{a_n} \tag{8.1}$$

where the sum is over n-tuples of non-negative integers a_{i}*. The degree of a monomial is the sum of its exponents (e.g. the degree of* $x_1^2 x_3 x_5^3$ *is* $2 + 1 + 3 = 6$*). The degree of a polynomial is determined by the highest degree of its monomials.*

Definition 8.2 (Homogeneous polynomial) *A homogeneous polynomial is a polynomial where all the monomials have the same degree (i.e. the sum of the exponents in each monomial is the same). For example,* $x^4 + x^2yz + xy^2z + x^2z^2 + y^2z^2 + z^4$ *is a homogeneous polynomial of degree four.*

Definition 8.3 (Ellipsoid) *An ellipsoid is a bounded, quadric surface (i.e. a surface that may be defined as the 0-level set of a homogeneous polynomial of degree two and is bounded such that it may be enclosed in a sufficiently large sphere).*

Despite a plethora of failure envelope formulations that have been proposed in the literature, most can be categorised into one of two main groups (there are some failure envelope formulations that do not fall within these two groups e.g. Taiebat & Carter 2000).

The first is a 'quasi-ellipsoid formulation' based on a non-homogeneous polynomial, where most (but not all) of the terms are of degree two. This is used primarily to approximate the 'cigar-shaped' failure envelopes that had been determined experimentally for shallow foundations on sand (Nova & Montrasio 1991, Gottardi & Butterfield 1993, Gottardi et al. 1999, Cassidy 1999, Bienen et al. 2006) and clay (Martin & Houlsby 2000).

The simplest member of this group of formulations is 'Model A' (Martin 1994):

$$f(\tilde{V},\tilde{H},\tilde{M}) = \tilde{H}^2 + \tilde{M}^2 - 16\tilde{V}^2(1-\tilde{V})^2 \tag{8.2}$$

Eq. 8.2 was used as a preliminary model to approximate the experimental failure envelope results for a spudcan in clay. For better agreement with the experimental results, Eq. 8.2 was modified to give 'Model B' (Martin 1994, Martin & Houlsby 2000):

$$f(\tilde{V},\tilde{H},\tilde{M}) = \tilde{H}^2 + \tilde{M}^2 - 2\bar{e}\tilde{H}\tilde{M} - \bar{\beta}^2\tilde{V}^{2\beta_1}(1-\tilde{V})^{2\beta_2} \tag{8.3}$$

where $\bar{e} = e_1 + e_2\tilde{V}(\tilde{V}-1)$, $\bar{\beta} = \frac{(\beta_1+\beta_2)^{\beta_1+\beta_2}}{\beta_1^{\beta_1}+\beta_2^{\beta_2}}$ and $e_1, e_2, \beta_1, \beta_2$ are fitting parameters. From the experimental results, the best-fit parameters are $e_1 = 0.518, e_2 = 1.18, \beta_1 = 0.764, \beta_2 = 0.882$. Slightly modified versions of Eq. 8.3 were later adopted as the yield surface of macro-element models for shallow foundations in sand (Cassidy 1999, Byrne 2000, Cassidy et al. 2002, 2004) and clay (Martin 1994, Martin & Houlsby 2001). A comprehensive review of the development and history of this group of formulations is not provided here, as it is not the focus of this chapter. Interested readers may refer to Martin (1994), Cassidy (1999), Byrne (2000) for this information.

For numerical modelling, Martin & Houlsby (2001) recommended the following form of Model B (Eq. 8.3) instead:

$$f(\tilde{V},\tilde{H},\tilde{M}) = \left(\tilde{H}^2 + \tilde{M}^2 - 2\bar{e}\tilde{H}\tilde{M}\right)^{\frac{1}{2\beta_2}} - \bar{\beta}^{\frac{1}{\beta_2}}\tilde{V}^{\frac{\beta_1}{\beta_2}}(1-\tilde{V}) \tag{8.4}$$

Similarly for Model A (Eq. 8.2), the recommended form is:

$$f(\tilde{V},\tilde{H},\tilde{M}) = \sqrt{\tilde{H}^2 + \tilde{M}^2} - 4\tilde{V}(1-\tilde{V}) \tag{8.5}$$

The failure envelope defined by the 0-level set of Eq. 8.5 is similar, but not equal to that of Eq. 8.2 (The 0-level set of Eq. 8.2 is equivalent to $\pm\sqrt{\tilde{H}^2 + \tilde{M}^2} \pm 4\tilde{V}(1-\tilde{V}) = 0$). The recommended form has some advantages pertaining to convexity, as will be explained later.

The second group of failure envelope formulations is an 'HM-based formulation', that is primarily used to approximate numerically determined failure envelopes. This includes the formulations proposed by Vulpe et al. (2014), Vulpe (2015), Feng & Gourvenec (2015) and Shen et al. (2016, 2017). This group of formulations is defined primarily in terms of $\tilde{H}^*, \tilde{M}^*$, where $\tilde{H}^* = \frac{\tilde{H}}{f_1(\tilde{V},\tilde{Q})}$ and $\tilde{M}^* = \frac{\tilde{M}}{f_2(\tilde{V},\tilde{Q})}$ for some functions f_1, f_2 such that $f_1(0,0) = 1, f_2(0,0) = 1$. In other words, a formulation for the HM failure envelope under zero V and Q loading is first derived. Thereafter, the effect of V and Q loading on the failure envelopes are incorporated by scaling $\tilde{H}$ and $\tilde{M}$ in the original formulation. The simplest member of this group is proposed by Vulpe et al. (2014):

$$f(\tilde{H}^*,\tilde{M}^*) = \left(|\tilde{H}^*|\right)^{\mathrm{a}} + \left(\tilde{M}^*\right)^{\mathrm{a}} + 2\mathrm{b}\left(\tilde{H}^*\tilde{M}^*\right) - 1 \tag{8.6}$$

where $a = 2.13$ or 1.63 depending on $\tilde{V}$, $b =$ -0.26 or -0.05 depending on $\tilde{V}$, $\tilde{H}^* = \tilde{H}/(1 - \tilde{V}^{4.69}), \tilde{M}^* = \tilde{M}/(1-\tilde{V}^{2.12})$.

Even though these two groups of formulations have been used very successfully to approximate failure envelope data, there are some shortcomings that have been identified. First, there is currently no systematic and general framework for deriving failure envelope formulations for n-dimensional ($n \geq 1$) loading. The failure envelope formulation is usually customised manually for different failure envelope shapes, and for different loading dimensions. As such, deriving formulations is a relatively laborious process. Second, there are numerical issues pertaining to the HM-based failure envelope formulations. The exponent parameters in Eq. 8.6 tend to be fractional, which together with the scaling approach, brings about some numerical problems. Third, these two groups of failure envelope formulations are not globally convex, which prevents the use of efficient, implicit elasto-plastic integration algorithms. Finally, they are not guaranteed to be thermodynamically consistent (if used as plastic potentials). Models that violate the laws of thermodynamics cannot be used with confidence to describe real-world behaviour.

To address the aforementioned shortcomings, a systematic framework for formulating failure envelopes is introduced, which comes with several key benefits:

Systematic There are no ad hoc steps in the process. The methodology behind the framework is clearly defined and can be readily followed.

General The framework can be applied to any dataset resulting from any arbitrary, n-dimensional loading. In other words, the framework can be used to derive formulations for most failure envelope shapes.

Convex The derived formulation is guaranteed to be globally convex, which comes with its own set of advantages.

Thermodynamically consistent The derived formulation is guaranteed to obey the First and Second Law of Thermodynamics, if used as plastic potentials.

Well-behaved function The derived formulation is continuous and real-valued in $\mathbb{R}^n$, is easily differentiable or integrable and has a continuous gradient and Hessian in $\mathbb{R}^n$, making it ideal for use as yield functions and plastic potentials.

8.2 Convexity

A function f is defined to be convex if its domain is a convex set and,

$$f(\lambda\vec{x} + (1-\lambda)\vec{y}) \leq \lambda f(\vec{x}) + (1-\lambda)f(\vec{y}) \tag{8.7}$$

for all $\vec{x}, \vec{y} \in$ domain of f and for $0 \leq \lambda \leq 1$ (Boyd & Vandenberghe 2004). Depending on the differentiability of f, there are two equivalent conditions to Eq. 8.7 that characterise the convexity of f.

If f is differentiable (i.e. its gradient $\nabla f(\vec{x})$ exists everywhere in its domain), f is convex if its domain is a convex set and

$$f(\vec{y}) \geq f(\vec{x}) + \nabla f(\vec{x})^{\intercal}(\vec{y} - \vec{x}) \tag{8.8}$$

for all $\vec{x}, \vec{y} \in$ domain of f. Eq. 8.8 is known as the first-order condition (Boyd & Vandenberghe 2004).

If f is twice differentiable (i.e. its Hessian $\nabla^2 f(\vec{x})$ exists everywhere in its domain), f is convex if its domain is a convex set and $\nabla^2 f(\vec{x})$ is positive semidefinite everywhere in its domain i.e.

$$\vec{y}^{\intercal}\nabla^{2}f(\vec{x})\vec{y} \geq 0 \tag{8.9}$$

for all $\vec{x}, \vec{y} \in$ domain of f. This is known as the second-order condition (Boyd & Vandenberghe 2004) and is the principal condition for assessing the convexity of functions in the current chapter. One way to determine whether a matrix is positive semidefinite is to check whether all of its eigenvalues are non-negative everywhere in its domain.

In this thesis, a globally convex function is defined as a function that is convex in the domain $\mathbb{R}^{n}$ (where n is interpreted in the context of the current work as the number of individual load and moment components applied to the foundation). It is beneficial to use a convex function to represent a failure envelope, as it allows the use of efficient, implicit elasto-plastic integration algorithms such as CPPM (Simo & Taylor 1985). Additionally, previous researchers (e.g. Panteghini & Lagioia 2014) have reported numerical instabilities when using implicit integration algorithms with yield functions f that are not convex in their entire domain (i.e. for $f > 0$ as well as $f = 0$). A yield surface should not be confused with a yield function. A yield surface is usually defined as the 0-level set of a yield function $f(\vec{x})$. A convex yield surface does not necessarily imply convexity of $f(\vec{x})$. Conversely, if $f(\vec{x})$ is convex, the yield surface is necessarily convex. These conditions arise from convex analysis relating convex functions and their sublevel sets (Boyd & Vandenberghe 2004).

It can be shown that some of the existing failure envelope formulations are not globally convex. For example, the Hessian of Model A in the form of Eq. 8.2 is:

$$\begin{bmatrix} 2 & 0 & 0 \\ 0 & 2 & 0 \\ 0 & 0 & -32(6\tilde{V}^{2} - 6\tilde{V} + 1) \end{bmatrix} \tag{8.10}$$

and its three eigenvalues are 2 (repeated) and $-32(6\tilde{V}^{2} - 6\tilde{V} + 1)$. Fig. 8.1 shows the non-repeated eigenvalue computed for $0 \leq \tilde{V} \leq 1$, which indicates that Eq. 8.2 is only convex for a limited range of $0.21 \leq \tilde{V} \leq 0.79$. That is why for numerical modelling, Eq. 8.5 is generally recommended. The three eigenvalues of the Hessian of Eq. 8.5 are 0, 8 and $1/\sqrt{\tilde{H}^{2} + \tilde{M}^{2}}$, which means that Eq. 8.5 is convex in all of $\mathbb{R}^{n}$, except for $\tilde{H} = 0, \tilde{M} = 0$ where one of the eigenvalues is undefined (the general convexity condition Eq. 8.7 may be used to assess the convexity at this point). As for the other formulations mentioned above, it can be shown that Eqs. 8.3, 8.4 and 8.6 are not globally convex.

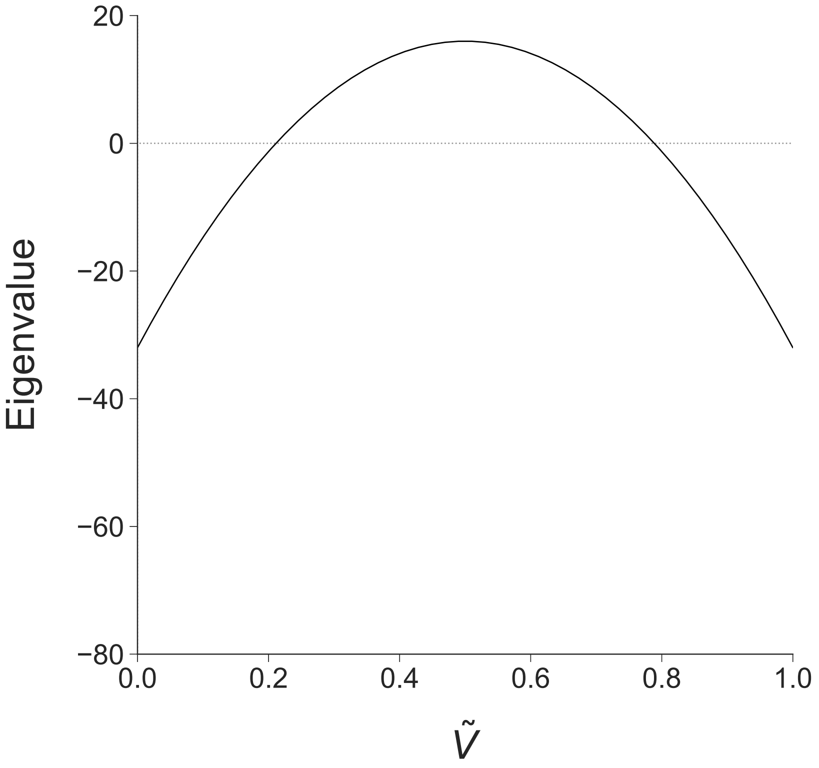

Figure 8.1: Variation of the non-repeated eigenvalue of Eq. 8.2 with respect to the magnitude of vertical loading.

Proving non-convexity for functions is straightforward (a single counterexample is sufficient). Proving convexity for functions, on the other hand, is much more difficult, especially for those with non-constant Hessians (such as Eq. 8.10). Recall that a convex function has to have a positive semidefinite Hessian for its entire domain. A heuristic approach that shows that a Hessian is positive semidefinite at some finite number of points (no matter how many) is insufficient to rigorously prove that it will remain positive semidefinite over its entire domain. An analytical approach is often required.

8.3 Well-behavedness

In this chapter, a well-behaved function is defined as a function that is continuous and real-valued in $\mathbb{R}^n$. The former is required for ease of numerical implementation, while the latter is required for proper evaluation of the yield surface. Furthermore, its gradient and Hessian should also be continuous and real-valued in $\mathbb{R}^n$.

Unfortunately, the HM-based failure envelope formulations tend to be not well-behaved. Take Eq. 8.6 as an example. For $\tilde{V} > 0.5$, its formulation is:

$$f(\tilde{H}^*, \tilde{M}^*) = \left(\left|\tilde{H}^*\right|\right)^{1.63} + \left(\tilde{M}^*\right)^{1.63} - 0.1\left(\tilde{H}^*\tilde{M}^*\right) - 1 \tag{8.11}$$

where $\tilde{H}^* = \tilde{H}/(1 - \tilde{V}^{4.69}), \tilde{M}^* = \tilde{M}/(1 - \tilde{V}^{2.12})$.

It is not real-valued for $\tilde{M} < 0$ or $\tilde{V} < 0$, as raising negative numbers by fractional powers result in complex values. This is a common theme for failure envelope formulations in this group, due to their extensive use of fractional exponents. Furthermore, the scaling approach results in a singularity in the function and its gradient when $\tilde{V} = 1$, which makes it numerically inconvenient to implement these formulations as yield surfaces.

8.4 Suitable Class of Failure Envelope Formulations

Ideally, a failure envelope formulation should possess the following characteristics:

1. Globally convex
2. Well-behaved
3. Can easily support n-dimensional loading ($n \geq 1$)

Definition 8.4 (Non-negative Polynomial) *A polynomial $f(x_1, \ldots, x_n)$ is defined as being non-negative if $f(x_1, \ldots, x_n) \geq 0 \ \forall x_1, \ldots, x_n \in \mathbb{R}^n$.*

A suitable class of functions that could meet these requirements are ellipsoids (which are homogeneous polynomials of degree 2). The standard ellipsoid can be defined in quadratic form as:

$$\vec{x}^\intercal \boldsymbol{A} \vec{x} = 1 \tag{8.12}$$

where $\boldsymbol{A}$ is a positive definite matrix and x is a vector. Because the Hessian of Eq. 8.12 is $2\boldsymbol{A}$ (which is positive definite), an ellipsoid is guaranteed to be globally convex. It is well-behaved and it can support any n number of loading dimensions (i.e. x can be a vector of $x_1, x_2, \ldots, x_n$ where each component represents a loading dimension such as V, Q etc.). This makes the ellipsoid an attractive candidate for approximating failure envelopes.

Nevertheless, an ellipsoid is rarely used as the basis for failure envelope formulations, as it is not expressive enough to approximate the widely varying failure envelope shapes. Intuitively, a possible solution would be to increase the degree of the polynomial to increase its expressiveness, just as one would use a higher degree polynomial to get a better match for a one-dimensional curve fitting task.

However, there is an issue: proving convexity is not straightforward for higher degrees polynomials. Polynomials of degree 1 are always convex and proving convexity for polynomials of degree two is straightforward as that amounts to checking whether a constant matrix is positive semidefinite. For higher degree polynomials, it has been shown (Ahmadi et al. 2013) that polynomials of odd degree ≥ 3 are not convex, while it is NP-hard (i.e. algorithmically difficult) to prove the convexity of polynomials of even degree ≥ 4.

This poses significant difficulties in identifying globally convex, higher degree polynomials that can fit the failure envelope data. While it is difficult to prove convexity of any arbitrary polynomial of even degree ≥ 4, there is a subset of polynomials (of even degree) that is guaranteed to be convex.

Definition 8.5 (Sum of squares (SOS) polynomials) *Sum of squares (SOS) polynomials are polynomials $f(x_1, \ldots, x_n)$ of degree $2m$ that can be expressed as:*

$$f(x_1, \ldots, x_n) = \sum_{i=1}^{k} g_{\mathrm{i}}(x_1, \ldots, x_n)^2$$

where $g_1(x_1, \ldots, x_n), \ldots, g_k(x_1, \ldots, x_n)$ are of degree m. If $f(x_1, \ldots, x_n)$ is SOS, then clearly $f(x_1, \ldots, x_n) \geq 0 \; \forall x_1, \ldots, x_n \in \mathbb{R}^{\mathrm{n}}$. Equivalently, $f(x_1, \ldots, x_n)$ is SOS if and only if there exists a positive semidefinite matrix $\boldsymbol{B}$ such that:

$$f(x_1, \ldots, x_n) = \vec{y}^{\intercal} \boldsymbol{B} \vec{y}$$

where $\vec{y}$ is the vector of all monomials of degree up to m (i.e. $\vec{y} = [1, x_1, x_2, \ldots, x_n, x_1 x_2, \ldots, x_n^m]$). This can be easily shown by doing a Cholesky factorisation on $\boldsymbol{B} = \boldsymbol{V}^{\intercal} \boldsymbol{V}$ to give:

$$f(x_1, \ldots, x_n) = \vec{y}^{\intercal} \boldsymbol{V}^{\intercal} \boldsymbol{V} \vec{y} = (\boldsymbol{V} \vec{y})^{\intercal} (\boldsymbol{V} \vec{y}) = \| \boldsymbol{V} \vec{y} \|^2$$

This subset of polynomials are known as sum of squares (SOS) polynomials. Recall that a necessary and sufficient condition for a function f to be convex is for its Hessian $\nabla^2 f$ to be positive semidefinite (i.e. $\vec{s}^{\intercal} \left(\nabla^2 f(\vec{x}) \right) \vec{s} \geq 0, \forall \vec{x}, \vec{s} \in$ domain of f). A more tractable and sufficient condition for a polynomial f to be convex is for its Hessian to be 'SOS positive semidefinite' (i.e. $\vec{s}^{\intercal} \left(\nabla^2 f(\vec{x}) \right) \vec{s}$ is SOS, $\forall \vec{x}, \vec{s} \in$ domain of f). Such polynomials are often called 'SOS-convex' polynomials (Ahmadi & Parrilo 2012).

The condition of a function being convex is not equivalent to the condition of a function being SOS-convex, unless the polynomial is univariate or quadratic. A function that is

SOS-convex is necessarily also convex, but a function that is convex is not necessarily SOS-convex. In other words, SOS-convex polynomials are a subset of all convex polynomials (Ahmadi & Parrilo 2012).

Finding SOS-convex polynomials is a much more tractable problem as it turns out to be equivalent to a convex optimisation (semidefinite programming) problem (Parrilo 2003), which can be solved efficiently. Imposing a polynomial $f(x_1, \ldots, x_n) = \vec{y}^{\intercal} \boldsymbol{B} \vec{y}$ to be SOS is equivalent to a semidefinite program where $\boldsymbol{B}$ is constrained to be positive semidefinite, together with a set of linear equality constraints on the coefficients of $f(x_1, \ldots, x_n)$. The conversion of a SOS problem to a semidefinite program will be demonstrated later with a simple example. Given their computational tractability and compatibility with the ideal characteristics of failure envelope formulations, SOS-convex polynomials will form the class of functions from which the failure envelope formulations will be derived from.

8.5 Thermodynamic Consistency

Definition 8.6 (First Law of Thermodynamics) *For an isolated system, the change in the internal energy of the system is equal to the heat absorbed by the system and the work done on it.*

Definition 8.7 (Second Law of Thermodynamics) *For an isolated system, the total entropy can never decrease over time. The Clausius–Duhem inequality is an expression of the second law of thermodynamics, which is commonly used in continuum mechanics to determine whether the constitutive relation of a material is thermodynamically consistent.*

For rate independent, isothermal deformation (as assumed in this thesis), the dissipation inequality, which combines the first and second laws of thermodynamics, implies that the mechanical dissipation $\gamma_{\text{diss}}^{\text{mech}}$ of the system must be non-negative (Ottosen & Ristinmaa 2005). For non-hardening elasto-plastic materials, the mechanical dissipation is equivalent to the rate of plastic work of the system $\dot{W}_{\text{p}}$ (Ottosen & Ristinmaa 2005). For macro-element models where the deformation of the system is described purely in terms of the global force resultants and the corresponding work-conjugate displacements, $\dot{W}_{\text{p}}$ is:

$$\dot{W}_{\text{p}} = \vec{P} \cdot \dot{\vec{S}}_{\text{p}} \geq 0 \tag{8.13}$$

where $\vec{P}$ is the global loads applied to the foundation and $\dot{\vec{S}}_{\text{p}}$ is the time derivative of the global plastic displacements of the foundation $\vec{S}_{\text{p}}$. In these macro-element models, $\delta \vec{S}_{\text{p}}$ is usually defined as:

$$\delta \vec{S}_{\mathrm{p}} = \delta\lambda \frac{\partial g}{\partial \vec{P}} \tag{8.14}$$

where g is the plastic potential of the macro-element model and $\delta\lambda$ is some non-negative scalar. In incremental form, Eq. 8.13 can be restated in terms of the normalised loads $\vec{\tilde{P}}$ and normalised plastic displacements $\vec{\tilde{S}}_{\mathrm{p}}$ as:

$$\vec{\tilde{P}} \cdot \delta \vec{\tilde{S}}_{\mathrm{p}} \geq 0 \tag{8.15}$$

where $\delta \vec{\tilde{S}}_{\mathrm{p}} = \delta\lambda \frac{\partial g}{\partial \vec{\tilde{P}}}$. Since $\delta\lambda \geq 0$, Eq. 8.15 is satisfied if:

$$\vec{\tilde{P}} \cdot \frac{\partial g}{\partial \vec{\tilde{P}}} \geq 0 \tag{8.16}$$

Eq. 8.16 is satisfied if associated flow rule is adopted (i.e. if the yield function is also the plastic potential), and the yield function is convex and contains the origin in its domain. To see this, if the plastic potential g is convex, Eq. 8.8 implies

$$\begin{aligned} g(\vec{\tilde{P}}_0) &\geq g(\vec{\tilde{P}}) + \nabla g(\vec{\tilde{P}})^{\intercal}(\vec{\tilde{P}}_0 - \vec{\tilde{P}}) \\ \nabla g(\vec{\tilde{P}})^{\intercal}(\vec{\tilde{P}} - \vec{\tilde{P}}_0) &\geq g(\vec{\tilde{P}}) - g(\vec{\tilde{P}}_0) \end{aligned} \tag{8.17}$$

where $\nabla g = \frac{\partial g}{\partial \vec{\tilde{P}}}$, $\vec{\tilde{P}}$ is the current load state on the yield surface (i.e. $f(\vec{\tilde{P}}) = 0$) and $\vec{\tilde{P}}_0$ is any load state inside or on the yield surface (i.e. $f(\vec{\tilde{P}}_0) \leq 0$). If associated flow is assumed, $g = f$ and thus, $g(\vec{\tilde{P}}) - g(\vec{\tilde{P}}_0) = f(\vec{\tilde{P}}) - f(\vec{\tilde{P}}_0) \geq 0$ (from the above definitions of $\vec{\tilde{P}}$ and $\vec{\tilde{P}}_0$). Therefore, Eq. 8.17 simplifies to:

$$\nabla g(\vec{\tilde{P}})^{\intercal}(\vec{\tilde{P}} - \vec{\tilde{P}}_0) \geq 0 \tag{8.18}$$

By substituting $\vec{\tilde{P}}_0 = \vec{0}$ into Eq. 8.18 (where $\vec{0}$ is the zero vector i.e. origin of the global load space), Eq. 8.16 is recovered. For the problems considered in this thesis, associated flow rule is assumed and thus, Eq. 8.16 is satisfied if the yield function is globally convex.

8.6 Methodology

This section describes the steps required to go from the failure envelope data to a formulation that approximates it.

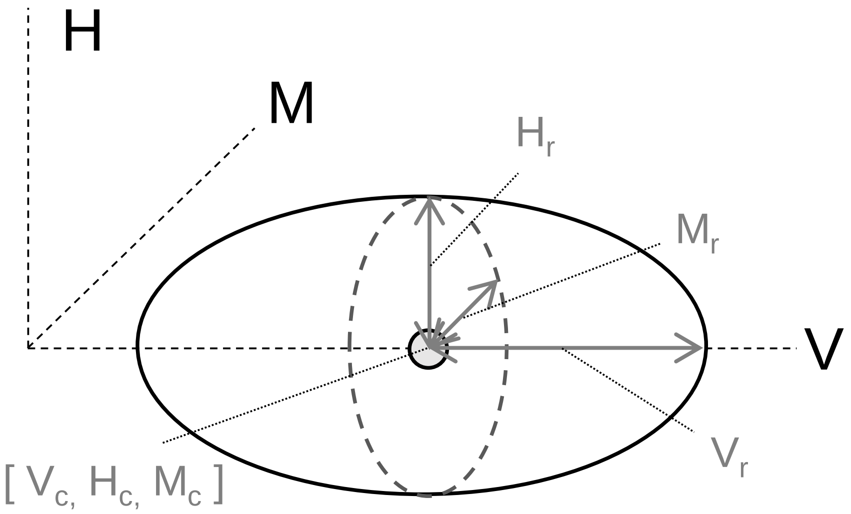

Figure 8.2: Schematic definition of χ_c and χ_r, with reference to an ellipsoid-shape VHM failure envelope (where χ here can be any of H, M, V).

8.6.1 Step 1. Standardise Data

First, standardise the failure envelope data by normalising the output as follows:

$$\bar{\chi} = \frac{\chi - \chi_\mathrm{c}}{\chi_\mathrm{r}} \tag{8.19}$$

where χ_c represents the χ-axis coordinate of the adopted 'centroid' of the failure envelope data and χ_r represents the distance between χ_c and the failure envelope along the χ-axis (see Fig. 8.2). Note that χ can be any of $H_\mathrm{x}, H_\mathrm{y}, M_\mathrm{x}, M_\mathrm{y}, V, Q$. The purpose of Eq. 8.19 is to scale the data such that the standardised data intersects each $\bar{\chi}$ axis at ±1. With regards to convexity, $f(\chi)$ is convex if $f(\bar{\chi})$ is convex, as Eq. 8.19 is an affine function and composition with an affine mapping preserves convexity (Boyd & Vandenberghe 2004).

There is some freedom in selecting the location of the centroid, as long as the resulting standardised failure envelope data intersects each $\bar{\chi}$ axis at ±1. If the centroid is selected at the origin of the coordinate system (e.g. $[V_\mathrm{c}, H_\mathrm{c}, M_\mathrm{c}] = [0, 0, 0]$) and the minimum uniaxial capacity χ_{0-} and maximum uniaxial capacity χ_0 are symmetrical (i.e. $\chi_{0-} = -\chi_0$), $\bar{\chi} = \tilde{\chi}$.

Following that, a dataset of standardised loads are obtained. For example, for HM loading, the dataset should contain $[\bar{H}_1, \bar{M}_1], \ldots, [\bar{H}_k, \bar{M}_k]$, where k is the number of rows of data. An optional step would be to remove 'redundancy' from the dataset, especially if the data are 'densely packed' (as would be the case for sequential swipe test results). This is done by rounding the data values to one or two decimal places and removing the duplicate rows of data. This would help speed up the optimisation process in Step 5.

8.6.2 Step 2. Define Failure Envelope Functional Form

Next, define the functional form of the failure envelope formulation to be of SOS-convex form (i.e. a polynomial $f(x_1, \ldots, x_n)$ of even degree $2m$, where $m \geq 1, m \in \mathbb{Z}$). Although SOS-convex polynomials may be non-homogeneous, this paper considers only homogeneous SOS-convex polynomials for simplicity. This homogeneous form allows straightforward identification of the polynomial coefficients for uniaxial loading, as will be explained in Step 3. For example, if $m = 2$ and the number of variables is 2, a 4th degree homogeneous polynomial can be obtained as:

$$f(x_1, x_2) = x_1^4 a_1 + x_1^3 x_2 a_2 + x_1^2 x_2^2 a_3 + x_1 x_2^3 a_4 + x_2^4 a_5 \tag{8.20}$$

where x_1, x_2 are the standardised loading variables (e.g. $\bar{V}, \bar{H}$) and $a_1, \ldots, a_5$ are the unknown coefficients to solve for.

Since $x_1, \ldots, x_n$ represent the standardised loading variables, the failure envelope is reached when any of $x_1, \ldots, x_n$ equals ± 1 (this represent the cases where the minimum or maximum uniaxial capacities are reached). Thus, the failure envelope is represented by $f(x_1, \ldots, x_n) = 1$, or in the usual convention, $f(x_1, \ldots, x_n) - 1 = 0$.

8.6.3 Step 3. Apply Uniaxial Loading Principles

The coefficients of all monomials containing only one variable must be 1. This is to correctly predict failure under uniaxial loading. Taking Eq. 8.20 as an example, a_1 and a_5 must be 1.

8.6.4 Step 4. Apply Symmetry Principles

Eliminate some of the unknown coefficients using symmetry principles. Consider Eq. 8.20 again. If the physics of the problem implies that $f(x_1, x_2) = f(-x_1, x_2)$, the coefficients of the monomials with x_1 of odd degree must be zero. Thus, a_2, a_4 in Eq. 8.20 must be zero.

8.6.5 Step 5. Set Up Convex Optimisation Problem

To identify the remaining unknown coefficients, a convex optimisation problem is set up, such that the unknown coefficients result in a failure envelope f that is closest (in a least squares sense) to the standardised data (obtained from Step 1) .

The objective is to find the unknown coefficients that make $f(\vec{x}_i) \approx 1$, for each row of standardised data $\vec{x}_i$. Thus, the objective function f_{obj} to minimise is:

$$f_{\text{obj}} = \sum_{i=1}^{k} \left(f(\vec{x}_i) - 1\right)^2 \tag{8.21}$$

where k is the number of rows of data.

To guarantee global convexity of the failure envelope, the following SOS constraint is applied to the Hessian $\nabla^2 f$ of the failure envelope f:

$$\vec{s}^{\mathsf{T}} \left(\nabla^2 f(\vec{x})\right) \vec{s} \;\text{ is SOS }\; \forall \vec{x}, \vec{s} \in \text{domain of } f \tag{8.22}$$

Putting it altogether, the optimisation problem can be cast as:

$$\begin{aligned} &\underset{a_1,\ldots,a_n}{\text{minimize}} && f_{\text{obj}} \\ &\text{subject to} && \vec{s}^{\mathsf{T}} \left(\nabla^2 f(\vec{x})\right) \vec{s} \text{ is SOS } \; \forall \vec{x}, \vec{s} \end{aligned} \tag{8.23}$$

However, the optimisation problem cannot be solved in the form of Eq. 8.23, as most optimisation solvers cannot accept SOS constraints directly. Thus, the SOS program defined in Eq. 8.23 has to be converted into an equivalent semidefinite program using a MATLAB toolbox called 'YALMIP' (Löfberg 2004), which can convert a SOS program into an equivalent semidefinite program automatically (Löfberg 2009). Thus, the unknown coefficients of the failure envelope formulation can be identified readily with this toolbox.

8.7 Examples

The following two examples show how the proposed framework can be used with failure envelopes of vastly different shapes. First, the aforementioned methodology was followed to derive failure envelope formulations for the surface and caisson foundations analysed in Chapter 7. Second, the Model B failure envelope (Eq. 8.3) was made globally convex by redefining it within the proposed framework. YALMIP was used, in conjunction with the SeDuMi semidefinite solver (Sturm 1999), to solve the SOS programs.

8.7.1 Surface And Caisson Foundations in Chapter 7

Step 1. Standardise Data

The sequential swipe test results for the VHM failure envelopes from Chapter 7 were standardised according to Eq. 8.19. Since $\chi_{0-} = -\chi_0$ for the examples analysed in Chapter 7, the adopted centroid of the failure envelope data is $[V_c, H_c, M_c] = [0, 0, 0]$. Thus, $[V_r, H_r, M_r] = [V_0, H_0, M_0]$ and $\bar{V} = \tilde{V}, \bar{H} = \tilde{H}$ and $\bar{M} = \tilde{M}$. There are two standardised datasets (one for the surface foundation and one for the caisson), each of which contains $[\bar{V}_1, \bar{H}_1, \bar{M}_1], \ldots, [\bar{V}_k, \bar{H}_k, \bar{M}_k]$, where k is the number of rows of data. To speed up the optimisation process, 'redundancy' was eliminated from the datasets by rounding the data values to two decimal places and removing the duplicate rows.

Step 2. Define Failure Envelope Functional Form

Two failure envelope functional forms (f_4, f_6) were defined using 4th and 6th degree homogeneous polynomials as follows:

$$\begin{aligned} f_4(\bar{V}, \bar{M}, \bar{H}) = {} & \bar{H}^4 a_1 + \bar{H}^3 \bar{M} a_2 + \bar{H}^2 \bar{M}^2 a_3 + \bar{H} \bar{M}^3 a_4 + \bar{M}^4 a_5 + \bar{H}^3 \bar{V} a_6 \\ & + \bar{H}^2 \bar{M} \bar{V} a_7 + \bar{H} \bar{M}^2 \bar{V} a_8 + \bar{M}^3 \bar{V} a_9 + \bar{H}^2 \bar{V}^2 a_{10} + \bar{H} \bar{M} \bar{V}^2 a_{11} \\ & + \bar{M}^2 \bar{V}^2 a_{12} + \bar{H} \bar{V}^3 a_{13} + \bar{M} \bar{V}^3 a_{14} + \bar{V}^4 a_{15} \end{aligned} \tag{8.24}$$

$$\begin{aligned} f_6(\bar{V}, \bar{M}, \bar{H}) = {} & \bar{H}^6 a_1 + \bar{H}^5 \bar{M} a_2 + \bar{H}^4 \bar{M}^2 a_3 + \bar{H}^3 \bar{M}^3 a_4 + \bar{H}^2 \bar{M}^4 a_5 \\ & + \bar{H} \bar{M}^5 a_6 + \bar{M}^6 a_7 + \bar{H}^5 \bar{V} a_8 + \bar{H}^4 \bar{M} \bar{V} a_9 + \bar{H}^3 \bar{M}^2 \bar{V} a_{10} \\ & + \bar{H}^2 \bar{M}^3 \bar{V} a_{11} + \bar{H} \bar{M}^4 \bar{V} a_{12} + \bar{M}^5 \bar{V} a_{13} + \bar{H}^4 \bar{V}^2 a_{14} + \bar{H}^3 \bar{M} \bar{V}^2 a_{15} \\ & + \bar{H}^2 \bar{M}^2 \bar{V}^2 a_{16} + \bar{H} \bar{M}^3 \bar{V}^2 a_{17} + \bar{M}^4 \bar{V}^2 a_{18} + \bar{H}^3 \bar{V}^3 a_{19} + \bar{H}^2 \bar{M} \bar{V}^3 a_{20} \\ & + \bar{H} \bar{M}^2 \bar{V}^3 a_{21} + \bar{M}^3 \bar{V}^3 a_{22} + \bar{H}^2 \bar{V}^4 a_{23} + \bar{H} \bar{M} \bar{V}^4 a_{24} + \bar{M}^2 \bar{V}^4 a_{25} \\ & + \bar{H} \bar{V}^5 a_{26} + \bar{M} \bar{V}^5 a_{27} + \bar{V}^6 a_{28} \end{aligned} \tag{8.25}$$

Step 3. Apply Uniaxial Loading Principles

Set $a_1 = 1, a_5 = 1, a_{15} = 1$ in f_4 and $a_1 = 1, a_7 = 1, a_{28} = 1$ in f_6.

Step 4. Apply Symmetry Principles

Symmetry in $\bar{H}$ and $\bar{M}$ dictates that $f(\bar{V}, \bar{M}, \bar{H}) = f(\bar{V}, -\bar{M}, -\bar{H})$. Thus, $a_6, a_7, a_8, a_9, a_{13}, a_{14}$ in f_4 are all zero. Similarly, a_8, a_9, a_{10}, $a_{11}, a_{12}, a_{13}, a_{19}, a_{20}, a_{21}$, a_{22}, a_{26}, a_{27} in f_6 are all zero.

Step 5. Set Up Convex Optimisation Problem

The SOS program in YALMIP was set up according to Eq. 8.23 (where f in Eq. 8.23 refers to either f_4 or f_6) and the remaining unknown coefficients were solved for.

Table 8.1: Best-fit coefficients in f_4 for the failure envelope data

Foundation	a_2	a_3	a_4	a_{10}	a_{11}	a_{12}
Surface	-0.36	0.9	-1.43	0.4	0.84	1.64
Caisson	3.55	5.12	3.51	1.72	3.59	2.07

Table 8.2: Best-fit coefficients in f_6 for the failure envelope data

Foundation	a_2	a_3	a_4	a_5	a_6	a_{14}	a_{15}
Surface	-0.33	1.22	-2.17	2.34	-1.86	0.03	0.34
Caisson	5.18	11.9	15.45	11.96	5.2	2.72	10.86
	a_{16}	a_{17}	a_{18}	a_{23}	a_{24}	a_{25}	
Surface	1.1	0.29	0.84	1.97	1.52	4.72	
Caisson	17.27	13.23	4.21	2.13	2.93	1.04	

Table 8.3: Minimised objective values for f_4 and f_6 at the end of the optimisation process for the surface and caisson foundation results from Chapter 7.

Foundation	min. f_{obj} for f_4	min. f_{obj} for f_6
Surface	36.96	31.05
Caisson	20.3	20.35

Results

Based on the optimisation results, the remaining unknown coefficients for f_4 and f_6 are listed in Tables 8.1 and 8.2 respectively. Figs. 8.3 and 8.4 compare the VH, VM and HM failure envelopes predicted by f_4, f_6 with the 3DFE results for the surface and caisson foundations analysed in Chapter 7. The differences between f_4 and f_6 can be seen more clearly in Fig. 8.5, which shows the HM failure envelopes predicted by f_4 and f_6, without the 3DFE results. The complete failure envelopes are shown here, so as to demonstrate that f_4 and f_6 are properly defined in all quadrants.

It is clear that both f_4 and f_6 are reasonably good approximations of the 3DFE failure envelope results; although there are some slight underprediction of the VM failure envelope for the suction caisson (see Fig. 8.4b). It can be observed that f_6 agrees better with the 3DFE results than f_4 for the surface foundation, but f_4 is marginally better for the caisson

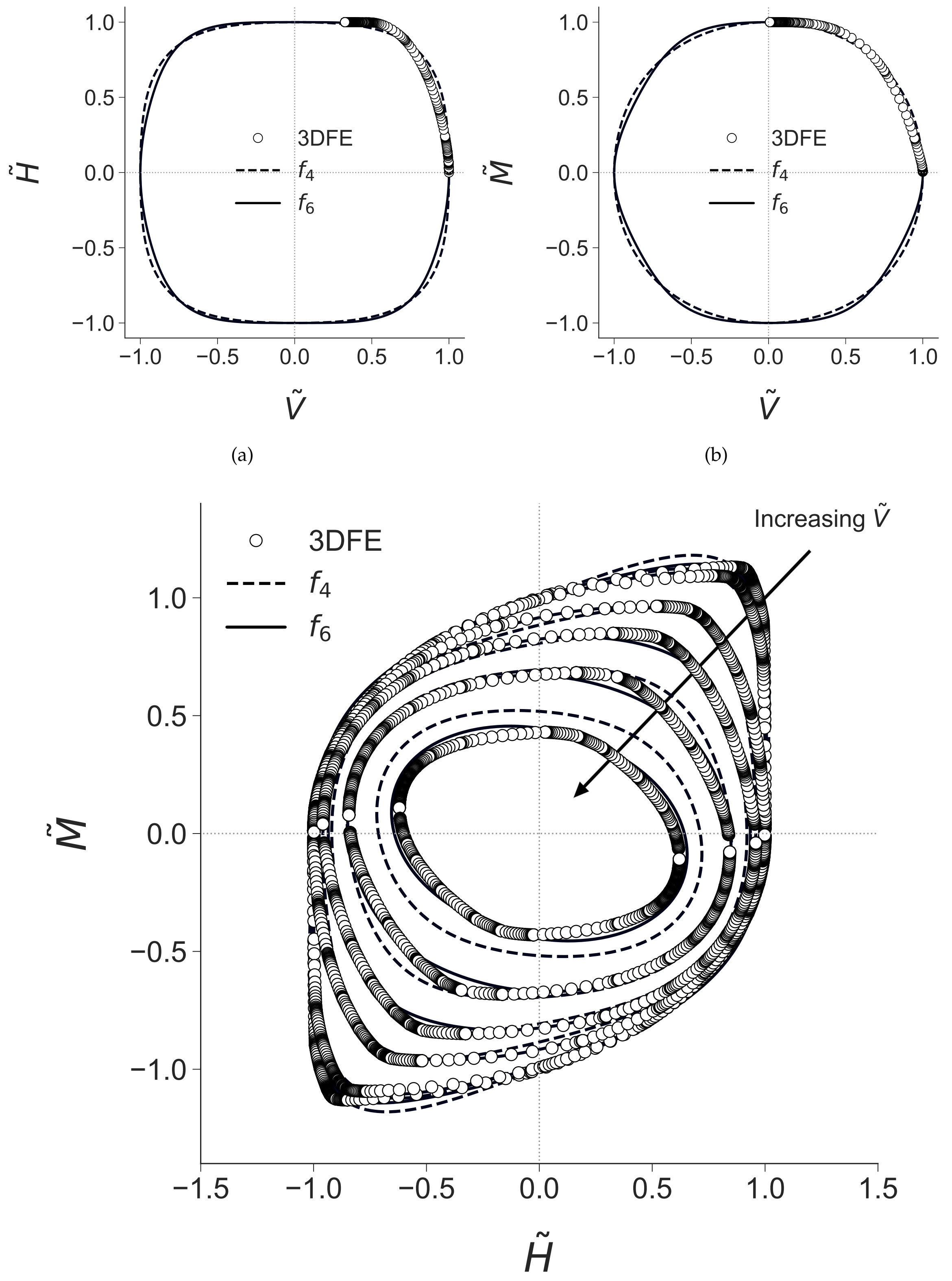

(a)

(b)

(c)

Figure 8.3: Comparison of VH, VM and HM failure envelopes predicted by f_4, f_6 with the 3DFE results for a surface foundation. The HM envelopes correspond to the following vertical load levels: $\tilde{V} = 0, 0.25, 0.5, 0.625, 0.75, 0.875$. The 3DFE results are from the sequential swipe test results in Chapter 7.

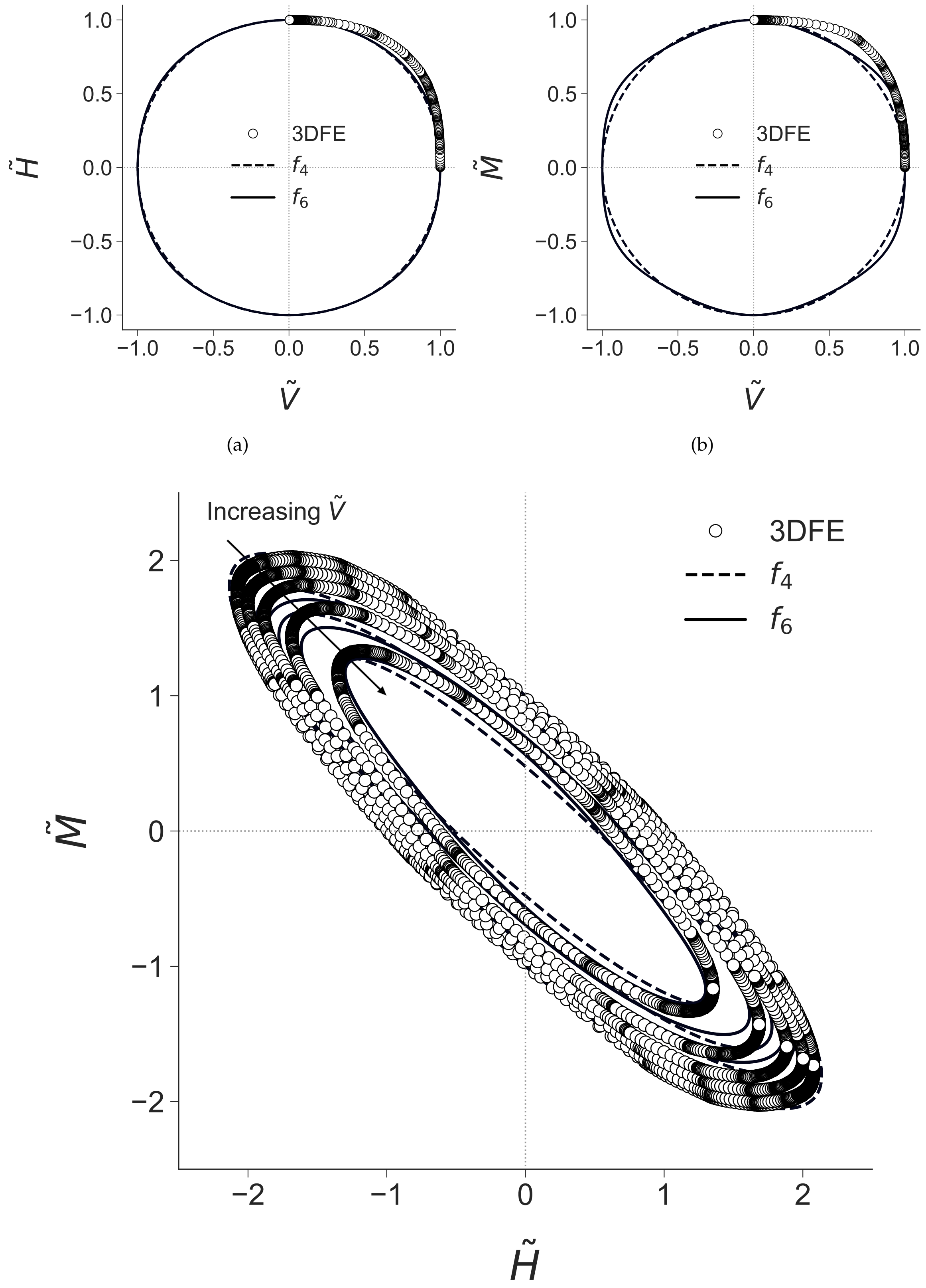

(a)

(b)

(c)

Figure 8.4: Comparison of VH, VM and HM failure envelopes predicted by f_4, f_6 with the 3DFE results for a suction caisson foundation. The HM envelopes correspond to the following vertical load levels: $\tilde{V} = 0, 0.25, 0.5, 0.625, 0.75, 0.875$. The 3DFE results are from the sequential swipe test results in Chapter 7.

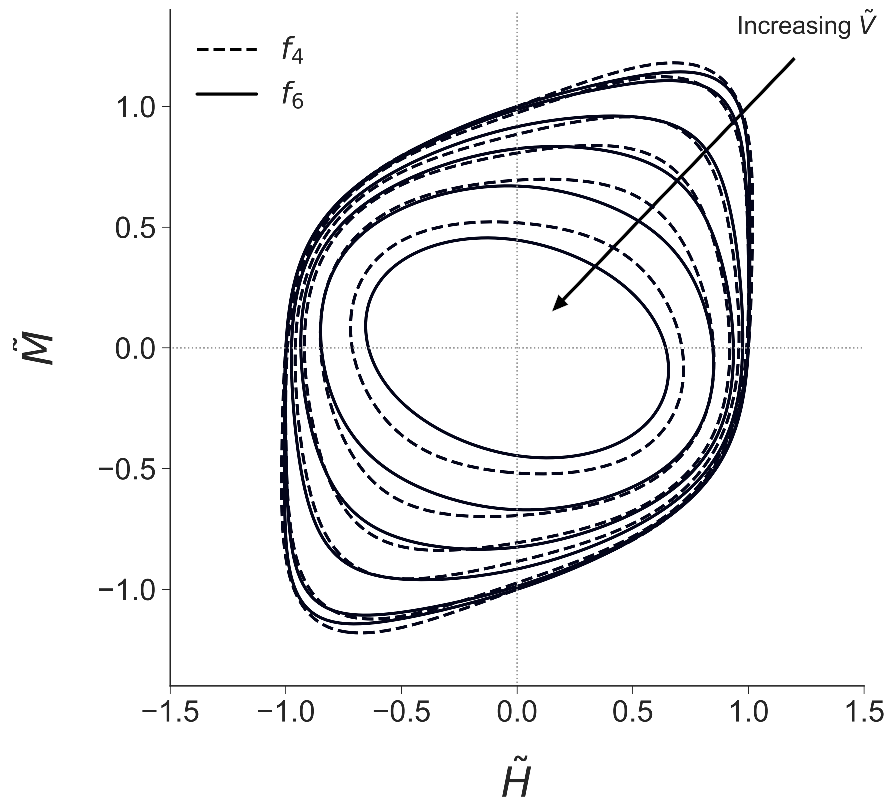

(a)

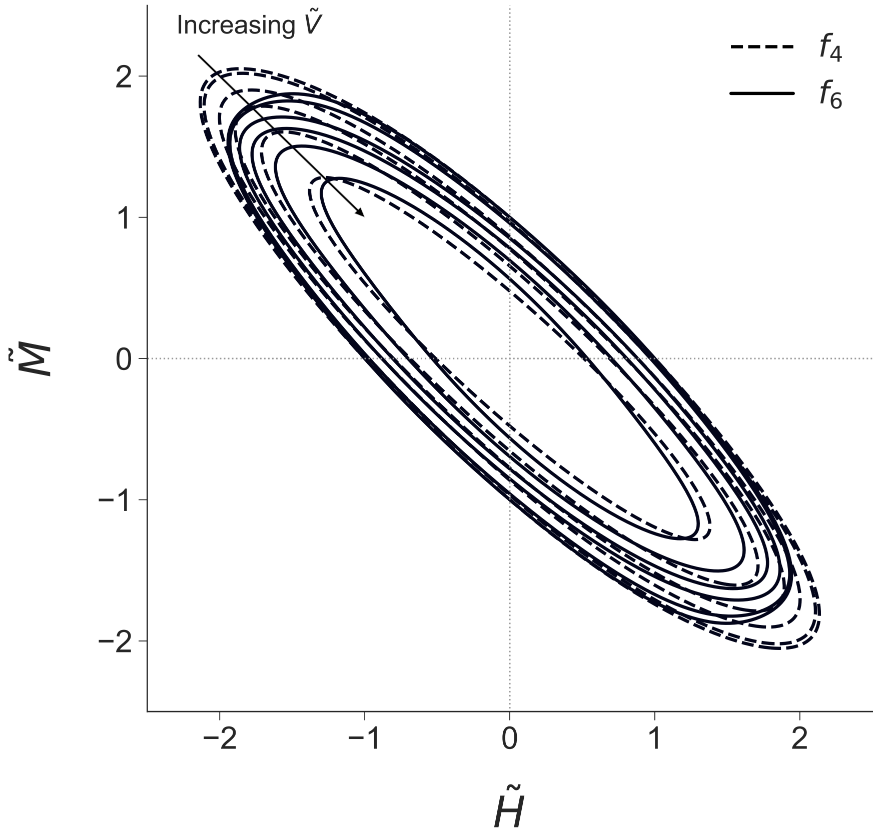

(b)

Figure 8.5: Comparison of HM failure envelopes predicted by f_4 and f_6, under increasing vertical loading (i.e. $\tilde{V} = 0, 0.25, 0.5, 0.625, 0.75, 0.875$) (a) Surface foundation (b) Suction caisson foundation.

(see Fig. 8.4c). This is corroborated by Table 8.3, which shows the minimised values of the objective function at the end of the optimisation process (the smaller the better).

8.7.2 Model B

Step 1. Standardise Data

Failure envelope data was generated using Eq. 8.3, in the form of the $\tilde{V}\tilde{H}$ failure envelope, $\tilde{V}\tilde{M}$ failure envelope and the $\tilde{H}\tilde{M}$ failure envelopes for $\tilde{V} = 0.125, 0.25, 0.375, 0.5, 0.625, 0.75, 0.875$. The data was standardised according to Eq. 8.19 but unlike the previous example, $\bar{\chi} \neq \tilde{\chi}$. The adopted centroid of the failure envelope data is $[\tilde{V}_\mathrm{c}, \tilde{H}_\mathrm{c}, \tilde{M}_\mathrm{c}] = [0.5, 0, 0]$. Thus, $[\tilde{V}_\mathrm{r}, \tilde{H}_\mathrm{r}, \tilde{M}_\mathrm{r}] = [0.5, 0.995, 0.995]$ and $[\bar{V}, \bar{H}, \bar{M}] = [(\tilde{V} - 0.5)/0.5, \tilde{H}/0.995, \tilde{M}/0.995]$. The standardised dataset contains $[\bar{V}_1, \bar{H}_1, \bar{M}_1], \ldots, [\bar{V}_k, \bar{H}_k, \bar{M}_k]$, where k is the number of rows of data. ‘Redundancy’ was eliminated from the dataset using the same procedure as the previous example.

Step 2. Define Failure Envelope Functional Form

The same failure envelope functional forms (f_4, f_6) (i.e. Eqs. 8.24 and 8.25) were used here.

Step 3. Apply Uniaxial Loading Principles

Set $a_1 = 1, a_5 = 1, a_{15} = 1$ in f_4 and $a_1 = 1, a_7 = 1, a_{28} = 1$ in f_6.

Step 4. Apply Symmetry Principles

Symmetry in $\bar{H}$ and $\bar{M}$ dictates that $f(\bar{V}, \bar{M}, \bar{H}) = f(\bar{V}, -\bar{M}, -\bar{H})$. Thus, $a_6, a_7, a_8, a_9, a_{13}, a_{14}$ in f_4 are all zero. Similarly, a_8, a_9, a_{10}, $a_{11}, a_{12}, a_{13}, a_{19}, a_{20}, a_{21}$, a_{22}, a_{26}, a_{27} in f_6 are all zero.

Step 5. Set Up Convex Optimisation Problem

The SOS program in YALMIP was set up according to Eq. 8.23 (where f in Eq. 8.23 refers to either f_4 or f_6) and the remaining unknown coefficients were solved for.

Results

Based on the optimisation results, the remaining unknown coefficients for f_4 and f_6 are listed in Tables 8.4 and 8.5 respectively. Fig. 8.6 compares the VH, VM and HM failure envelopes predicted by f_4, f_6 with the original Model B equation (Eq. 8.3). It is clear that both

Table 8.4: Best-fit coefficients in f_4 for the Model B failure envelope data

a_2	a_3	a_4	a_{10}	a_{11}	a_{12}
-0.86	2	-0.86	3.48	-2.93	3.48

Table 8.5: Best-fit coefficients in f_6 for the Model B failure envelope data

a_2	a_3	a_4	a_5	a_6	a_{14}	a_{15}	a_{16}	a_{17}	a_{18}	a_{23}	a_{24}	a_{25}
-1.35	3.59	-2.74	3.59	-1.35	3.56	-4.94	8.94	-4.94	3.56	7.37	-6.59	7.37

Table 8.6: Minimised objective values for f_4 and f_6 at the end of the optimisation process for the Model B equation (Eq. 8.3).

	min. f_{obj} for f_4	min. f_{obj} for f_6
Model B	8.23	11.22

f_4 and f_6 are reasonably good approximations of the original Model B equation. Table 8.6 shows the minimised objective values for f_4 and f_6 at the end of the optimisation process, which suggests that f_4 agrees better with the original Model B equation than f_6.

Fig. 8.6a, b show that the ends of f_4 and f_6 at $\tilde{V} = 0$ and $\tilde{V} = 1$ are more 'rounded' than that of Model B, and the gradients there point along the $\tilde{V}$ axis (correctly predicting vertical plastic displacement under pure vertical loading, if associated flow is assumed). This is of particular interest, as much work (Martin 1994) has previously gone into achieving such a behaviour with Model B. In general, the results show that the framework can provide a globally convex and well-behaved representation of Model B that is reasonably close to the original form.

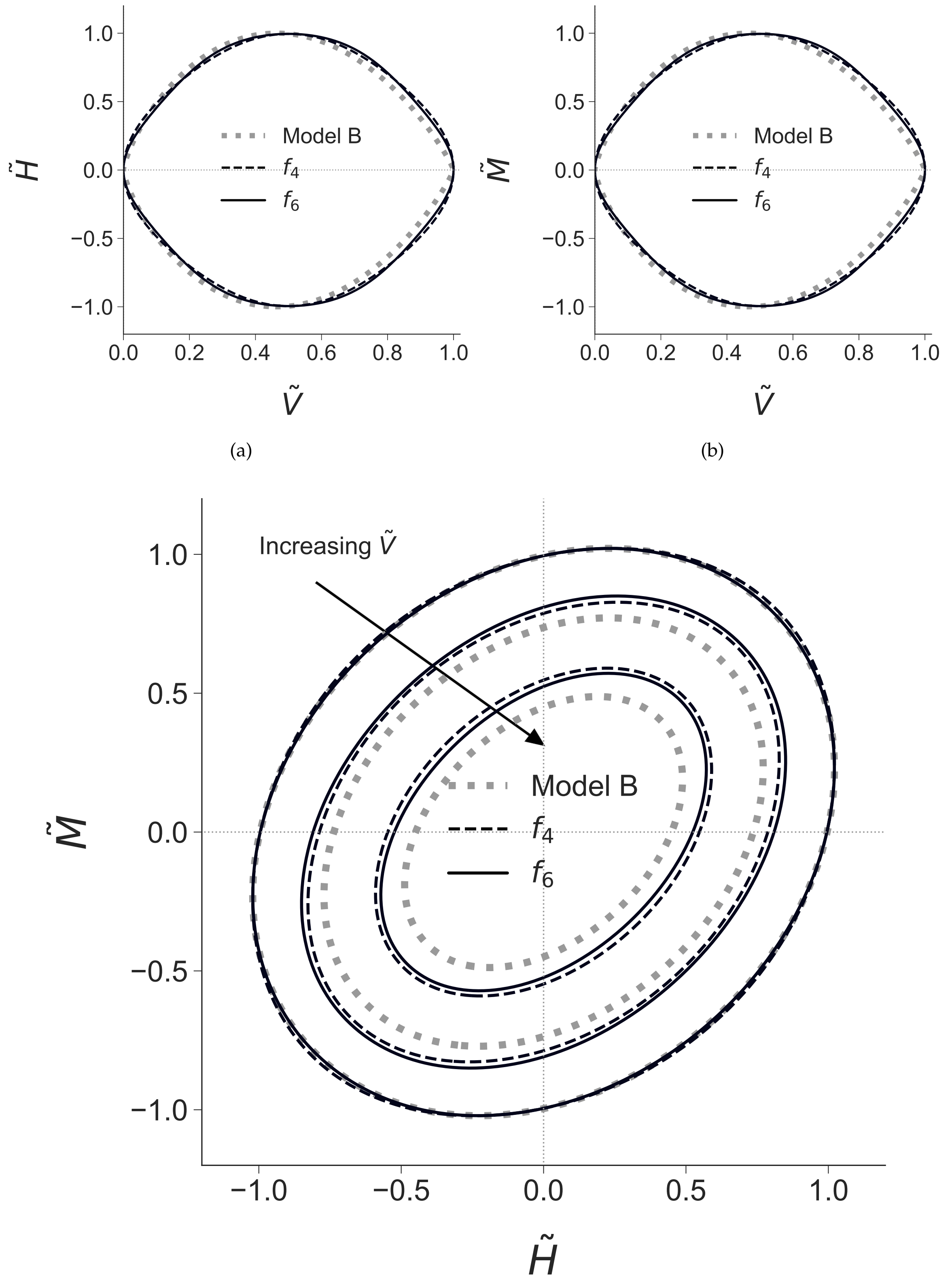

(a)

(b)

(c)

Figure 8.6: Comparison of VH, VM, and HM failure envelopes predicted by f_4, f_6 with the original Model B equation. The HM failure envelopes correspond to the following vertical load levels: $\tilde{V} = 0.5, 0.75, 0.875$.

8.7.3 Discussion

A key observation from the above results is that higher degree polynomials do not necessarily mean better fits. For example, f_6 agrees better with the 3DFE results for the surface foundation than f_4, but the opposite is true for the caisson. This may seem counter-intuitive from experience with one-dimensional, general polynomial curve-fitting, but the characteristics of homogeneous polynomials are different from that of general polynomials.

Lower degree, general polynomials can always be represented perfectly with higher degree, general polynomials, but lower degree, homogeneous polynomials cannot be represented perfectly with higher degree, homogeneous polynomials. For example, a circle of radius 1 (i.e. a 2^{nd} degree, homogeneous polynomial $x^2 + y^2 = 1$) cannot be represented perfectly with a 4^{th} degree, homogeneous polynomial. Thus, it is generally recommended to try a lower degree homogenous polynomial in Step 2, before going for higher degrees.

To show that f_4 and f_6 are SOS-convex, their Hessian conditions (i.e. Eq. 8.22) may be decomposed into SOS forms. For example, for f_4 in the Model B example, the Hessian condition can be decomposed into SOS form using YALMIP as:

$$
\begin{aligned}
\vec{s}^{\mathsf{T}}\left(\nabla^2 f_4(\vec{x})\right)\vec{s} = {} & \left(-3.2753\bar{V}\bar{V}_1 - 3.0429\bar{M}\bar{M}_1 + 0.9482\bar{M}\bar{H}_1 + 0.9482\bar{H}\bar{M}_1 - 3.0429\bar{H}\bar{H}_1\right)^2 \\
& + \left(-2.0892\bar{V}\bar{M}_1 + 2.0892\bar{V}\bar{H}_1 - 2.0892\bar{M}\bar{V}_1 + 2.0892\bar{H}\bar{V}_1\right)^2 \\
& + \left(-1.1810\bar{V}\bar{M}_1 - 1.1810\bar{V}\bar{H}_1 - 1.1810\bar{M}\bar{V}_1 - 1.1810\bar{H}\bar{V}_1\right)^2 \\
& + \left(1.5231\bar{M}\bar{M}_1 - 1.5231\bar{H}\bar{H}_1\right)^2 \\
& + \left(-1.2962\bar{M}\bar{H}_1 + 1.2962\bar{H}\bar{M}_1\right)^2 \\
& + \left(0.1446\bar{V}\bar{V}_1 + 0.2929\bar{M}\bar{M}_1 + 1.1897\bar{M}\bar{H}_1 + 1.1896\bar{H}\bar{M}_1 + 0.2929\bar{H}\bar{H}_1\right)^2 \\
& + \left(0.7876\bar{V}\bar{M}_1 + 0.7875\bar{V}\bar{H}_1 - 0.7876\bar{M}\bar{V}_1 - 0.7875\bar{H}\bar{V}_1\right)^2 \\
& + \left(0.7618\bar{V}\bar{M}_1 - 0.7619\bar{V}\bar{H}_1 - 0.7618\bar{M}\bar{V}_1 + 0.7619\bar{H}\bar{V}_1\right)^2 \\
& + \left(1.1186\bar{V}\bar{V}_1 - 0.5788\bar{M}\bar{M}_1 + 0.0746\bar{M}\bar{H}_1 + 0.0745\bar{H}\bar{M}_1 - 0.5788\bar{H}\bar{H}_1\right)^2
\end{aligned}
\tag{8.26}
$$

where $\vec{x} = [\bar{V}, \bar{M}, \bar{H}]^{\mathsf{T}}, \vec{s} = [\bar{V}_1, \bar{M}_1, \bar{H}_1]^{\mathsf{T}} \in$ domain of f_4. It is clear from Eq. 8.26 that $\vec{s}^{\mathsf{T}}\left(\nabla^2 f_4(\vec{x})\right)\vec{s} \geq 0$ throughout its domain and thus, f_4 is convex.

Interestingly, although the SOS constraint was applied to the Hessian condition (i.e. $\vec{s}^{\mathsf{T}}\left(\nabla^2 f_4(\vec{x})\right)\vec{s}$) and not the function (i.e. f_4) itself, the resultant f_4 in the Model B example turns out to be an SOS polynomial, as shown below:

$$
\begin{aligned}
f_4(\vec{x}) = {} & (1.4695\bar{H}\bar{V} - 1.4695\bar{M}\bar{V})^2 \\
& + \left(-0.4415\bar{H}^2 + 1.3770\bar{H}\bar{M} - 0.4415\bar{M}^2 - 0.3958\bar{V}^2\right)^2 \\
& + (1.0047\bar{H}\bar{V} + 1.0047\bar{M}\bar{V})^2 \\
& + \left(0.7205\bar{H}^2 - 0.7205\bar{M}^2\right)^2 \\
& + \left(0.1189\bar{H}^2 + 0.3311\bar{H}\bar{M} + 0.1189\bar{M}^2 + 0.8867\bar{V}^2\right)^2 \\
& + \left(-0.5214\bar{H}^2 - 0.2656\bar{H}\bar{M} - 0.5214\bar{M}^2 + 0.2390\bar{V}^2\right)^2
\end{aligned}
\tag{8.27}
$$

Thus, not only is the Hessian of f_4 positive semidefinite, f_4 itself is non-negative.

8.8 Strengths and Limitations

The proposed failure envelope formulation framework resolves the aforementioned issues with existing failure envelope formulations and offers several key advantages over them:

1. It is systematic and removes a lot of guesswork from the formulation process.
2. It is general and can be applied to any failure envelope dataset of arbitrary loading dimensions. In fact, as long as the dataset is standardised accordingly, this framework can be used as a general multi-dimensional convex hypersurface fitting framework for any point cloud dataset.
3. It produces failure envelope formulations that are guaranteed to be globally convex.
4. It produces failure envelope formulations that are guaranteed to be thermodynamically consistent, if they are used as plastic potentials (to support associated flow).
5. It produced well-behaved formulations that are easily differentiable and integrable.

Chapter 9

Cohesive Soil

In Section 2.5, a new class of Winkler models, called 'Elasto-plastic Winkler model', was introduced. In this chapter, the required soil reaction yield surfaces f for predicting suction caisson behaviour in homogeneous, undrained clay (assuming no separation at the soil-foundation interface) are derived through calibration against 3DFE analyses. In previous numerical studies, undrained clay was modelled as an incompressible, elasto-plastic, cohesive material with either the Tresca or von Mises yield criterion. For convenience, clay modelled using the Tresca and von Mises yield criteria will be referred to as 'Tresca soil' and 'von Mises soil' respectively. Before looking at the general suction caisson problem, it is apt to look at the simpler surface foundation problem to gain familiarity with the derivation process for the soil reaction yield surface formulation.

9.1 Surface Foundations

This section looks at the derivation of a failure envelope formulation, that approximates the computed failure envelope (from 3DFE analyses) for a rigid, circular surface foundation on undrained clay under 6DoF loading. The failure envelope for a circular surface foundation is equivalent to the yield surface of the base soil reaction for a suction caisson of $L/D = 0$.

9.1.1 Introduction

The failure envelope problem for a rigid, circular surface foundation on undrained clay is a well-researched one (Taiebat & Carter 2000, Gourvenec & Randolph 2003, Randolph & Puzrin 2003, Vulpe et al. 2014, Shen et al. 2017). However, most of the previous research determine the failure envelopes for surface foundations under planar VHM loading, instead of the general 6DoF loading. The failure envelope formulations in Eqs. 9.1 and 9.2 have been proposed by Taiebat & Carter (2000) and Vulpe et al. (2014) respectively, for a rigid, circular surface foundation on Tresca soil under planar VHM loading:

$$f(\tilde{V},\tilde{H},\tilde{M}) = \tilde{V}^2 + \left(\tilde{M}\left(1 - 0.3\tilde{H}\operatorname{sgn}(\tilde{M})\right)\right)^2 + \left|\tilde{H}^3\right| - 1 \tag{9.1}$$

$$f(\tilde{V},\tilde{H},\tilde{M}) = \left(\left|\frac{\tilde{H}}{\xi_{\mathrm{H}}}\right|\right)^a + \left(\frac{\tilde{M}}{\xi_{\mathrm{M}}}\right)^a + 2b\left(\frac{\tilde{H}\tilde{M}}{\xi_{\mathrm{H}}\xi_{\mathrm{M}}}\right) - 1 \tag{9.2}$$

where

$$\begin{aligned} a &= 2.13 \text{ if } \tilde{V} \leq 0.5 \text{ else } 1.63 \\ b &= -0.26 \text{ if } \tilde{V} \leq 0.5 \text{ else } -0.05 \\ \xi_{\mathrm{H}} &= 1 - \tilde{V}^{4.69} \\ \xi_{\mathrm{M}} &= 1 - \tilde{V}^{2.12} \end{aligned}$$

Based on his Model B failure envelope formulation for spudcan foundations in clay under planar VHM loading (Eq. 8.3), Martin (1994) proposed the following extension to support 6DoF loading:

$$\begin{aligned} f(\tilde{Q},\tilde{V},\tilde{H}_{\mathrm{y}},\tilde{M}_{\mathrm{x}},\tilde{H}_{\mathrm{x}},\tilde{M}_{\mathrm{y}}) = {} & \left(\tilde{H}_{\mathrm{x}}{}^2 + \tilde{H}_{\mathrm{y}}{}^2\right) + \left(\tilde{M}_{\mathrm{x}}{}^2 + \tilde{M}_{\mathrm{y}}{}^2\right) \\ & - b\tilde{V}^{2\beta_1}\left(1 - \tilde{V}^{2\beta_2}\right) + \tilde{Q}^2 \\ & - 2a\left(\tilde{H}_{\mathrm{y}}\tilde{M}_{\mathrm{x}} - \tilde{H}_{\mathrm{x}}\tilde{M}_{\mathrm{y}}\right) \end{aligned} \tag{9.3}$$

where a, b, β_1, β_2 are fitting parameters. Eq. 9.3 was later adopted by Bienen et al. (2006) and Salciarini & Tamagnini (2009) for the yield surfaces of their macro-element models for circular, surface foundations on sand. Note that Eq. 9.3 assumes no horizontal, moment or torsional capacity, if no vertical loading is applied. Thus, it is not applicable for the numerical study in this chapter, where there are horizontal, moment and torsional capacities at zero vertical load. Nevertheless, a comparison will be made later to see the difference between Eq. 9.3 and the derived failure envelope formulation.

Recently, Shen et al. (2017) investigated the failure envelope for a rigid, circular surface foundation on Tresca soil under 6DoF loading. They found that the HM failure envelope changes when H and M are non-planar. However, they were not able to derive a failure envelope formulation that captures the variation of the failure envelope with different H and M directions. Thus, they proposed the following formulation, which approximates a conservative, lower bound failure envelope for all possible H and M directions:

$$\left(\frac{\tilde{H}}{\xi_{\mathrm{H}}}\right)^2 + \left(\frac{\tilde{M}}{\xi_{\mathrm{M}}}\right)^a \left(1 - b\frac{\tilde{H}}{\xi_{\mathrm{H}}}\right) - 1 = 0 \tag{9.4}$$

where

$$a = 2.1 + 0.2(1 + \mathrm{sgn}(\tilde{H})) - (1.1 - 0.1(1 + \mathrm{sgn}(\tilde{H})))\tilde{V} + (2.4 - 1.8(1 + \mathrm{sgn}(\tilde{H})))\tilde{V}^2$$

$$b = 0.5 + 0.1(1 + \mathrm{sgn}(\tilde{H})) - 0.1\tilde{V} - 0.6\tilde{V}^2$$

$$\xi_{\mathrm{H}} = \xi_{\mathrm{H0}} \left(1 - \left(\frac{\tilde{Q}}{\xi_{\mathrm{Q}}}\right)^{1.75}\right)^{0.571}$$

$$\xi_{\mathrm{M}} = \left(1 - \tilde{V}^{3.57}\right) \left(1 - \left(\frac{\tilde{Q}}{\xi_{\mathrm{Q}}}\right)^{1.5+0.1\tilde{V}+1.4\tilde{V}^2}\right)^{\frac{1}{5.3+\tilde{V}-6\tilde{V}^2}}$$

$$\xi_{\mathrm{Q}} = 1 \text{ if } \tilde{V} \leq 0.5 \text{ else } \left(1 - (2\tilde{V} - 1)^4\right)^{0.4}$$

$$\xi_{\mathrm{H0}} = 1 \text{ if } \tilde{V} \leq 0.5 \text{ else } \left(1 - (2\tilde{V} - 1)^2\right)^{0.667}$$

Although the failure envelope problem for a rigid, circular surface foundation on clay has been well-researched, there are still some issues that have not been addressed in previous studies. First, there is currently no failure envelope formulation for 6DoF loading, that predicts non-zero horizontal, moment and torsional capacities at zero vertical load, and captures the variation of the failure envelope with different H and M directions. This is required to properly approximate the failure envelope data in the current numerical study. Second, Eq. 9.4 is unsuited for use as a yield surface or plastic potential in macro-element or Winkler models, as it is unwieldy to differentiate and the gradient is undefined at $\tilde{V} = 1$ due to a singularity there. Furthermore, Eq. 9.4 is undefined for negative Q, V and M, making it unsuitable for use in numerical models that accept general 6DoF loading inputs (which may be positive or negative valued). Lastly, most of the existing formulations are not globally convex (hence disallowing the use of efficient, implicit elasto-plastic integration algorithms) and are not guaranteed to be thermodynamically consistent (if used as plastic potentials).

To address the above issues, 3DFE analyses of a rigid, circular surface foundation on undrained clay under 6DoF loading were carried out to determine the failure envelope. The clay was modelled as a linear elastic, perfectly plastic soil with a von Mises yield criterion. Using the 3DFE results and the framework introduced in Chapter 8, a more robust failure envelope formulation for a rigid, circular surface foundation on clay under 6DoF loading is derived, where the variation of the failure envelope with different H and M directions is properly captured in the formulation. The proposed failure envelope is globally convex, which allows efficient, implicit elasto-plastic integration algorithms to be used. Moreover, it is guaranteed to be thermodynamically consistent, if used as a plastic potential.

9.1.2 Methodology

This section describes the 3DFE modelling that was performed to determine the failure envelope for a circular surface foundation under 6DoF loading. The 3DFE model consists of a rigid, circular surface foundation of diameter D on homogeneous elasto-plastic soil.

Mesh

The diameter and depth of the mesh domain were set to $6D$ and $2.5D$ respectively, which was verified to be large enough to avoid boundary effects. Mesh convergence analyses were carried out to determine the mesh fineness. A representative mesh is shown in Fig. 9.1.

Material Properties

The soil was defined as a homogeneous, isotropic linear elastic, perfectly plastic material, where the undrained shear strength s_u is uniform throughout the soil domain. A von Mises yield criterion with an associated flow rule was adopted for the soil model. The soil and foundation were modelled as weightless materials, as soil weight does not affect the failure states. The Poisson's ratio ν of the soil was set to 0.49, while its Young's modulus E was set to $1000\sqrt{3}s_\mathrm{u}$, although this may be set arbitrarily as the elastic behavior does not affect the final failure states (Chen & Liu 1990). First-order, fully-integrated, linear, brick elements C3D8H were assigned to the soil elements. The surface foundation was made entirely rigid using rigid body constraints. The reference point was set at the centre of its base. Separation at the soil-foundation interface was prevented using tie constraints.

Boundary Conditions

Definition 9.1 (*m*-swipe sequential swipe test) *An m-swipe sequential swipe test is defined to be a sequential swipe test with m equally spaced displacement increments in each quadrant of the displacement space (as described in Chapter 7).*

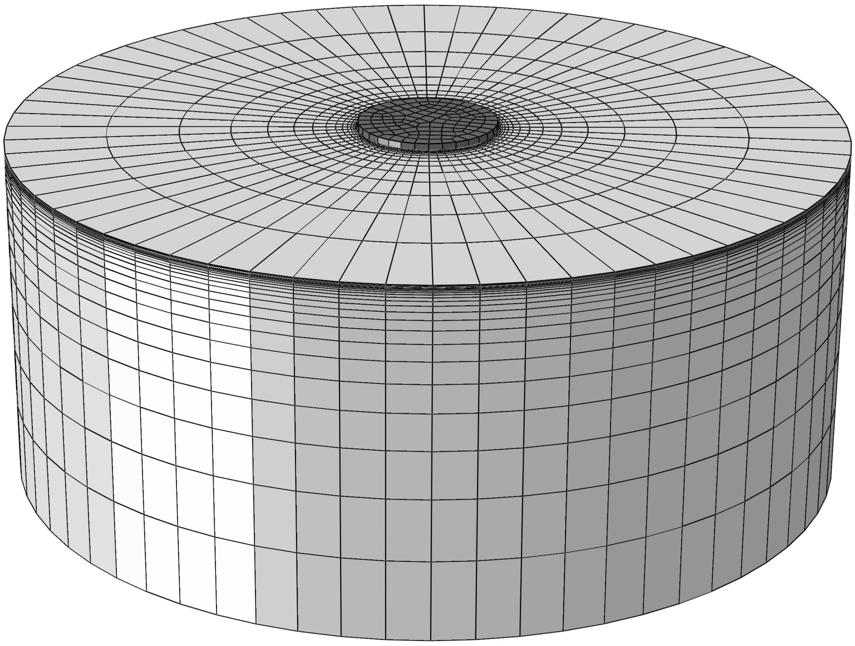

(a)

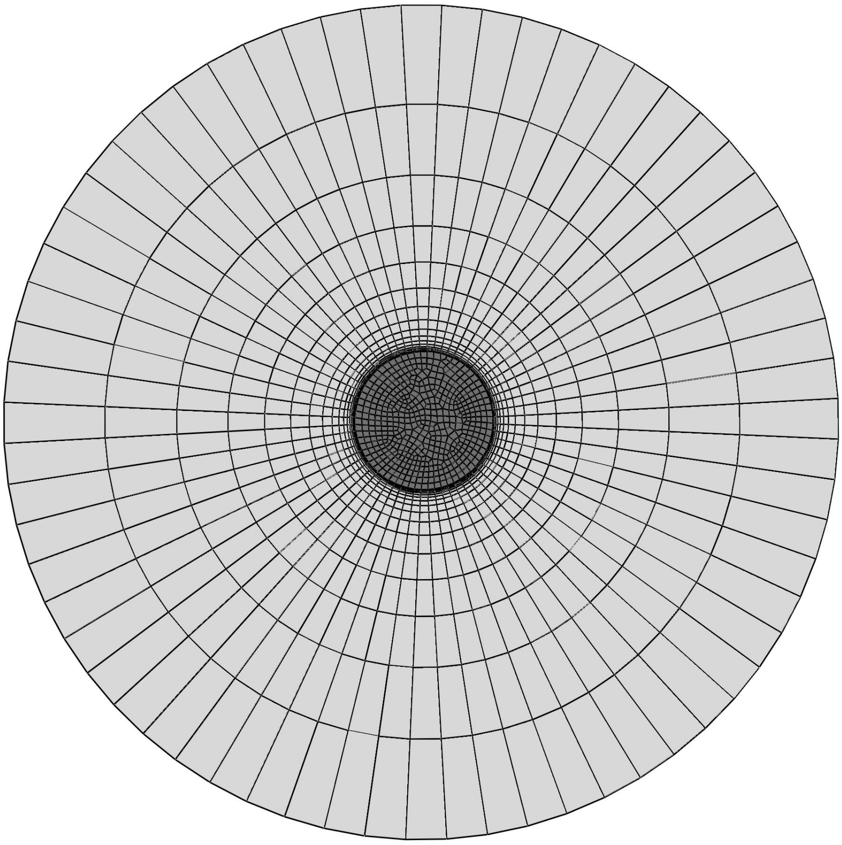

(b)

Figure 9.1: (a) Oblique view of the full 3DFE model. The diameter and depth of the mesh domain are $6D$ and $2.5D$ respectively. (b) Plan view of the full 3DFE model.

First, the uniaxial load capacities (Q_0, V_0, H_0, M_0) of the surface foundation were obtained by prescribing translations of $0.1D$ and rotations of 0.1 in the respective axes (e.g. S_z for V_0), which was sufficiently large to reach capacity (i.e. the load had reached steady state). Next, HM failure envelope was determined using 16-swipe sequential swipe tests, while load boundary conditions were set in the Q and V spaces (i.e. the $QVHM$ failure envelope was explored by finding HM contours of the failure envelope at fixed levels of Q and V). Four torsional and vertical load levels were each applied: $\tilde{Q} = 0, 0.25, 0.5, 0.75$ and $\tilde{V} = 0, 0.25, 0.5, 0.75$. Thus, there are 16 distinct combinations of $\tilde{Q}$-$\tilde{V}$ loadings applied.

Definition 9.2 ($H_\mathrm{i}, M_\mathrm{j}, M_\mathrm{j}', \alpha_{\mathrm{HM}'}$) *$H_\mathrm{i}$ and M_j are the lateral and moment loads along some general axes i, j, which can be the x-axis, y-axis or any axis on the x-y plane. The absolute axis directions of H_i and M_j are not important. What is important is the relative direction of one axis to the other, which is represented by a parameter $\alpha_{\mathrm{HM}'}$. $\alpha_{\mathrm{HM}'}$ is the angle between the H_i and M_j' axes, where the M_j' axis is clockwise orthogonal to the M_j axis (see Fig. 9.2). Conveniently, $\alpha_{\mathrm{HM}'} = 0$ represents the standard, planar HM loading case as described by Butterfield et al. (1997).*

$\alpha_{\mathrm{HM}'}$ is not defined as the angle between the H_i and M_j axes, as this definition cannot differentiate between $\pm H_\mathrm{i}$ or $\pm M_\mathrm{j}$ for planar HM loading. For planar HM loading, the angle between H_i and M_j is always 90 degrees, regardless of whether they are positive or negative valued. This implies that the results should be identical in all HM quadrants, which is not true. Thus, there is a need for another reference M_j'. For planar HM loading, the angle between H_i and M_j' (or -H_i and -M_j') is 0 degree, while the angle between $-H_\mathrm{i}$ and M_j' (or H_i and -M_j') is 180 degrees. This definition is able to distinguish the correct symmetry of these various loading scenarios.

The HM failure envelopes were determined for planar and non-planar HM loading. To obtain the HM failure points for different $\alpha_{\mathrm{HM}'}$ values, the sequential swipe test was carried out by applying the rotation Θ_x along the x-axis, while the lateral displacement S_H was applied along three axes ($\alpha_{\mathrm{S}\Theta} = 0, \pi/4, \pi/2$) (see Fig. 9.3). Note that the resultant H may not be co-directional with the S_H direction (i.e. $\alpha_{\mathrm{S}\Theta} \neq \alpha_{\mathrm{HM}'}$), as the elasto-plastic stiffness matrix of the foundation may not be diagonal. Thus, the resultant H from $\alpha_{\mathrm{S}\Theta} = \pi/4$ correspond to a range of $\alpha_{\mathrm{HM}'}$ values.

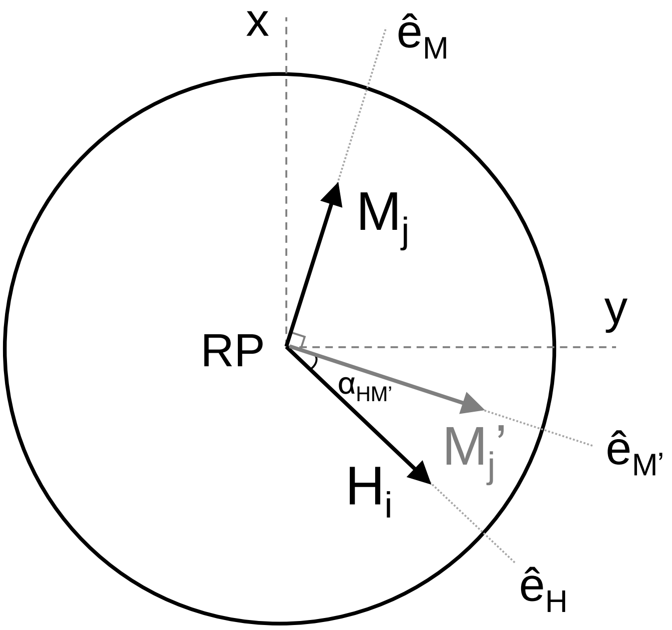

Figure 9.2: Conventions adopted for general *H-M* loading.

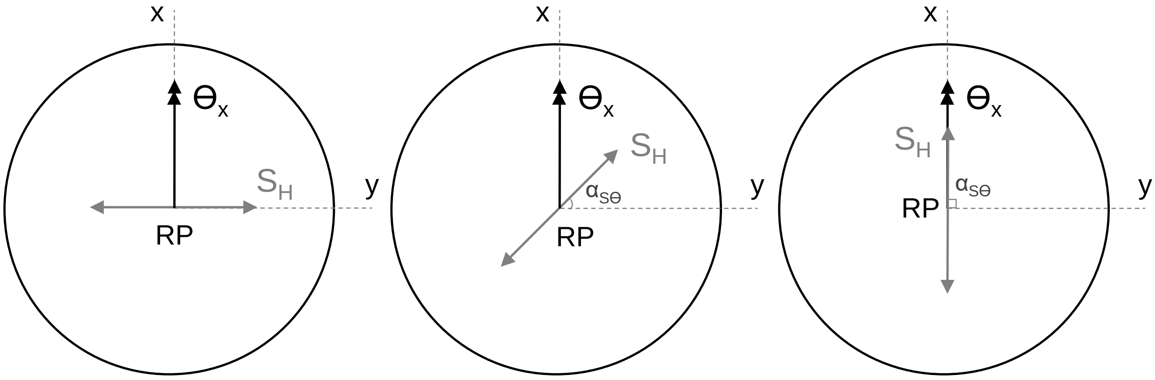

Figure 9.3: Displacement boundary conditions applied for *H-M* loading.

Validation

To validate that the 3DFE model has been set up correctly, Table 9.1 compares the 3DFE uniaxial load capacity results with the analytical solutions and 3D FELA results (from Chapter 7). It is evident that the 3DFE results agree well with the analytical solutions and the 3D FELA results, thus validating the 3DFE model. The torsional capacity slightly overestimates the analytical solution, as contact breaking is not allowed at the soil-foundation interface for the 3DFE model. For interested readers, the derivations of the analytical solutions are included in Appendix A.3. For the vertical capacity, the 3DFE computed value of 5.63 compares well with the known exact solutions (albeit for Tresca soil) of 5.69 (Shield 1955) and 6.05 (Eason & Shield 1960) for a smooth and rough surface foundation respectively.

Table 9.1: Uniaxial capacities of the surface foundation, where $A = \pi D^2/4$ refers to the foundation base area.

	$\frac{Q_0}{ADs_u}$	$\frac{V_0}{As_u}$	$\frac{H_0}{As_u}$	$\frac{M_0}{ADs_u}$
3DFE	0.344	5.63	1.04	0.73
3D FELA (LB)	-	5.45	1.00	0.667
3D FELA (UB)	-	5.77	1.00	0.715
3D FELA (Average)	-	5.61	1.00	0.691
Analytical	0.333	-	1	-

9.1.3 Results

The results of the $QVHM$ failure envelope are presented primarily in terms of its projections on the HM plane (i.e. HM contours), which are referred to as HM failure envelopes. Furthermore, the failure envelopes are presented in terms of the normalised loads ($\tilde{Q}, \tilde{V}, \tilde{H}_\mathrm{i}, \tilde{M}_\mathrm{j}$). Because of symmetry, the 3DFE results were obtained for only one or two quadrants. However, the predicted failure envelopes are shown for all quadrants.

VHM Failure Envelopes

Fig. 9.4 shows the variation of the HM failure envelopes under different V load levels, for $\alpha_{\mathrm{HM'}} = 0$ and $\tilde{Q} = 0$. It is evident that as V loading increases, the available HM capacity decreases, as depicted by the smaller HM failure envelopes. The drop in HM capacity is minor for $\tilde{V} \leq 0.5$, but increases rapidly for $\tilde{V} > 0.5$. Furthermore, the asymmetry in the HM space becomes negligble at high V loading (e.g. $\tilde{V} = 0.75$), indicating that V loading has significant influence on the interaction between H and M loading.

Effect of $\alpha_{\mathrm{HM'}}$ on VHM Failure Envelopes

Fig. 9.5 shows the effect of $\alpha_{\mathrm{HM'}}$ (i.e. non-planar HM loading) on the HM failure envelopes under different V load levels, for $\tilde{Q} = 0$. There is less 3DFE data points in Fig. 9.5b, c as the resultant H from $\alpha_{\mathrm{S\Theta}} = \pi/4$ corresponds to a range of $\alpha_{\mathrm{HM'}}$ (recall that $\alpha_{\mathrm{S\Theta}} \neq \alpha_{\mathrm{HM'}}$). The asymmetry in the HM space decreases as $\alpha_{\mathrm{HM'}}$ increases from 0, until there is no asymmetry at $\alpha_{\mathrm{HM'}} = \pi/2$. This makes physical sense, as the response should be symmetric if lateral loading is applied along the rotational axis.

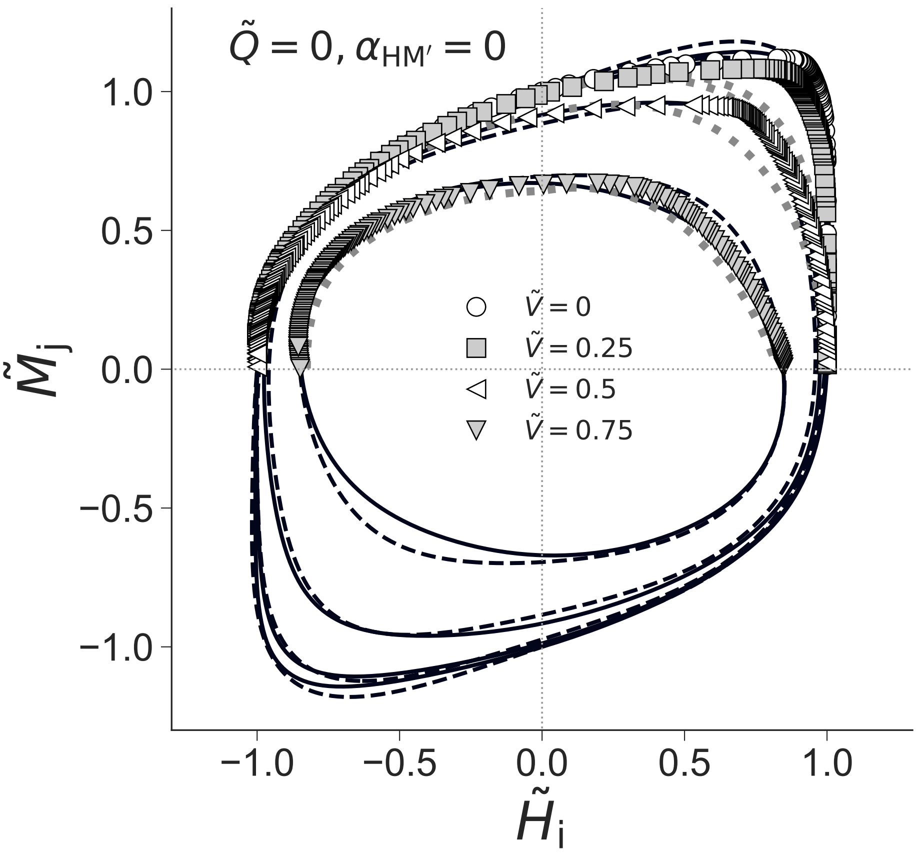

Figure 9.4: HM failure envelopes for $\alpha_{\mathrm{HM'}} = 0$, $\tilde{V} = 0, 0.25, 0.5, 0.75$, $\tilde{Q} = 0$. The black dashed and solid lines are the failure envelopes predicted by Eqs. 9.5 and 9.6 respectively. The grey dotted lines are the failure envelopes predicted by Eq. 9.4 (Shen et al. 2017), which is undefined for negative M values.

$QVHM$ Failure Envelopes

Fig. 9.6 shows the effect of Q loading on the HM failure envelopes under different V load levels, for $\alpha_{\mathrm{HM'}} = 0$. As Q loading increases, the available HM capacity decreases, as shown by the smaller HM failure envelopes. However, the general shape of the HM failure envelopes remain the same as Q loading increases. Thus, unlike V loading, Q loading has minimal influence on the interaction between H and M loading.

Effect of $\alpha_{\mathrm{HM'}}$ on $QVHM$ Failure Envelopes

Fig. 9.7 shows some of the effects of $\alpha_{\mathrm{HM'}}$ and combined V and Q loading on the HM failure envelopes, which are in line with the observed trends described in the previous figures.

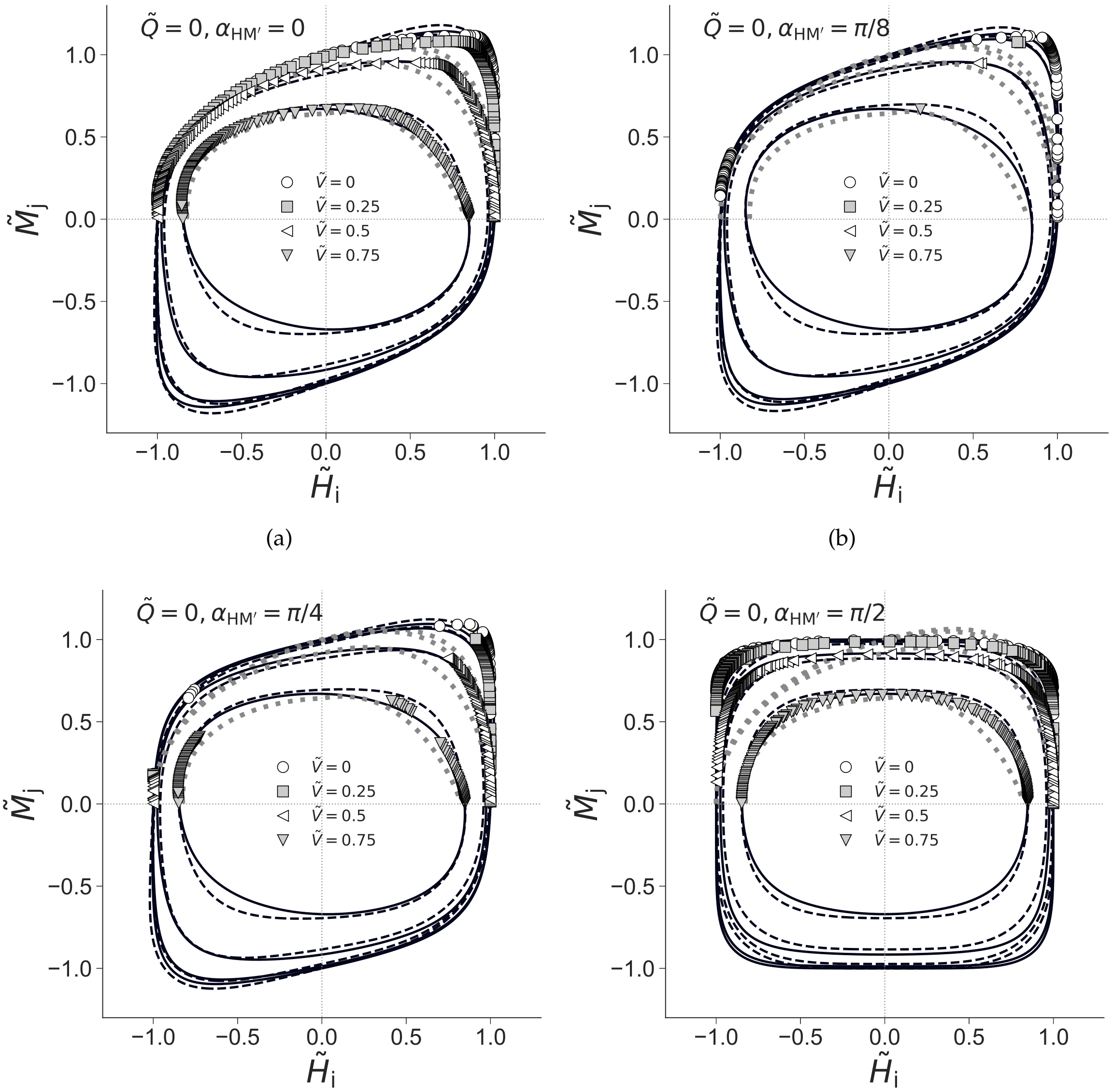

(a)

(b)

(c)

(d)

Figure 9.5: HM failure envelopes for $\alpha_{\mathrm{HM'}} = 0, \pi/8, \pi/4, \pi/2$, $\tilde{V} = 0, 0.25, 0.5, 0.75$, $\tilde{Q} = 0$. The black dashed and solid lines are the failure envelopes predicted by Eqs. 9.5 and 9.6 respectively. The grey dotted lines are the failure envelopes predicted by Eq. 9.4 (Shen et al. 2017), which is undefined for negative M values.

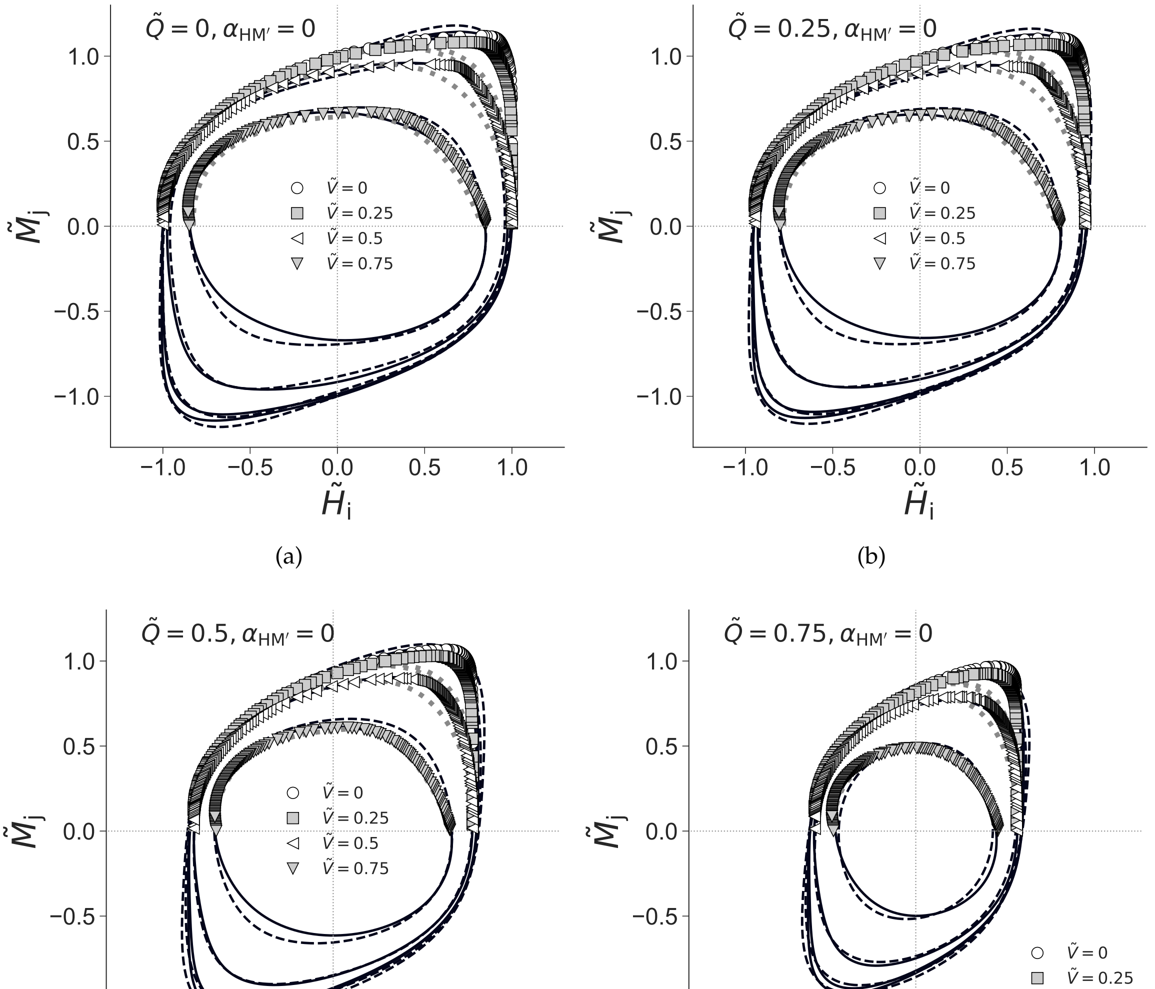

(a)

(b)

(c)

(d)

Figure 9.6: HM failure envelopes for $\alpha_{\mathrm{HM'}}=0$, $\tilde{V}=0, 0.25, 0.5, 0.75$, $\tilde{Q}=0, 0.25, 0.5, 0.75$. The black dashed and solid lines are the failure envelopes predicted by Eqs. 9.5 and 9.6 respectively. The grey dotted lines are the failure envelopes predicted by Eq. 9.4 (Shen et al. 2017), which is undefined for negative M values.

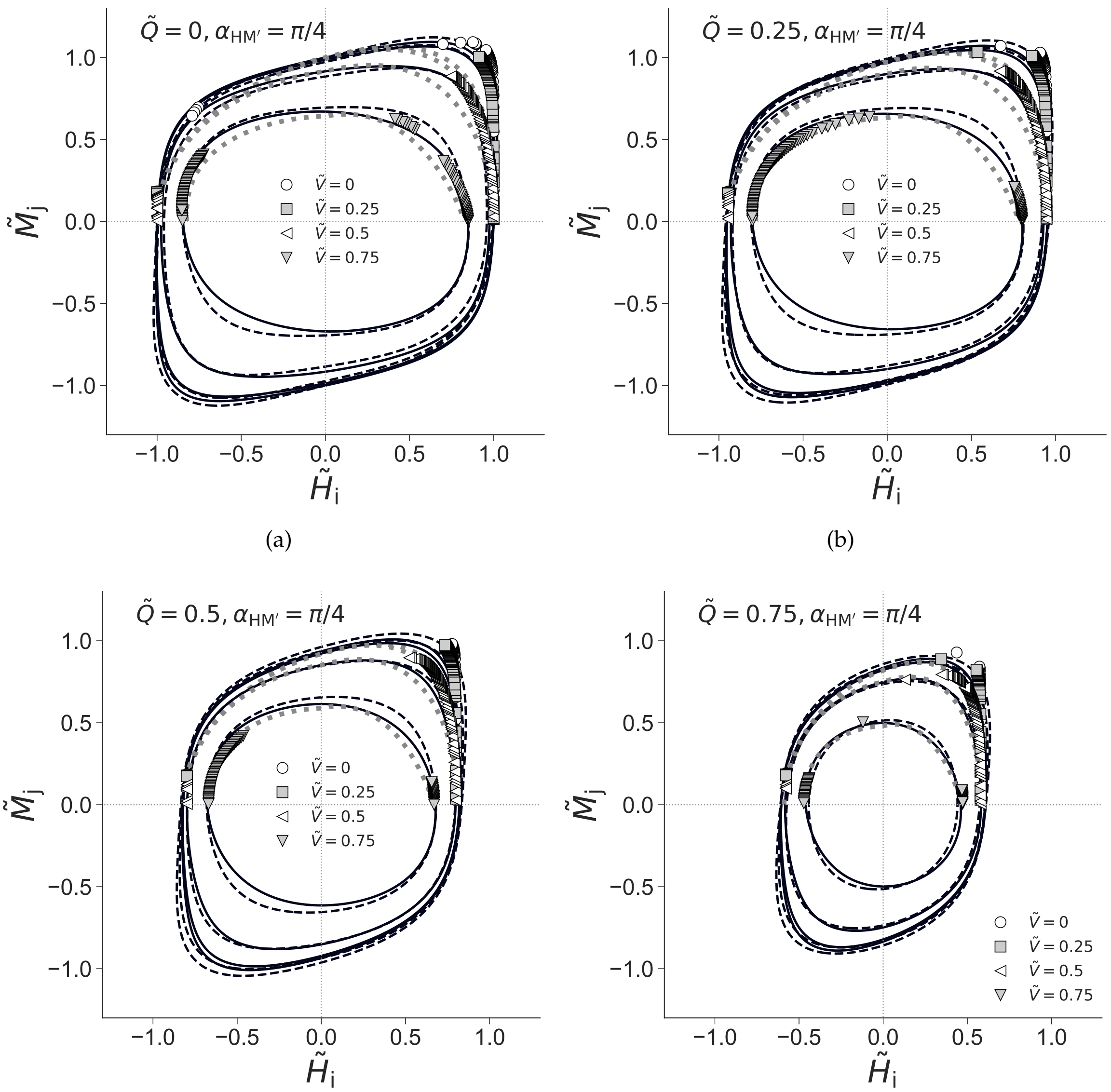

(a) (b)

(c) (d)

Figure 9.7: HM failure envelopes for $\alpha_{\mathrm{HM'}} = \pi/4$, $\tilde{V} = 0, 0.25, 0.5, 0.75$, $\tilde{Q} = 0, 0.25, 0.5, 0.75$. The black dashed and solid lines are the failure envelopes predicted by Eqs. 9.5 and 9.6 respectively. The grey dotted lines are the failure envelopes predicted by Eq. 9.4 (Shen et al. 2017), which is undefined for negative M values.

9.1.4 Calibration

Following the procedures detailed in Chapter 8, SOS optimisation against the 3DFE failure points was carried out to derive two failure envelope formulations to approximate the 3DFE failure envelope. The first failure envelope formulation is a 4th degree SOS polynomial f_4 as follows:

$$\begin{aligned} f_4(\tilde{Q}, \tilde{V}, \tilde{H}_\mathrm{i}, \tilde{M}_\mathrm{j}, \alpha_{\mathrm{HM}'}) = {} & \tilde{H}_\mathrm{i}{}^4 + \tilde{M}_\mathrm{j}{}^4 + \tilde{V}^4 + \tilde{Q}^4 - 1 \\ & + I_\mathrm{HM} + I_\mathrm{VH} + I_\mathrm{VM} + I_\mathrm{QH} + I_\mathrm{QM} \\ & + I_\mathrm{VHM} + I_\mathrm{QHM} \end{aligned} \tag{9.5}$$

where

$$\begin{aligned} I_\mathrm{HM} &= \tilde{H}_\mathrm{i}{}^2(\tilde{H}_\mathrm{i}\tilde{M}_\mathrm{j}\cos\alpha_{\mathrm{HM}'})(-0.36) \\ &\quad + (\tilde{H}_\mathrm{i}\tilde{M}_\mathrm{j}\cos\alpha_{\mathrm{HM}'})^2(0.9) \\ &\quad + (\tilde{M}_\mathrm{j}{}^2)(\tilde{H}_\mathrm{i}\tilde{M}_\mathrm{j}\cos\alpha_{\mathrm{HM}'})(-1.43) \\ I_\mathrm{VH} &= \tilde{H}_\mathrm{i}{}^2\tilde{V}^2(0.4) \\ I_\mathrm{VM} &= \tilde{M}_\mathrm{j}{}^2\tilde{V}^2(1.64) \\ I_\mathrm{QH} &= \tilde{H}_\mathrm{i}{}^2\tilde{Q}^2(2.61) \\ I_\mathrm{QM} &= \tilde{M}_\mathrm{j}{}^2\tilde{Q}^2(0.33) \\ I_\mathrm{VHM} &= (\tilde{H}_\mathrm{i}\tilde{M}_\mathrm{j}\cos\alpha_{\mathrm{HM}'})\tilde{V}^2(0.84) \\ I_\mathrm{QHM} &= (\tilde{H}_\mathrm{i}\tilde{M}_\mathrm{j}\cos\alpha_{\mathrm{HM}'})\tilde{Q}^2(-0.84) \end{aligned}$$

The second failure envelope formulation is a 6th degree SOS polynomial f_6 as follows:

$$\begin{aligned} f_6(\tilde{Q}, \tilde{V}, \tilde{H}_\mathrm{i}, \tilde{M}_\mathrm{j}, \alpha_{\mathrm{HM}'}) = {} & \tilde{H}_\mathrm{i}{}^6 + \tilde{M}_\mathrm{j}{}^6 + \tilde{V}^6 + \tilde{Q}^6 - 1 \\ & + I_\mathrm{HM} + I_\mathrm{VH} + I_\mathrm{VM} + I_\mathrm{QH} + I_\mathrm{QM} \\ & + I_\mathrm{VHM} + I_\mathrm{QHM} \\ & + I_\mathrm{QV} + I_\mathrm{QVH} + I_\mathrm{QVM} + I_\mathrm{QVHM} \end{aligned} \tag{9.6}$$

Table 9.2: Minimised objective values for f_4 and f_6 at the end of the optimisation process for the 3DFE failure envelope results.

Foundation	min. f_{obj} for f_4	min. f_{obj} for f_6
Surface	114.46	86.26

where

$$
\begin{aligned}
I_{\mathrm{HM}} = {} & (\tilde{H}_{\mathrm{i}}\tilde{M}_{\mathrm{j}}\cos\alpha_{\mathrm{HM'}})\tilde{H}_{\mathrm{i}}{}^{4}(-0.33) + (\tilde{H}_{\mathrm{i}}\tilde{M}_{\mathrm{j}}\cos\alpha_{\mathrm{HM'}})^{2}\tilde{H}_{\mathrm{i}}{}^{2}(1.22) \\
& + (\tilde{H}_{\mathrm{i}}\tilde{M}_{\mathrm{j}}\cos\alpha_{\mathrm{HM'}})^{3}(-2.17) + (\tilde{H}_{\mathrm{i}}\tilde{M}_{\mathrm{j}}\cos\alpha_{\mathrm{HM'}})^{2}\tilde{M}_{\mathrm{j}}{}^{2}(2.34) \\
& + (\tilde{H}_{\mathrm{i}}\tilde{M}_{\mathrm{j}}\cos\alpha_{\mathrm{HM'}})\tilde{M}_{\mathrm{j}}{}^{4}(-1.86) \\
I_{\mathrm{VH}} = {} & \tilde{H}_{\mathrm{i}}{}^{2}\tilde{V}^{4}(1.97) + \tilde{H}_{\mathrm{i}}{}^{4}\tilde{V}^{2}(0.03) \\
I_{\mathrm{VM}} = {} & \tilde{M}_{\mathrm{j}}{}^{4}\tilde{V}^{2}(0.84) + \tilde{M}_{\mathrm{j}}{}^{2}\tilde{V}^{4}(4.72) \\
I_{\mathrm{QH}} = {} & \tilde{H}_{\mathrm{i}}{}^{4}\tilde{Q}^{2}(4.56) + \tilde{H}_{\mathrm{i}}{}^{2}\tilde{Q}^{4}(3.47) \\
I_{\mathrm{QM}} = {} & \tilde{M}_{\mathrm{j}}{}^{4}\tilde{Q}^{2}(1.65) + (\tilde{M}_{\mathrm{j}}{}^{2})\tilde{Q}^{4}(0.16) \\
I_{\mathrm{VHM}} = {} & (\tilde{H}_{\mathrm{i}}\tilde{M}_{\mathrm{j}}\cos\alpha_{\mathrm{HM'}})\tilde{H}_{\mathrm{i}}{}^{2}\tilde{V}^{2}(0.34) + \tilde{H}_{\mathrm{i}}{}^{2}\tilde{M}_{\mathrm{j}}{}^{2}\tilde{V}^{2}(1.1) \\
& + (\tilde{H}_{\mathrm{i}}\tilde{M}_{\mathrm{j}}\cos\alpha_{\mathrm{HM'}})\tilde{M}_{\mathrm{j}}{}^{2}\tilde{V}^{2}(0.29) + (\tilde{H}_{\mathrm{i}}\tilde{M}_{\mathrm{j}}\cos\alpha_{\mathrm{HM'}})\tilde{V}^{4}(1.52) \\
I_{\mathrm{QHM}} = {} & \tilde{H}_{\mathrm{i}}{}^{2}(\tilde{H}_{\mathrm{i}}\tilde{M}_{\mathrm{j}}\cos\alpha_{\mathrm{HM'}})\tilde{Q}^{2}(-1.92) + \tilde{H}_{\mathrm{i}}{}^{2}\tilde{M}_{\mathrm{j}}{}^{2}\tilde{Q}^{2}(4.62) \\
& + (\tilde{H}_{\mathrm{i}}\tilde{M}_{\mathrm{j}}\cos\alpha_{\mathrm{HM'}})\tilde{M}_{\mathrm{j}}{}^{2}\tilde{Q}^{2}(-4.53) + (\tilde{H}_{\mathrm{i}}\tilde{M}_{\mathrm{j}}\cos\alpha_{\mathrm{HM'}})\tilde{Q}^{4}(-0.58) \\
I_{\mathrm{QV}} = {} & \tilde{V}^{4}\tilde{Q}^{2}(0.55) + \tilde{V}^{2}\tilde{Q}^{4}(0.12) \\
I_{\mathrm{QVH}} = {} & \tilde{H}_{\mathrm{i}}{}^{2}\tilde{V}^{2}\tilde{Q}^{2}(0.46) \\
I_{\mathrm{QVM}} = {} & \tilde{M}_{\mathrm{j}}{}^{2}\tilde{V}^{2}\tilde{Q}^{2}(0.67) \\
I_{\mathrm{QVHM}} = {} & (\tilde{H}_{\mathrm{i}}\tilde{M}_{\mathrm{j}}\cos\alpha_{\mathrm{HM'}})\tilde{V}^{2}\tilde{Q}^{2}(1.75)
\end{aligned}
$$

For comparison, the *HM* failure envelopes approximated by Eqs. 9.5 and 9.6 are also shown in Figs 9.4 to 9.7. It is evident that both f_4 and f_6 approximates the 3DFE failure points very well. Table 9.2 shows the minimised objective values for f_4 and f_6 at the end of the optimisation process, which suggests that f_6 agrees better with the 3DFE failure envelope results than f_4.

Each of the I terms in Eqs. 9.5 and 9.6 represents the interaction between two or more loads. For example, I_{HM} represents the interaction between lateral and moment loading, while I_{VHM} represents the interaction between vertical, lateral and moment loading. If there is no interaction between any of the loads (i.e. all the I terms are zero), the failure envelope would be a super-ellipsoid (i.e. a 'generalised ellipsoid' where the exponents of the terms may not be 2).

Redefinition Of Failure Envelope Formulations

Note that Eqs. 9.5 and 9.6 are defined in terms of $\tilde{Q}, \tilde{V}, \tilde{H}_{\mathrm{i}}, \tilde{M}_{\mathrm{j}}, \alpha_{\mathrm{HM}'}$. Since $H_{\mathrm{i}}, M_{\mathrm{j}}$ are lateral and moment loads on undefined axes, it shall be defined in terms of $H_{\mathrm{x}}, H_{\mathrm{y}}, M_{\mathrm{x}}, M_{\mathrm{y}}$. First, let the unit vectors $\hat{e}_{\mathrm{H}}$, $\hat{e}_{\mathrm{M}}$ and $\hat{e}_{\mathrm{M}}{}'$ represent the directions of the H_{i}, M_{j} and $M_{\mathrm{j}}{}'$ axes respectively (see Fig. 9.2). Since $\hat{e}_{\mathrm{H}} \cdot \hat{e}_{\mathrm{M}}{}' = \cos\alpha_{\mathrm{HM}'}$:

$$\begin{aligned} H_{\mathrm{i}} M_{\mathrm{j}} \cos\alpha_{\mathrm{HM}'} &= H_{\mathrm{i}} M_{\mathrm{j}} \hat{e}_{\mathrm{H}} \cdot \hat{e}_{\mathrm{M}}{}' \\ &= (H_{\mathrm{i}} \hat{e}_{\mathrm{H}}) \cdot \left(M_{\mathrm{j}} \hat{e}_{\mathrm{M}}{}' \right) \\ &= \vec{H}_{\mathrm{i}} \cdot \vec{M}_{\mathrm{j}}{}' \end{aligned} \tag{9.7}$$

Now, define $\vec{H}_{\mathrm{i}}$ and $\vec{M}_{\mathrm{j}}$ as the resultant lateral $\vec{H}_{\mathrm{r}}$ and moment $\vec{M}_{\mathrm{r}}$ loads:

$$\vec{H}_{\mathrm{i}} = \vec{H}_{\mathrm{r}} = [H_{\mathrm{x}}, H_{\mathrm{y}}] \tag{9.8}$$

$$\vec{M}_{\mathrm{j}} = \vec{M}_{\mathrm{r}} = [M_{\mathrm{x}}, M_{\mathrm{y}}] \tag{9.9}$$

Thus, $\vec{M}_{\mathrm{j}}{}' = \vec{M}_{\mathrm{r}}{}' = [-M_{\mathrm{y}}, M_{\mathrm{x}}]$. The dot product of $\vec{H}_{\mathrm{i}}$ and $\vec{M}_{\mathrm{j}}{}'$ is:

$$\begin{aligned} \vec{H}_{\mathrm{i}} \cdot \vec{M}_{\mathrm{j}}{}' &= [H_{\mathrm{x}}, H_{\mathrm{y}}] \cdot [-M_{\mathrm{y}}, M_{\mathrm{x}}] \\ &= H_{\mathrm{y}} M_{\mathrm{x}} - H_{\mathrm{x}} M_{\mathrm{y}} \end{aligned} \tag{9.10}$$

Using Eqs 9.7 and 9.10, the term $\tilde{H}_{\mathrm{i}} \tilde{M}_{\mathrm{j}} \cos\alpha_{\mathrm{HM}'}$ in Eqs. 9.5 and 9.6 can be expanded to:

$$\begin{aligned} \tilde{H}_{\mathrm{i}} \tilde{M}_{\mathrm{j}} \cos\alpha_{\mathrm{HM}'} &= \frac{H_{\mathrm{i}} M_{\mathrm{j}} \cos\alpha_{\mathrm{HM}'}}{H_0 M_0} \\ &= \frac{H_{\mathrm{y}} M_{\mathrm{x}} - H_{\mathrm{x}} M_{\mathrm{y}}}{H_0 M_0} \\ &= \tilde{H}_{\mathrm{y}} \tilde{M}_{\mathrm{x}} - \tilde{H}_{\mathrm{x}} \tilde{M}_{\mathrm{y}} \end{aligned} \tag{9.11}$$

Therefore, Eq. 9.5 can be redefined as:

$$\begin{aligned} f_4(\tilde{Q}, \tilde{V}, \tilde{H}_{\mathrm{y}}, \tilde{M}_{\mathrm{x}}, \tilde{H}_{\mathrm{x}}, \tilde{M}_{\mathrm{y}}) = &\left(\tilde{H}_{\mathrm{x}}{}^2 + \tilde{H}_{\mathrm{y}}{}^2 \right)^2 + \left(\tilde{M}_{\mathrm{x}}{}^2 + \tilde{M}_{\mathrm{y}}{}^2 \right)^2 + \tilde{V}^4 + \tilde{Q}^4 - 1 \\ &+ I_{\mathrm{HM}} + I_{\mathrm{VH}} + I_{\mathrm{VM}} + I_{\mathrm{QH}} + I_{\mathrm{QM}} \\ &+ I_{\mathrm{VHM}} + I_{\mathrm{QHM}} \end{aligned} \tag{9.12}$$

where

$$\begin{aligned}
I_{\mathrm{HM}} &= \left(\tilde{H}_{\mathrm{x}}{}^2 + \tilde{H}_{\mathrm{y}}{}^2\right)(\tilde{H}_{\mathrm{y}}\tilde{M}_{\mathrm{x}} - \tilde{H}_{\mathrm{x}}\tilde{M}_{\mathrm{y}})(-0.35) \\
&\quad + (\tilde{H}_{\mathrm{y}}\tilde{M}_{\mathrm{x}} - \tilde{H}_{\mathrm{x}}\tilde{M}_{\mathrm{y}})^2(0.89) \\
&\quad + \left(\tilde{M}_{\mathrm{x}}{}^2 + \tilde{M}_{\mathrm{y}}{}^2\right)(\tilde{H}_{\mathrm{y}}\tilde{M}_{\mathrm{x}} - \tilde{H}_{\mathrm{x}}\tilde{M}_{\mathrm{y}})(-1.43) \\
I_{\mathrm{VH}} &= \left(\tilde{H}_{\mathrm{x}}{}^2 + \tilde{H}_{\mathrm{y}}{}^2\right)\tilde{V}^2(0.4) \\
I_{\mathrm{VM}} &= \left(\tilde{M}_{\mathrm{x}}{}^2 + \tilde{M}_{\mathrm{y}}{}^2\right)\tilde{V}^2(1.66) \\
I_{\mathrm{QH}} &= \left(\tilde{H}_{\mathrm{x}}{}^2 + \tilde{H}_{\mathrm{y}}{}^2\right)\tilde{Q}^2(2.6) \\
I_{\mathrm{QM}} &= \left(\tilde{M}_{\mathrm{x}}{}^2 + \tilde{M}_{\mathrm{y}}{}^2\right)\tilde{Q}^2(0.34) \\
I_{\mathrm{VHM}} &= (\tilde{H}_{\mathrm{y}}\tilde{M}_{\mathrm{x}} - \tilde{H}_{\mathrm{x}}\tilde{M}_{\mathrm{y}})\tilde{V}^2(0.82) \\
I_{\mathrm{QHM}} &= (\tilde{H}_{\mathrm{y}}\tilde{M}_{\mathrm{x}} - \tilde{H}_{\mathrm{x}}\tilde{M}_{\mathrm{y}})\tilde{Q}^2(-0.85)
\end{aligned}$$

Similarly, Eq. 9.6 can be redefined as:

$$\begin{aligned}
f_6(\tilde{Q}, \tilde{V}, \tilde{H}_{\mathrm{y}}, \tilde{M}_{\mathrm{x}}, \tilde{H}_{\mathrm{x}}, \tilde{M}_{\mathrm{y}}) &= \left(\tilde{H}_{\mathrm{x}}{}^2 + \tilde{H}_{\mathrm{y}}{}^2\right)^3 + \left(\tilde{M}_{\mathrm{x}}{}^2 + \tilde{M}_{\mathrm{y}}{}^2\right)^3 + \tilde{V}^6 + \tilde{Q}^6 - 1 \\
&\quad + I_{\mathrm{HM}} + I_{\mathrm{VH}} + I_{\mathrm{VM}} + I_{\mathrm{QH}} + I_{\mathrm{QM}} \\
&\quad + I_{\mathrm{VHM}} + I_{\mathrm{QHM}} \\
&\quad + I_{\mathrm{QV}} + I_{\mathrm{QVH}} + I_{\mathrm{QVM}} + I_{\mathrm{QVHM}}
\end{aligned} \tag{9.13}$$

where

$$
\begin{aligned}
I_{\mathrm{HM}} = {} & (\tilde{H}_{\mathrm{y}}\tilde{M}_{\mathrm{x}} - \tilde{H}_{\mathrm{x}}\tilde{M}_{\mathrm{y}})\left(\tilde{H}_{\mathrm{x}}{}^{2} + \tilde{H}_{\mathrm{y}}{}^{2}\right)^{2}(-0.33) \\
& + (\tilde{H}_{\mathrm{y}}\tilde{M}_{\mathrm{x}} - \tilde{H}_{\mathrm{x}}\tilde{M}_{\mathrm{y}})^{2}\left(\tilde{H}_{\mathrm{x}}{}^{2} + \tilde{H}_{\mathrm{y}}{}^{2}\right)(1.19) \\
& + (\tilde{H}_{\mathrm{y}}\tilde{M}_{\mathrm{x}} - \tilde{H}_{\mathrm{x}}\tilde{M}_{\mathrm{y}})^{3}(-2.22) \\
& + (\tilde{H}_{\mathrm{y}}\tilde{M}_{\mathrm{x}} - \tilde{H}_{\mathrm{x}}\tilde{M}_{\mathrm{y}})^{2}\left(\tilde{M}_{\mathrm{x}}{}^{2} + \tilde{M}_{\mathrm{y}}{}^{2}\right)(2.43) \\
& + (\tilde{H}_{\mathrm{y}}\tilde{M}_{\mathrm{x}} - \tilde{H}_{\mathrm{x}}\tilde{M}_{\mathrm{y}})\left(\tilde{M}_{\mathrm{x}}{}^{2} + \tilde{M}_{\mathrm{y}}{}^{2}\right)^{2}(-1.87) \\
I_{\mathrm{VH}} = {} & \left(\tilde{H}_{\mathrm{x}}{}^{2} + \tilde{H}_{\mathrm{y}}{}^{2}\right)\tilde{V}^{4}(1.97) + \left(\tilde{H}_{\mathrm{x}}{}^{2} + \tilde{H}_{\mathrm{y}}{}^{2}\right)^{2}\tilde{V}^{2}(0.03) \\
I_{\mathrm{VM}} = {} & \left(\tilde{M}_{\mathrm{x}}{}^{2} + \tilde{M}_{\mathrm{y}}{}^{2}\right)^{2}\tilde{V}^{2}(0.92) + \left(\tilde{M}_{\mathrm{x}}{}^{2} + \tilde{M}_{\mathrm{y}}{}^{2}\right)\tilde{V}^{4}(4.41) \\
I_{\mathrm{QH}} = {} & \left(\tilde{H}_{\mathrm{x}}{}^{2} + \tilde{H}_{\mathrm{y}}{}^{2}\right)^{2}\tilde{Q}^{2}(4.55) + \left(\tilde{H}_{\mathrm{x}}{}^{2} + \tilde{H}_{\mathrm{y}}{}^{2}\right)\tilde{Q}^{4}(3.61) \\
I_{\mathrm{QM}} = {} & \left(\tilde{M}_{\mathrm{x}}{}^{2} + \tilde{M}_{\mathrm{y}}{}^{2}\right)^{2}\tilde{Q}^{2}(1.61) + \left(\tilde{M}_{\mathrm{x}}{}^{2} + \tilde{M}_{\mathrm{y}}{}^{2}\right)\tilde{Q}^{4}(0.2) \\
I_{\mathrm{VHM}} = {} & (\tilde{H}_{\mathrm{y}}\tilde{M}_{\mathrm{x}} - \tilde{H}_{\mathrm{x}}\tilde{M}_{\mathrm{y}})\left(\tilde{H}_{\mathrm{x}}{}^{2} + \tilde{H}_{\mathrm{y}}{}^{2}\right)\tilde{V}^{2}(0.32) \\
& + \left(\tilde{H}_{\mathrm{x}}{}^{2} + \tilde{H}_{\mathrm{y}}{}^{2}\right)\left(\tilde{M}_{\mathrm{x}}{}^{2} + \tilde{M}_{\mathrm{y}}{}^{2}\right)\tilde{V}^{2}(1.03) \\
& + (\tilde{H}_{\mathrm{y}}\tilde{M}_{\mathrm{x}} - \tilde{H}_{\mathrm{x}}\tilde{M}_{\mathrm{y}})\left(\tilde{M}_{\mathrm{x}}{}^{2} + \tilde{M}_{\mathrm{y}}{}^{2}\right)\tilde{V}^{2}(0.33) \\
& + (\tilde{H}_{\mathrm{y}}\tilde{M}_{\mathrm{x}} - \tilde{H}_{\mathrm{x}}\tilde{M}_{\mathrm{y}})\tilde{V}^{4}(1.46) \\
I_{\mathrm{QHM}} = {} & \left(\tilde{H}_{\mathrm{x}}{}^{2} + \tilde{H}_{\mathrm{y}}{}^{2}\right)(\tilde{H}_{\mathrm{y}}\tilde{M}_{\mathrm{x}} - \tilde{H}_{\mathrm{x}}\tilde{M}_{\mathrm{y}})\tilde{Q}^{2}(-1.63) \\
& + \left(\tilde{H}_{\mathrm{x}}{}^{2} + \tilde{H}_{\mathrm{y}}{}^{2}\right)\left(\tilde{M}_{\mathrm{x}}{}^{2} + \tilde{M}_{\mathrm{y}}{}^{2}\right)\tilde{Q}^{2}(4.47) \\
& + (\tilde{H}_{\mathrm{y}}\tilde{M}_{\mathrm{x}} - \tilde{H}_{\mathrm{x}}\tilde{M}_{\mathrm{y}})\left(\tilde{M}_{\mathrm{x}}{}^{2} + \tilde{M}_{\mathrm{y}}{}^{2}\right)\tilde{Q}^{2}(-4.53) \\
& + (\tilde{H}_{\mathrm{y}}\tilde{M}_{\mathrm{x}} - \tilde{H}_{\mathrm{x}}\tilde{M}_{\mathrm{y}})\tilde{Q}^{4}(-0.51) \\
I_{\mathrm{QV}} = {} & \tilde{V}^{4}\tilde{Q}^{2}(0.62) + \tilde{V}^{2}\tilde{Q}^{4}(0.04) \\
I_{\mathrm{QVH}} = {} & \left(\tilde{H}_{\mathrm{x}}{}^{2} + \tilde{H}_{\mathrm{y}}{}^{2}\right)\tilde{V}^{2}\tilde{Q}^{2}(0.4) \\
I_{\mathrm{QVM}} = {} & \left(\tilde{M}_{\mathrm{x}}{}^{2} + \tilde{M}_{\mathrm{y}}{}^{2}\right)\tilde{V}^{2}\tilde{Q}^{2}(0.77) \\
I_{\mathrm{QVHM}} = {} & (\tilde{H}_{\mathrm{y}}\tilde{M}_{\mathrm{x}} - \tilde{H}_{\mathrm{x}}\tilde{M}_{\mathrm{y}})\tilde{V}^{2}\tilde{Q}^{2}(1.45)
\end{aligned}
$$

9.1.5 Discussion

The failure envelope for a rigid, circular surface foundation on undrained clay under 6DoF loading has been determined using 3DFE analyses, and f_4 and f_6 (Eqs. 9.12, and 9.13) have been derived to approximate the 3DFE failure envelope. Although f_6 is more accurate than f_4, it is more convenient to use f_4 as the yield surface or plastic potential in numerical models, as it is more concise. Thus, f_4 was implemented as the yield surface f^{base} and the plastic potential g^{base} for the base soil reactions in oxCaisson-LEPP, for a suction caisson of $L/D = 0$. The uniaxial capacities are defined by the 3DFE results in Table 9.1, while the elastic behaviour is defined by the linear elastic soil reactions described in Chapter 3.

Fig. 9.8 compares the oxCaisson-LEPP predictions of the load-displacement behaviour and the HM failure envelope with the 3DFE results, for a sequential swipe test in the HM space under planar HM loading (i.e. $\alpha_{\text{HM}'} = 0$) with $\tilde{V} = 0.25$ and $\tilde{Q} = 0$. Evidently, there are some minor differences with the predictions. For example, the total normalised vertical displacements S_z/D that resulted from maintaining $\tilde{V} = 0.25$ during the sequential swipe test are 0.00635 and 0.0108 for the 3DFE model and oxCaisson-LEPP respectively. Nevertheless, the overall oxCaisson-LEPP predictions match the 3DFE results very well. Moreover, the oxCaisson-LEPP is 440 times faster than the 3DFE model, as it took only 14 seconds (or 15 seconds if an explicit elasto-plastic integration algorithm was used) to generate the data points in Fig. 9.8, while the 3DFE model took 1.7 hours.

Comparison With Previous Work

For 6DoF loading, Figs. 9.4 to 9.7 also include the failure envelopes predicted by Eq. 9.4. It is clear from these figures that the failure envelopes predicted by f_4 and f_6 are more accurate than that of Eq. 9.4. In particular, f_4 and f_6 capture the change in the HM failure envelope asymmetry as $\alpha_{\text{HM}'}$ varies. In contrast, the HM failure envelopes predicted by Eq. 9.4 do not vary with $\alpha_{\text{HM}'}$, which results in incorrect, asymmetric HM failure envelopes when $\alpha_{\text{HM}'} = \pi/2$. Furthermore, Eq. 9.4 is undefined for negative moment values, as it raises negative numbers to fractional powers, resulting in complex numbers. This makes Eq. 9.4 unsuitable for use as a yield surface in numerical models.

For VHM planar loading, Fig. 9.9 compares the HM failure envelopes predicted by f_4, f_6 and the existing formulations (Eqs. 9.1, 9.2, 9.4) with the 3DFE results. Evidently, f_4 and f_6 are significant improvements over these existing formulations. With regards to the existing formulations, Eq. 9.4 is generally more accurate than Eqs. 9.1 and 9.2. However, Eq. 9.1 has the advantage that it can be used as a yield surface in numerical models, as it is defined in all quadrants, unlike Eqs. 9.2 and 9.4.

As for the failure envelopes on the other planes, Fig. 9.10 compares the VH, VM, QH and QM failure envelopes predicted by f_4, f_6 and the existing formulations (Eqs. 9.1, 9.2,

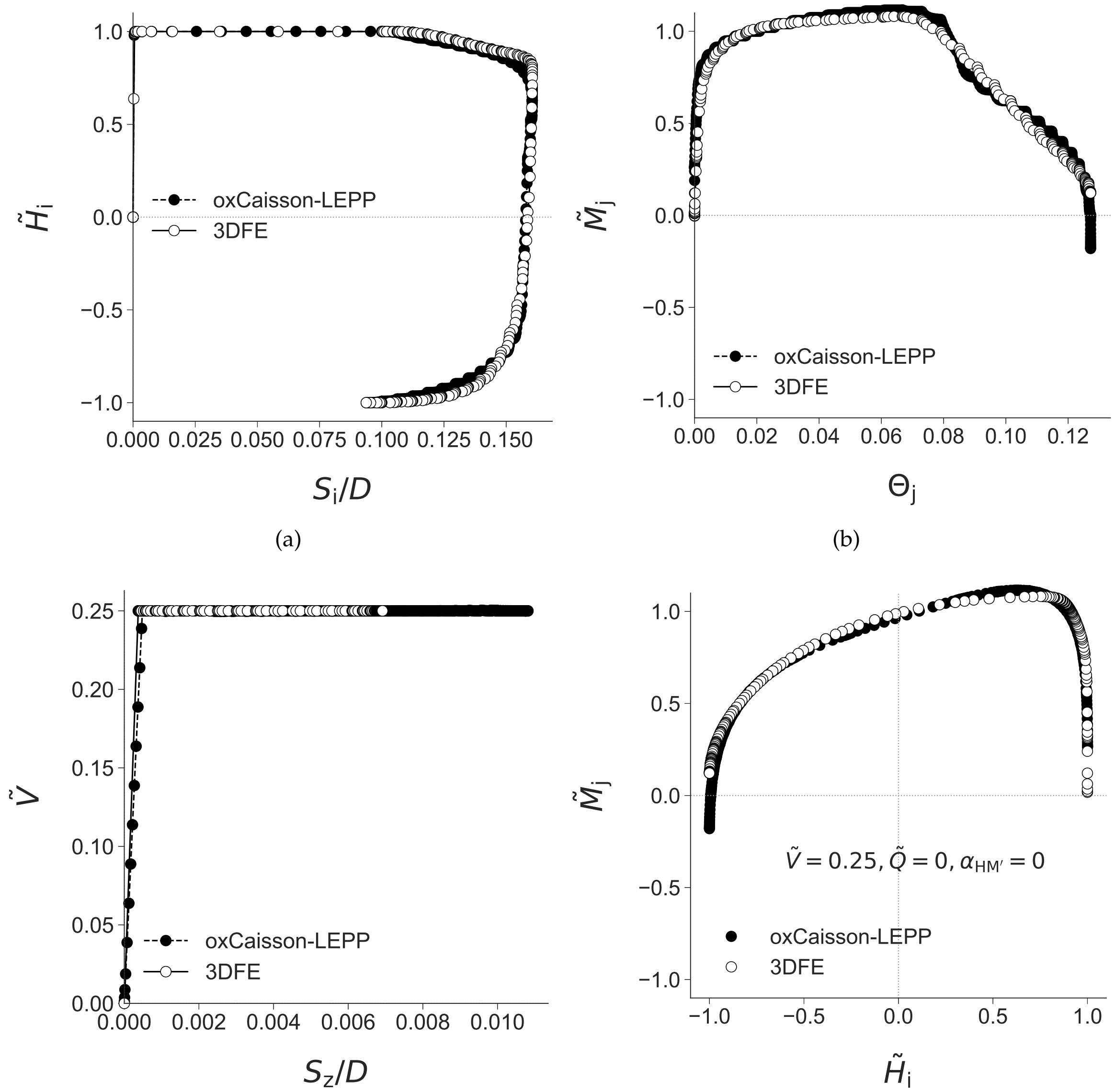

(a) (b)

(c) (d)

Figure 9.8: Comparison of sequential swipe tests in the HM space for a circular surface foundation, for $\alpha_{HM'} = 0$, $\tilde{V} = 0.25$, $\tilde{Q} = 0$ (a)-(c) Load-displacement behaviour (d) HM failure envelope.

9.4) with the 3DFE results. Evidently, f_4 and f_6 are in excellent agreement with the 3DFE results. Eq. 9.4 is the most accurate out of the existing formulations, but it is only defined for $0 \leq \tilde{V} < 1$ (it is undefined for $\tilde{V} = 1$ due to a singularity there). This highlights the main shortcoming of the functional form adopted by Eqs. 9.2 and 9.4: it is undefined in some negative domains and for $\tilde{V} = 1$.

Finally, the functional forms of Eqs. 9.12 and 9.13 are compared with that of Eq. 9.3. They are similar in that they are all simple polynomial expressions. Eq. 9.3 contains the terms $\tilde{H}_y\tilde{M}_x - \tilde{H}_x\tilde{M}_y$, which implies that it correctly predicts symmetric HM failure envelopes at $\alpha_{HM'} = \pi/2$. The main differences are the degree of the polynomials and that

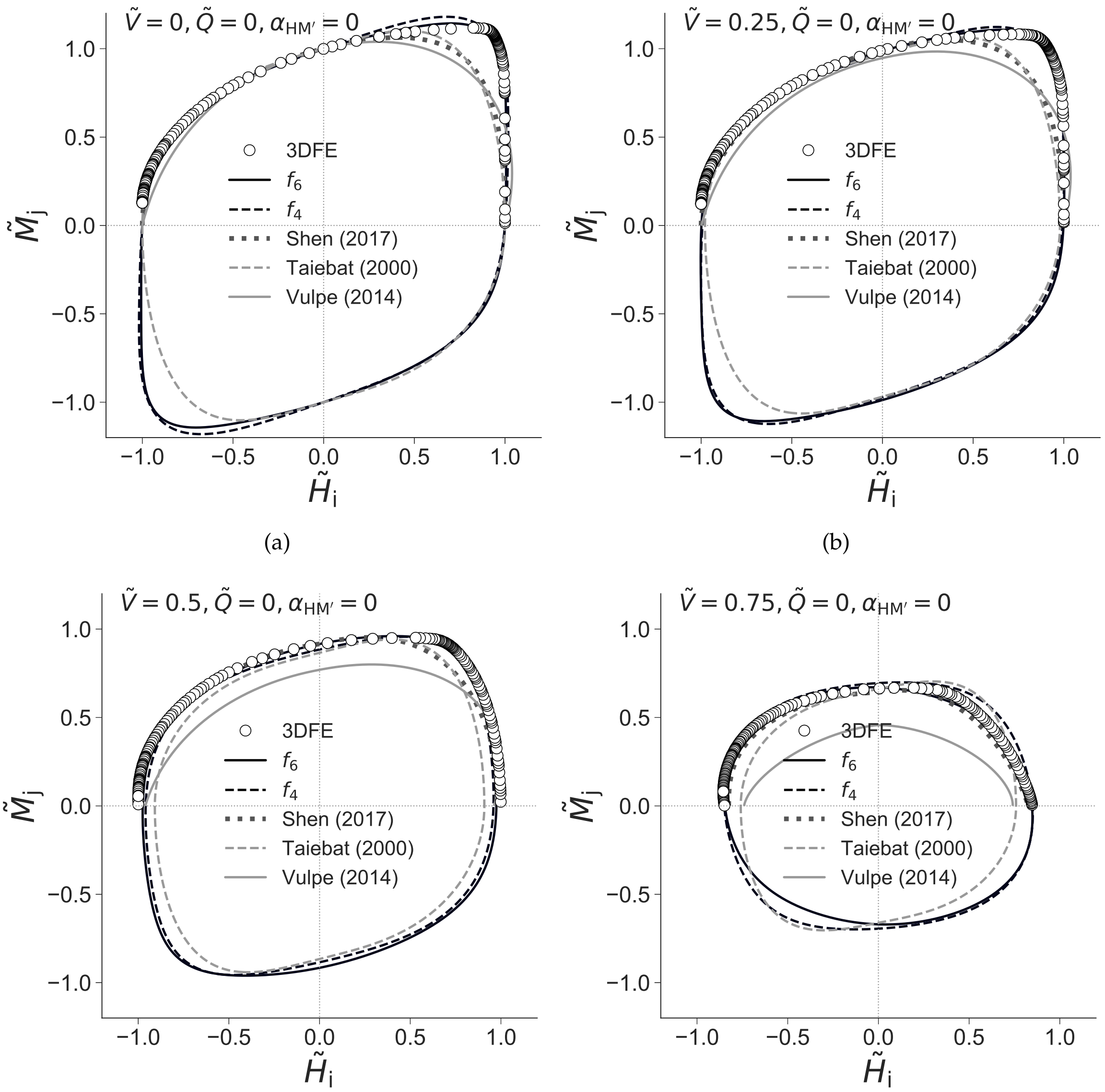

(a) (b)

(c) (d)

Figure 9.9: HM failure envelopes for $\alpha_{\mathrm{HM'}} = 0$, $\tilde{V} = 0, 0.25, 0.5, 0.75$, $\tilde{Q} = 0$. Note that the failure envelopes proposed by Shen et al. (2017) and Vulpe et al. (2014) are undefined for negative M values.

Eq. 9.3 is a non-homogeneous polynomial. Also, there are cross product terms involving Q (e.g. $I_{\mathrm{QH}}, I_{\mathrm{QM}}$) in Eqs. 9.12 and 9.13, while there is none in Eq. 9.3.

Strengths And Limitations

Although Eqs. 9.12 and 9.13 may look intimidating due to their lengths, they are actually simple expressions that are easily differentiable and integrable, making them suitable for use as yield functions in numerical models such as oxCaisson-LEPP. This is in stark contrast to the existing formulations, which are numerically inconvenient to implement due to its complicated derivatives, lack of definition in some quadrants and existence of singularities.

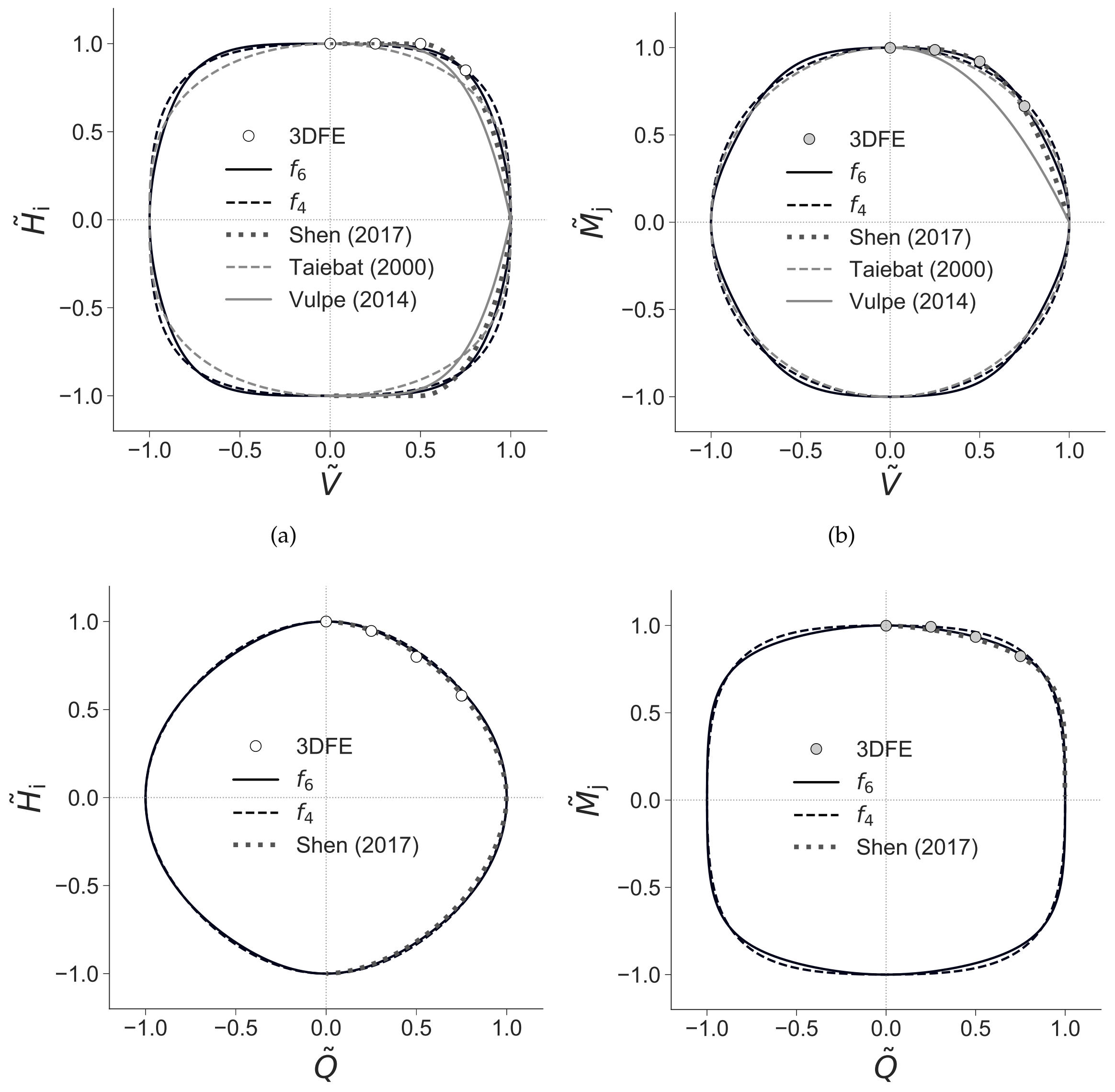

(a) (b)

(c) (d)

Figure 9.10: VH, VM, QH and QM failure envelopes. Note that the failure envelopes proposed by Shen et al. (2017) and Vulpe et al. (2014) are undefined for negative V, Q, M and V, M values respectively.

Other advantages include guarantees of global convexity and thermodynamics consistency, which are associated with a range of benefits as explained in Chapter 8.

The length of f_6 is certainly an inconvenience for simple design jobs such as evaluations of ULS conditions. However, while it may be tedious to implement f_6, it is not complicated and the implementation is a one-off operation. Nevertheless, f_4 is generally recommended, as it offers reasonable accuracy, while still being sufficiently concise.

9.2 Suction Caisson Foundations

The previous section describes a failure envelope formulation for surface foundations on undrained clay under 6DoF loading, which is also the yield surface formulation f^{base} for the base soil reaction for a caisson of $L/D = 0$. This section continues that work to derive yield surface formulations for the skirt and base soil reactions for caissons of $0 < L/D \leq 2$.

9.2.1 Introduction

Compared to surface foundations, there is less research on failure envelopes for suction caissons, especially under 6DoF loading. However, there are considerable volume of related work done on skirted strip foundations (which are plane strain versions of suction caissons). Bransby & Randolph (1998, 1999), Bransby & Yun (2009) and Gourvenec & Barnett (2011) did a series of plane-strain finite element analyses on skirted strip foundations in Tresca soil under planar VHM loading and several key results were obtained.

First, Bransby & Randolph (1998, 1999) proposed the following failure envelope formulations for skirted strip foundations:

$$f(\tilde{V},\tilde{H},\tilde{M}^*) = \left|\tilde{V}\right|^{2.5} - \left(1-\left|\tilde{H}\right|\right)^{1/3}\left(1-\left|\tilde{M}^*\right|\right) + 0.5\left|\tilde{M}^*\right|\left|\tilde{H}\right|^{5} \tag{9.14}$$

where $\tilde{M}^* = \tilde{M} - z_{\text{rotation}}H/M_0$ and z_{rotation} is the vertical distance from the caisson skirt base to the centre of rotation. Unfortunately, z_{rotation} is difficult to identify, as it varies with the loading conditions, caisson dimensions and soil profiles.

Second, Bransby & Yun (2009) found that a skirted strip foundation can have significantly less capacity than that of an equivalent solid embedded foundation, due to deformation of the soil plug. Hence, the commonly adopted assumption of the soil plug being rigid should be reconsidered. They also suggested that general recommendations for the failure envelope shapes of skirted strip foundations are problematic, as they vary significantly with different embedment ratios.

Third, Gourvenec & Barnett (2011) proposed the following failure envelope formulation for skirted strip foundation:

$$f(\tilde{V},\tilde{H},\tilde{M}^*) = \left(\frac{\tilde{H}}{\xi_{\text{H}}}\right)^{a} + \left(\frac{\tilde{M}^*}{\xi_{\text{M}}}\right)^{a} + 2b\left(\frac{\tilde{H}\tilde{M}^*}{\xi_{\text{H}}\xi_{\text{M}}}\right) - 1 \tag{9.15}$$

where

$$
\begin{aligned}
\tilde{M}^* &= \tilde{M} + LH/M_0 \\
a &= 1.3 + 1.05(L/D) - 0.55(L/D)^2 \\
b &= 0.15 - 1.45(L/D) + 0.67(L/D)^2 \\
\xi_{\mathrm{H}} &= 1 - 0.217\tilde{V} + 1.009\tilde{V}^2 - 1.792\tilde{V}^3 \\
\xi_{\mathrm{M}} &= 1 - 0.112\tilde{V} + 0.535\tilde{V}^2 - 1.423\tilde{V}^3
\end{aligned}
$$

The transformation of $\tilde{M}$ to $\tilde{M}^*$ is required as Gourvenec & Barnett (2011) took the centre of the caisson skirt base as the loading reference point, while this thesis takes the centre of the caisson lid base as the loading reference point (see Fig. 2.1a).

On a more recent note, Hung & Kim (2014) carried out a 3DFE numerical study on the failure envelopes for suction caissons in Tresca soil under planar VHM loading (assuming no separation at the soil-foundation interface) and proposed the following failure envelope formulation:

$$f(\tilde{V},\tilde{H},\tilde{M}) = \tilde{H}^2 + \tilde{M}^2 - abc\left(\tilde{H}\tilde{M}\right) + \tilde{V}^2 - 1 \tag{9.16}$$

where

$$
\begin{aligned}
a &= 0.304(L/D)^{0.33} \\
b &= 5.58(kD/s_{\mathrm{um}})^{-0.049} \;\; \geq 5 \\
c &= 0.94 + 0.2\tilde{V}^{2.4} \\
s_{\mathrm{u}} &= s_{\mathrm{um}} + kz \quad (s_{\mathrm{um}} \text{ is the undrained shear strength at ground level})
\end{aligned}
$$

Unfortunately, Eq. 9.16 cannot be used to predict the failure envelopes for undrained clay with homogeneous s_{u} (i.e. $k = 0$), as the parameter $b \to \infty$ as $k \to 0$.

Vulpe (2015) also carried out a 3DFE numerical study on the failure envelopes for suction caissons in Tresca soil under planar VHM loading (assuming no separation at the soil-foundation interface) and proposed a failure envelope formulation similar to Eq. 9.15:

$$f(\tilde{V},\tilde{H},\tilde{M}^*) = \left(\left|\frac{\tilde{H}}{\xi_{\mathrm{H}}}\right|\right)^a + \left(\frac{\tilde{M}^*}{\xi_{\mathrm{M}}}\right)^a + 2b\left(\frac{\tilde{H}\tilde{M}^*}{\xi_{\mathrm{H}}\xi_{\mathrm{M}}}\right) - 1 \tag{9.17}$$

where

$$\begin{aligned}\tilde{M}^* &= \tilde{M} + LH/M_0\\ a &= 1.63, 1.89, 2.1, 1.83 \text{ for } L/D = 0, 0.1, 0.25, 0.5 \text{ respectively}\\ b &= -0.05, -0.16, -0.44, -0.66 \text{ for } L/D = 0, 0.1, 0.25, 0.5 \text{ respectively}\\ \xi_\mathrm{H} &= 1 - \tilde{V}^{4.14}\\ \xi_\mathrm{M} &= 1 - \tilde{V}^{2.12}\end{aligned}$$

Karapiperis & Gerolymos (2014) conducted a 3DFE numerical study on the failure envelopes for non-skirted, cuboid caissons in von Mises soil under planar VHM loading (assuming no separation at the soil-foundation interface) and they proposed the following failure envelope formulation:

$$f(\tilde{V}, \tilde{H}, \tilde{M}) = \left(\frac{\tilde{H}}{\xi_\mathrm{H}}\right)^{n_1} + \left(\frac{\tilde{M}}{\xi_\mathrm{M}}\right)^{n_2} + n_3 \left(\frac{\tilde{H}}{\xi_\mathrm{H}}\right)\left(\frac{\tilde{M}}{\xi_\mathrm{M}}\right) - 1 \tag{9.18}$$

where

$$\begin{aligned}n_1 &= 2\\ n_2 &= 2\\ n_3 &= 1.84 - 0.21(L/D)^{-1.98}\\ \xi_\mathrm{H} &= \left(1 - \tilde{V}\right)^{0.17}\\ \xi_\mathrm{M} &= \left(1 - \tilde{V}\right)^{0.17}\end{aligned}$$

Eq. 9.18, which was derived based on the 3DFE results for $1 \leq L/D \leq 3$, is unsuitable for caissons with $L/D \ll 1$, as the parameter $n_3 \rightarrow -\infty$ as $L/D \rightarrow 0$. Furthermore, Eq. 9.18 is not directly applicable for suction caissons, as it was calibrated using a non-skirted, cuboid caisson. Nevertheless, it will still be used for comparison purposes later, as it was calibrated using the same von Mises soil model as the current study.

Given the limited research on suction caisson failure envelopes, there are still some questions that have not been addressed. First, the failure envelope of suction caissons in undrained clay under 6DoF loading is not clear, as there is no previous research on it. At best, the work by Vulpe (2015), which considers only planar VHM loading, represents the current state of the art. Second, all of the previous works focused exclusively on the global failure envelope of the caissons. There has been no research on the local yield surfaces of the soil reactions along the caisson skirt and on the caisson base, which can provide crucial insights into the distribution of the soil response at failure.

To address the above questions, 3DFE analyses of a rigid suction caisson in von Mises soil under 6DoF loading were carried out. The primary outputs of interest are not only the global failure envelope, but also the local yield surfaces of the skirt and base soil reactions. Just as the failure envelope is determined from the limiting global load response, the local yield surfaces are determined from the limiting responses of the skirt and base soil reactions. Using the 3DFE results and the framework introduced in Chapter 8, yield surface formulations f^{skirt} and f^{base} were derived for the skirt and base soil reactions respectively. Thereafter, f^{skirt} and f^{base} were incorporated into oxCaisson-LEPP and the predictions of oxCaisson-LEPP were validated against the 3DFE results.

9.2.2 Methodology

The 3DFE model consists of a rigid, suction caisson of diameter D and skirt thickness $d_{\text{skirt}}/D = 0.005$ on homogeneous, elasto-plastic soil. The foundation diameter D was held constant at unit length, while four skirt lengths ($L/D = 0.25, 0.5, 1, 2$) were analysed.

Mesh

The diameter and depth of the mesh domain were set to $6D$ and $2L + 2.5D$ respectively, which was large enough to avoid boundary effects. Mesh convergence analyses were carried out to determine the mesh fineness. A representative mesh is shown in Fig. 9.11.

Material Properties

The soil properties used here is the same as that described in Section 9.1.2. The caisson was made entirely rigid using rigid body constraints. Its reference point was set at the centre of its lid base (see Fig. 2.1a). Separation between the soil and foundation was prevented using tie constraints at the soil-foundation interface.

Boundary Conditions

The boundary conditions applied here is the same as that described in Section 9.1.2.

Validation

To validate that the 3DFE model has been set up correctly, Table 9.3 compares the uniaxial capacity results with published results for Tresca soil (Vulpe 2015, Fu et al. 2017) and the

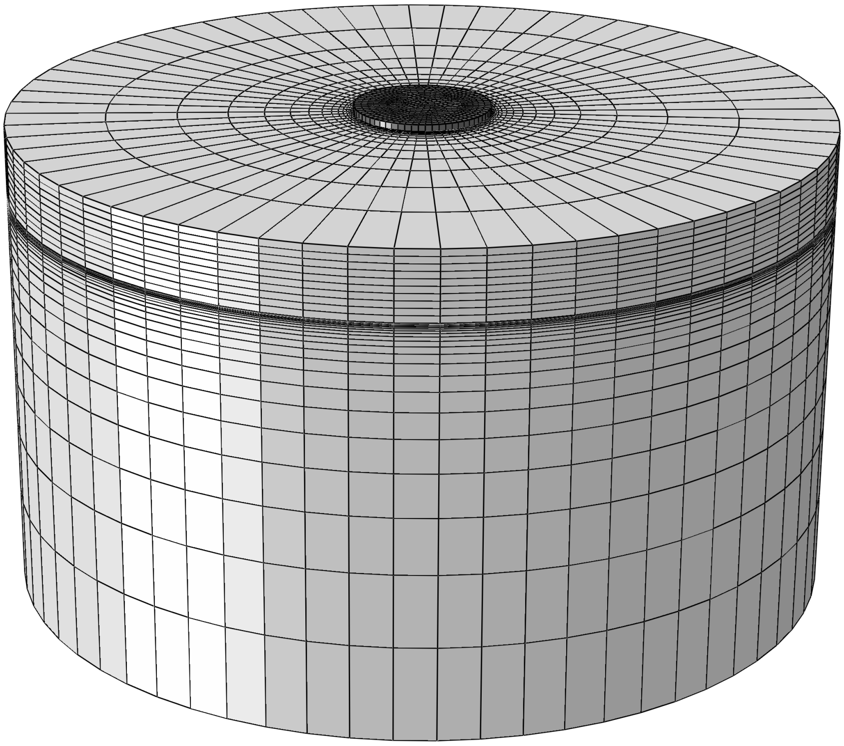

(a)

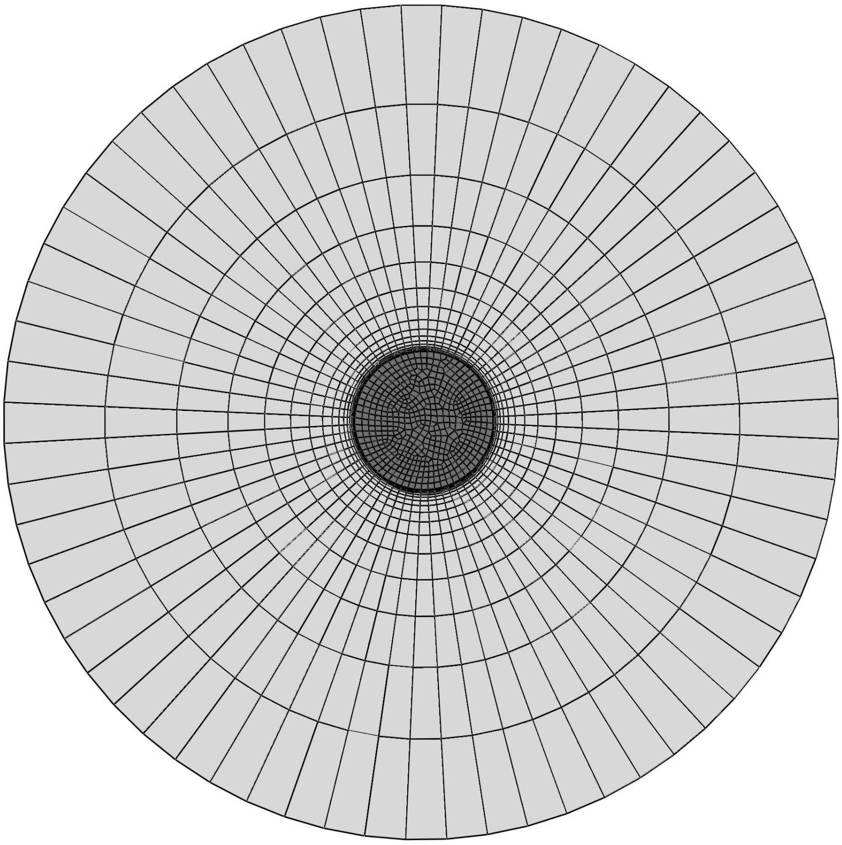

(b)

Figure 9.11: (a) Oblique view of the full 3DFE model. The diameter and depth of the mesh domain are $6D$ and $2L + 2.5D$ respectively. (b) Plan view of the full 3DFE model.

3D FELA results from Chapter 7. Evidently, the 3DFE results agree well with the 3D FELA results and are consistent with the published results, albeit with slight discrepancies due to the different soil model (Tresca soil) used in the published studies. The 3DFE torsional capacities were slightly higher than the analytical solutions, which is likely due to the fact that the 3DFE model does not allow contact breaking at the soil-foundation interface. For interested readers, the derivations of the analytical solutions are included in Appendix A.4.

Table 9.3: Uniaxial capacities of a caisson of $L/D = 0.5, 1$, where $A = \pi D^2/4$ refers to the foundation base area.

	L/D	$\frac{Q_0}{ADs_u}$	$\frac{V_0}{As_u}$	$\frac{H_0}{As_u}$	$\frac{M_0}{ADs_u}$
3DFE	0.5	1.39	10.09	4.94	1.64
Fu et al. (2017)	0.5	-	10.51	4.47	1.6
Vulpe (2015)	0.5	-	10.69	4.17	1.48
Analytical	0.5	1.333	-	-	-
3DFE	1	2.42	13.12	5.92	3.71
3D FELA (LB)	1	-	12.52	5.52	3.36
3D FELA (UB)	1	-	13.68	6.28	3.96
3D FELA (Average)	1	-	13.10	5.90	3.66
Analytical	1	2.333	-	-	-

9.2.3 Results

Definition 9.3 (q_0, v_0, h_0, m_0) *q_0, v_0, h_0, m_0 are the 'uniaxial capacities' of the torsional, vertical, lateral and moment soil reactions respectively. Like their global counterparts (Q_0, V_0, H_0, M_0), they are the ultimate, limiting value of each soil reaction, assuming that the other soil reactions are zero. For example, q_0 is the limiting value of q, for $v = 0, h = 0, m = 0$.*

Note that h_0 and m_0 are not obtained from the results corresponding to H_0 and M_0 respectively. For example, even if the caisson is experiencing zero global moment loading (i.e. $M = 0$) for the result of H_0, there are still non-zero moment soil reactions on the local level. This implies that $\alpha_{HM'} \neq \alpha_{hm'}$. Thus, h_0 and m_0 are determined by identifying the intersection of the hm yield surface with the h and m axes respectively, for $v = 0, q = 0$.

Definition 9.4 ($\tilde{q}, \tilde{v}, \tilde{h}_{\mathrm{i}}, \tilde{m}_{\mathrm{j}}$) *$\tilde{q}, \tilde{v}, \tilde{h}_{\mathrm{i}}, \tilde{m}_{\mathrm{j}}$ are the soil reactions normalised by their corresponding uniaxial capacities (i.e. $\tilde{q}, \tilde{v}, \tilde{h}_{\mathrm{i}}, \tilde{m}_{\mathrm{j}} = q/q_0, v/v_0, h_{\mathrm{i}}/h_0, m_{\mathrm{j}}/m_0$ respectively, where h_{i} and m_{j} are the lateral and moment soil reactions along some general axes i, j). Note that $\tilde{q}, \tilde{v}, \tilde{h}_{\mathrm{i}}, \tilde{m}_{\mathrm{j}}$ correspond to $\tilde{q}^{\mathrm{skirt}}, \tilde{v}^{\mathrm{skirt}}, \tilde{h}_{\mathrm{i}}^{\mathrm{skirt}}, \tilde{m}_{\mathrm{j}}^{\mathrm{skirt}}$ and $\tilde{q}^{\mathrm{base}}, \tilde{v}^{\mathrm{base}}, \tilde{h}_{\mathrm{i}}^{\mathrm{base}}, \tilde{m}_{\mathrm{j}}^{\mathrm{base}}$ for the skirt and base soil reactions respectively.*

Definition 9.5 ($\alpha_{\mathrm{hm}'}$) *$\alpha_{\mathrm{hm}'}$ is the direct analogy of $\alpha_{\mathrm{HM}'}$ for the soil reactions. Just as $\alpha_{\mathrm{HM}'}$ is the angle between the H_{i} axis and the M_{j}' axis (see Fig. 9.2), $\alpha_{\mathrm{hm}'}$ is the angle between the h_{i} axis and the m_{j}' axis (which is clockwise orthogonal to the m_{j} axis). Note that $\alpha_{\mathrm{hm}'}^{\mathrm{skirt}}$ and $\alpha_{\mathrm{hm}'}^{\mathrm{base}}$ correspond to the angle between the $h_{\mathrm{i}}^{\mathrm{skirt}}$ and $m_{\mathrm{j}}^{\mathrm{skirt}\prime}$ axes and the $h_{\mathrm{i}}^{\mathrm{base}}$ and $m_{\mathrm{j}}^{\mathrm{base}\prime}$ axes respectively.*

For the subsequent discussions, $\alpha_{\mathrm{hm}'}$ may refer to either $\alpha_{\mathrm{hm}'}^{\mathrm{skirt}}$ or $\alpha_{\mathrm{hm}'}^{\mathrm{base}}$, depending on the context. For example, when discussing about base yield surfaces, $\alpha_{\mathrm{hm}'}$ would refer to $\alpha_{\mathrm{hm}'}^{\mathrm{base}}$. Conversely, when discussing about skirt yield surfaces, $\alpha_{\mathrm{hm}'}$ would refer to $\alpha_{\mathrm{hm}'}^{\mathrm{skirt}}$.

The results of the base and skirt yield surfaces are presented primarily in terms of its projections on the *hm* plane (i.e. *hm* contours), which are referred to as *hm* yield surfaces. Furthermore, the yield surfaces are presented in terms of the normalised soil reactions ($\tilde{q}, \tilde{v}, \tilde{h}_{\mathrm{i}}, \tilde{m}_{\mathrm{j}}$). Because of symmetry, the 3DFE results were obtained for only one or two quadrants. However, the predicted failure envelopes are shown for all quadrants.

As most of the linear elastic skirt soil reactions were calibrated using the average soil reactions along the caisson skirt in Chapter 3, the skirt yield surfaces f^{skirt} were also calibrated using the average of the ultimate, limiting soil reactions along the skirt.

Uniaxial Capacities For Soil Reactions

Fig. 9.12 shows the variation of the uniaxial capacities (q_0, v_0, h_0, m_0) with L/D for the skirt and base soil reactions. For the uniaxial capacities of the skirt soil reactions, it can be observed that as L/D increases, the lateral capacity increases and the moment capacity decreases slightly, while the vertical and torsional capacities remain constant. For the uniaxial capacities of the base soil reactions, the vertical capacity increases with L/D before plateauing after $L/D > 1$. Similarly, the lateral capacity increases slightly with L/D before plateauing after $L/D > 1$. In contrast, the moment and torsional capacities remain constant. The following approximating functions were derived to approximate the uniaxial capacities of the skirt and base soil reactions:

$$\frac{v_0^{\text{skirt}}}{A^{\text{skirt}}s_{\text{u}}} = 1 \quad \text{(Analytical Solution)} \tag{9.19}$$

$$\frac{h_0^{\text{skirt}}}{A^{\text{skirt}}s_{\text{u}}} = 1.11(1 - \mathrm{e}^{-0.75L/D}) + 1.73 \tag{9.20}$$

$$\frac{m_0^{\text{skirt}}}{A^{\text{skirt}}Ds_{\text{u}}} = -0.171(1 - \mathrm{e}^{-1.32L/D}) + 0.337 \tag{9.21}$$

$$\frac{q_0^{\text{skirt}}}{A^{\text{skirt}}Ds_{\text{u}}} = 0.5 \quad \text{(Analytical Solution)} \tag{9.22}$$

$$\frac{v_0^{\text{base}}}{A^{\text{base}}s_{\text{u}}} = 3.8(1 - \mathrm{e}^{-2.19L/D}) + 5.63 \tag{9.23}$$

$$\frac{h_0^{\text{base}}}{A^{\text{base}}s_{\text{u}}} = 0.41(1 - \mathrm{e}^{-2.56L/D}) + 1 \tag{9.24}$$

$$\frac{m_0^{\text{base}}}{A^{\text{base}}Ds_{\text{u}}} = 0.73 \tag{9.25}$$

$$\frac{q_0^{\text{base}}}{A^{\text{base}}Ds_{\text{u}}} = 1/3 \quad \text{(Analytical Solution)} \tag{9.26}$$

where $A^{\text{base}} = \pi D^2/4$ is the area of the caisson base and $A^{\text{skirt}} = \pi D$ is the external surface area of the caisson skirt per metre skirt length.

Associated Flow

It was found that associated flow applies in the soil reaction space, which simplifies the calibration of oxCaisson-LEPP as the yield function f is also the plastic potential g. For example, Fig. 9.13 shows the directions of the incremental plastic displacements for the skirt and base soil reactions in the *hm* space. The figure shows that the incremental plastic displacements are approximately normal to the yield surface (approximated by the black solid line), which implies that associated flow applies at the soil reaction level. More examples are shown in Fig. 9.14.

These incremental plastic displacements are taken to be equal to the incremental total displacements ($\delta s_{\text{i}}, \delta\theta_{\text{j}}$) at the end of each incremental swipe, as the loads had stabilised by then, indicating that elastic deformation is no longer occurring. For the skirt soil reactions, the incremental plastic displacements shown in Fig. 9.13 refer to the average incremental plastic displacements along the skirt.

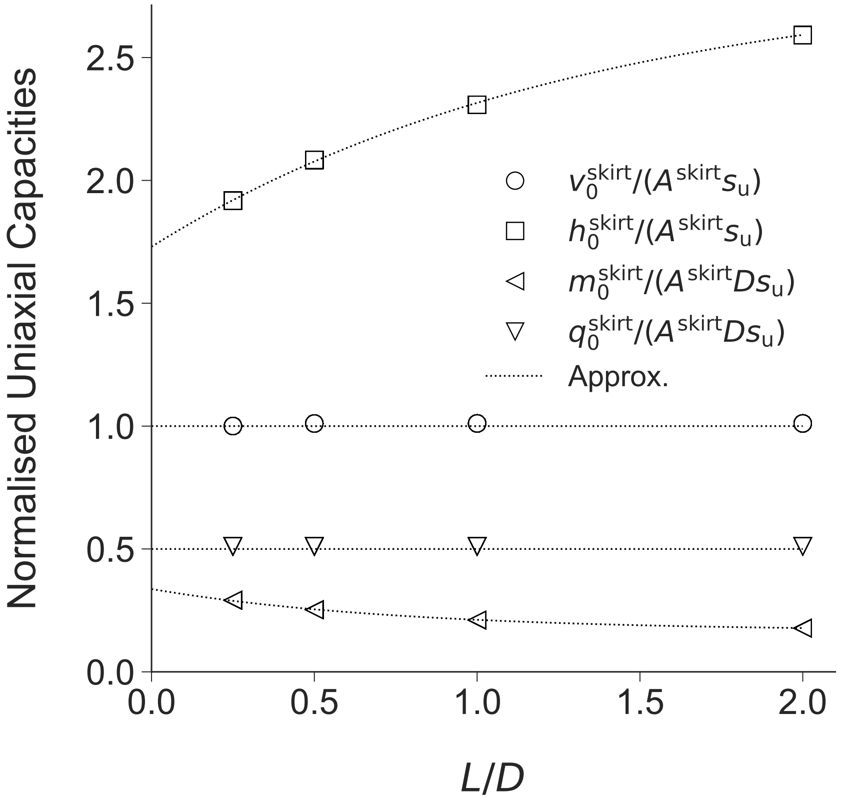

(a)

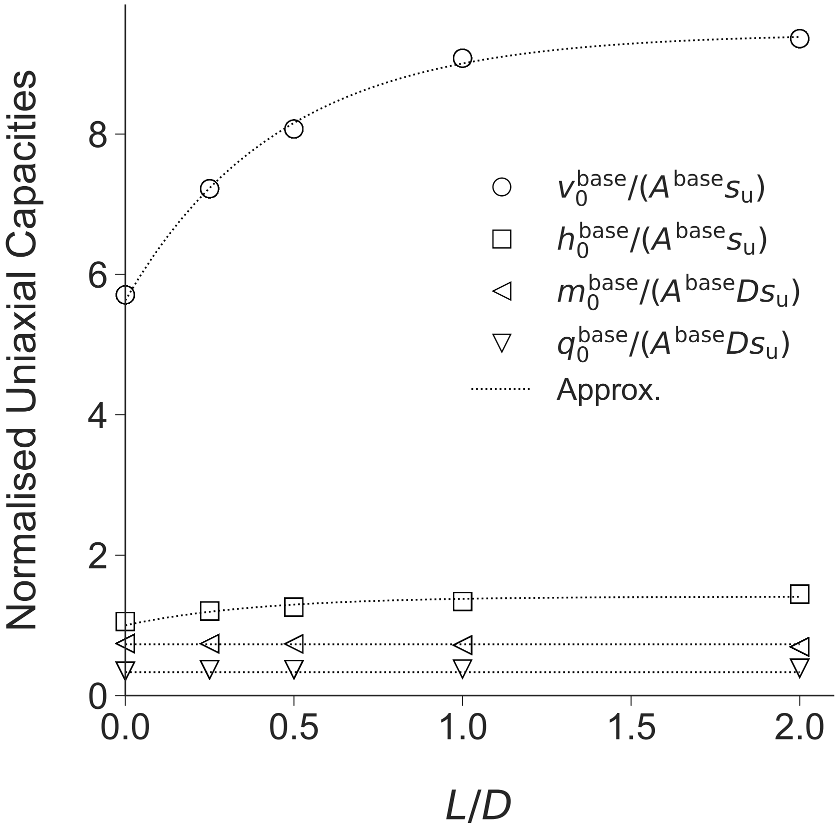

(b)

Figure 9.12: Variation of the normalised uniaxial capacities of the skirt and base soil reactions with L/D (a) Uniaxial capacities of the skirt soil reactions (b) Uniaxial capacities of the base soil reactions. The dotted lines are the uniaxial capacities predicted by Eqs. 9.19 to 9.26.

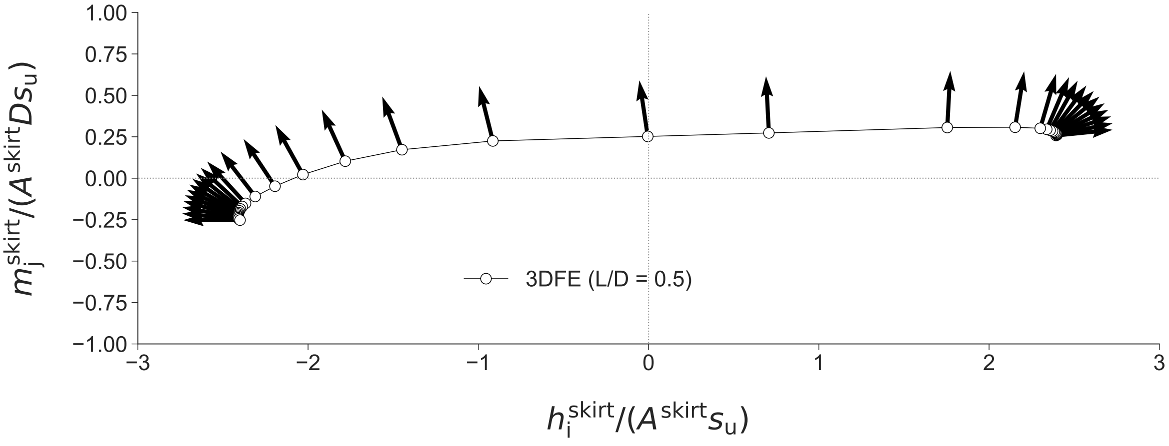

(a)

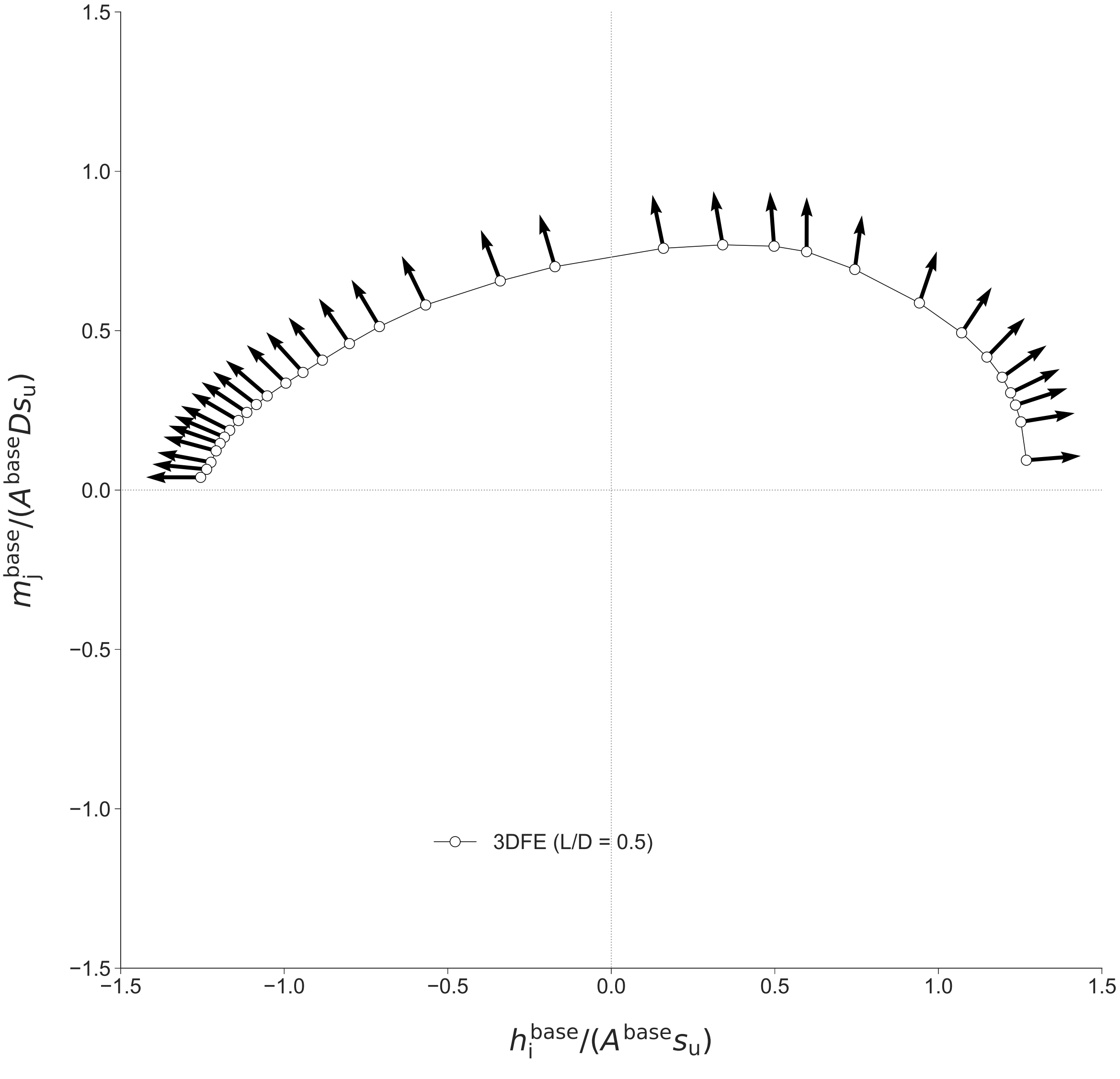

(b)

Figure 9.13: Juxtaposition of the incremental plastic displacement directions (as indicated by the arrows) of the skirt and base soil reactions with their associated yield points in hm soil reaction space, for a caisson of $L/D = 0.5$ and for $\alpha_{\mathrm{hm}'} = 0$, $\tilde{V} = 0$, $\tilde{Q} = 0$. The directions of the incremental plastic displacement are approximately normal to the yield surface, suggesting that associated flow applies in the soil reactions space. (a) Skirt soil reactions (b) Base soil reactions.

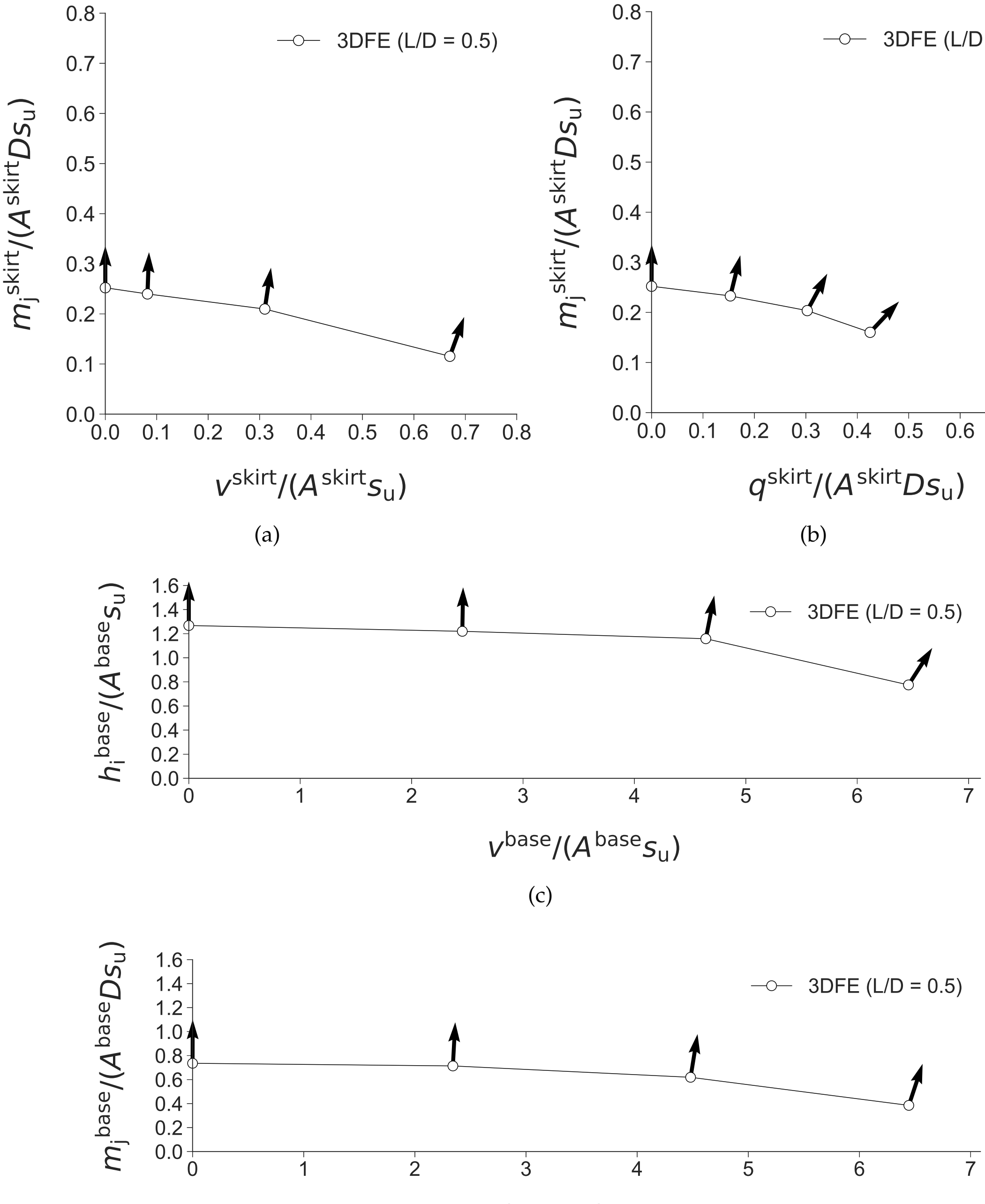

(a)

(b)

(c)

(d)

Figure 9.14: Juxtaposition of the incremental plastic displacement directions (as indicated by the arrows) of the skirt and base soil reactions with their associated yield points in different soil reaction spaces, for a caisson of $L/D = 0.5$ and for $\alpha_{hm'} = 0$, $\tilde{V} = 0$, $\tilde{Q} = 0$ (a) m-v for the skirt soil reactions (b) m-q for the skirt soil reactions (c) h-v for the base soil reactions (d) m-v for the base soil reactions.

Effect of L/D on hm Yield Surfaces

Fig. 9.15 shows the variation of the skirt and base hm yield surfaces under increasing L/D, for $\alpha_{\mathrm{HM}'} = 0, \tilde{V} = 0$ and $\tilde{Q} = 0$. It can be observed that the skirt yield surfaces get more angular as L/D increases, but the shapes of the yield surfaces remain quite similar, with all being parallelogram-like. The base yield surfaces for $L/D > 0$ are largely the same, but are distinct from the base yield surface for $L/D = 0$ in that they are more rounded in shape. This suggests that the asymmetry in the hm space is less significant for $L/D > 0$.

vhm Yield Surfaces

Fig. 9.16 shows the variation of the skirt and base hm yield surfaces for a caisson of $L/D = 0.5$ at different V load levels, for $\alpha_{\mathrm{hm}'} = 0$ and $\tilde{Q} = 0$. It is evident that as V loading increases, the available hm capacity for both the skirt and base soil reactions decreases, as depicted by the smaller yield surfaces. It can be observed that the drop in hm capacity is minor for $\tilde{V} \leq 0.5$, but increases rapidly for $\tilde{V} > 0.5$. Unlike the base yield surfaces, the increase in V loading has minimal effect on the hm asymmetry for the skirt yield surfaces.

An interesting observation is that although the global vertical load V was fixed while each hm yield surface was determined, the distribution of V between the skirt and base soil reactions is not constant (see Fig. 9.19a). Thus, each yield point in the hm yield surface may be associated with a different $\tilde{v}$ value, which causes some scatter in the yield points in Fig. 9.16. For example, for the hm yield surface corresponding to $\tilde{V} = 0.75$, $\tilde{v} \neq 0.75$ for each data point in the yield surface and $\tilde{v}$ may vary from one data point to another.

For simplicity, the average $\tilde{v}$ of all the data points in each hm yield surface (corresponding to a fixed $\tilde{V}$) were calculated and that value is representative of the $\tilde{v}$ associated with each hm yield surface. The average $\tilde{v}$ for each hm yield surface are shown in the bottom left of each subfigure in Fig. 9.16, in the order of the outermost yield surface to the innermost. In Fig. 9.16, $\tilde{V} = 0, 0.25, 0.5, 0.75$ corresponds to average $\tilde{v} = 0, 0.06, 0.24, 0.59$ for the skirt yield surfaces and average $\tilde{v} = 0, 0.30, 0.56, 0.79$ for the base yield surfaces. Thus, it appears that the vertical base soil reaction tends to reach its capacity earlier than the vertical skirt soil reaction, which contradicts 'conventional wisdom' for soil-pile interaction, where the skin friction along the pile length is fully mobilised before the end bearing force.

Further investigation reveals that under uniaxial vertical loading, the vertical skirt soil

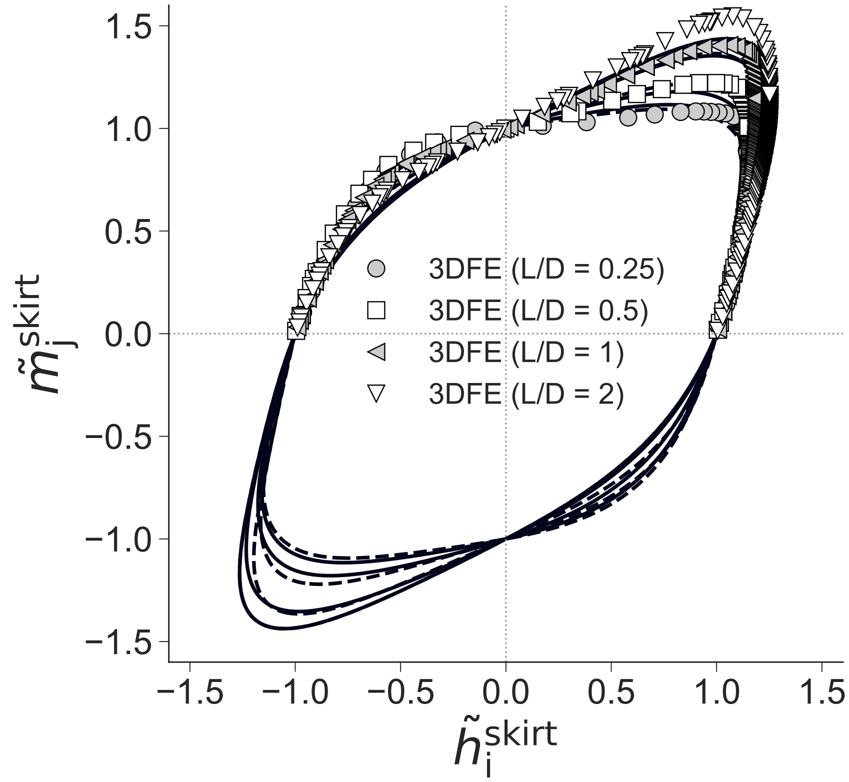

(a)

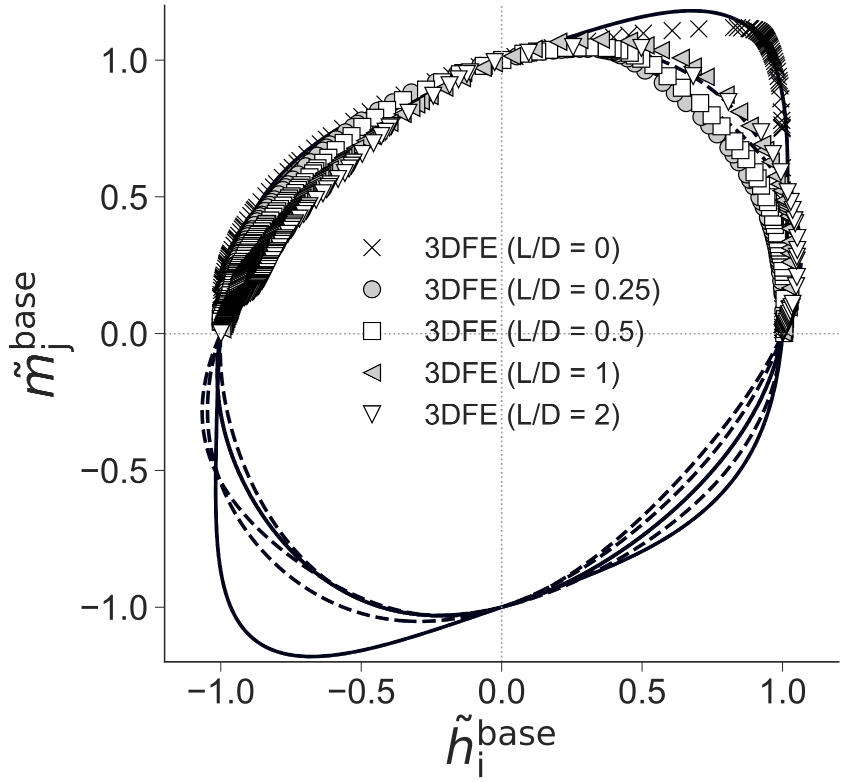

(b)

Figure 9.15: hm yield surfaces for a caisson of $L/D = 0, 0.25, 0.5, 1, 2$ for $\alpha_{hm'} = 0$, $\tilde{V} = 0$, $\tilde{Q} = 0$. (a) Skirt yield surfaces (b) Base yield surfaces. The black solid lines are the yield surfaces predicted by Eqs. 9.28 and 9.29, while the black dashed lines are those predicted by Eq. 9.27 and Tables 9.4 and 9.5.

reaction for a suction caisson foundation does indeed reach capacity before the base soil reaction, mirroring the soil-pile interaction. However, as the sequential swipe in the HM load space commences, the situation reverses and the skirt soil reaction is now mobilised more than the base soil reaction. This is evident from Fig. 9.19a, which shows the variation of the normalised vertical soil reactions (with respect to their respective capacities) during the progress of the sequential swipe for $\tilde{V} = 0.5$. It can be observed that after the application of the vertical load ($\tilde{V} = 0.5$) and before the start of the swipe, approximately 85% of the vertical skirt soil reaction capacity and 41% of the vertical base soil reaction capacity were mobilised. After the swipe commenced, the mobilisation of the average skirt soil reaction decreased and fluctuated between 20% to 40% of its capacity, while the mobilisation of the base soil reaction increased and fluctuated between 50% to 60% of its capacity.

Effect of $\alpha_{\mathrm{hm}'}$ on vhm Yield Surfaces

Figs. 9.17 and 9.18 show the effect of $\alpha_{\mathrm{hm}'}$ on the hm yield surfaces for a caisson of $L/D = 0.5$ at different V load levels, for $\tilde{Q} = 0$. Note that there are much less 3DFE data points for $\alpha_{\mathrm{hm}'} > 0$, as the results from $\alpha_{\mathrm{S\Theta}} = \pi/4, \pi/2$ are scattered around $0 \leq \alpha_{\mathrm{hm}'} \leq \pi/2$. In spite of the lack of data points, the observable trend is that the asymmetry in the hm space decreases as $\alpha_{\mathrm{hm}'}$ increases from 0, until there is no asymmetry at $\alpha_{\mathrm{hm}'} = \pi/2$.

$qvhm$ Yield Surfaces

Figs. 9.20 and 9.21 show the effect of Q loading on the hm yield surfaces for a caisson of $L/D = 0.5$ at different V load levels, for $\alpha_{\mathrm{hm}'} = 0$. It can be observed that as Q loading increases, the available hm capacity for both the skirt and base soil reactions decreases, as depicted by the smaller yield surfaces. However, the shapes of the skirt and base hm yield surfaces remain the same as Q loading increases. The average $\tilde{q}$ associated with all the data points are shown at the bottom left of each subfigure. Unlike the behaviour for vertical loading, Fig. 9.19b shows that the skirt soil reaction generally remains more mobilised than its base counterpart during the sequential swipe in the HM load space. This is confirmed by the comparisons of the average $\tilde{q}$ for the skirt and base soil reactions in Figs. 9.20 and 9.21, which indicate that (on average) the torsional skirt soil reaction is mobilised more than its base counterpart during the sequential swipes.

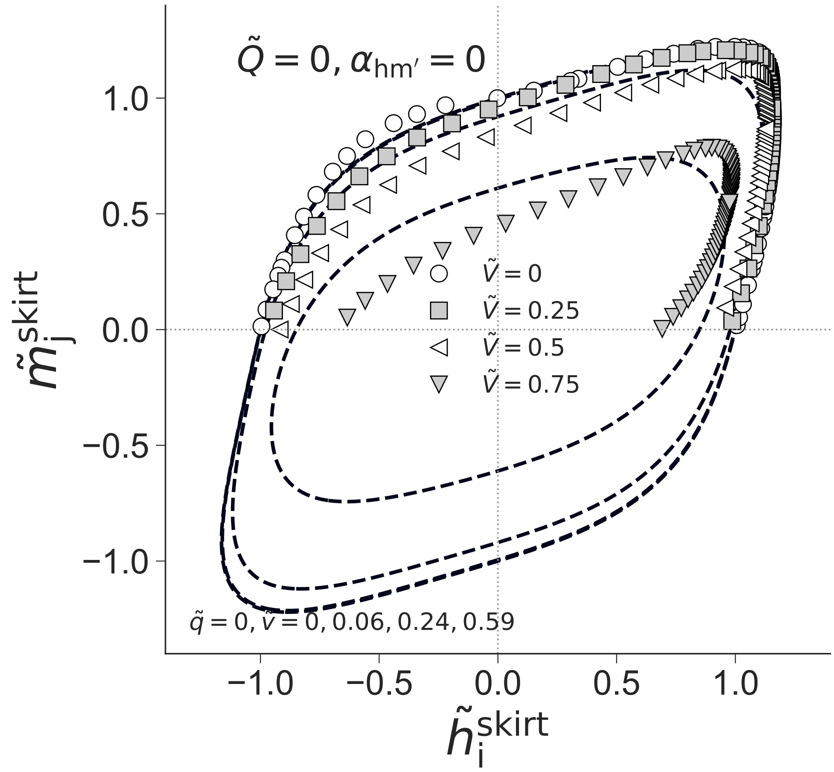

(a)

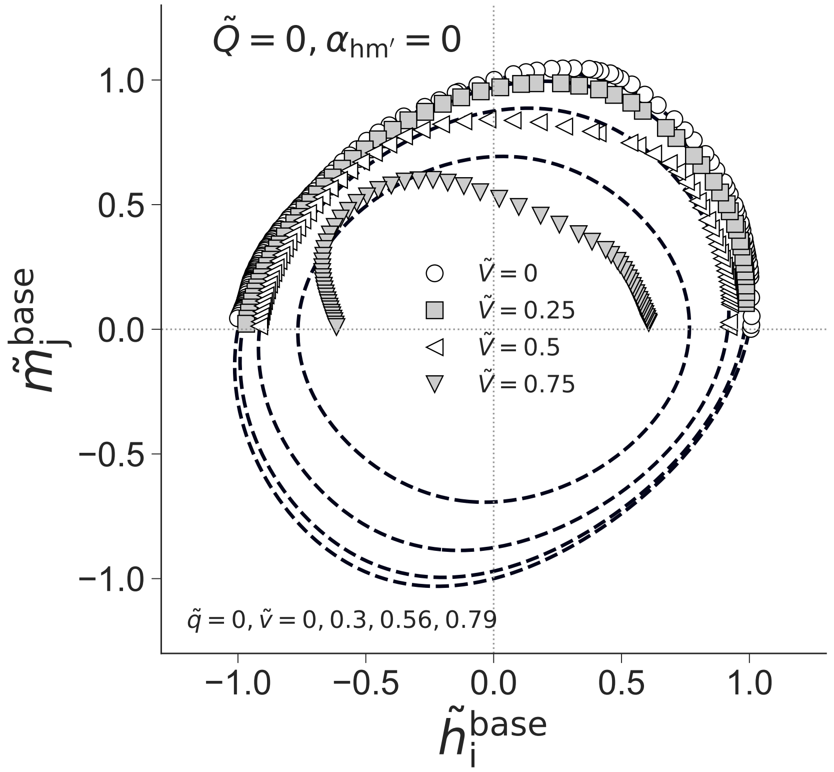

(b)

Figure 9.16: hm yield surfaces for a caisson of $L/D = 0.5$ and for $\alpha_{\mathrm{hm'}} = 0$, $\tilde{V} = 0, 0.25, 0.5, 0.75$, $\tilde{Q} = 0$. (a) Skirt yield surfaces (b) Base yield surfaces. The black dashed lines are the yield surfaces predicted by Eqs. 9.28 and 9.29. The average $\tilde{q}$ and $\tilde{v}$ of the data points are shown in the bottom left of each subfigure. $\tilde{q}$ corresponds to all the data points, while $\tilde{v}$ corresponds to the data points in each yield surface. The higher $\tilde{v}$ is, the smaller the yield surface (i.e. $\tilde{v} = 0$ and the max $\tilde{v}$ correspond to the outermost and innermost yield surfaces respectively).

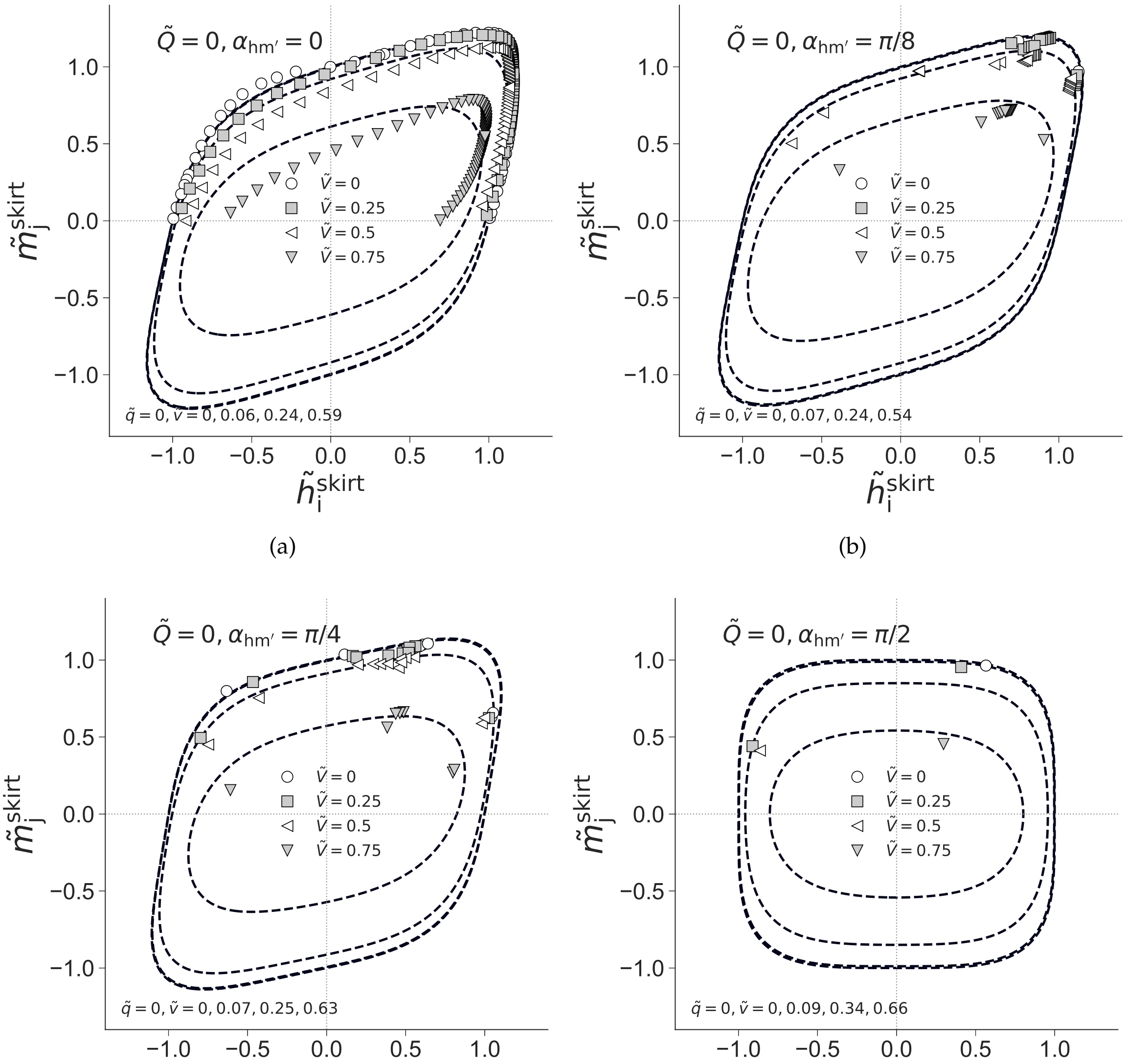

(a)

(b)

(c)

(d)

Figure 9.17: Skirt hm yield surfaces for a caisson of $L/D = 0.5$ and for $\alpha_{\mathrm{hm}'} = 0, \pi/8, \pi/4, \pi/2$, $\tilde{V} = 0, 0.25, 0.5, 0.75$, $\tilde{Q} = 0$. The black dashed lines are the yield surfaces predicted by Eqs. 9.28 and 9.29. The average $\tilde{q}$ and $\tilde{v}$ of the data points are shown in the bottom left of each subfigure. $\tilde{q}$ corresponds to all the data points, while $\tilde{v}$ corresponds to the data points in each yield surface. The higher $\tilde{v}$ is, the smaller the yield surface (i.e. $\tilde{v} = 0$ and the max $\tilde{v}$ correspond to the outermost and innermost yield surfaces respectively).

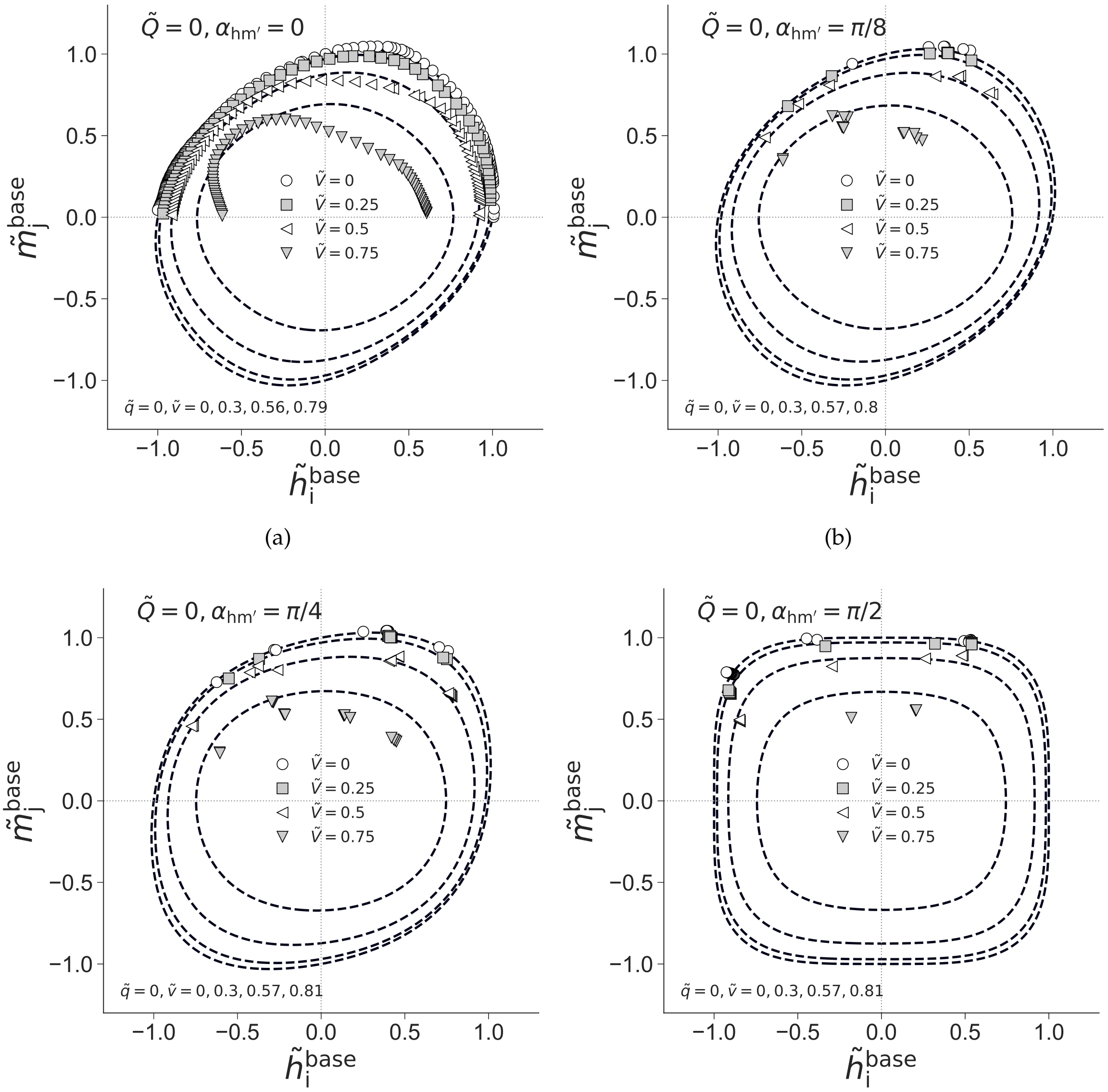

(a) (b)

(c) (d)

Figure 9.18: Base hm yield surfaces for a caisson of $L/D = 0.5$ and for $\alpha_{\mathrm{hm}'} = 0, \pi/8, \pi/4, \pi/2$, $\tilde{V} = 0, 0.25, 0.5, 0.75$, $\tilde{Q} = 0$. The black dashed lines are the yield surfaces predicted by Eqs. 9.28 and 9.29. The average $\tilde{q}$ and $\tilde{v}$ of the data points are shown in the bottom left of each subfigure. $\tilde{q}$ corresponds to all the data points, while $\tilde{v}$ corresponds to the data points in each yield surface. The higher $\tilde{v}$ is, the smaller the yield surface (i.e. $\tilde{v} = 0$ and the max $\tilde{v}$ correspond to the outermost and innermost yield surfaces respectively).

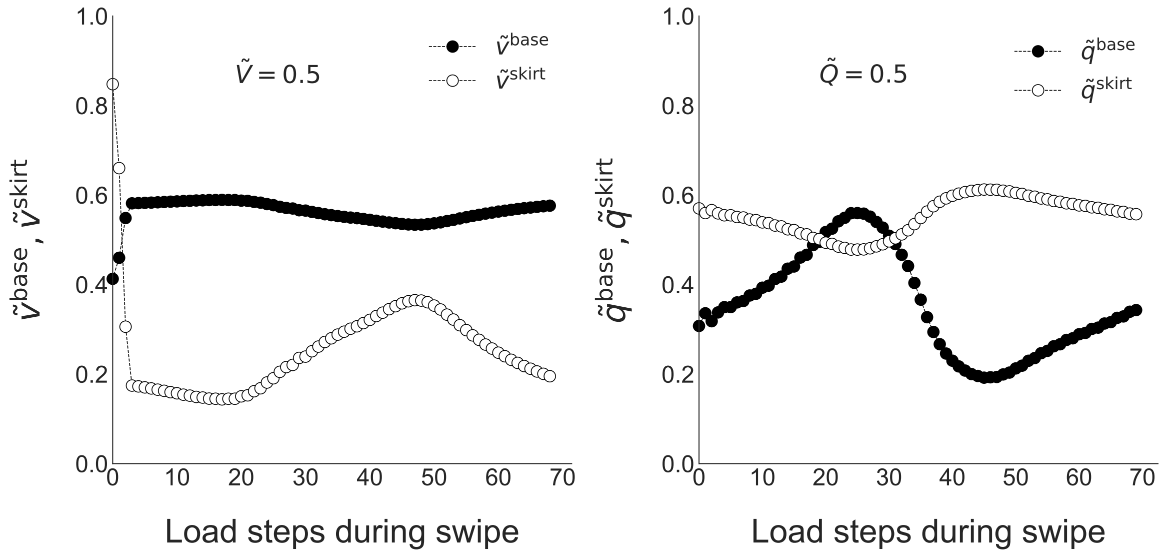

(a) (b)

Figure 9.19: (a) Variation of the normalised vertical skirt and base soil reactions for a caisson of $L/D = 0.5$ for $\alpha_{\text{hm}'} = 0$, $\tilde{V} = 0.5$, $\tilde{Q} = 0$ (b) Variation of the normalised torsional skirt and base soil reactions for a caisson of $L/D = 0.5$ for $\alpha_{\text{hm}'} = 0$, $\tilde{V} = 0$, $\tilde{Q} = 0.5$. The starting points correspond to the normalised soil reactions at the end of applying the global 'dead load' of either $\tilde{V} = 0.5$ for (a) or $\tilde{Q} = 0.5$ for (b). The starting points show that the skirt soil reactions are initially mobilised more than the base soil reactions for both vertical and torsional loading. For a vertical dead load, the situation reverses after the sequential swipe in the HM load space commences, and the vertical base soil reaction is now mobilised more than its skirt counterpart. However, for a torsional dead load, the situation generally remains the same (except for some parts of the swipe process) and the torsional skirt soil reaction remains more mobilised than its base counterpart.

Effect of $\alpha_{\text{hm}'}$ on $qvhm$ Yield Surfaces

Figs. 9.22 and 9.23 show some of the effects of $\alpha_{\text{hm}'}$ and combined V and Q loading on the hm yield surfaces for a caisson of $L/D = 0.5$, which are in line with the observed trends described in the previous figures.

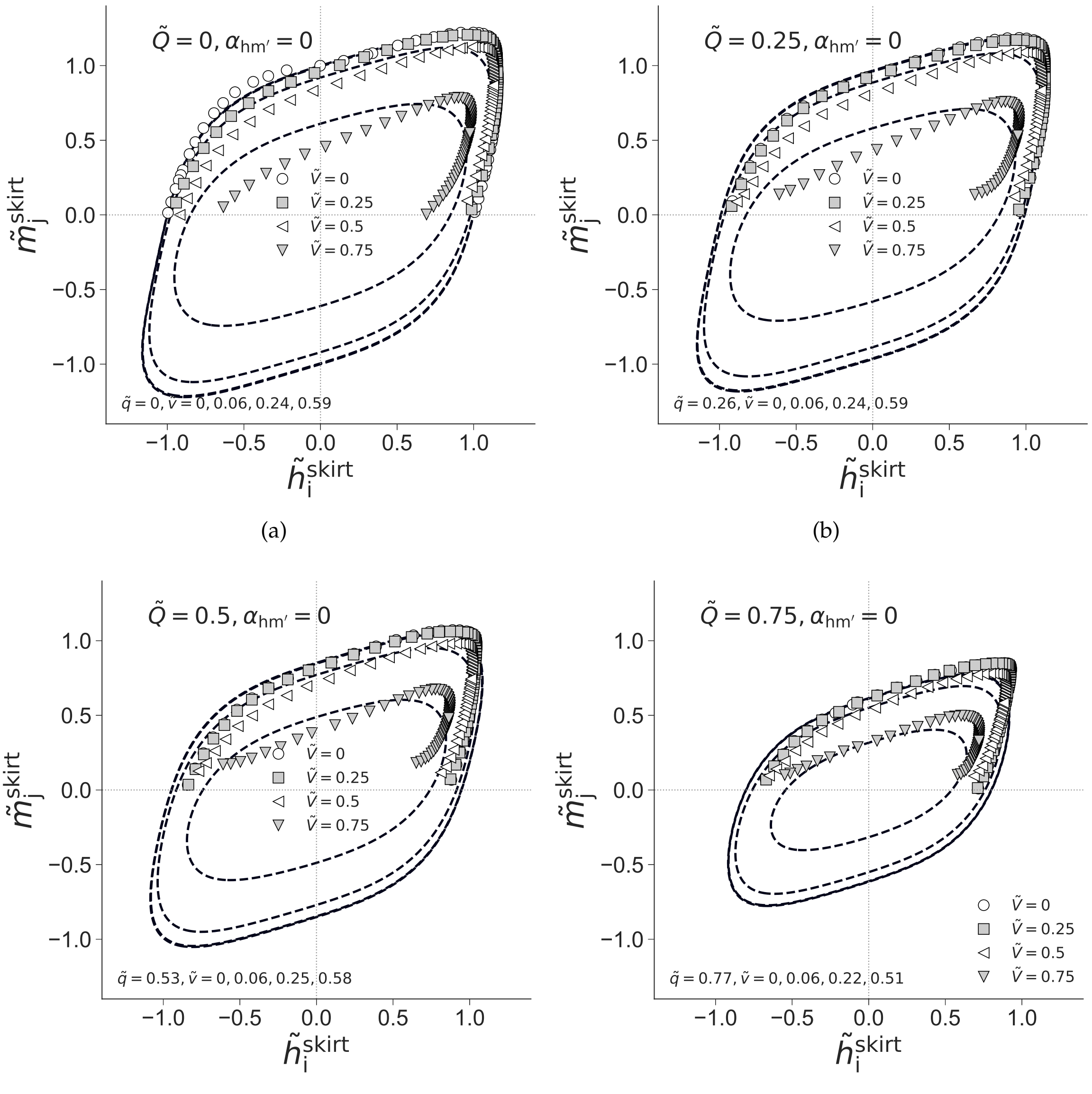

(a) (b)

(c) (d)

Figure 9.20: Skirt hm yield surfaces for a caisson of $L/D = 0.5$ and for $\alpha_{\mathrm{hm}'} = 0$, $\tilde{V} = 0, 0.25, 0.5, 0.75$, $\tilde{Q} = 0, 0.25, 0.5, 0.75$. The black dashed lines are the yield surfaces predicted by Eqs. 9.28 and 9.29. The average $\tilde{q}$ and $\tilde{v}$ of the data points are shown in the bottom left of each subfigure. $\tilde{q}$ corresponds to all the data points, while $\tilde{v}$ corresponds to the data points in each yield surface. The higher $\tilde{v}$ is, the smaller the yield surface (i.e. $\tilde{v} = 0$ and the max $\tilde{v}$ correspond to the outermost and innermost yield surfaces respectively).

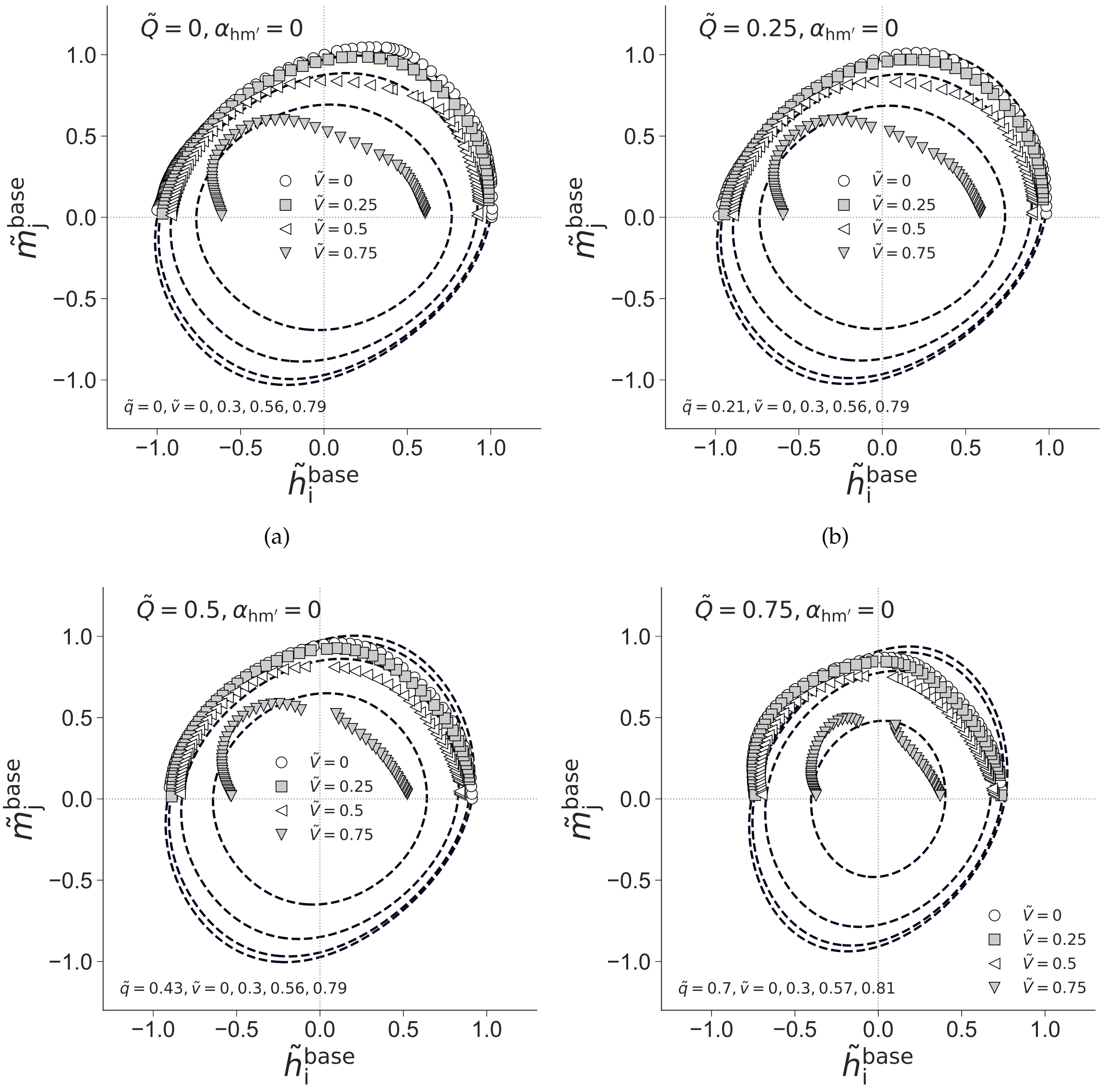

(a)

(b)

(c)

(d)

Figure 9.21: Base hm yield surfaces for a caisson of $L/D = 0.5$ and for $\alpha_{\mathrm{hm}'} = 0$, $\tilde{V} = 0, 0.25, 0.5, 0.75$, $\tilde{Q} = 0, 0.25, 0.5, 0.75$. The black dashed lines are the yield surfaces predicted by Eqs. 9.28 and 9.29. The average $\tilde{q}$ and $\tilde{v}$ of the data points are shown in the bottom left of each subfigure. $\tilde{q}$ corresponds to all the data points, while $\tilde{v}$ corresponds to the data points in each yield surface. The higher $\tilde{v}$ is, the smaller the yield surface (i.e. $\tilde{v} = 0$ and the max $\tilde{v}$ correspond to the outermost and innermost yield surfaces respectively).

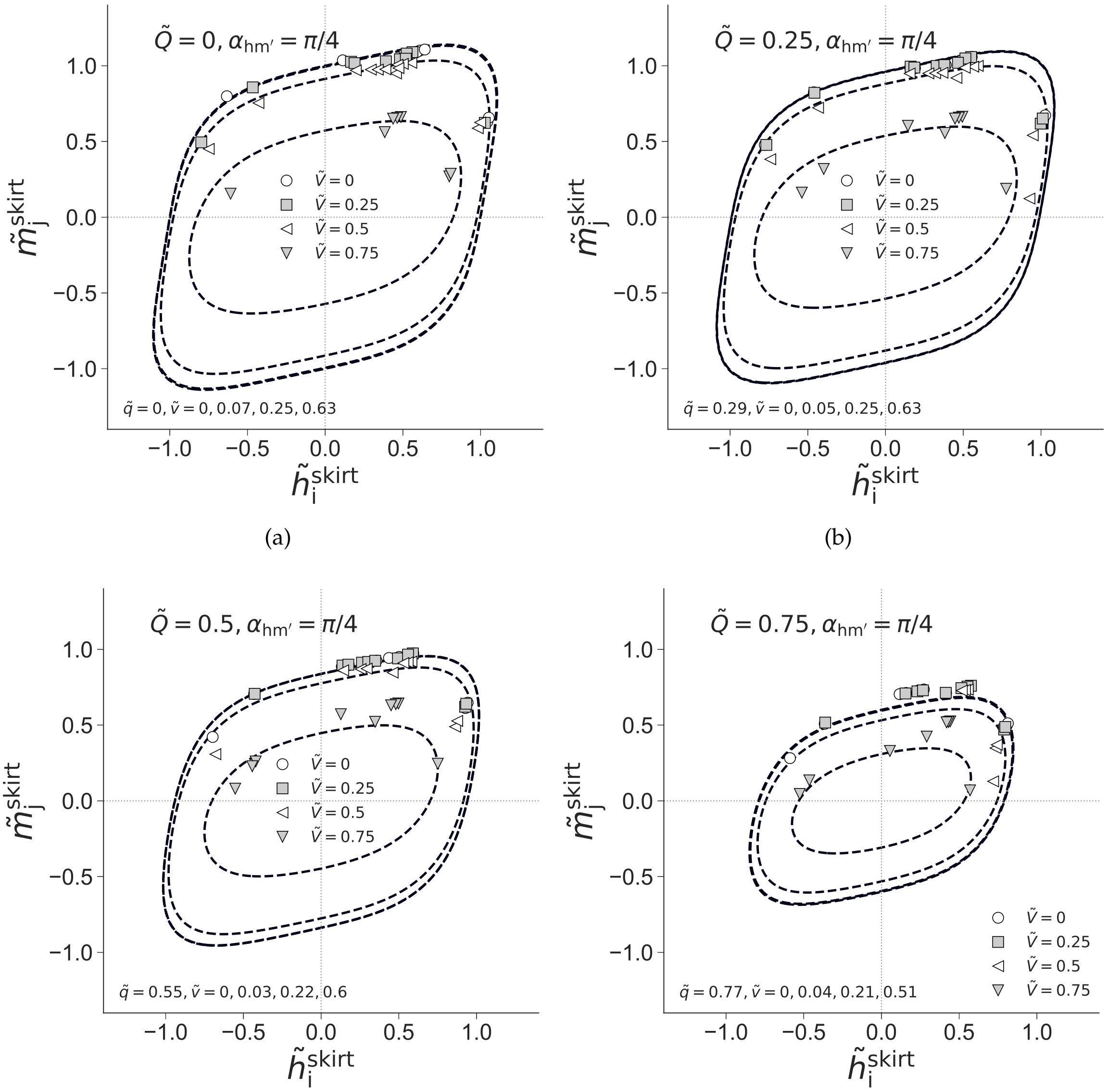

(a) (b) (c) (d)

Figure 9.22: Skirt hm yield surfaces for a caisson of $L/D = 0.5$ and for $\alpha_{\mathrm{hm'}} = \pi/4$, $\tilde{V} = 0, 0.25, 0.5, 0.75$, $\tilde{Q} = 0, 0.25, 0.5, 0.75$. The black dashed lines are the yield surfaces predicted by Eqs. 9.28 and 9.29. The average $\tilde{q}$ and $\tilde{v}$ of the data points are shown in the bottom left of each subfigure. $\tilde{q}$ corresponds to all the data points, while $\tilde{v}$ corresponds to the data points in each yield surface. The higher $\tilde{v}$ is, the smaller the yield surface (i.e. $\tilde{v} = 0$ and the max $\tilde{v}$ correspond to the outermost and innermost yield surfaces respectively).

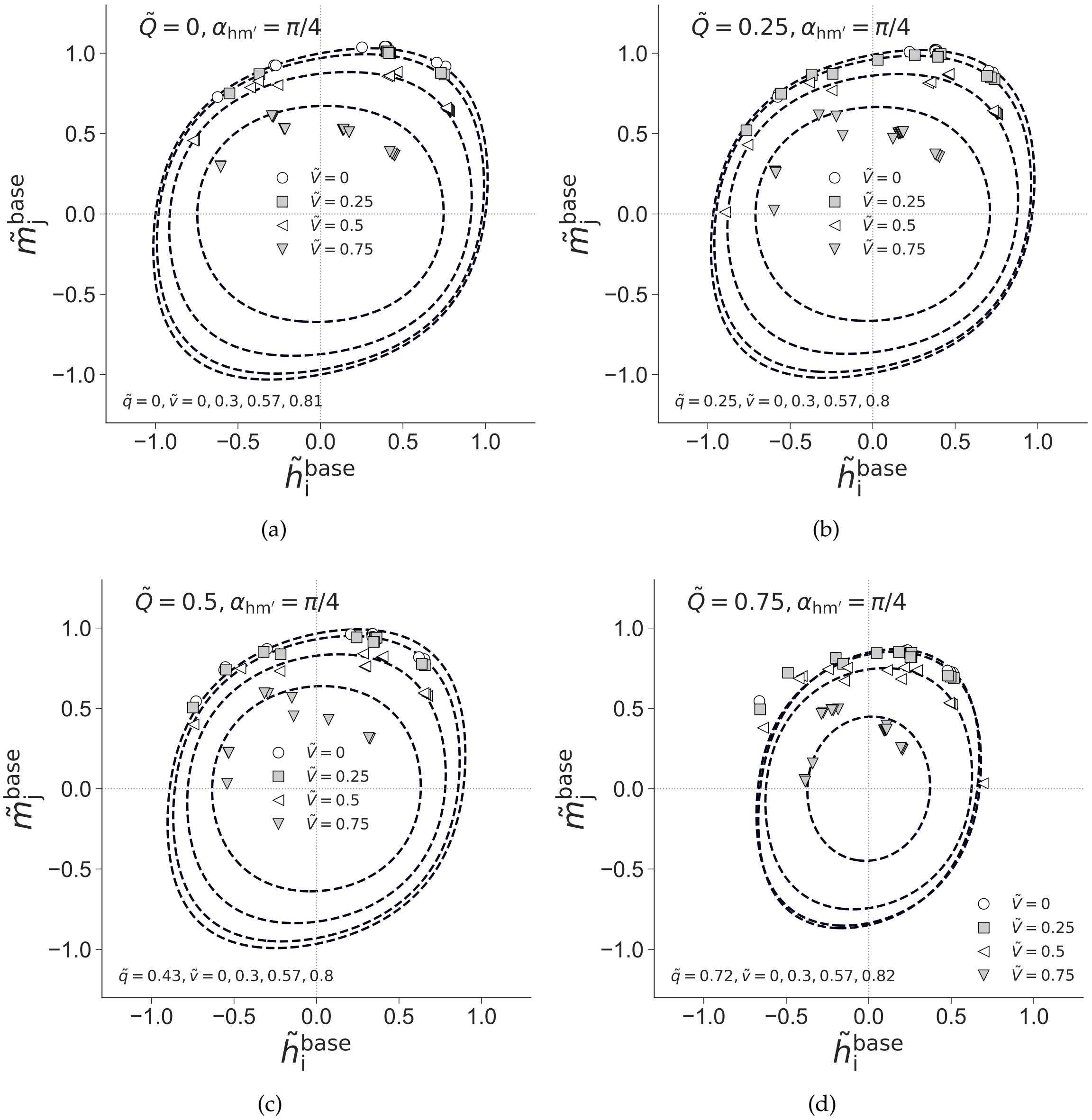

(a)

(b)

(c)

(d)

Figure 9.23: Base hm yield surfaces for a caisson of $L/D = 0.5$ and for $\alpha_{\mathrm{hm'}} = \pi/4$, $\tilde{V} = 0, 0.25, 0.5, 0.75$, $\tilde{Q} = 0, 0.25, 0.5, 0.75$. The black dashed lines are the yield surfaces predicted by Eqs. 9.28 and 9.29. The average $\tilde{q}$ and $\tilde{v}$ of the data points are shown in the bottom left of each subfigure. $\tilde{q}$ corresponds to all the data points, while $\tilde{v}$ corresponds to the data points in each yield surface. The higher $\tilde{v}$ is, the smaller the yield surface (i.e. $\tilde{v} = 0$ and the max $\tilde{v}$ correspond to the outermost and innermost yield surfaces respectively).

9.2.4 Calibration

Following the procedures detailed in Chapter 8, SOS optimisation against the 3DFE soil reaction yield points was carried out to derive the skirt and base yield surface formulations for each L/D. The derived formulations for the skirt yield surface f^{skirt} and base yield surface f^{base} are based on a 4th degree SOS polynomial as follows:

$$\begin{aligned} f(\tilde{q},\tilde{v},\tilde{h}_{\text{i}},\tilde{m}_{\text{j}},\alpha_{\text{hm}'},a_1,\ldots,a_9) = {} & {\tilde{h}_{\text{i}}}^4 + {\tilde{m}_{\text{j}}}^4 + \tilde{v}^4 + \tilde{q}^4 - 1 \\ & + I_{\text{hm}} + I_{\text{vh}} + I_{\text{vm}} + I_{\text{qh}} + I_{\text{qm}} + I_{\text{qv}} \\ & + I_{\text{vhm}} + I_{\text{qhm}} \end{aligned} \tag{9.27}$$

where

$$\begin{aligned} I_{\text{hm}} &= {\tilde{h}_{\text{i}}}^2(\tilde{h}_{\text{i}}\tilde{m}_{\text{j}}\cos\alpha_{\text{hm}'})a_1 \\ &\quad + (\tilde{h}_{\text{i}}\tilde{m}_{\text{j}}\cos\alpha_{\text{hm}'})^2 a_2 \\ &\quad + ({\tilde{m}_{\text{j}}}^2)(\tilde{h}_{\text{i}}\tilde{m}_{\text{j}}\cos\alpha_{\text{hm}'})a_3 \\ I_{\text{vh}} &= {\tilde{h}_{\text{i}}}^2\tilde{v}^2 a_4 \\ I_{\text{vhm}} &= (\tilde{h}_{\text{i}}\tilde{m}_{\text{j}}\cos\alpha_{\text{hm}'})\tilde{v}^2 a_5 \\ I_{\text{vm}} &= {\tilde{m}_{\text{j}}}^2\tilde{v}^2 a_6 \\ I_{\text{qh}} &= {\tilde{h}_{\text{i}}}^2\tilde{q}^2 a_7 \\ I_{\text{qhm}} &= (\tilde{h}_{\text{i}}\tilde{m}_{\text{j}}\cos\alpha_{\text{hm}'})\tilde{q}^2 a_8 \\ I_{\text{qm}} &= {\tilde{m}_{\text{j}}}^2\tilde{q}^2 a_9 \\ I_{\text{qv}} &= \tilde{v}^2\tilde{q}^2 a_{10} \end{aligned}$$

Note that $\tilde{q},\tilde{v},\tilde{h}_{\text{i}},\tilde{m}_{\text{j}},\alpha_{\text{hm}'}$ in Eq. 9.27 correspond to $\tilde{q}^{\text{skirt}},\tilde{v}^{\text{skirt}},\tilde{h}_{\text{i}}^{\text{skirt}},\tilde{m}_{\text{j}}^{\text{skirt}},\alpha_{\text{hm}'}^{\text{skirt}}$ for the skirt yield surfaces and $\tilde{q}^{\text{base}},\tilde{v}^{\text{base}},\tilde{h}_{\text{i}}^{\text{base}},\tilde{m}_{\text{j}}^{\text{base}},\alpha_{\text{hm}'}^{\text{base}}$ for the base yield surfaces. Based on the optimisation results, the best-fit $a_1,\ldots,a_{10}$ parameters for f^{skirt} and f^{base} are listed in Tables 9.4 and 9.5 respectively.

Generalisation Of Yield Surface Formulations

The f^{skirt} and f^{base} formulations based on Eq. 9.27 and Tables 9.4 and 9.5 are not general enough (i.e. they only support the L/D ratios listed in the tables). Thus, a generalised f^{skirt} formulation was approximated as follows:

$$f^{\text{skirt}}(\tilde{q},\tilde{v},\tilde{h}_{\text{i}},\tilde{m}_{\text{j}},\alpha_{\text{hm}'},L/D) = \mathrm{e}^{-2(L/D)^2} f_0^{\text{skirt}} + \left(1-\mathrm{e}^{-2(L/D)^2}\right) f_1^{\text{skirt}} \tag{9.28}$$

Table 9.4: Best-fit parameters in Eq. 9.27 for the skirt yield surface f^{skirt} in clay

Set	L/D	a_1	a_2	a_3	a_4	a_5	a_6	a_7	a_8	a_9	a_{10}
1	0.25	-1.11	0.76	-0.76	1.38	-2.14	5.83	0.28	-0.57	1.35	2.34
2	0.5	-0.97	0.87	-1.26	1.43	-3.44	5.69	0.37	-1.17	1.72	2.14
3	1	-1.1	1.4	-1.8	1.22	-4.05	5.36	0.29	-0.95	1.44	2.3
4	2	-1.59	2.15	-2.16	0.59	-3.21	4.43	0.12	-0.68	1.55	3.76

Table 9.5: Best-fit parameters in Eq. 9.27 for the base yield surface f^{base} in clay

Set	L/D	a_1	a_2	a_3	a_4	a_5	a_6	a_7	a_8	a_9	a_{10}
1	0	-0.35	0.89	-1.43	0.4	0.82	1.66	2.6	-0.85	0.341	0
2	0.25	-0.26	2.23	-0.99	0.44	0.32	0.69	2.68	-0.62	0.77	0
3	0.5	-0.7	2.61	-1.07	0.73	0.55	1.27	2.76	-0.84	0.71	0
4	1	-1.32	2.87	-1.38	1.17	1.82	2	2.83	-1.23	0.59	0
5	2	-1.74	3.6	-1.25	0.76	1.44	1.96	3.22	-1.41	0.4	0

where f_0^{skirt} and f_1^{skirt} are Eq. 9.27 with $a_1, \ldots, a_{10}$ being Set 1 and Set 4 from Table 9.4 respectively. Similarly, a generalised f^{base} formulation was approximated as follows:

$$f^{\text{base}}(\tilde{q},\tilde{v},\tilde{h}_{\text{i}},\tilde{m}_{\text{j}},\alpha_{\text{hm}'},L/D) = \mathrm{e}^{-100L/D} f_0^{\text{base}} + \left(1-\mathrm{e}^{-100L/D}\right) f_1^{\text{base}} \tag{9.29}$$

where f_0^{base} and f_1^{base} are Eq. 9.27 with $a_1, \ldots, a_{10}$ being Set 1 and Set 3 from Table 9.5 respectively. The terms $\mathrm{e}^{-2(L/D)^2}$ and $\mathrm{e}^{-100L/D}$ in Eqs. 9.28 and 9.29 were adopted as they best capture the variation of the soil reaction yield surfaces with respect to L/D.

Fig. 9.15 compares the hm yield surfaces predicted by Eq. 9.27 and Tables 9.4 and 9.5 with that predicted by Eqs. 9.28 and 9.29. It is evident that Eqs. 9.28 and 9.29 are reasonable approximations of Eq. 9.27 and Tables 9.4 and 9.5. It was a design choice to have approximately a common base yield surface for $L/D > 0$, as the base yield surfaces for $L/D > 0$ did not vary much. Furthermore, there was no straightforward trend with respect to L/D (the base yield surface grows inwards when it transitions from $L/D = 0$ to 0.25, but grows outwards as L/D increases further to 2).

For comparison, Figs. 9.16 to 9.23 also include the predictions of Eqs. 9.28 and 9.29. In general, the predictions of Eqs. 9.28 and 9.29 approximate the 3DFE predictions reasonably well, especially the salient features such as the size and shape of the yield surfaces.

However, one key issue remains: guarantees of global convexity and thermodynamics consistency only apply to Eq. 9.27, if the parameters in Tables 9.4 and 9.5 are used. Eqs. 9.28 and 9.28 do not have these guarantees, as they were not derived from the SOS optimisation process. However, the following proof will show that Eqs. 9.28 and 9.28 are indeed globally convex and thermodynamically consistent for $L/D \geq 0$.

Theorem 9.6 *Eqs. 9.28 and 9.29 are convex and thermodynamically consistent for* $L/D \geq 0$.

Proof f_0^{skirt}, f_1^{skirt}, f_0^{base}, f_1^{base} are all convex and thermodynamically consistent functions, as they were constrained to be so during the SOS optimisation process. Since $\mathrm{e}^{-2(L/D)^2}$ and $1 - \mathrm{e}^{-2(L/D)^2}$ are both non-negative for $L/D \geq 0$, Eq. 9.28 is a non-negative weighted sum of f_0^{skirt} and f_1^{skirt}. Similarly, Eq. 9.29 is a non-negative weighted sum of f_0^{base} and f_1^{base}. It is known that a non-negative weighted sum of convex functions is itself a convex function (Boyd & Vandenberghe 2004). Thus, Eqs. 9.28 and 9.29 are convex functions for $L/D \geq 0$.

Other than being non-negative weighted sums, Eqs. 9.28 and 9.29 are also convex combinations of $f_0^{\text{skirt}}, f_1^{\text{skirt}}$ and $f_0^{\text{base}}, f_1^{\text{base}}$ respectively. Since f_0^{skirt}, f_1^{skirt}, f_0^{base}, f_1^{base} are all ≥ -1, Eqs. 9.28 and 9.29 are also ≥ -1. Neglecting the -1 term in Eqs. 9.28 and 9.29, the homogeneous polynomial components of Eqs. 9.28 and 9.29 are ≥ 0. As described in Theorem **??**, that is sufficient to guarantee thermodynamics consistency. Thus, it is shown that Eqs. 9.28 and 9.29 are convex and thermodynamically consistent for $L/D \geq 0$. ☐

Redefinition Of Yield Surface Formulations

Following the procedures in Section 9.1.4, Eqs. 9.28 and 9.29 can be defined in terms of $h_{\mathrm{x}}, h_{\mathrm{y}}, v, m_{\mathrm{x}}, m_{\mathrm{y}}, q$, by redefining Eq. 9.27. For example, the term $\tilde{h}_{\mathrm{i}}\tilde{m}_{\mathrm{j}} \cos \alpha_{\mathrm{hm}'}$ in Eq. 9.27 can be replaced by $\tilde{h}_{\mathrm{y}}\tilde{m}_{\mathrm{x}} - \tilde{h}_{\mathrm{x}}\tilde{m}_{\mathrm{y}}$. Thus, Eq. 9.27 can be redefined as:

$$\begin{aligned} f(\tilde{q}, \tilde{v}, \tilde{h}_{\mathrm{y}}, \tilde{m}_{\mathrm{x}}, \tilde{h}_{\mathrm{x}}, \tilde{m}_{\mathrm{y}}) = {} & \left(\tilde{h}_{\mathrm{x}}{}^2 + \tilde{h}_{\mathrm{y}}{}^2\right)^2 + \left(\tilde{m}_{\mathrm{x}}{}^2 + \tilde{m}_{\mathrm{y}}{}^2\right)^2 + \tilde{v}^4 + \tilde{q}^4 - 1 \\ & + I_{\mathrm{hm}} + I_{\mathrm{vh}} + I_{\mathrm{vm}} + I_{\mathrm{qh}} + I_{\mathrm{qm}} + I_{\mathrm{qv}} \\ & + I_{\mathrm{vhm}} + I_{\mathrm{qhm}} \end{aligned} \tag{9.30}$$

where

$$
\begin{aligned}
I_{\mathrm{hm}} &= \left(\tilde{h}_{\mathrm{x}}{}^{2} + \tilde{h}_{\mathrm{y}}{}^{2}\right)(\tilde{h}_{\mathrm{y}}\tilde{m}_{\mathrm{x}} - \tilde{h}_{\mathrm{x}}\tilde{m}_{\mathrm{y}})a_{1} \\
&\quad + (\tilde{h}_{\mathrm{y}}\tilde{m}_{\mathrm{x}} - \tilde{h}_{\mathrm{x}}\tilde{m}_{\mathrm{y}})^{2}a_{2} \\
&\quad + \left(\tilde{m}_{\mathrm{x}}{}^{2} + \tilde{m}_{\mathrm{y}}{}^{2}\right)(\tilde{h}_{\mathrm{y}}\tilde{m}_{\mathrm{x}} - \tilde{h}_{\mathrm{x}}\tilde{m}_{\mathrm{y}})a_{3} \\
I_{\mathrm{vh}} &= \left(\tilde{h}_{\mathrm{x}}{}^{2} + \tilde{h}_{\mathrm{y}}{}^{2}\right)\tilde{v}^{2}a_{4} \\
I_{\mathrm{vhm}} &= (\tilde{h}_{\mathrm{y}}\tilde{m}_{\mathrm{x}} - \tilde{h}_{\mathrm{x}}\tilde{m}_{\mathrm{y}})\tilde{v}^{2}a_{5} \\
I_{\mathrm{vm}} &= \left(\tilde{m}_{\mathrm{x}}{}^{2} + \tilde{m}_{\mathrm{y}}{}^{2}\right)\tilde{v}^{2}a_{6} \\
I_{\mathrm{qh}} &= \left(\tilde{h}_{\mathrm{x}}{}^{2} + \tilde{h}_{\mathrm{y}}{}^{2}\right)\tilde{q}^{2}a_{7} \\
I_{\mathrm{qhm}} &= (\tilde{h}_{\mathrm{y}}\tilde{m}_{\mathrm{x}} - \tilde{h}_{\mathrm{x}}\tilde{m}_{\mathrm{y}})\tilde{q}^{2}a_{8} \\
I_{\mathrm{qm}} &= \left(\tilde{m}_{\mathrm{x}}{}^{2} + \tilde{m}_{\mathrm{y}}{}^{2}\right)\tilde{q}^{2}a_{9} \\
I_{\mathrm{qv}} &= \tilde{v}^{2}\tilde{q}^{2}a_{10}
\end{aligned}
$$

Therefore, Eqs. 9.28 and 9.29 are redefined through f_0^{skirt}, f_1^{skirt},f_0^{base}, f_1^{base}, which can now be defined in terms of Eq. 9.30.

9.2.5 Discussion

The calibration of oxCaisson-LEPP can be summarised as follows:

Uniaxial capacities q_0, v_0, h_0, m_0 The uniaxial capacities of the skirt and base soil reactions are defined using Eqs. 9.19 to 9.26.

Yield surface f Eq. 9.28 is defined as the skirt yield surface f^{skirt}, while Eq. 9.29 is defined as the base yield surface. They may be defined in terms of Eq. 9.27 or 9.30.

Plastic potential g As associated flow is assumed, Eqs. 9.28 and 9.29 are defined as the plastic potentials for the skirt and base soil reactions respectively.

Elastic behaviour The elastic skirt and base soil reactions are as defined in Chapter 3.

Fig. 9.24 compares the oxCaisson-LEPP predictions of the global load-displacement behaviour and HM failure envelopes for a caisson of $L/D = 0.5$ with the 3DFE results. In this figure, an 8-swipe sequential swipe test in the HM space under planar HM loading (i.e. $\alpha_{\mathrm{HM}'} = 0$) was carried out, with $\tilde{V} = 0.25$ and $\tilde{Q} = 0$. Evidently, there is excellent agreement between the oxCaisson-LEPP predictions and the 3DFE results. For example, the HM failure envelope predicted by oxCaisson-LEPP matches the 3DFE predictions very well. Moreover, there is good agreement with the total normalised vertical displacements S_z/D that resulted from maintaining $\tilde{V} = 0.25$ during the sequential swipe test (0.00279 for the 3DFE model and 0.00259 for oxCaisson-LEPP). The linear elastic vertical stiffness is slightly overpredicted by the 3DFE model due to boundary effects, as the mesh domain used in this chapter is smaller than that used in Chapter 3. However, the boundary effects do not affect the failure results.

For further insights into the prediction of the HM failure envelope by oxCaisson-LEPP, Fig. 9.25 shows the history of the global H and M loads and the local h and m soil reactions. Note that the skirt soil reactions shown in the figure correspond to the skirt soil reactions at $z/L = 0.5$. For clarity, the skirt and base yield surfaces defined in oxCaisson-LEPP are also shown in the figure.

It can be observed that as the global HM failure envelope is being explored, the skirt and base soil reactions travel along their respective yield surfaces. With 25% of the global vertical capacity (i.e. $\tilde{V} = 0.25$) applied onto the caisson, the sequential swipe in the HM load space mobilised (on average) 31% of the vertical base soil reaction capacity and 1% of the vertical skirt soil reaction capacity. This is in line with the observations in Fig. 9.16, which shows that the application of $\tilde{V} = 0.25$ corresponds to an average $\tilde{v}$ of 0.06 and 0.3 (i.e. 6% and 30% of the soil reaction vertical capacities) for the skirt and base soil reactions respectively, during the sequential swipe.

It is clear that oxCaisson-LEPP can reproduce the 3DFE predictions very well. However, its biggest advantage is its efficiency. oxCaisson-LEPP is 25 times faster than the 3DFE model as it took only 2.3 minutes (or 10.5 minutes if an explicit elasto-plastic integration algorithm was used) to generate the data points in Fig. 9.24, while the 3DFE model took 58.1 minutes. The relative increase in efficiency for oxCaisson-LEPP is much less for this example, compared to that shown in Section 9.1.5, as the oxCaisson-LEPP simulation for a surface foundation uses only one base soil element, while this example uses ten skirt soil elements and one base soil element. Due to the lack of native (i.e. without additional toolboxes) parallel processing abilities in MATLAB, the time-consuming elasto-plastic integration process had to be done sequentially, one soil element at a time. Rewriting oxCaisson-LEPP in another programming language which allows for parallel elasto-plastic integration should allow for efficiency closer to that of the surface foundation example.

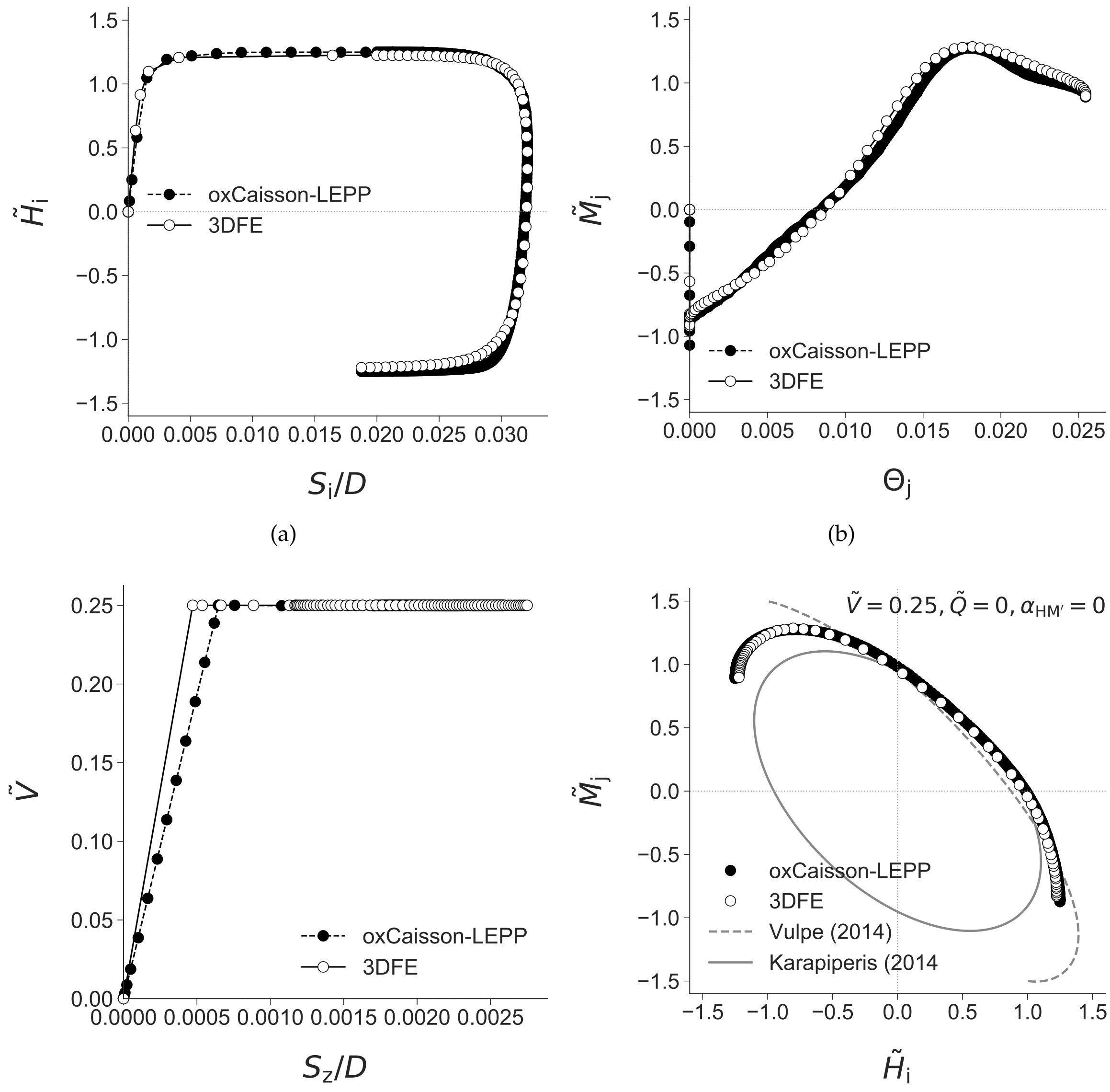

(a) (b)

(c) (d)

Figure 9.24: Comparison of sequential swipe tests in the HM space for a caisson of $L/D = 0.5$ and for $\alpha_{\mathrm{HM}'} = 0$, $\tilde{V} = 0.25$, $\tilde{Q} = 0$ (a)-(c) Load-displacement behaviour (d) HM failure envelope. Note that the failure envelope predicted by Vulpe (2015) is incomplete, as the formulation is undefined for some values in the HM space.

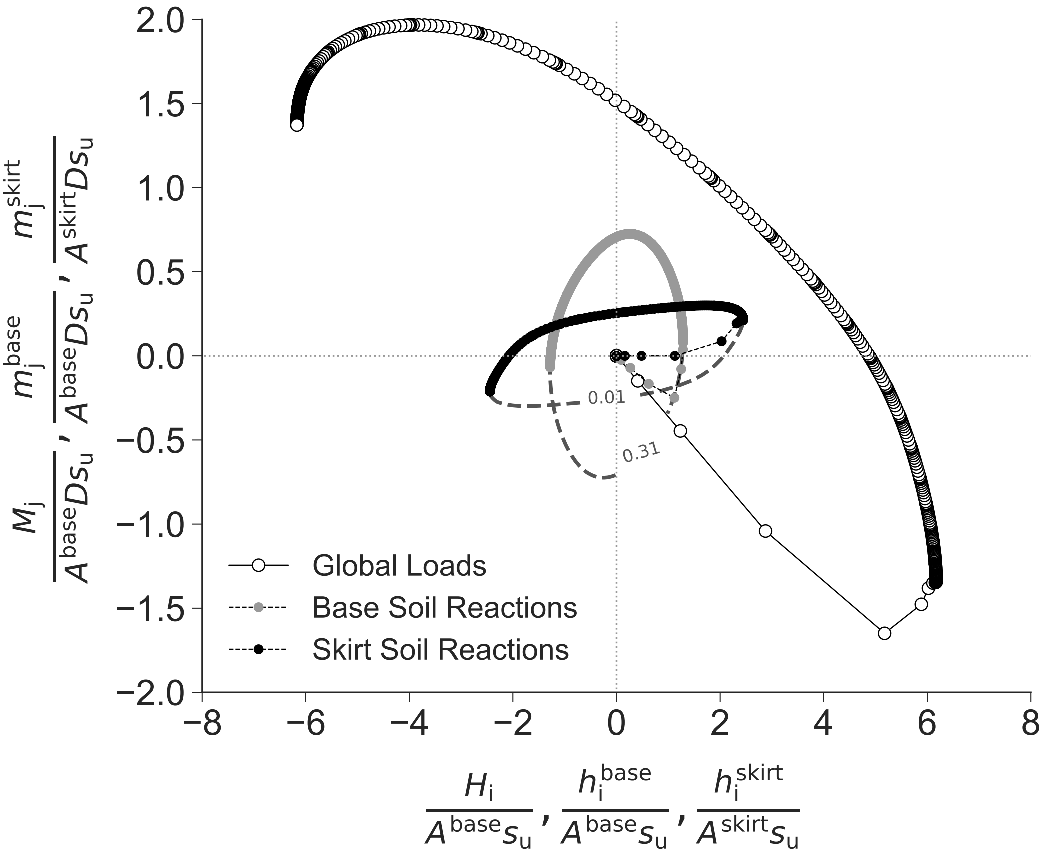

Figure 9.25: Load history of the oxCaisson-LEPP predictions in the global HM and local hm spaces for a caisson of $L/D = 0.5$, for $\alpha_{HM'} = 0$, $\tilde{V} = 0.25$, $\tilde{Q} = 0$. Note that the skirt soil reactions shown in the figure correspond to the skirt soil reactions at $z/L = 0.5$. The contour labels, which show the average $\tilde{v}$ for the data points in each hm yield surface, indicate that although a global $\tilde{V} = 0.25$ was applied onto the caisson, the base soil reaction used 31% of its vertical capacity, while the skirt soil reaction used only 1% of its vertical capacity. The global HM envelope may be computed from the local hm soil reaction yield surfaces by integrating the effect of the h and m soil reactions along the skirt length, with respect to the loading reference point (RP). Note that the h soil reaction affects both the global H and M computations.

Comparison With Previous Work

The HM failure envelopes predicted by the existing 3DFE failure envelope formulations (Eqs. 9.17 and 9.18) are also shown in Fig. 9.24d. The HM failure envelope prediction of Karapiperis & Gerolymos (2014) has the best agreement with the 3DFE results, which is surprising given that Karapiperis & Gerolymos (2014) used a non-skirted, cuboid caisson in their simulations while Vulpe (2015) used a suction caisson in their simulations. One possible reason could be that Karapiperis & Gerolymos (2014) used the von Mises yield criterion for their soil model while Vulpe (2015) used the Tresca yield criterion. Notably, the formulation of Vulpe (2015) is undefined for some values in the HM space due to the same 'raising negative numbers to fractional powers' issue discussed in Section 9.1.

Nevertheless, it is clear that the predictions of oxCaisson-LEPP are significant improvements over that of the existing failure envelope formulations. This is remarkable as oxCaisson-LEPP was calibrated on the local level (i.e. through the soil reactions), instead of the global level (i.e. through the global load response). Yet, the global predictions of oxCaisson-LEPP agree well with the global 3DFE results, despite the simplified yield surfaces adopted in oxCaisson-LEPP.

Strengths And Limitations

oxCaisson-LEPP offers several key advantages over existing design methods. First, it can be used directly to derive the failure envelope for caissons in clay of any arbitrary, non-homogeneous s_u profiles. This removes the need to derive failure envelopes for different, idealised, non-homogeneous s_u profiles (as had been done in a large volume of work e.g. Gourvenec & Randolph 2003, Gourvenec & Barnett 2011, Vulpe et al. 2014, Vulpe 2015). Thus, it can be used to assess ULS conditions for any undrained clay profile.

Second, compared to existing macro-element models (e.g. Cassidy et al. 2006), oxCaisson-LEPP is more widely applicable, as it is a more general model that can be used directly in any arbitrary, non-homogeneous or multi-layered soil. In contrast, the macro-element models can only be used when the soil and foundation properties are similar to the calibration data. Thus, oxCaisson-LEPP can be used to assess SLS conditions under complicated, combined loading conditions, for any undrained clay profile.

The above advantages are of course subject to further verifications on the accuracy of the oxCaisson-LEPP predictions for the non-homogeneous s_u case. However, existing Winkler models, e.g. *p-y* method (API 2002, DNV 2013), have already been used fairly successfully in most non-homogeneous grounds.

One notable limitation is that oxCaisson-LEPP uses only one yield surface for each soil reaction. Thus, the load-displacement behaviour may not match the highly non-linear behaviour of clay at small strains, as discussed in Chapter 6. While this can be resolved by using multiple yield surfaces for each soil reaction, this comes at the expense of increased computational effort. This additional complexity may not be desirable, as the main goal of oxCaisson-LEPP is to provide a rapid but approximate solution to the soil-caisson interaction problem for preliminary designs. Further refinement of the shortlisted designs can always be done using more advanced 3DFE analyses.

Chapter 10

Case Study

In this chapter, the oxCaisson family of design methods, as described in Chapters 3 to 9, are used in an example case study to determine the optimal dimensions of a suction caisson foundation supporting an offshore wind turbine.

10.1 Introduction

As mentioned in Chapter 1, the design of a foundation requires satisfaction of three key limit states: FLS, SLS and ULS. For simplicity, this chapter considers only the SLS and ULS cases. The SLS condition requires the displacement and rotation of the foundation to be under certain limits, while the ULS condition requires the design geotechnical and structural capacities of the foundation to exceed the extreme design loads. The main objective of the design process is to find the most cost effective design, while satisfying the limit states conditions. This process is usually iterative and involves the following:

1. Select an initial estimate of the foundation dimensions.
2. Compute the behaviour of the foundation under the design loads.
3. Check if the computed foundation behaviour satisfies the limit states conditions.
4. If the conditions are satisfied but are overly conservative, try smaller dimensions. If the conditions are not satisfied, try larger dimensions.
5. Iterate until the most cost effective design that meets the conditions is obtained.

The above iterative process is usually done manually and is thus time consuming and labour intensive. Fortunately, this iterative process can be avoided as the design problem is essentially a constrained optimisation problem.

Doherty & Lehane (2017) automated the design of a monopile foundation by casting it as an optimisation problem, where the objective is to minimise the foundation design cost, subject to the constraints posed by the limit states conditions. In the study, Doherty & Lehane (2017) determined the optimal embedded length and diameter of the minimum weight monopile foundation that satisfies both ULS and SLS conditions. The study further simplifies the design process by approximating the soil response with lateral soil reactions (Suryasentana & Lehane 2014) that accepts digital Cone Penetration Test (CPT) data as direct input. This removes a significant amount of engineering judgement and subjectivity from the design process (in terms of interpreting the soil parameters), thus reducing a large source of uncertainty in foundation design (Doherty et al. 2018).

This chapter describes an example case study where the optimal skirt length L and diameter D are determined for a mono-suction caisson foundation supporting an offshore wind turbine. Unlike monopile foundations, the design of a suction caisson foundation is heavily influenced by its installability. To highlight this, the optimal design was first obtained without considering whether the caisson can be installed. Thereafter, the optimal design was updated after considering the installability of the design.

10.2 Methodology

The case study in this chapter adopts the same design loads employed by Doherty & Lehane (2017), as shown in Table 10.1. Note that the effects of vertical loading (e.g. self-weight) are not considered here. These design loads are based on a case history for an offshore wind turbine located in the London Array wind farm, which has a water depth of approximately 25 m. The 3.6 MW wind turbine was supported by a driven steel monopile with a diameter of 5.7 m and an embedment length of about 40 m.

Table 10.1: SLS and ULS design loads for the London Array wind farm (Doherty & Lehane 2017).

	SLS	ULS
Max lateral load at ground level	5.33 MN	7.20 MN
Max bending moment at ground level	219 MNm	295.65 MNm

Ground conditions at the wind farm were reported to be silica sand. However, as

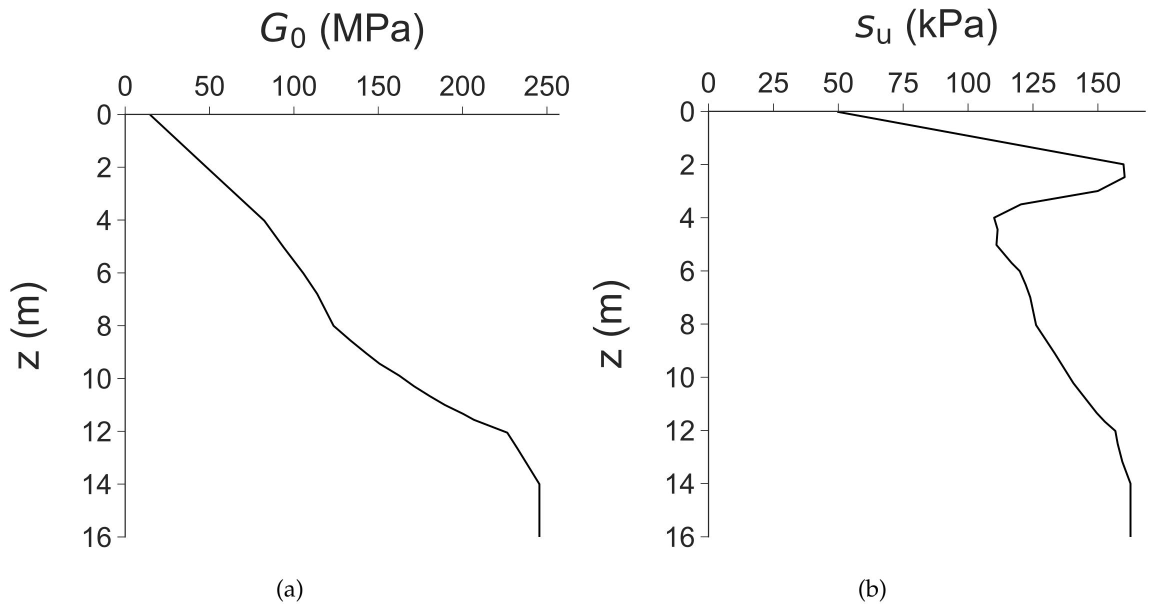

Figure 10.1: Design initial shear modulus G_0 and undrained shear strength s_u profiles (Byrne et al. 2017) adopted in this case study. The G_0 and s_u profiles are assumed to be uniform at depths below 14 m.

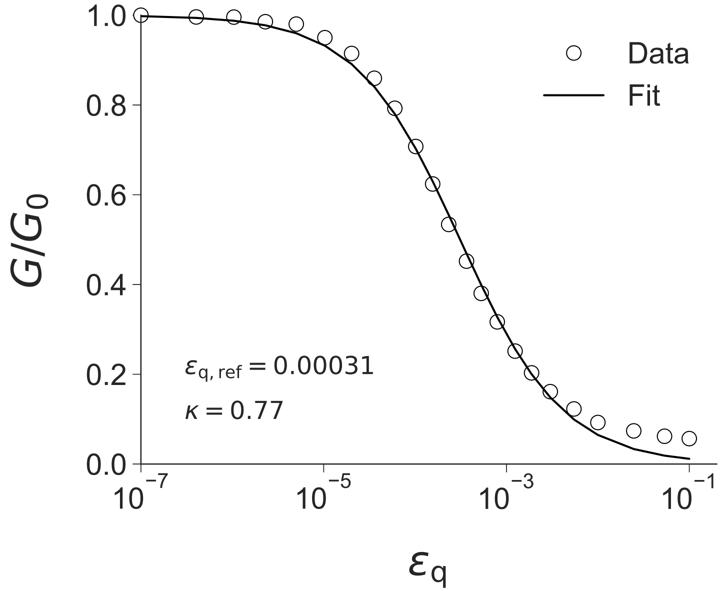

Figure 10.2: Best-fit secant shear modulus degradation profile for Cowden clay using Eq. 6.8, based on the published data in Zdravković et al. (2015).

oxCaisson-LEPP has only been calibrated for cohesive soil, this case study adopts a different soil profile from the actual case history. The Cowden stiff clay profile that was used in the PISA project (Byrne et al. 2017) is employed in this case study. Fig. 10.1 shows the design initial shear modulus G_0 and undrained shear strength s_u profiles. The small-strain, non-linearity parameters for Cowden clay were estimated as $\varepsilon_{q,\mathrm{ref}} = 0.00031$ and $\kappa = 0.77$ from the LS regression results of the published data (Zdravković et al. 2015). Fig. 10.2 shows the best-fit secant shear modulus degradation profile based on these parameters.

Design Problem

The objective of the design problem is to find the lowest cost foundation design that satisfies the limit state conditions. The cost of a foundation is assumed to be primarily determined by its material cost, which depends on its steel volume. For this study, the normalised wall thickness d_{skirt}/D is assumed to be 0.005 (following Houlsby, Kelly, Huxtable & Byrne (2005)), and the normalised lid thickness d_{lid}/D is assumed to be 0.05. The steel volume of the caisson is:

$$\begin{aligned}
\text{Vol}_{\text{caisson}} &= L\pi D^2 \left(\frac{d_{\text{skirt}}}{D} - \left(\frac{d_{\text{skirt}}}{D} \right)^2 \right) + \left(\frac{d_{\text{lid}}}{D} \right) \frac{\pi D^3}{4} \\
&= L\pi D^2 \left(0.005 - (0.005)^2 \right) + (0.05) \frac{\pi D^3}{4} \\
&= \pi D^3 \left(0.004975 \frac{L}{D} + 0.0125 \right)
\end{aligned} \tag{10.1}$$

For this study, the following SLS and ULS conditions apply. For SLS, the rotation of the foundation at ground level θ_{M} cannot exceed 0.5° (DNV 2013). For ULS, the design loads in Table 10.1 cannot exceed the capacity of the foundation (structural capacities are not considered here, as the suction caisson foundation is assumed to be linear elastic). This was defined in terms of a 'distance to failure' measure d_{ULS}, which measures how close the ULS design loads are to the global failure envelope of the foundation.

Specifically, d_{ULS} is the magnitude of the ULS design loads, relative to the magnitude of its codirectional projection on the failure envelope. The codirectional projection was identified by fitting a 2$^{\text{nd}}$ degree polynomial to the failure points close to the ULS design loads direction, and finding the intersection between the best-fit polynomial and the ULS design loads projection. Fig. 10.3 describes d_{ULS}, with respect to an idealised HM failure envelope for a caisson. $\text{d}_{\text{ULS}} = 1$ means that the ULS design loads are on the failure envelope, while $\text{d}_{\text{ULS}} > 1$ means that the ULS design loads are outside the failure envelope.

Therefore, the design problem can be cast as the following optimisation problem:

$$\begin{aligned}
\underset{D,\, L/D}{\text{minimize}} \quad & \pi D^3 \left(0.004975 \frac{L}{D} + 0.0125 \right) \\
\text{subject to} \quad & \text{d}_{\text{ULS}} \leq 1 \quad (\text{ULS}), \\
& \theta_{\text{M}} \leq 0.5^\circ \quad (\text{SLS})
\end{aligned} \tag{10.2}$$

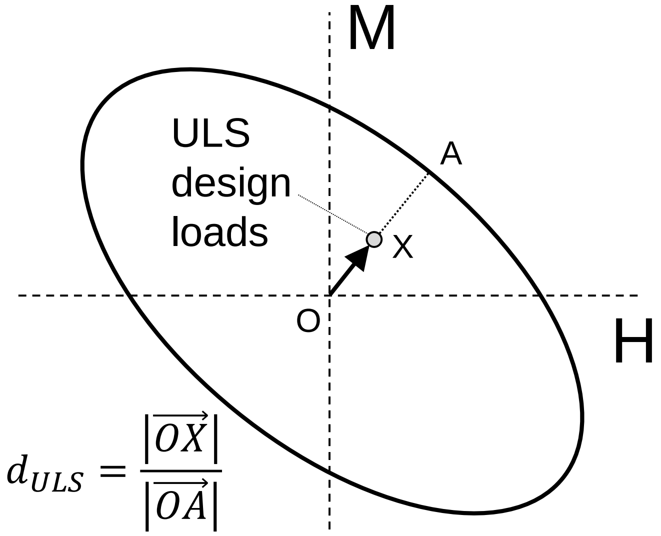

Figure 10.3: $\mathrm{d_{ULS}}$ is the ratio of the magnitude of the ULS design loads to the magnitude of its codirectional projection on the global failure envelope (i.e. Point A in the figure). $\mathrm{d_{ULS}} = 1$ means that the ULS design loads are on the failure envelope, while $\mathrm{d_{ULS}} > 1$ means that the ULS design loads are outside the failure envelope.

where the decision variables are D and L/D. oxCaisson-NLE and oxCaisson-LEPP were used to compute θ_{M}, while oxCaisson-LEPP was used to compute $\mathrm{d_{ULS}}$, where the HM failure envelopes were computed using 4-swipe sequential swipe tests (see Chapter 7).

Solver

To solve Eq. 10.2, the 'fmincon' solver in the optimisation toolbox of MATLAB was used. fmincon can find the minimum of an optimisation problem specified by:

$$\begin{aligned} \underset{\vec{x}}{\text{minimize}} \quad & f(\vec{x}) \\ \text{subject to} \quad & c(\vec{x}) \leq 0, \\ & \vec{lb} \leq \vec{x} \leq \vec{ub} \end{aligned} \tag{10.3}$$

where $f(\vec{x})$ is the objective function, $c(\vec{x})$ is the inequality constraints function, $\vec{x}$ are the decision variables and $\vec{lb}, \vec{ub}$ are the lower and upper bounds of the decision variables. To convert Eq. 10.2 into the form of Eq. 10.3, the following are defined:

- $\vec{x} = [D, L/D]$, $\vec{lb} = [6, 0]$, $\vec{ub} = [18, 2]$
- $f(\vec{x}) = \pi D^3 \left(0.004975\frac{L}{D} + 0.0125\right)$
- $c(\vec{x}) = \begin{bmatrix} \mathrm{d_{ULS}} - 1 \\ \theta_{\mathrm{M}} - 0.5 \end{bmatrix}$

fmincon requires an initial estimate of $\vec{x}$, which was set to $[12, 1]$ (average of $\vec{lb}$ and $\vec{ub}$).

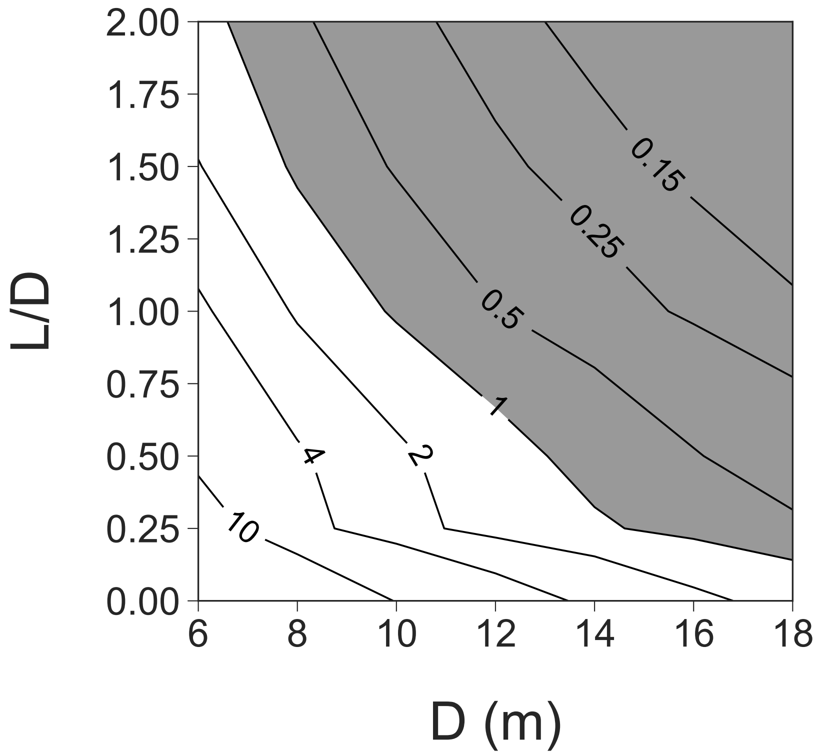

Figure 10.4: Contour plots of d_{ULS} (value shown in contour label), as computed by oxCaisson-LEPP. The filled region represents the feasible combinations of D and L/D that satisfy the ULS constraint of $d_{\mathrm{ULS}} \leq 1$.

10.3 Results

A graphical approach was first used to estimate the solution to the optimisation problem. The contours of d_{ULS} and θ_{M} were generated by interpolation from a set of computed data points corresponding to $D = 6, 8, 10, 12, 14, 16, 18$ and $L/D = 0, 0.25, 0.5, 1, 1.5, 2$. It took 14 minutes to compute the d_{ULS} data points using oxCaisson-LEPP, while it took 6 minutes to compute the θ_{M} data points using oxCaisson-NLE (7 minutes for oxCaisson-LEPP).

Fig. 10.4 plots the d_{ULS} contours, where each contour defines the combinations of D and L/D that produce a certain amount of d_{ULS}. The filled region represents the feasible combinations of D and L/D that satisfy the ULS constraint of $d_{\mathrm{ULS}} \leq 1$.

Fig. 10.5 plots the θ_{M} contours computed by oxCaisson-LEPP and oxCaisson-NLE, where each contour defines the combinations of D and L/D that produce a certain amount of θ_{M}. The filled region represents the feasible combinations of D and L/D that satisfy the SLS constraint of $\theta_{\mathrm{M}} \leq 0.5°$. For Fig. 10.5a, the feasible region is a coarse extrapolation based on the computed θ_{M} data points, which never exceed 0.5°. Note that convergence issues prevented the computation of θ_{M} in the region where $d_{\mathrm{ULS}} > 1$.

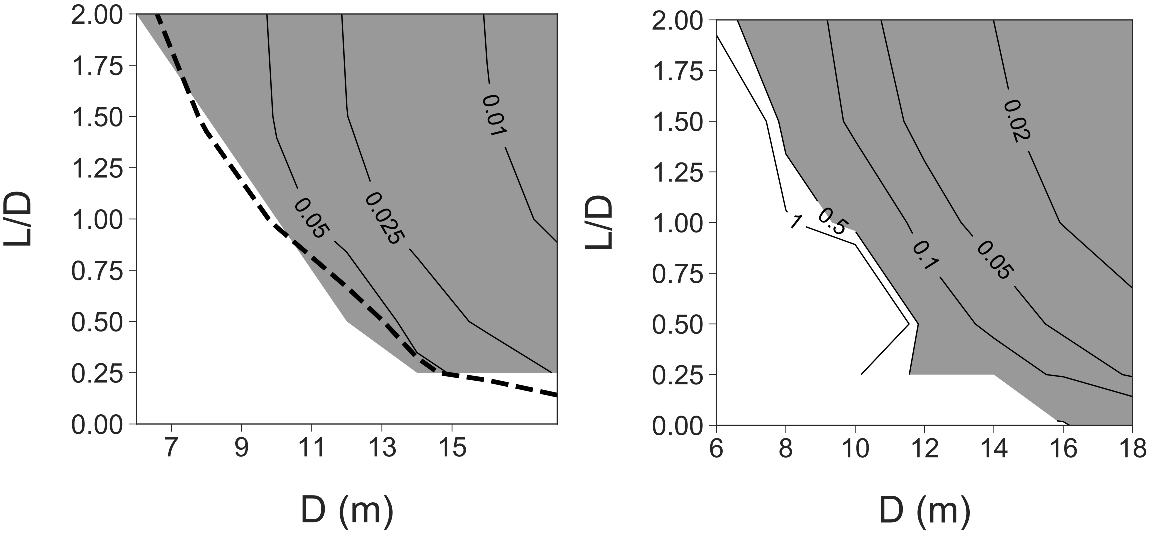

(a)

(b)

Figure 10.5: Contour plots of θ_M (value shown in contour label) (a) using oxCaisson-LEPP (b) using oxCaisson-NLE. The filled region represents the feasible combinations of D and L/D that satisfy the SLS constraint of $\theta_M \leq 0.5°$. The unfilled region includes combinations of D and L/D where no solution can be obtained (as the SLS design loads exceed the capacity of the foundation). The black dashed line in (a) represents the contour of $d_{ULS} = 1$ from Fig. 10.4. Some of the contours in (b) do not extend to $L/D = 0$, as no solution could be obtained for parts of the unfilled region where $L/D \leq 0.25$.

Fig. 10.6 plots the contours for the suction caisson steel volume (i.e. the objective function of Eq. 10.2) in terms of D and L/D. It is clear that the minimum volume lies in the region of low D and high L/D. This can be readily observed from Eq. 10.2, which shows that the suction caisson steel volume varies linearly with L/D, but cubically with D. Furthermore, Fig. 10.6 overlays the SLS (obtained using oxCaisson-NLE) and ULS constraints, which shows that the ULS constraint governs. The filled region represents the feasible combinations of D and L/D that satisfy both the SLS and ULS conditions. Based on the contours, the optimal dimensions is estimated to be the point at the top left corner of the feasible region, corresponding to D = 6.7 m, L/D = 2 and caisson steel volume = 21.2 m^3.

Solver Results

Fig. 10.6 shows the progress of the optimisation problem solver, starting from the initial point ($D = 12$ m, $L/D = 1$) until the final, optimal point ($D = 6.4$ m, $L/D = 2$), which are close to the values ($D = 6.7$ m, $L/D = 2$) estimated by the graphical approach. A better estimate can be obtained using the graphical approach by computing more data points for more accurate contours, but that would require more computational time. The optimal dimensions were obtained by the solver after 11 trials (taking 13 minutes) and correspond

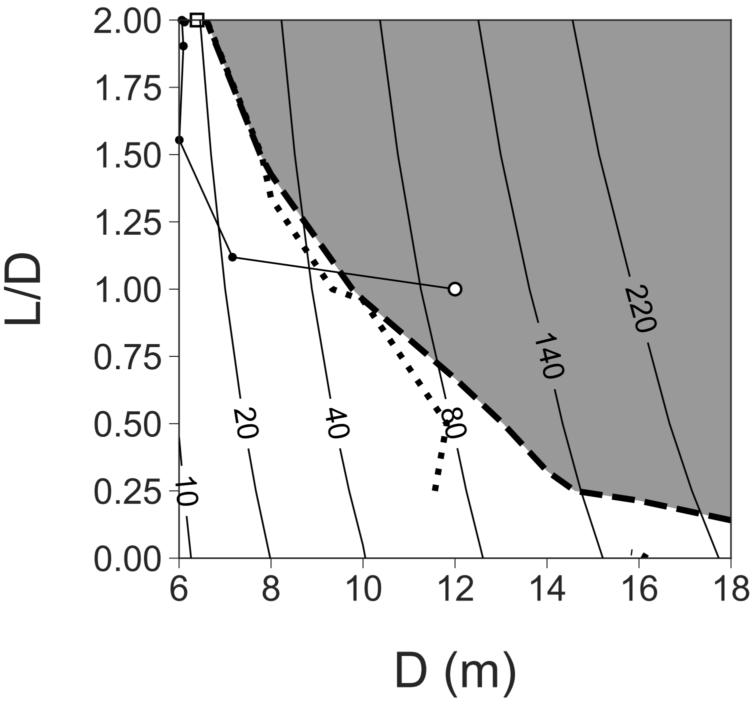

Figure 10.6: Contour plots of the suction caisson steel volume (value shown in contour label in m^3 units). The thick black dotted and dashed lines represent the SLS (obtained using oxCaisson-NLE) and ULS constraints respectively. The filled region represents the feasible combinations of D and L/D that satisfy both the SLS and ULS constraints. The above figure also includes the progress of the optimisation problem solver, starting from the initial estimate (shown as the white circle marker) until the final, optimal result (shown as the white square marker).

to a caisson steel volume of 18.5 m^3.

10.4 Discussion

The design problem could be solved quickly because oxCaisson is very efficient. This would be impractical, if the 3DFE method was used to compute the foundation response. The graphical approach took 20 minutes, while the solver approach took 13 minutes. One advantage of the graphical approach is that it allows a better understanding of the design problem through visualisation of the feasible parameter space, which is not possible with the solver approach. The main disadvantages of the graphical approach are that the solution process is not automated, its solution is not as accurate as the solver approach and it is not suitable for optimisation problems with more than two decision variables.

For comparison purposes, a 3DFE analysis of a suction caisson foundation with the optimal dimensions (D = 6.4 m, L/D = 2) in von Mises soil (using the G_0 and s_u profiles in Fig. 10.1) was carried out. Fig. 10.7a compares the oxCaisson-LEPP predictions of θ_M (under the SLS design loads) with the 3DFE results. It is clear that the predicted θ_M

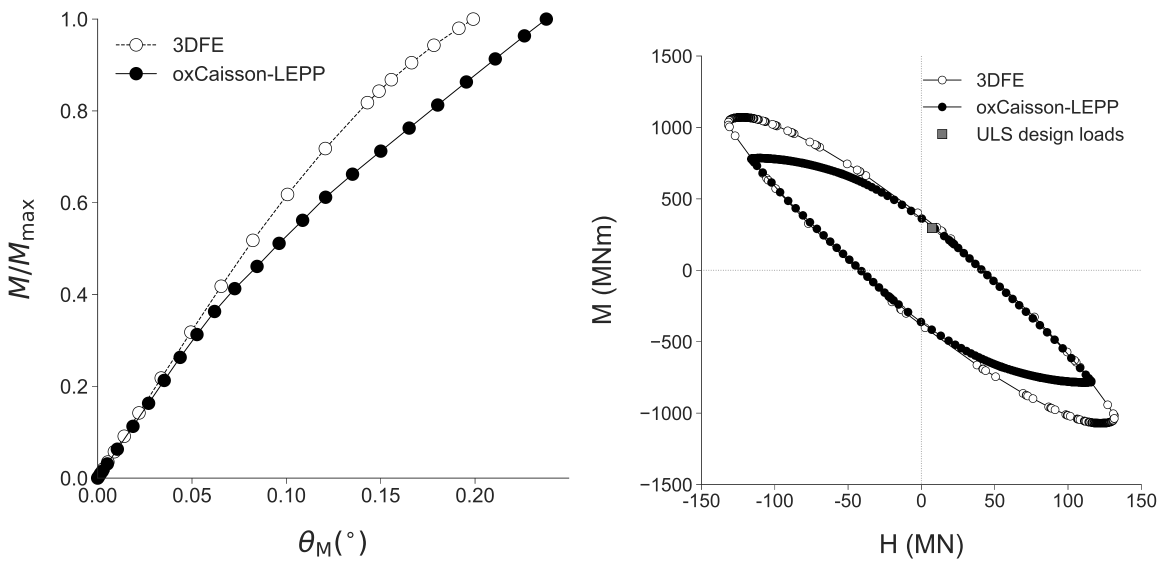

(a) (b)

Figure 10.7: Comparison of the oxCaisson-LEPP predictions with the 3DFE results for (a) Ground level rotation θ_M of the foundation (b) Global HM failure envelope.

agrees reasonably well with the 3DFE results and is less than 0.5°, thus satisfying the SLS constraint. Fig. 10.7b compares the oxCaisson-LEPP predictions of the global HM failure envelope with the 3DFE results. Again, the predictions agree very well with the 3DFE results in the HM quadrants where H and M are of the same sign, and less so in the other quadrants. Fig. 10.7b also shows that the ULS design loads are not outside of the HM failure envelope, thus satisfying the ULS constraint.

Installability Constraint

As mentioned earlier, the design of a suction caisson foundation is heavily influenced by its installability. Since the water depth of this case study is assumed to be 25 m, the maximum suction pressure available before cavitation is 350 kPa (this is a highly simplified calculation, as the actual value depends on multiple factors such as the pump location, whether the pump can truly reduce the pressure to zero etc.). Thus, installability requirements impose the following additional constraint on the optimisation problem: the suction pressure required to install the caisson should not exceed 350 kPa.

The suction pressure required to install the caisson can be computed using the procedures described by Houlsby & Byrne (2005*a*). Assuming a total vertical load of 3 MN and $\alpha_o = \alpha_i = 0.5$ during installation, the suction pressure required to install a caisson with the optimal dimensions ($D = 6.4$ m, $L/D = 2$) is 962 kPa, which is more than 350

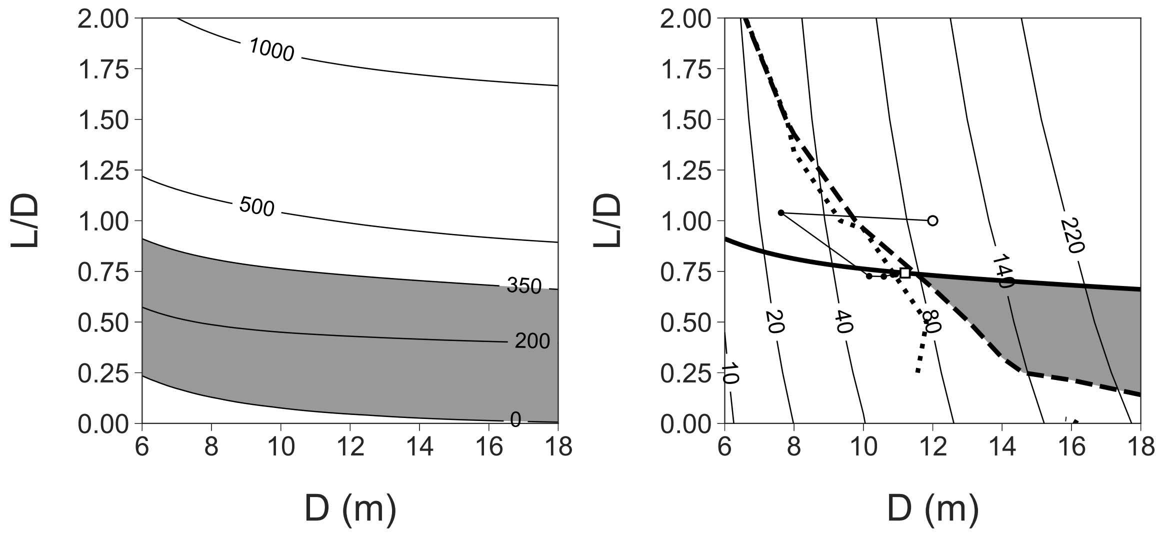

(a)

(b)

Figure 10.8: (a) Contour plots of the suction pressure (value shown in contour label in kPa units) required for the installation of the caisson. The filled region represents the feasible combinations of D and L/D that can be installed by suction, while the unfilled region below the filled region represents the combinations of D and L/D that can be installed by self-weight alone. (b) Contour plots of the caisson steel volume (value shown in contour label). The filled region represents the feasible combinations of D and L/D that satisfy the ULS, SLS and installability constraints. The thick black dotted, dashed and solid lines represent the SLS (obtained using oxCaisson-NLE), ULS and installability constraints respectively. The progress of the solver is also shown in (b), starting from the initial estimate (shown as the white circle marker) until the final, optimal result (shown as the white square marker).

kPa. Thus, this caisson cannot be installed. Fig. 10.8a shows the contours of the suction pressure required to install caissons of varying dimensions. The filled region represents the feasible combinations of D and L/D that can be installed, while the unfilled region below it represents the caisson dimensions that can be installed by self-weight alone.

The optimisation problem was solved again, with the additional constraint that the suction pressure required for installation must not exceed 350 kPa. Fig. 10.8b shows the updated feasible region satisfying this additional constraint and the progress of the solver. Based on the solver results, the optimal dimensions of the caisson that can be installed is $D = 11.2$ m and $L/D = 0.74$, which correspond to a caisson steel volume of 71.4 m^3 (which is about 4 times the original, optimal steel volume of 18.5 m^3, obtained without considering installability). All constraints are met, as the computed $\mathrm{d}_{\mathrm{ULS}}$ is 0.9996, θ_{M} is 0.22° and the suction pressure required for installation is 349.9 kPa.

To conclude, this chapter has demonstrated the use of the oxCaisson design methods to optimise the design for a suction caisson foundation. The analysis here is highly simplified, and a real design case needs to take into consideration structural fatigue behaviour for FLS, structural capacity for ULS and cyclic loading behaviour for SLS. Nevertheless, the design approach adopted in this chapter was found to be very efficient, which not only reduces design time, but may also result in improved design outcomes.

Chapter 11

Conclusion

Recent trends in the offshore wind industry have generated a pressing need for new design methods for suction caisson foundations that are both fast and accurate. This thesis addresses this need by developing a family of computationally efficient design methods (called oxCaisson) that are highly suited for time-critical applications such as large scale foundation design optimisation for offshore wind farms. The main contributions of the thesis are summarised below:

11.1 Contributions

Chapter 3 The key contributions of this chapter are threefold.

1. This work presents a complete Winkler model for suction caisson foundations under 6DoF loading.

2. This work provides the first rigorously validated set of Winkler formulations that represent the true soil reactions acting on the suction caisson foundations. Formulations used in previous models are either coarse approximations (e.g. plane strain conditions) or unrealistic back-calculated values that do not necessarily match the true physics of the soil-foundation interaction problem. The discussions in the chapter have also shown how the back-calculation approach may lead to misleading conclusions about the nature of the local soil response.

3. The formulations derived in this work also apply for 'short' monopiles with $0.5 \leq L/D \leq 2$, which nicely fills the gap in the current solution set (most formulations currently available for monopiles are meant for $L/D > 2$).

Chapter 4 There are two main sections in this chapter. The first section looks at the classic vertical stiffness problem for a rigid, circular surface foundation on non-homogeneous, linear elastic soil. The key contributions of this section are twofold.

1. This chapter provides verification on the reliability of two widely used design methods, that appear to conflict with each other.
2. Instead of just being an empirical comparison of these two design methods, this chapter introduces a novel theoretical framework to interpret them. This provides a common base to analyse these two design methods and provides a better understanding of the reasons behind the model accuracy or lack thereof.

The second section looks at the 6DoF stiffness problem for a suction caisson in non-homogeneous, linear elastic soil. The key contributions of this section are twofold.

1. A numerical study is presented to highlight the inadequacy of using Winkler models for suction caissons that have been calibrated for homogeneous soil, for analysis in non-homogeneous soil.
2. This section introduces a novel design method, termed the ‘modulus weighting method’, that determines the ‘equivalent homogeneous’ soil reactions for non-homogeneous soil. This design method is based on an energy-based framework and has been shown to be applicable to not only oxCaisson, but also other Winkler models that have been calibrated for homogeneous soil.

Chapter 5 This chapter demonstrates that the linear elastic soil reactions that were derived for rigid caissons may also be used to predict the behaviour of flexible caissons, simply by representing the caisson skirt with deformable frame elements. This indirectly shows that the linear elastic soil reactions are approximately independent of the suction caisson properties.

Chapter 6 The key contributions of this chapter are threefold.

1. A numerical study is presented to carry out full scale 3DFE analyses to investigate the existence of scaling relationships between the load-displacement behaviour of the soil reactions and elemental stress-strain behaviour. Previous studies used a highly simplified pile slice model to investigate the existence of these relationships.

2. This study investigates the existence of scaling relationships for the soil reactions in all 6DoF and for suction caisson foundations. Moreover, as the soil reactions for caisson foundations include a skirt component (typically associated with pile design methods) and a base component (typically associated with surface foundation design methods), this work can be considered as a generalisation of the previous studies on piles and surface foundations.
3. The identified scaling relationships allow convenient derivation of site-specific soil reactions that better correspond to the soil sample behaviour in laboratory tests, thus providing more realistic predictions of caisson behaviour.

Chapter 7 This chapter assesses the accuracy and efficiency of various numerical procedures for determining failure envelopes. The conclusion that the sequential swipe test is the best amongst the finite element based procedures is surprising, given the popularity of the displacement probe test.

Chapter 8 The key contribution of this chapter is the introduction of a systematic framework for formulation of globally convex and thermodynamically consistent n-dimensional failure envelopes that are suitable for use as yield functions and plastic potentials. The proposed framework overcomes some of the limitations of the existing formulations for failure envelopes, as follows. First, they are not always globally convex, which prevents the use of efficient, implicit elasto-plastic integration algorithms. Second, they are not guaranteed to be thermodynamically consistent if used as plastic potentials, as they may result in negative plastic work. Finally, the existing methods to formulate failure envelopes are generally ad hoc and not expressive enough to fit arbitrary datasets.

Chapter 9 The contributions of this chapter are twofold.

1. This work presents globally convex and thermodynamically consistent failure envelopes for rigid, circular surface foundations on von Mises soil under 6DoF loading.
2. ‘Failure envelopes’ for caisson foundations are derived on a local basis (i.e. the soil reaction yield surfaces), which provides key insights into the distribution of the soil response at failure. Furthermore, validation studies have shown that the global failure envelope can be accurately reproduced with the local soil reaction yield surfaces. The

advantage of deriving these soil reaction yield surfaces is that they could be applied directly to any arbitrary, non-homogeneous or multi-layered ground.

11.2 Future Directions

This thesis lays the foundational grounds for the oxCaisson family of design methods. It develops the theory and practical framework upon which future researchers can use, extend and apply to other foundation problems, not limited to just suction caisson foundations. Looking forward, oxCaisson may be extended to address other problems not covered in this thesis, some of which are highlighted below:

Cohesionless Soil The methodology in Chapter 9 may be similarly applied to derive soil reaction yield surface formulations for caissons in cohesionless soil. Cohesionless soil may be represented in the 3DFE analyses using linear elastic, perfectly plastic materials with pressure-sensitive yield criterion such as the Drucker-Prager yield criterion. This would enable oxCaisson-LEPP to predict caisson behaviour in sand, although the importance of non-associated flow would render this process non-trivial.

Non-homogeneous Yield Strength Profiles Chapter 4 shows that the naive predictions of oxCaisson-LE in non-homogeneous, linear elastic soil may be inaccurate. However, it is hypothesised that the naive predictions of oxCaisson-LEPP in grounds with arbitrary, non-homogeneous yield strength profiles is fairly accurate. This is because plastic response tends to be much more localised, compared to elastic response. However, this hypothesis needs to be confirmed by 3DFE analyses.

Interface effects All the 3DFE analyses in this thesis assume a fully bonded interface. Further analyses are required to assess the effect of gapping or different interface roughness on the soil reactions. At the moment, different interface roughness can be approximated by reducing the yield strength input into the soil reaction formulations. However, this heuristic measure has to be validated by 3DFE analyses.

Multiple Yield Surfaces with Hardening oxCaisson-LEPP may be extended to allow for multiple yield surfaces, which would allow the predicted load-displacement behaviour to agree better with the 3DFE results. Also, hardening rules (such as kinematic hardening) may be incorporated for more realistic predictions under cyclic loading, which is one aspect that is not covered in this thesis.

Appendix A

Appendix

A.1 Derivation of Stiffness Solution of Mayne & Poulos (1999)

The following exposition will explain the derivation of Eq. 4.3. Note that $G_{\mathrm{mayne}}, \tilde{\sigma}_{\mathrm{z}}, \tilde{\sigma}_{\mathrm{r}}$ and q_{z} have been defined in the main text. The main principle behind the design method of Mayne & Poulos (1999) is that the vertical displacement S_{z} at the centre of the foundation base is equal to the integration of the vertical strains directly beneath it:

$$\begin{aligned}
S_{\mathrm{z}} &= \int_0^{\infty} \varepsilon_{\mathrm{z}}\, dz \\
S_{\mathrm{z}} &= D \int_0^{\infty} \varepsilon_{\mathrm{z}}\, d\tilde{z} \\
S_{\mathrm{z}} &= D \int_0^{\infty} \frac{\sigma_{\mathrm{z}} - 2\nu\sigma_{\mathrm{r}}}{E}\, d\tilde{z} \\
S_{\mathrm{z}} &= q_{\mathrm{z}} D \int_0^{\infty} \frac{\tilde{\sigma}_{\mathrm{z}} - 2\nu\tilde{\sigma}_{\mathrm{r}}}{E}\, d\tilde{z}
\end{aligned} \tag{A.1}$$

Redefining E in terms of G:

$$\begin{aligned}
S_{\mathrm{z}} &= \frac{q_{\mathrm{z}} D}{2(1+\nu)} \int_0^{\infty} \frac{\tilde{\sigma}_{\mathrm{z}} - 2\nu\tilde{\sigma}_{\mathrm{r}}}{G}\, d\tilde{z} \\
S_{\mathrm{z}} \left(\frac{\pi D^2}{4}\right) &= \frac{VD}{2(1+\nu)} \int_0^{\infty} \frac{\tilde{\sigma}_{\mathrm{z}} - 2\nu\tilde{\sigma}_{\mathrm{r}}}{G}\, d\tilde{z} \\
\left(\frac{\pi D(1+\nu)}{2}\right) &= \frac{V}{S_{\mathrm{z}}} \int_0^{\infty} \frac{\tilde{\sigma}_{\mathrm{z}} - 2\nu\tilde{\sigma}_{\mathrm{r}}}{G}\, d\tilde{z} \\
\frac{V}{S_{\mathrm{z}}} &= \left(\frac{\pi D(1+\nu)}{2}\right) \frac{1}{\int_0^{\infty} \frac{\tilde{\sigma}_{\mathrm{z}} - 2\nu\tilde{\sigma}_{\mathrm{r}}}{G}\, d\tilde{z}} \\
\frac{V}{S_{\mathrm{z}}} &= \left(\frac{\pi D(1+\nu)}{2(1-\nu^2)}\right) \frac{1-\nu^2}{\int_0^{\infty} \frac{\tilde{\sigma}_{\mathrm{z}} - 2\nu\tilde{\sigma}_{\mathrm{r}}}{G}\, d\tilde{z}} \\
K_{\mathrm{V}} &= \left(\frac{\pi D}{2(1-\nu)}\right) G_{\mathrm{mayne}}
\end{aligned} \tag{A.2}$$

Eq. A.2 predicts the stiffness of a flexible, circular surface foundation. For a rigid, circular surface foundation, a factor of $\pi/4$ (Mayne & Poulos 1999) should be applied such that $(S_z)_{\text{flexible}} = (S_z)_{\text{rigid}} / (\pi/4)$, which produces Eq. 4.3 (copied below):

$$K_V = \frac{2D}{1-\nu} G_{\text{mayne}} \tag{A.3}$$

Homogeneous Half-space Since $\int_0^\infty \tilde{\sigma}_z - 2\nu\tilde{\sigma}_r \, d\tilde{z} = 1 - \nu^2$ for a homogeneous elastic half-space, substituting $G_{\text{mayne}} = G$ into Eq. A.3 gives the analytical solution (Eq. 4.2).

Flexible Foundation To reproduce the given formulation ($S_z = q_z D I_G (1-\nu^2)/E_b$) for a flexible, circular surface foundation in Fig. 10 of Mayne & Poulos (1999), $E(z) = E_b + k_E z$ can be substituted into Eq. A.1 (where E_b = Young's modulus at ground level and k_E = rate of change of the modulus with depth):

$$\begin{aligned} S_z &= q_z D \int_0^\infty \frac{\tilde{\sigma}_z - 2\nu\tilde{\sigma}_r}{E} \, d\tilde{z} \\ S_z &= \frac{q_z D}{E_b} \int_0^\infty \frac{\tilde{\sigma}_z - 2\nu\tilde{\sigma}_r}{1 + \tilde{z}/\beta} \, d\tilde{z} \\ S_z &= \frac{q_z D}{E_b} I_G (1-\nu^2) \end{aligned} \tag{A.4}$$

where

$$\begin{aligned} I_G &= \frac{1}{(1-\nu^2)} \int_0^\infty \frac{\tilde{\sigma}_z - 2\nu\tilde{\sigma}_r}{1 + \tilde{z}/\beta} \, d\tilde{z} \\ \beta &= E_b/(k_E D) \end{aligned}$$

If the half-space is homogeneous, $\beta = \infty$. Thus, $I_G = 1$. If the half-space has zero modulus at the ground level (i.e. $E_b = 0$), Eq. A.1 should be used to compute S_z instead of Eq. A.4. However, when carrying out the integration numerically, the integration limits should start from a small number e.g. 10^{-9}, as the integrand has a singularity at $z = 0$. For example,

$$\begin{aligned} S_z &= q_z D \int_{10^{-9}}^\infty \frac{\tilde{\sigma}_z - 2\nu\tilde{\sigma}_r}{k_E D \tilde{z}} \, d\tilde{z} \\ S_z &= \frac{q_z}{k_E} \int_{10^{-9}}^\infty \frac{\tilde{\sigma}_z - 2\nu\tilde{\sigma}_r}{\tilde{z}} \, d\tilde{z} \end{aligned} \tag{A.5}$$

For $\nu = 0.5$, this simplifies to:

$$\begin{aligned} S_z &= \frac{q_z}{2(1+\nu)k_G} \int_{10^{-9}}^\infty \frac{\tilde{\sigma}_z - 2\nu\tilde{\sigma}_r}{\tilde{z}} \, d\tilde{z} \\ S_z &= \frac{q_z}{2(1+0.5)k_G} (1.5) \\ S_z &= \frac{q_z}{2k_G} \end{aligned} \tag{A.6}$$

which matches the analytical solution of Gibson (1967), where k_G is the rate of change of the shear modulus with depth.

A.2 Computation of ε_q from Triaxial and Simple Shear Test Results

This section describes the computation of the deviatoric strain ε_q from the results of triaxial and simple shear tests. Expanding Eq. 6.7 in terms of the strain components:

$$\varepsilon_\mathrm{q} = \sqrt{\frac{4}{3}\left(\frac{1}{6}\left[(\varepsilon_{11}-\varepsilon_{22})^2+(\varepsilon_{22}-\varepsilon_{33})^2+(\varepsilon_{33}-\varepsilon_{11})^2\right]+\varepsilon_{12}^2+\varepsilon_{23}^2+\varepsilon_{31}^2\right)} \tag{A.7}$$

For simple shear tests, Eq. A.7 simplifies to:

$$\begin{aligned}\varepsilon_\mathrm{q} &= \sqrt{\frac{4}{3}\left(\frac{1}{6}\left[(\varepsilon_{11}-\varepsilon_{22})^2+(\varepsilon_{22}-\varepsilon_{33})^2+(\varepsilon_{33}-\varepsilon_{11})^2\right]+\varepsilon_{12}^2+\varepsilon_{23}^2+\varepsilon_{31}^2\right)}\\ &= \sqrt{\frac{4}{3}\left(0+(\gamma/2)^2+0\right)}\\ &= \frac{|\gamma|}{\sqrt{3}}\end{aligned} \tag{A.8}$$

where γ is the shear strain. For triaxial tests, Eq. A.7 simplifies to:

$$\begin{aligned}\varepsilon_\mathrm{q} &= \sqrt{\frac{4}{3}\left(\frac{1}{6}\left[(\varepsilon_{11}-\varepsilon_{22})^2+(\varepsilon_{22}-\varepsilon_{33})^2+(\varepsilon_{33}-\varepsilon_{11})^2\right]+\varepsilon_{12}^2+\varepsilon_{23}^2+\varepsilon_{31}^2\right)}\\ &= \sqrt{\frac{4}{3}\left(\frac{1}{6}\left[(\varepsilon_r-\varepsilon_r)^2+(\varepsilon_r-\varepsilon_a)^2+(\varepsilon_a-\varepsilon_r)^2\right]+0\right)}\\ &= \frac{2}{3}\left|\varepsilon_a-\varepsilon_r\right|\end{aligned} \tag{A.9}$$

where ε_a and ε_r are the axial and radial strain respectively. For undrained triaxial tests, $\varepsilon_r = -\varepsilon_a/2$, $\varepsilon_\mathrm{q} = \varepsilon_a$ and $\gamma_\mathrm{max} = \varepsilon_a - \varepsilon_r = 1.5\varepsilon_a$ (Powrie 2013). Thus, $\varepsilon_\mathrm{q} = 2\gamma_\mathrm{max}/3$.

A.3 Undrained Capacities of a Rigid, Circular Surface Foundation on Cohesive Soil under Torsional or Lateral Loading

Following the procedures described by Dunne & Martin (2017), the undrained capacities of a rigid, circular surface foundation on cohesive soil under torsional or lateral loading are determined. For torsional loading, the lower bound (LB) solution is obtained by assuming that at capacity, the magnitude of the soil shear stress at the soil-foundation interface is s_u in the shearing direction (see Fig. A.1). Thus, the LB torsional capacity Q_0 is:

$$\begin{aligned}Q_0 &= \int x\tau_\mathrm{y} - y\tau_\mathrm{x}\,dA\\ &= \int (r\cos\theta)s_\mathrm{u}\cos\theta + (r\sin\theta)s_\mathrm{u}\sin\theta\,dA\\ &= s_\mathrm{u}\int_0^{2\pi}\int_0^{D/2}\left(r\cos^2\theta + r\sin^2\theta\right)r\,dr\,d\theta\\ &= s_\mathrm{u}\pi D^3/12\end{aligned} \tag{A.10}$$

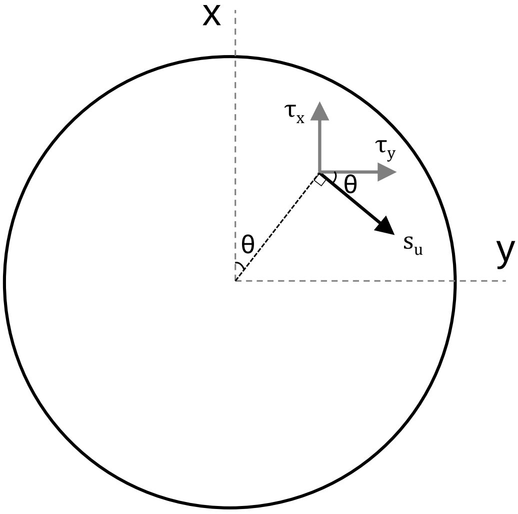

Figure A.1: Conventions for the soil shear stress components at some arbitrary point on the soil-foundation interface. Note that $\tau_\mathrm{x} = -s_\mathrm{u} \sin\theta$ and $\tau_\mathrm{y} = s_\mathrm{u} \cos\theta$.

The upper bound (UB) solution can be obtained by equating the internal and external work done for a virtual torsional displacement $\delta\Theta_\mathrm{z}$:

$$\begin{aligned} W^{\mathrm{ext}} &= W^{\mathrm{int}} \\ Q_0\, \delta\Theta_\mathrm{z} &= \int s_\mathrm{u} \left(r\delta\Theta_\mathrm{z}\right) dA \\ Q_0 &= s_\mathrm{u} \int_0^{2\pi} \int_0^{D/2} (r)\, r\, dr\, d\theta \\ Q_0 &= s_\mathrm{u} \pi D^3/12 \end{aligned} \tag{A.11}$$

The LB solution (which is not fully rigorous as it does not extend the interface stress field into the rest of the soil domain) matched exactly with the UB solution, indicating an exact theoretical solution. Thus, the normalised, analytical torsional capacity is $\frac{Q_0}{ADs_\mathrm{u}} = 1/3$, where $A = \pi D^2/4$ is the area of the surface foundation base.

Similarly, the LB solution for lateral loading can be obtained trivially as:

$$\begin{aligned} H_0 &= \int s_\mathrm{u}\, dA \\ H_0 &= s_\mathrm{u} A \end{aligned} \tag{A.12}$$

which matches exactly with the UB solution as follows:

$$\begin{aligned} W^{\mathrm{ext}} &= W^{\mathrm{int}} \\ H_0\, \delta S_\mathrm{H} &= \int s_\mathrm{u} \left(\delta S_\mathrm{H}\right) dA \\ H_0 &= s_\mathrm{u} A \end{aligned} \tag{A.13}$$

Thus, the normalised, analytical lateral capacity is $\frac{H_0}{As_\mathrm{u}} = 1$.

A.4 Undrained Capacities of a Rigid Suction Caisson Foundation in Cohesive Soil under Torsional Loading

The following exposition derives the torsional capacity of a rigid suction caisson on cohesive soil, following the procedures described by Dunne & Martin (2017). For torsional loading, the capacity Q_0 is the sum of the soil resistance along the caisson skirt ${Q_0}^{\mathrm{skirt}}$ and on the caisson base (including the soil plug) ${Q_0}^{\mathrm{base}}$. The lower bound (LB) solution for ${Q_0}^{\mathrm{base}}$ can be obtained using Eq. A.10, while the LB solution for ${Q_0}^{\mathrm{skirt}}$ is:

$$\begin{aligned}
{Q_0}^{\mathrm{skirt}} &= L \int x\tau_{\mathrm{y}} - y\tau_{\mathrm{x}}\, dl \\
&= L(D/2)^2 \int_0^{2\pi} (\cos\theta) s_{\mathrm{u}} \cos\theta + (\sin\theta) s_{\mathrm{u}} \sin\theta \, d\theta \\
&= L(D/2)^2 s_{\mathrm{u}} \int_0^{2\pi} \left(\cos^2\theta + \sin^2\theta\right) d\theta \\
&= s_{\mathrm{u}} \pi L D^2/2
\end{aligned} \tag{A.14}$$

Therefore, the LB solution for the torsional capacity is:

$$\begin{aligned}
Q_0 &= {Q_0}^{\mathrm{skirt}} + {Q_0}^{\mathrm{base}} \\
&= s_{\mathrm{u}} \pi L D^2/2 + s_{\mathrm{u}} \pi D^3/12 \\
&= s_{\mathrm{u}} \pi D^2 \left(L/2 + D/12\right)
\end{aligned} \tag{A.15}$$

Similarly, the upper bound (UB) solution for ${Q_0}^{\mathrm{base}}$ can be obtained using Eq. A.11, while the UB solution for ${Q_0}^{\mathrm{skirt}}$ can be obtained by equating the internal and external work done for a virtual torsional displacement $\delta\Theta_{\mathrm{z}}$:

$$\begin{aligned}
W^{\mathrm{ext}} &= W^{\mathrm{int}} \\
{Q_0}^{\mathrm{skirt}}\, \delta\Theta_{\mathrm{z}} &= L \int s_{\mathrm{u}} \left((D/2)\delta\Theta_{\mathrm{z}}\right) dl \\
{Q_0}^{\mathrm{skirt}} &= L(D/2)^2 s_{\mathrm{u}} \int_0^{2\pi} d\theta \\
{Q_0}^{\mathrm{skirt}} &= s_{\mathrm{u}} \pi L D^2/2
\end{aligned} \tag{A.16}$$

Therefore, the UB solution for the torsional capacity is $s_{\mathrm{u}} \pi D^2 \left(L/2 + D/12\right)$, which matched exactly with the LB solution, indicating an exact theoretical solution. Thus, the normalised, analytical torsional capacity is $\frac{Q_0}{ADs_{\mathrm{u}}} = 2(L/D) + 1/3$, where $A = \pi D^2/4$ is the area of the caisson base.

Bibliography

Achmus, M., Akdag, C. & Thieken, K. (2013), 'Load-bearing behavior of suction bucket foundations in sand', *Applied Ocean Research* **43**, 157–165.

Ahmadi, A. A., Olshevsky, A., Parrilo, P. A. & Tsitsiklis, J. N. (2013), 'NP-hardness of deciding convexity of quartic polynomials and related problems', *Mathematical Programming* **137**(1-2), 453–476.

Ahmadi, A. A. & Parrilo, P. A. (2012), 'A convex polynomial that is not sos-convex', *Mathematical Programming* **135**(1-2), 275–292.

API (2002), *Recommended Practice for Planning, Designing and Constructing Fixed Offshore Platforms — Working Stress Design*, 21st edn, API Publishing Services, Washington, D.C.

Astley, R. J. (1992), *Finite elements in solids and structures*, 1st edn, Chapman & Hall, London.

Atkinson, J. H. (2000), 'Non-linear soil stiffness in routine design', *Géotechnique* **50**(5), 487–508.

Aubeny, C. & Murff, J. D. (2005), 'Simplified limit solutions for the capacity of suction anchors under undrained conditions', *Ocean Engineering* **32**(7), 864–877.

Aubeny, C. P., Han, S. W. & Murff, J. D. (2003), 'Inclined load capacity of suction caissons', *International Journal for Numerical and Analytical Methods in Geomechanics* **27**(14), 1235–1254.

Bell, R. W. (1991), The analysis of offshore foundations subjected to combined loading, MSc thesis, University of Oxford.

Bienen, B., Byrne, B. W., Houlsby, G. T. & Cassidy, M. J. (2006), 'Investigating six-degree-of-freedom loading of shallow foundations on sand', *Géotechnique* **56**(6), 367–379.

Bienen, B., Klinkvort, R. T., O'Loughlin, C. D., Zhu, F. & Byrne, B. W. (2018*a*), 'Suction caissons in dense sand, part I: installation, limiting capacity and drainage', *Géotechnique* (Ahead of Print).

Bienen, B., Klinkvort, R. T., O'Loughlin, C. D., Zhu, F. & Byrne, B. W. (2018*b*), 'Suction caissons in dense sand, part II: vertical cyclic loading into tension', *Géotechnique* (Ahead of Print).

Booker, J. R., Balaam, N. P. & Davis, E. H. (1985), 'The behaviour of an elastic non-homogeneous half-space. Part II-circular and strip footings', *International Journal for Numerical and Analytical Methods in Geomechanics* **9**(4), 369–381.

Borowicka, H. (1943), 'Uber ausmittig belastete, starre Platten auf elastich-isotropem Untergrund', *Archive of Applied Mechanics* **14**, 1–8.

Boswell, L. F. & Scott, C. R. (1975), 'A flexible circular plate on a heterogeneous elastic half-space: influence coefficients for contact stress and settlement', *Géotechnique* **25**(3), 604–610.

Boussinesq, M. J. (1885), Application des potentiels a l'etude de l'equilibre et du mouvement des solides elastiques, principalement au calcul des deformations et des pressions que produisent, dans ces solides, des efforts quelconques exerces sur une petite partie de leur surface , Technical report, GauthierVillars, Paris.

Boyd, S. & Vandenberghe, L. (2004), *Convex optimization*, Cambridge University Press.

Bransby, M. F. (1999), 'Selection of p-y curves for the design of single laterally loaded piles', *International Journal for Numerical and Analytical Methods in Geomechanics* **23**(15), 1909–1926.

Bransby, M. F. & Randolph, M. F. (1998), 'Combined Loading of Skirted Foundations', *Géotechnique* **48**(5), 637–655.

Bransby, M. F. & Randolph, M. F. (1999), 'The effect of embedment depth on the undrained response of skirted foundations to combined loading', *Soils and Foundations* **39**(4), 19–33.

Bransby, M. F. & Yun, G. J. (2009), 'The undrained capacity of skirted strip foundations under combined loading', *Géotechnique* **59**(2), 115–125.

Butterfield, R., Houlsby, G. T. & Gottardi, G. (1997), 'Standardized sign conventions and notation for generally loaded foundations', *Géotechnique* **47**(5), 1051–1054.

Bye, A., Erbrich, C., Rognlien, B. & Tjelta, T. I. (1995), 'Geotechnical design of bucket foundations', *Proceedings of Offshore Technology Conference (OTC 7793)* .

Byrne, B. W. (2000), Investigations of Suction Caissons in Dense Sand, DPhil thesis, University of Oxford.

Byrne, B. W. & Houlsby, G. T. (2003), 'Foundations for offshore wind turbines.', *Philosophical transactions. Series A, Mathematical, physical, and engineering sciences* **361**(1813), 2909–30.

Byrne, B. W., Houlsby, G. T., Martin, C. M. & Fish, P. (2000), 'Suction Caisson Foundations for Offshore Wind Turbines', *Wind Engineering* **26**(3), 145 – 155.

Byrne, B. W., McAdam, R., Burd, H. J., Houlsby, G. T., Martin, C. M., Beuckelaers, W. J. A. P., Zdravkovic, L., Taborda, D. M. G., Potts, D. M., Jardine, R. J., Ushev, E., Liu, T., Abadias, D., Gavin, K., Igoe, D., Doherty, P., Skov Gretlund, J., Pacheco Andrade, M., Muir Wood, A., Schroeder, F. C., Turner, S. & Plummer, M. A. L. (2017), PISA: New Design Methods for Offshore Wind Turbine Monopiles, *in* 'Proceedings of the 8th International Conference for Offshore Site Investigation and Geotechnics', London.

Byrne, B. W., McAdam, R., Burd, H. J., Houlsby, G. T., Martin, C. M., Zdravkovic, L., Taborda, D. M. G., Potts, D. M., Jardine, R. J., Sideri, M., Schroeder, F. C., Gavin, K., Doherty, P., Igoe, D., Muir Wood, A., Kallehave, D. & Skov Gretlund, J. (2015), New design methods for large diameter piles under lateral loading for offshore wind applications, *in* '3rd International Symposium on Frontiers in Offshore Geotechnics (ISFOG 2015)', Oslo, pp. 10–12.

Carrier, W. D. & Christian, J. T. (1973), 'Rigid circular plate resting on a non-homogeneous elastic half-space', *Géotechnique* **23**(1), 67–84.

Cassidy, M. J. (1999), Non-linear analysis of jack-up structures subjected to random waves, DPhil thesis, University of Oxford.

Cassidy, M. J., Byrne, B. W. & Houlsby, G. T. (2002), 'Modelling the behaviour of circular footings under combined loading on loose carbonate sand', *Géotechnique* **52**(10), 705–712.

Cassidy, M. J., Martin, C. M. & Houlsby, G. T. (2004), 'Development and application of force resultant models describing jack-up foundation behaviour', *Marine Structures* **17**(3-4), 165–193.

Cassidy, M., Randolph, M. & Byrne, B. (2006), 'A plasticity model describing caisson behaviour in clay', *Applied Ocean Research* **28**(5), 345–358.

Cerfontaine, B., Collin, F. & Charlier, R. (2016), 'Numerical modelling of transient cyclic vertical loading of suction caissons in sand', *Géotechnique* **66**(2), 121–136.

Chen, W. F. & Liu, X. L. (1990), *Limit analysis and soil plasticity*, Elsevier Ltd., Amsterdam.

Darendeli, M. B. (2001), Development of a new family of normalized modulus reduction and material damping curves, PhD thesis, University of Texas at Austin.

Dassault Systèmes (2014), *Abaqus user manual*, Simula Corp., Providence, RI.

DNV (2013), *DNV-OS-J101 Design of Offshore Wind Turbine Structures*, Det Norske Veritas, Oslo, Norway.

Dobry, R., Vicente, E., O'Rourke, M. & Roesset, M. (1982), 'Horizontal stiffness and damping of single piles', *Journal of Geotechnical and Geoenvironmental Engineering* **108**(3), 439–459.

Doherty, J. P., Gourvenec, S. & Gaone, F. M. (2018), 'Insights from a shallow foundation load-settlement prediction exercise', *Computers and Geotechnics* **93**, 269–279.

Doherty, J. P., Houlsby, G. T. & Deeks, A. J. (2005), 'Stiffness of Flexible Caisson Foundations Embedded in Nonhomogeneous Elastic Soil', *Journal of Geotechnical and Geoenvironmental Engineering* **131**, 1498–1508.

Doherty, J. P. & Lehane, B. M. (2017), An Automated Approach for Designing Monopiles Subjected to Lateral Loads, *in* 'Proceedings of 36th International Conference on Ocean, Offshore Arctic Engineering, OMAE 2017', Trondheim, Norway.

Dormand, J. R. & Prince, P. J. (1980), 'A family of embedded Runge-Kutta formulae', *Journal of Computational and Applied Mathematics* **6**(1), 19–26.

Dunne, H. P. & Martin, C. M. (2017), 'Capacity of rectangular mudmat foundations on clay under combined loading', *Géotechnique* **67**(2), 168–180.

Dunne, H. P., Martin, C. M., Muir, L., Brown, N. & Wallerand, R. (2015), Undrained bearing capacity of skirted mudmats on inclined seabeds, *in* 'Frontiers in Offshore Geotechnics III', CRC Press, pp. 783–788.

Eason, G. & Shield, R. T. (1960), 'The plastic indentation of a semi-infinite solid by a perfectly rough circular punch', *J. Appl. Math. Phys. (ZAMP)* **11**(1), 33–43.

Erbrich, C. & Tjelta, T. I. (1999), Installation of Bucket Foundations and Suction Caissons in Sand - Geotechnical Performance, *in* 'Offshore Technology Conference', Houston, Paper 10990.

Fahey, M. & Carter, J. P. (1993), 'A finite element study of the pressuremeter test in sand using a nonlinear elastic plastic model', *Canadian Geotechnical Journal* **30**(2), 348–362.

Feng, X. & Gourvenec, S. (2015), 'Consolidated undrained load-carrying capacity of subsea mudmats under combined loading in six degrees of freedom', *Géotechnique* **65**(7), 563–575.

Feng, X., Randolph, M. F., Gourvenec, S. & Wallerand, R. (2014), 'Design approach for rectangular mudmats under fully three-dimensional loading', *Géotechnique* **64**(1), 51–63.

Foglia, A., Gottardi, G., Govoni, L. & Ibsen, L. B. (2015), 'Modelling the drained response of bucket foundations for offshore wind turbines under general monotonic and cyclic loading', *Applied Ocean Research* **52**, 80–91.

Fu, D., Bienen, B., Gaudin, C. & Cassidy, M. J. (2014), 'Undrained capacity of a hybrid subsea skirted mat with caissons under combined loading', *Canadian Geotechnical Journal* **51**(8), 934–949.

Fu, D., Gaudin, C., Tian, Y., Cassidy, M. J. & Bienen, B. (2017), 'Uniaxial Capacities of Skirted Circular Foundations in Clay', *Journal of Geotechnical and Geoenvironmental Engineering* **143**(7), 04017022.

Gao, H., Chiu, C.-H. & Lee, J. (1992), 'Elastic contact versus indentation modeling of multilayered materials', *International Journal of Solids and Structures* **29**(20), 2471–2492.

Gazetas, G. (1991), 'Formulas and Charts for Impedances of Surface and Embedded Foundations', *Journal of Geotechnical Engineering* **117**(9), 1363–1381.

Gerolymos, N. & Gazetas, G. (2006*a*), 'Development of Winkler model for static and dynamic response of caisson foundations with soil and interface nonlinearities', *Soil Dynamics and Earthquake Engineering* **26**(5), 363–376.

Gerolymos, N. & Gazetas, G. (2006*b*), 'Static and dynamic response of massive caisson foundations with soil and interface nonlinearities — validation and results', *Soil Dynamics and Earthquake Engineering* **26**(5), 377–394.

Gerolymos, N. & Gazetas, G. (2006*c*), 'Winkler model for lateral response of rigid caisson foundations in linear soil', *Soil Dynamics and Earthquake Engineering* **26**(5), 347–361.

Gerolymos, N., Zafeirakos, A. & Karapiperis, K. (2015), 'Generalized failure envelope for caisson foundations in cohesive soil: Static and dynamic loading', *Soil Dynamics and Earthquake Engineering* **78**, 154–174.

Gibson, R. (1967), 'Some results concerning displacements and stresses in a non-homogeneous elastic halfspace', *Géotechnique* **17**(1), 58–67.

Gottardi, G. & Butterfield, R. (1993), 'On the bearing capacity of surface footings on sand under general planar loads', *Soils and Foundations* **33**(3), 68–79.

Gottardi, G., Houlsby, G. T. & Butterfield, R. (1999), 'Plastic response of circular footings on sand under general planar loading', *Géotechnique* **49**(4), 453–469.

Gourvenec, S. (2007), 'Failure envelopes for offshore shallow foundations under general loading', *Géotechnique* **57**(9), 715–728.

Gourvenec, S. & Barnett, S. (2011), 'Undrained failure envelope for skirted foundations under general loading', *Géotechnique* **61**(3), 263–270.

Gourvenec, S. & Randolph, M. F. (2003), 'Effect of strength non-homogeneity on the shape of failure envelopes for combined loading of strip and circular foundations on clay', *Géotechnique* **53**(6), 575–586.

Green, A. (1954), 'The plastic yielding of metal junctions due to combined shear and pressure', *Journal of the Mechanics and Physics of Solids* **2**(3), 197–211.

Guo, W. D. & Randolph, M. F. (1996), 'Torsional Piles in Non-homogeneous Media', *Computers and Geotechnics* **19**(4), 265–286.

Guo, W. D. & Randolph, M. F. (1997), 'Vertically loaded piles in non-homogeneous media', *International Journal for Numerical and Analytical Methods in Geomechanics* **21**(8), 507–532.

Hardin, B. O. & Black, W. L. (1966), 'Sand stiffness under various triaxial stresses', *Journal of Soil Mechanics and Foundation Division* **92**(SM2), 667–692.

Hardin, B. O. & Black, W. L. (1968), 'Vibration modulus of normally consolidated clays', *Journal of Soil Mechanics and Foundation Division* **94**(SM2), 353–369.

Hardin, B. O. & Drnevich, V. P. (1972), 'Shear Modulus and Damping in Soils: Design Equations and Curves', *Journal of Soil Mechanics and Foundation Division* (SM7), 667–692.

Houlsby, G. T. & Byrne, B. W. (2001), 'Discussion: Comparison of European bearing capacity calculation methods for shallow foundations', *Proceedings of the Institution of Civil Engineers - Geotechnical Engineering* **149**(1), 63–64.

Houlsby, G. T. & Byrne, B. W. (2005*a*), 'Design procedures for installation of suction caissons in clay and other materials', *Proceedings of the Institution of Civil Engineers - Geotechnical Engineering* **158**(2), 75–82.

Houlsby, G. T. & Byrne, B. W. (2005*b*), 'Design procedures for installation of suction caissons in sand', *Proceedings of the Institution of Civil Engineers - Geotechnical Engineering* **158**(3), 135–144.

Houlsby, G. T. & Cassidy, M. J. (2002), 'A plasticity model for the behaviour of footings on sand under combined loading', *Géotechnique* **52**(2), 117–129.

Houlsby, G. T., Ibsen, L. B. & Byrne, B. W. (2005), Suction caissons for wind turbines, *in* 'Frontiers in Offshore Geotechnics: ISFOG 2005', Perth, pp. 75–94.

Houlsby, G. T., Kelly, R. B., Huxtable, J. & Byrne, B. W. (2005), 'Field trials of suction caissons in clay for offshore wind turbine foundations', *Géotechnique* **55**(4), 287–296.

Huang, J. & Griffiths, D. V. (2009), 'Return Mapping Algorithms and Stress Predictors for Failure Analysis in Geomechanics', *Journal of Engineering Mechanics* **135**(4), 276–284.

Hughes, T. J. R. (2000), *The Finite Element Method: Linear Static and Dynamic Finite Element Analysis*, Dover Publications, New York.

Hung, L. C. & Kim, S. (2014), 'Evaluation of Undrained Bearing Capacities of Bucket Foundations Under Combined Loads', *Marine Georesources and Geotechnology* **32**(1), 76–92.

Hutchinson, J. R. (2001), 'Shear Coefficients for Timoshenko Beam Theory', *Journal of Applied Mechanics* **68**(1), 87–92.

Kallehave, D., Byrne, B. W., LeBlanc Thilsted, C. & Mikkelsen, K. K. (2015), 'Optimization of monopiles for offshore wind turbines.', *Philosophical Transactions of the Royal Society A, Mathematical, Physical, and Engineering Sciences* **373**, 1–15.

Karapiperis, K. & Gerolymos, N. (2014), 'Combined loading of caisson foundations in cohesive soil: Finite element versus Winkler modeling', *Computers and Geotechnics* **56**, 100–120.

Karatzia, X. & Mylonakis, G. (2017), 'Horizontal Stiffness and Damping of Piles in Inhomogeneous Soil', *Journal of Geotechnical and Geoenvironmental Engineering* **143**(4), 04016113.

Kassir, M. K. & Chuaprasert, M. F. (1974), 'A Rigid Punch in Contact With a Nonhomogeneous Elastic Solid', *Journal of Applied Mechanics* **41**(4), 1019–1024.

Kelly, R. B., Houlsby, G. T. & Byrne, B. W. (2006), 'A comparison of field and laboratory tests of caisson foundations in sand and clay', *Géotechnique* **56**(9), 617–626.

Kraft, L., Ray, R. & Kagawa, T. (1981), 'Theoretical t-z curves', *Journal of the Geotechnical Engineering Division,. ASCE* **107**(11), 1543–1561.

Lehane, B. M., Elkhatib, S. & Terzaghi, S. (2014), 'Extraction of suction caissons in sand', *Géotechnique* **64**(9), 735–739.

Löfberg, J. (2004), YALMIP : a toolbox for modeling and optimization in MATLAB, *in* '2004 IEEE International Conference on Robotics and Automation', IEEE, pp. 284–289.

Löfberg, J. (2009), 'Pre- and post-processing sum-of-squares programs in practice', *IEEE Transactions on Automatic Control* **54**(5), 1007–1011.

Makrodimopoulos, A. & Martin, C. M. (2006), 'Lower bound limit analysis of cohesive-frictional materials using second-order cone programming', *International Journal for Numerical Methods in Engineering* **66**(4), 604–634.

Makrodimopoulos, A. & Martin, C. M. (2007), 'Upper bound limit analysis using simplex strain elements and second-order cone programming', *International Journal for Numerical and Analytical Methods in Geomechanics* **31**(6), 835–865.

Mana, D. S. K., Gourvenec, S. & Martin, C. M. (2013), 'Critical Skirt Spacing for Shallow Foundations under General Loading', *Journal of Geotechnical and Geoenvironmental Engineering* **139**(9), 1554–1566.

Martin, C. M. (1994), Physical and Numerical Modelling of Offshore Foundations Under Combined Loads, DPhil thesis, University of Oxford.

Martin, C. M. (2011), 'The use of adaptive finite-element limit analysis to reveal slip-line fields', *Géotechnique Letters* **1**, 23–29.

Martin, C. M. & Houlsby, G. T. (2000), 'Combined loading of spudcan foundations on clay: laboratory tests', *Géotechnique* **50**(4), 325–338.

Martin, C. M. & Houlsby, G. T. (2001), 'Combined loading of spudcan foundations on clay: numerical modelling', *Géotechnique* **51**(8), 687–699.

Martin, C. M. & White, D. J. (2012), 'Limit analysis of the undrained bearing capacity of offshore pipelines', *Géotechnique* **62**(9), 847–863.

Mayne, P. W. & Poulos, H. G. (1999), 'Approximate Displacement Influence Factors for Elastic Shallow Foundations', *Journal of Geotechnical and Geoenvironmental Engineering* **125**(6), 453–460.

Mehravar, M., Harireche, O. & Faramarzi, A. (2016), 'Evaluation of undrained failure envelopes of caisson foundations under combined loading', *Applied Ocean Research* **59**, 129–137.

Meyerhof, G. G. (1951), 'The Ultimate Bearing Capacity of Foudations', *Géotechnique* **2**, 301–332.

Mindlin, R. D. (1936), 'Force at a point in the interior of a semi-infinite solid', *Physics* **7**(5), 195–202.

Mindlin, R. D. (1949), 'Compliance of elastic bodies in contact', *Journal of Applied Mechanics* **16**, 259–268.

Mosek (2014), *MOSEK modeling manual*.

Murchison, J. M. & O'Neill, M. W. (1983), Evaluation of p-y relationships in cohesionless soils, Technical report, American Petroleum Institute, Houston, Texas.

Nouri, H., Biscontin, G. & Aubeny, C. P. (2014), 'Undrained Sliding Resistance of Shallow Foundations Subject to Torsion', *Journal of Geotechnical and Geoenvironmental Engineering* **140**(8), 04014042.

Nova, R. & Montrasio, L. (1991), 'Settlements of shallow foundations on sand', *Géotechnique* **41**(2), 243–256.

Novak, M., Aboul-Ella, F. & Nogami, T. (1978), 'Dynamic soil reactions for plane strain case', *Journal of the Engineering Mechanics Division* **104**(4), 953–959.

ORE Catapult (2017), Cost Reduction Monitoring Framework 2016 - Summary Report to the Offshore Wind Programme Board, Technical Report January 2016.

Osman, A. S., White, D. J., Britto, A. M. & Bolton, M. D. (2007), 'Simple prediction of the undrained displacement of a circular surface foundation on non-linear soil', *Géotechnique* **57**(9), 729–737.

Ottosen, N. S. & Ristinmaa, M. (2005), *The mechanics of constitutive modeling*, Elsevier.

Oztoprak, S. & Bolton, M. D. (2013), 'Stiffness of sands through a laboratory test database', *Géotechnique* **63**(1), 54–70.

Palix, E., Willems, T. & Kay, S. (2010), Caisson capacity in clay : VHM resistance envelope – Part 1 : 3D FEM numerical study, *in* 'Proceedings of Frontiers in Offshore Geotechnics (ISFOG)', Perth, pp. 753–758.

Panteghini, A. & Lagioia, R. (2014), 'A fully convex reformulation of the original Matsuoka-Nakai failure criterion and its implicit numerically efficient integration algorithm', *International Journal for Numerical and Analytical Methods in Geomechanics* **38**(6), 593–614.

Parrilo, P. A. (2003), 'Semidefinite programming relaxations for semialgebraic problems', *Mathematical Programming* **96**(2), 293–320.

Poulos, H. G. (1979), 'Settlement of single piles in non homogeneous soil', *Journal of Geotechnical Engineering Div. A, A.S.C.E* **105**(5), 627–641.

Poulos, H. G. & Davis, E. H. (1974), *Elastic solution for soil and rock mechanics*, John Wiley & Sons, New York.

Powrie, W. (2013), *Soil mechanics: concepts and applications*, CRC Press.

Randolph, M. F. & Puzrin, A. M. (2003), 'Upper bound limit analysis of circular foundations on clay under general loading', *Géotechnique* **53**(9), 785–796.

Reddy, J. N. (2015), *An Introduction to Nonlinear Finite Element Analysis: With Applications to*

Heat Transfer, Fluid Mechanics, and Solid Mechanics, second edn, Oxford University Press, Oxford.

Reissner, E. (1944), 'On the Theory of Elastic Plates', *Journal of Mathematics and Physics* **23**, 184–191.

Roscoe, K. & Schofield, A. N. (1957), 'The stability of short pier foundations in sand', *British Welding Journal* pp. 12–18.

Russell, S. & Norvig, P. (2005), *Artificial Intelligence: A Modern Approach*, 3rd edn, Pearson, New Jersey.

Salciarini, D. & Tamagnini, C. (2009), 'A hypoplastic macroelement model for shallow foundations under monotonic and cyclic loads', *Acta Geotechnica* **4**(3), 163–176.

Selvadurai, A. P. S. (1996), 'The settlement of a rigid circular foundation resting on a half-space exhibiting a near surface elastic non-homogeneity', *International Journal for Numerical and Analytical Methods in Geomechanics* **20**, 351–364.

Shen, Z., Bie, S. & Guo, L. (2017), 'Undrained capacity of a surface circular foundation under fully three-dimensional loading', *Computers and Geotechnics* **92**, 57–67.

Shen, Z., Feng, X. & Gourvenec, S. (2016), 'Undrained capacity of surface foundations with zero-tension interface under planar V-H-M loading', *Computers and Geotechnics* **73**, 47–57.

Shibuya, S., Hwang, S. & Mitachi, T. (1997), 'Elastic shear modulus of soft clays from shear wave velocity measurement', *Géotechnique* **47**(3), 593–601.

Shield, R. (1955), On the plastic flow of metals under conditions of axial symmetry, *in* 'Proceedings of the Royal Society A: Mathematical, Physical and Engineering Sciences', Vol. 233, pp. 267–287.

Shonberg, A., Harte, M., Aghakouchak, A., Brown, C. S. D., Pacheco Andrade, M. & Liingaard, M. A. (2017), Suction bucket jackets for offshore wind turbines: applications from in situ observations, *in* 'Proceedings of TC 209 Workshop - 19th International Conference on Soil Mechanics and Geotechnical Engineering (ICSMGE)', Seoul, pp. 65–77.

Si, H. (2015), 'TetGen, a Quality Tetrahedral Mesh Generator', *AMC Transactions on Mathematical Software* **41**(2), 11.

Simo, J. C. & Taylor, R. L. (1985), 'Consistent tangent operators for rate-independent elastoplasticity', *Computer Methods in Applied Mechanics and Engineering* **48**(1), 101–118.

Spence, D. A. (1968), 'Self Similar Solutions to Adhesive Contact Problems with Incremental Loading', *Proceedings of the Royal Society of London. Series A. Mathematical and Physical Sciences* **305**(1480), 55–80.

Sturm, J. F. (1999), 'Using SeDuMi 1.02, a MATLAB toolbox for optimization over symmetric cones', *Optimization Methods and Software* **11**(1), 625–653.

Suryasentana, S. K., Byrne, B. W. & Burd, H. J. (2017), Weighting functions for the stiffness of circular surface footings on multi-layered non-homogeneous elastic half-spaces under general loading, *in* 'Proceedings of 19th International Conference on Soil Mechanics and Geotechnical Engineering (ICSMGE)', Seoul.

Suryasentana, S. K. & Lehane, B. M. (2014), 'Numerical derivation of CPT-based p–y curves for piles in sand', *Géotechnique* **64**(3), 186–194.

Taiebat, H. A. & Carter, J. P. (2000), 'Numerical studies of the bearing capacity of shallow foundations on cohesive soil subjected to combined loading', *Geotechnique* **50**(4), 409–418.

Taiebat, H. A. & Carter, J. P. (2010), 'A failure surface for circular footings on cohesive soils', *Géotechnique* **60**(4), 265–273.

Tan, F. (1990), Centrifuge and theoretical modelling of conical footings on sand, PhD thesis, University of Cambridge.

Terzaghi, K. (1943), *Theoretical Soil Mechanics*, John Wiley and Sons, New York.

Thieken, K., Achmus, M. & Schröder, C. (2014), 'On the behavior of suction buckets in sand under tensile loads', *Computers and Geotechnics* **60**, 88–100.

Tran, M. N. & Randolph, M. F. (2008), 'Variation of suction pressure during caisson installation in sand', *Géotechnique* **58**(1), 1–11.

Vardanega, P. J. & Bolton, M. D. (2013), 'Stiffness of Clays and Silts : Normalizing Shear Modulus and Shear Strain', *Journal of Geotechnical and Geoenvironmental Engineering* **9**, 1575–1589.

Vardanega, P. J. & Bolton, M. D. (2014), 'Stiffness of Clays and Silts: Modeling Considerations', *Journal of Geotechnical and Geoenvironmental Engineering* **140**(6), 06014004.

Varun, Assimaki, D. & Gazetas, G. (2009), 'A simplified model for lateral response of large diameter caisson foundations-Linear elastic formulation', *Soil Dynamics and Earthquake Engineering* **29**(2), 268–291.

Vásquez, L. F. G., Maniar, D. R. & Tassoulas, J. L. (2010), 'Installation and Axial Pullout of Suction Caissons: Numerical Modeling', *Journal of Geotechnical and Geoenvironmental Engineering* **136**(8), 1137–1147.

Vesić, A. (1973), 'Analysis of Ultimate Loads of Shallow Foundations', *Journal of the Soil Mechanics and Foundations* **99**(1), 45–73.

Vrettos, C. (1991), 'Time-harmonic boussinesq problem for a continuously non-homogeneous soil', *Earthquake Engineering Structural Dynamics* **20**, 961–977.

Vulpe, C. (2015), 'Design method for the undrained capacity of skirted circular foundations under combined loading: effect of deformable soil plug', *Géotechnique* **65**(8), 669–683.

Vulpe, C., Gourvenec, S. & Power, M. (2014), 'A generalised failure envelope for undrained capacity of circular shallow foundations under general loading', *Géotechnique Letters* **4**(3), 187–196.

WindEurope (2017), The European offshore wind industry - Key trends and statistics 2016, Technical report.

Winkler, E. (1867), *Die Lehre von der Elastizitat und Festigkeit*, Dominicus, Prague.

Wroth, C. P., Randolph, M. F., Houlsby, G. T. & Fahey, M. (1979), A review of the engineering properties of soils with particular reference to the shear modulus, Technical report, CUED/D-Soils TR75, Cambridge University Engineering Department, Cambridge.

Zdravković, L., Taborda, D. M. G., Potts, D. M., Jardine, R. J., Sideri, M., Schroeder, F. C., Byrne, B. W., McAdam, R., Burd, H. J., Houlsby, G. T., Martin, C. M., Gavin, K., Doherty, P., Igoe, D., Muir Wood, A., Kallehave, D. & Skov Gretlund, J. (2015), Numerical modelling of large diameter piles under lateral loading for offshore wind applications, *in* '3rd International Symposium on Frontiers in Offshore Geotechnics (ISFOG 2015)', pp. 759–764.

Zhang, Y. & Andersen, K. H. (2017), 'Scaling of lateral pile p-y response in clay from laboratory stress-strain curves', *Marine Structures* **53**, 124–135.

Zhang, Y., Bienen, B., Cassidy, M. J. & Gourvenec, S. (2011), 'The undrained bearing capacity of a spudcan foundation under combined loading in soft clay', *Marine Structures* **24**(4), 459–477.

Zhu, B., Byrne, B. W. & Houlsby, G. T. (2013), 'Long-Term Lateral Cyclic Response of Suction Caisson Foundations in Sand', *Journal of Geotechnical and Geoenvironmental Engineering* **139**(1), 73–83.